Title	トラップ誘起持続発光材料のメカニズムと応用
Author(s)	林, 存鍵
Citation	
Issue Date	2025-03
Type	Thesis or Dissertation
Text version	ETD
URL	http://hdl.handle.net/10119/19930
Rights	
Description	Supervisor: 上田 純平, 先端科学技術研究科, 博士

Japan Advanced Institute of Science and Technology

Doctoral Dissertation

Mechanisms and Applications

of Trap-Induced Persistent Luminescence Materials

Cunjian Lin

Supervisor: Jumpei Ueda

Graduate School of Advanced Science and Technology

Japan Advanced Institute of Science and Technology

Materials Science

March 2025

Abstract

In **Chapter 1**, I first explore the historical development of organic and inorganic Persistent Luminescence (PersL) materials, then review the major types of PersL materials and key breakthrough works, as well as their operating principles and typical applications.

Chapter 2 provides a comprehensive overview of the fundamental theoretical principles underlying organic and inorganic long-lasting emission. The mechanisms of organic afterglow include: (1) afterglow resulting from triplet-to-singlet spin-forbidden transitions (phosphorescence and delayed fluorescence), (2) PersL arising from charge-separated states (electron transporting mode, hole transporting mode, and two-photon ionization), (3) trap-induced PersL, and (4) chemiluminescence. In the case of inorganic PersL, the mechanisms involve: (1) the electron trapping-detrapping model, (2) the hole trapping-detrapping model, and (3) the bandgap engineering effect. Furthermore, five stimulation methods are introduced for trap-induced PersL in both organic and inorganic materials, including: (1) thermal stimulation, (2) optical stimulation, (3) mechanical stimulation, (4) electrical stimulation, and (5) magnetic stimulation.

Chapters 3-6 constitute the core of this thesis, structured as follows: Abstract, Introduction, Experimental Procedure, Results and Discussion, Conclusion, Reference, and Supporting Information. Notably, the problems or challenges in the PersL field, as well as the significance of the undertaken research works, will be thoroughly addressed in the 'Introduction' part. **Chapters 1-2** provide both the data support and theoretical foundation needed for the research topics. In trap-induced PersL systems, two key research targets emerge: trap and luminescent center. From a mechanistic perspective, **Chapter 3** primarily focuses on the depth regulation of trap states, while **Chapters 4-6** concentrate on the modulation of emission color and the excitation forms at the luminescent centers. From an application standpoint, **Chapters 3-4** emphasize optical

information storage and anti-counterfeiting, whereas **Chapters 5-6** focus on the application of electroluminescent TTIs.

In **Chapter 3**, we introduced a novel TADF guest, incorporating electron-accepting naphthalimide with two cyan groups into a host-guest PersL system, revealing for the first time the link between molecular design and trap depth. The D-A-D wedge-shaped TADF emitter TCN was employed, enabling multi-mode excitation, deep traps, low aggregation-induced quenching, and high thermal stability. UV, visible light (425-630 nm), and X-rays efficiently triggered deep traps (~0.72 eV), closely matching theoretical calculations. TL at 385 K, with NIR stimulation up to 1300 nm, allowed retention for over 45 days. This multi-mode optical storage system extended applications to blue-laser writing, X-ray time-lapse imaging, and NIR electronic signatures.

In **Chapter 4**, inspired by charge separation in organic xCT systems and charge trapping/detrapping in inorganic PersL phosphors, we introduced xCT states and trap states into a host-guest organic system to achieve visible-light-charged NIR PersL. For the first time, xCT interactions enabled efficient charge separation across excitation wavelengths from 380 to nearly 700 nm. By engineering energy levels, we achieved NIR PersL with durations exceeding 4 hours in a pTAP@TPBi film, setting a record for organic systems. We also demonstrated a trap depth over 1.0 eV under visible light excitation. This approach, validated across various charge transfer aggregates, allowed tunable trap depths and emission wavelengths by adjusting electron-donating segments. Exploiting the exceptional light energy storage of organics, we proposed triple-mode NIR anti-counterfeiting using mobile phone flashlights and information storage *via* blue laser direct writing.

In **Chapter 5**, we used TIP in host-guest systems to create a unique OLED emission layer, achieving over 100 s of afterglow and 60 min of energy storage after charging with a direct current electric field. This marked a record for the longest electrically excited afterglow in light-emitting devices. The mechanism involved the capture of

injected holes and electrons by luminescent centers and traps in the emission layer. The trap depth, measured at 0.24 eV under electrical charging, aligned with optical excitation results, confirming electrical charging as an efficient trigger for PersL. The temperature-dependent decay and energy storage properties expanded OLED applications to TTIs.

In **Chapter 6**, we developed structurally optimized AC electroluminescent devices (ELDs) incorporating zinc sulfide PersL phosphors encapsulated in high-dielectric-constant alumina (ZnS@AlOx), achieving AC-driven inorganic PersL for the first time. The PersL intensity in these devices lasted over 15 minutes post-AC charging, setting a record for electrically excited afterglow duration. The mechanism involved the capture of separated electrons by intrinsic defects in metal-doped ZnS under AC-driven hot-electron impact. The estimated trap depth of 0.32 eV under AC charging aligned with results from light irradiation, demonstrating the efficiency of electrical charging in triggering PersL. With temperature-dependent decay characteristics and over 24 hours of energy storage, these ELDs showed potential for applications as TTIs.

Keywords

Persistent Luminescence, Trap State, Luminescent Center, Light Energy Storage, Thermal Stimulation

Contents

Chapter 1

General Introduction

Persistent Luminescence (PersL), also referred to as "afterglow", is a phenomenon of prolonged light emission lasting from microseconds to days after turning off the excitation sources. This material has garnered considerable attention in the potential applications, including emergency sign, light-emitting diodes (LEDs), bioimaging, information storage, sensing, *etc.*[1-4] Inorganic PersL materials have a rich history spanning over 1,000 years, with early mentions in the Chinese text 湘山野录 from 960-1279 A.D.[1] The first scientific reports on afterglow phenomenon emerged in the 17th century with the Bologna stone, synthesized from barite ($BaSO_4$), marking the dawn of modern PersL materials.[5] Until the late 19th century, zinc sulfide doped with copper (ZnS:Cu) became the predominant afterglow material, widely utilized in military and civilian applications.[1] However, its limited performance led researchers to incorporate radioactive elements [radium (Ra), promethium (Pm) or tritium (^3H)] to enhance light output, raising significant health concerns by the 1990s and causing a decline in its use.[1] In response, Nemoto & Co. developed a new generation of afterglow phosphors, culminating in the creation of $SrAl_2O_4$:Eu^{2+}, Dy^{3+} in 1996.[6] This phosphor offered substantially brighter and longer afterglow properties without relying on radioactive materials. In the past two decades, lanthanide-doped aluminates and silicates such as $CaAl_2O_4$:Eu^{2+}, Nd^{3+},[7] $Sr_4Al_{14}O_{25}$: Eu^{2+}, Dy^{3+},[8, 9] and $Sr_2MgSi_2O_7$:Eu^{2+}, Dy^{3+} [10] have achieved commercial success.

In comparison, the discovery and research of organic PersL materials began later. The discovery of long-lifetime organic phosphorescence was first reported in 1895.[11] In 1933, phosphorescence was recognized as a spin-forbidden transition from the lowest triplet to the ground state.[12] After that, significant advancements have been realized in controlling excited-state lifetimes, extending applications to bioimaging and organic LEDs (OLEDs).[13, 14] Meanwhile, the concept of thermally activated delayed

fluorescence (TADF) was reported in 1964. In 2012, TADF-typed OLEDs was realized, achieving 100% internal efficiency in pure organics through precise modification of the energy gap.[15]

Great success has been made in organic and inorganic PersL material systems and related applications. Before systematically introducing research progress in the past decades, we first need to make a distinction between the different naming conventions of the 'glow-in-the-dark' phenomenon. In the inorganic system, the naming convention for afterglow is relatively straightforward and is generally referred to as 'PersL'. The mechanism of inorganic PersL is usually considered to be induced by trap states, which include intrinsic defects and energy gap.[1, 2, 16] In contrast, in organic systems, the naming convention of afterglow is inconsistent. According to the differences in the emission color, the phenomenon of afterglow is widely accepted to be referred as 'phosphorescence' or 'delayed fluorescence'.[17] Among them, phosphorescence is bathochromic shifted compared to fluorescence emission wavelengths. Depending on performance, it can also be referred to as 'ultralong organic phosphorescence' (UOP), 'room-temperature phosphorescence' (RTP), *etc*.[18, 19] Meanwhile, delayed fluorescence has the same emission wavelength and peak shape as fluorescence. Based on the underlying mechanism, it can be further divided into 'TADF', [20] 'triplet-triplet annihilation' (TTA) delayed fluorescence, [21] 'hybridized local and charge-transfer state' (HLCT) delayed fluorescence, [22] *etc*. Notably, compared to fluorescence, the longer lifetime of phosphorescence or delayed fluorescence is typically ranging from microseconds to seconds. In 2017, Prof. Adachi and Prof. Kabe from Kyushu University developed hour-level afterglow based on charge-separated and recombination states, which they named long PersL (LPL).[23] The duration of the exciplex is similar to that of the inorganic PersL system. Furthermore, in our recently published work in *Nature Photonics*, I and collaborators revealed that there are also trap states in organic PersL systems, and we named this system 'trap-induced PersL' (TIP).[24] A detailed description of the mechanism will be provided in **Chapter 2**. In the

four works discussed in this dissertation (**Chapters 3-6**), both the organic and inorganic material systems involve trap-induced PersL.

Section 1.1 reviews the main types of PersL materials and the related breakthrough works, aiming to establish a connection between material types and PersL performance. **Section 1.2** reviews the usage principles and typical applications. **Section 1.3** briefly describes this dissertation.

1.1 Introduction of Persistent Luminescence Materials

1.1.1 Organic Persistent Luminescence Materials

Organic PersL materials are attracting increasing attention due to their remarkable optical properties and unique advantages, such as intrinsic flexibility, ease of molecular structure modification, and suitability for large-area processing.[17, 18, 25, 26] In this part (**1.1.1**), deep-trap PersL materials are categorized into five types based on the major compositions, including (1) single-component crystals or amorphous powders, (2) host-guest complexes or blend films, (3) polymers, (4) nanoparticles, and (5) organic-inorganic hybrids. The molecular formula, usable excitation light sources, PersL wavelength (emission peak), and lifetime or decay time of these materials are summarized in Table 1.1. Moreover, a brief review will be provided of several breakthrough studies involving five organic PersL systems.
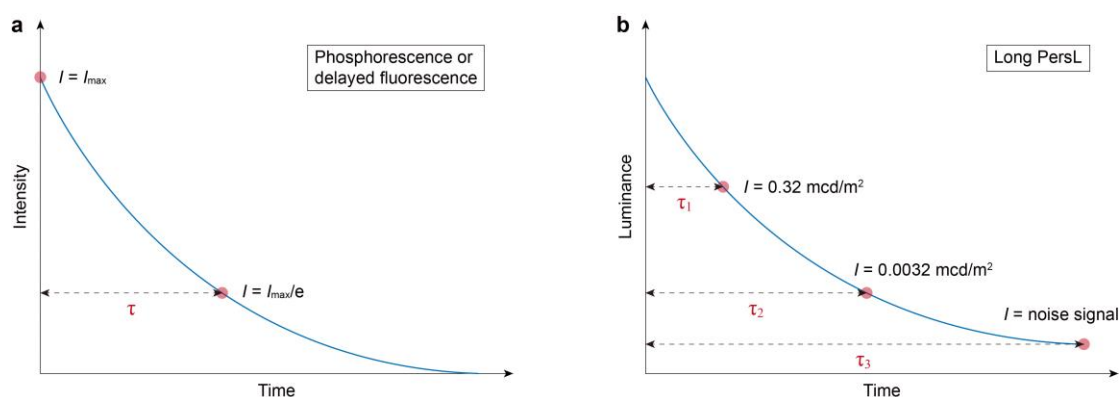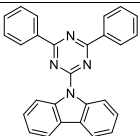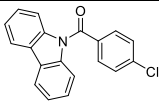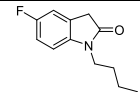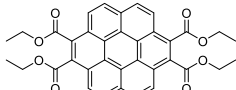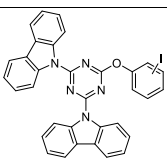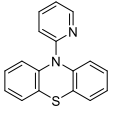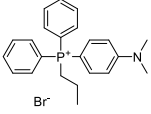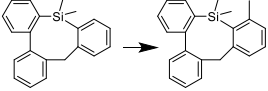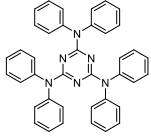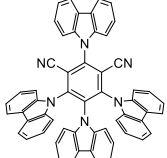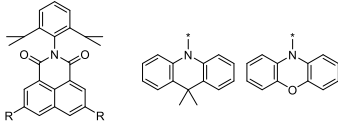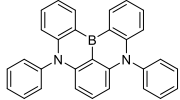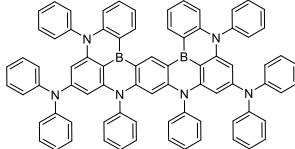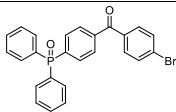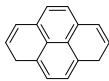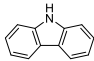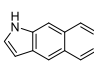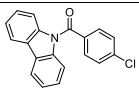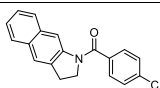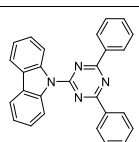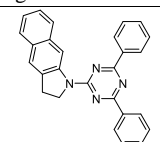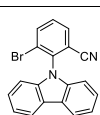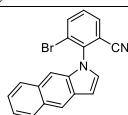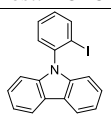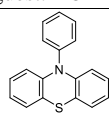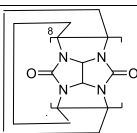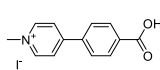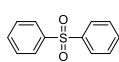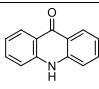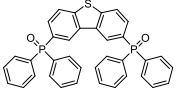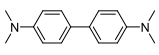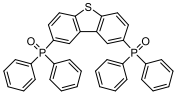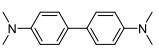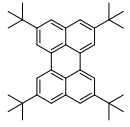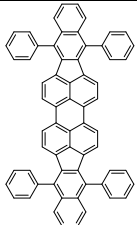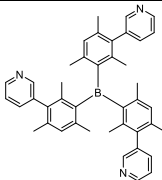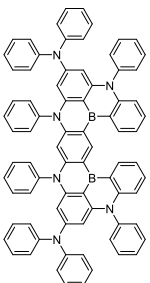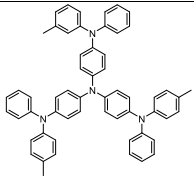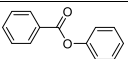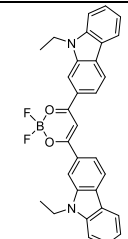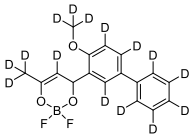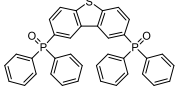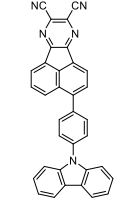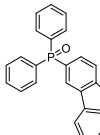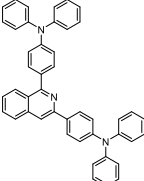
Figure 1.1 Definition of lifetime and decay time. a, Schematic illustration of the definition of phosphorescence or delayed fluorescence lifetime. **b**, Schematic illustration of the definition of long PersL lifetimes. The PersL lifetimes can be defined as the time when the emission intensity drops to 0.32 mcd/m^2 (τ_1), 0.0032 mcd/m^2 (τ_2) and noise level of photodetector (τ_3).
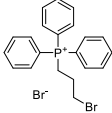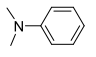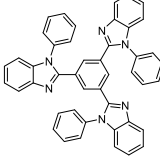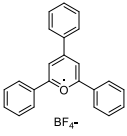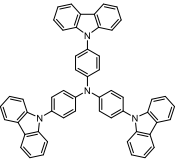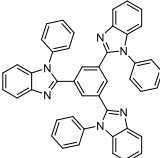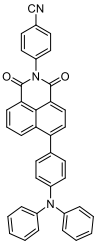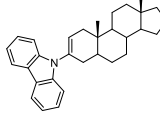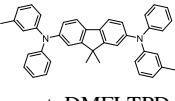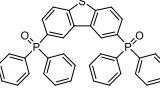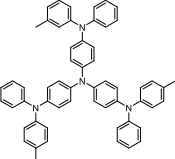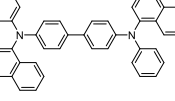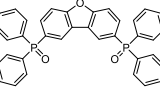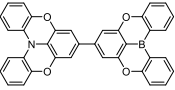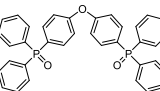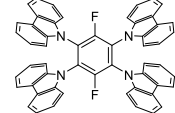
Currently, the definition of lifetime in the field of organic PersL is inconsistent. Especially since achieving hour-level LPL in organic systems for the first time,[23] researchers have found it difficult to compare the lifetime differences of different organic PersL systems. In Table 1.1, two reference metrics are provided here: *lifetime* and *decay time*, whose specific differences are displayed in Figure 1.1. First, as schematically shown in Figure 1.1a, the luminescence lifetime is generally defined as the time when the emission intensity drops to 1/e of the initial intensity in the case of single-exponential fitting.[27] In contrast, a widely accepted definition of the PersL lifetime in organics has not been defined. In long PersL material systems (visible to the naked eye for tens of minutes or more), using decay time to describe their performance is more accurate than referring to it as lifetime. In Figure 1.1b, three time points are given. τ_2 is defined as the time when the PersL intensity decays to 0.0032 mcd/m^2, which represents the minimum threshold of light detectable by dark-adapted human eyes.[6] τ_1 is defined as the time when it decays to 0.32 mcd/m^2. This value is widely used in the field of inorganic PersL materials but rarely in organics.[1] Finally, τ_3 is defined as the time when it decays to the noise level of the photodetector (detection limit), which has already been used as the lifetime of long-lasting emission in organics. Theoretically, if the precision of the testing equipment is high enough, the decay time can be infinitely long. However, the organic long PersL system is still in the early stages of development, and its brightness and decay duration are still not comparable to those of inorganic PersL materials. In many cases, it is not possible to quantify the decay performance of organic systems using the 0.32 mcd/m^2 standard. It is worth noting that a longer lifetime is not always preferable. In applications like OLEDs and scintillator X-ray imaging, a shorter lifetime indicates higher efficiency due to faster spin-flipping from the triplet state to the singlet state. The reviewed organic material systems and following three works (**Chapters 3-5**) mainly focus on long-lasting luminescent materials.
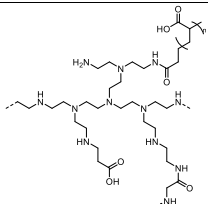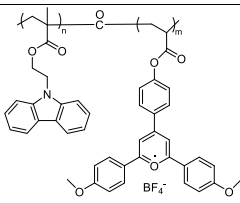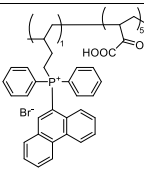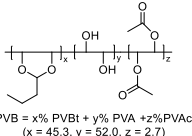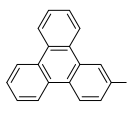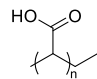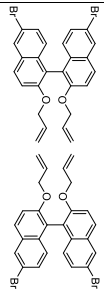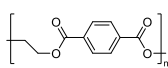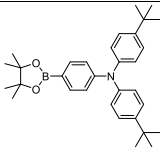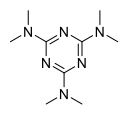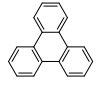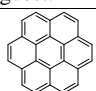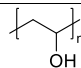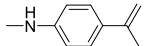
Table 1.1 Representative organic PersL materials and their major properties.
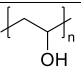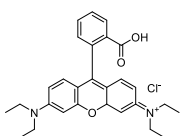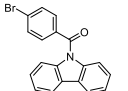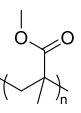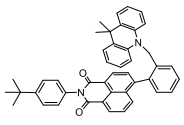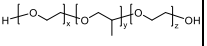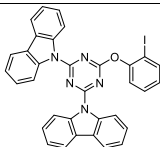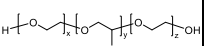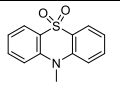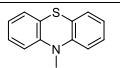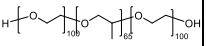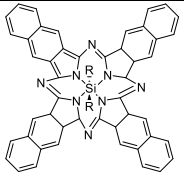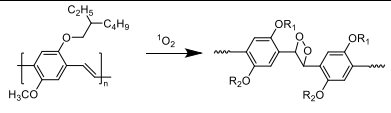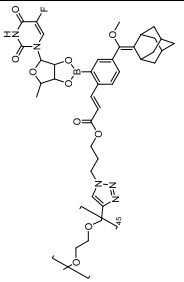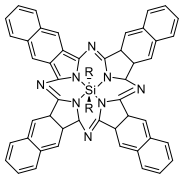
System	Molecular formula	Ex. source	PersL peak [nm]	Lifetime [μs-ms][a] or Decay time [s-h][c-d]	Ref.
Single-component crystals or amorphous powders	DPhCzT	UV	530, 575	1.05-1.35 s [a]	[28]
	CPhCz	UV to blue light	532	0.82 s [a]/ 104 s [b]	[29]
	FPO	UV	479, 579	0.7 s [a]	[30]
	Co-tCE	UV to blue light	480, 560	2.03 s [a]	[31]
	o-ITC/m-ITC/p-ITC	X-ray	535/ 525/ 530	46.5/ 72.2/ 106 ms [a]	[32]
	PY-T	X-ray	542	28.4 ms [a]	[33]
	DAP-Br	UV	450	98.5 ms [a]/ >12 min [b]	[34]
	4aa → 4ab	UV	520	6.5 s at 77 K [a]/ 480-794 ms at RT [b]	[35]
	triamino-s-triazine derivative 1	UV	464/ 496/ 523	303/ 421/ 447 ms [a]	[36]
	4CzIPN	UV	507	5.1 μs [a]	[15]

13
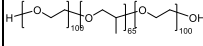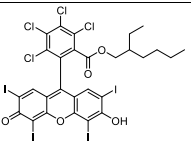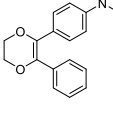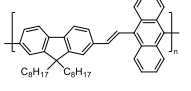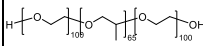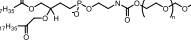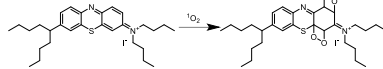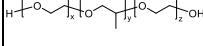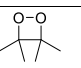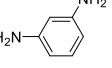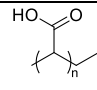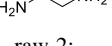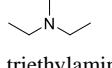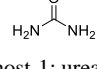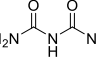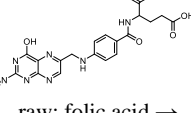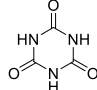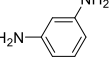
Single-component crystals or amorphous powders						
	2DN/ 2PN		UV	646/725	36.4/ 14.0 μs [a)]	[37]
	DABNA-1		UV	459	93.7 μs [a)]	[38]
	v-DABNA		UV	469	4.1 μs [a)]	[39]

Host-guest complexes or blend films						
	host: DPOBP-Br	guest: PY	UV	650-800	166 ms [a)]	[40]
	host: Cz	guest: Bd	UV	390-450, 540-650	52-297 ms [a)]	[41, 42]
	host: CPhCz	guest: CPhBd		475, 530, 575	>8ms [a)]	
	host: DPhCzT	guest: DPhBdT		475, 500, 530, 575		
	host: BCPC	guest: BCPB	UV/ force	565, 613, 674	114.2 ms [a)]	[43]
	host: oIPhCz	guest: PhPz	UV/ X-ray	554	26.37 ms [a)]	[44]
	host: curcubit[8]uril	guest: carboxypyridinium salt	UV/ two photon (590-730 nm) / X-ray	504	327.72 ms [a)]	[45]
	host: diphenylsulfone	guest: 9(10H)-acridone	UV: 254/365	>500/<500	~380/~135 ms [a)]	[46]
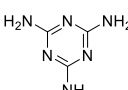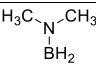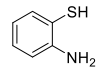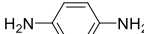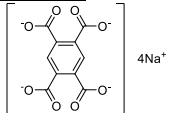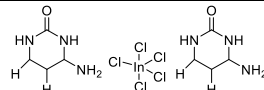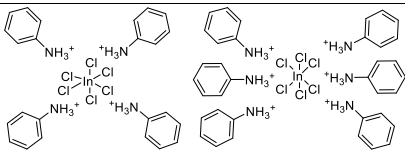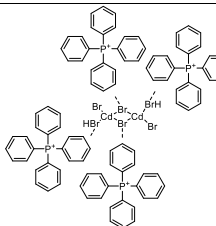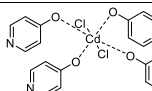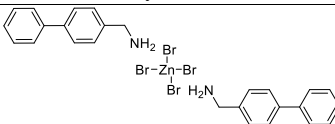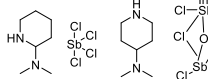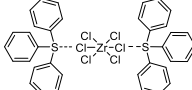
Host-guest complexes or blend films	host/guest	excitation	emission (nm)	lifetime	ref
	host: PPT / guest: TMB	UV	526	0.63-2.20 s [a)] / >1h [b)]	[23]
	host: PPT / guest-1: TMB / guest-2: TBPe / guest-3: DBP	UV	Warm white: 522, 497, 665	92 s [b)]	[47]
	host: 3TPYMB / guest-1: m-MTDATA / guest-2: v-DABNA	UV to green light	477	>4h [b)]	[48]
	host: PhB / guest-1: D-BF$_2$bdk / guest-2: DCzBF$_2$	UV and NIR laser	609	208.8 ms [a)] / ~1h [b)]	[49]
	host: PPT / guest: CzPhAP	UV	586	>1s [a)] / >1000 s [b)]	[50]
	host: DBTSPO / guest: KZLDTPA	UV	Standard white: 465, 577	91.6 and112.3 ms [a)] / 20-40 min [b)]	[51]
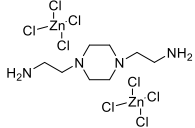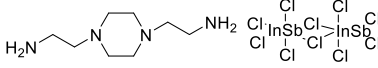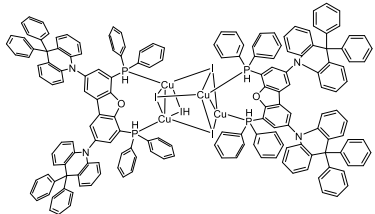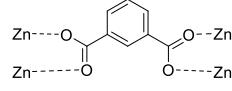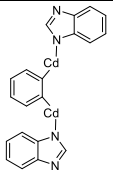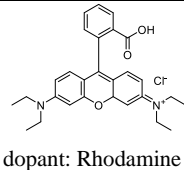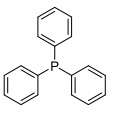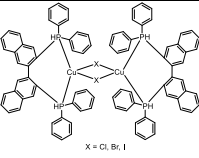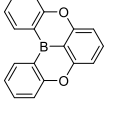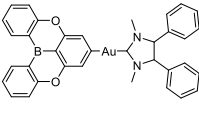
	Host	Guest	Excitation	λ (nm)	Lifetime	Ref.
Host-guest complexes or blend films	host: TPP-3C2B	guest: DMA	UV	500	159 ms [a]/ >7h [b]	[52]
	host: TPBi	guest-1: TPP[+] guest-2: TCTA	UV	555, 603	14600 s [b]	[53]
	host: TPBi	guest: TN	UV	575	126 ms [a]/ 24 h [b]	[24]
	host: CzSte	guest: DMFLTPD	UV/ Voltage	402, 512	0.61 s [a]/ 0.39 s [a]	[54]
	host: PPT	guest:m-MTDATA	UV/ Voltage: 20-40 V	500	>100 s [b]/ >30 s [b]	[55]
	host: PPT	guest: NPB	UV/ Voltage: 9 V	414, 540	332-356 ms [a]	[56]
	host: PPF	guest: BO-NO	Voltage: 6 V	531	40.6, 157.2 ms [a]	[57]
	host: DPEPO	guest: TCz-F	Current density: 1-10 mA cm^{-2}	580	1.17-9.83 μs [a]	[58]

Polymers	 PEI-*co*-PAA	UV to NIR	524	30.33-69.22 ms [a)]/ >15 s [b)]	[59]
	 CP1-CP4, different n/m ratio	UV to visible light	690-732	>10 min [c)]	[60]
	 RTP polymer	UV	490, 520	735 ms, 414 ms [a)]	[61]
	 host: PVB PVB = x% PVBt + y% PVA +z%PVAc (x = 45.3, y = 52.0, z = 2.7)	guest: TpB	UV	472	5.33-5.82 s [a)]	[62]
	host: PAA	guest: (*R*)-MBNA/ (*S*)-MBNA	UV	551	0.68 s [a)]	[49]
	host: PET	guest: CBBU	UV	500	>10000 s [b)]	[63]
	host: melamine-formaldehyde (MF)	guest: PA	UV	466	4.55 s [a)]	[64]
		guest: COR	UV	448, 568/ White light at 95 °C	4.79-4.83 s [a)]	
	host: PVA	guest: P-NHCH$_3$	UV	445	1925.8 ms [a)]	[65]

Polymers	host: PVA guest-1: BrCz-OCH$_3$	guest-2: Rhodamine B (RB)	UV	BrCz-OCH$_3$@PVA: 500/ Doped with RB: 590-800	1.65 s [a)]	[66]
	host: PMMA	guest: NIC-DMAC	UV	580	210 ms [a)]	[67]
Nanoparticles	shell: F127 (PEG-*b*-PPG-*b*-PEG)	dopant: ITC	X-ray	530	30.2 ms [a)]	[68]
	shell: F127 (PEG-*b*-PPG-*b*-PEG)	dopant-1:CS-CH$_3$ dopant-2:CzS-CH$_3$	UV	~500	dopant crystal: 39 ms, 17 s [a)]/ nanoparticles: >25 min [d)]	[69]
	shell: PEG-*b*-PPG-*b*-PEG	dopant-1: NCBS dopant-2: MEHPPV→PPV dioxetane	NIR + blue light	780	>6.6 min [d)]	[70, 71]
	shell: PEG-AE-5-DFUR	dopant: NCBS	NIR light + H$_2$O$_2$	820	>20 s [d)]	[72]

Nanoparticles	shell: PEG-*b*-PPG-*b*-PEG	dopant-1: RB	UV	780	>5 s [d]	[73]
	dopant-2: DO	dopant-3: PFVA				
	shell-1: PEG-*b*-PPG-*b*-PEG	shell-2: DSPE-PEG2000	White light and 660 nm laser	710	>20 min [d]	[74]
	dopant: mMB → mMB-dioxetane					
	shell: F127 (PEG-*b*-PPG-*b*-PEG)	raw: *solanum nigrum L.* dopant-1: CDs dopant-2: dioxetane	UV	670, 720	29.7-46.4 min [d]	[75]
	host: nano SiO2	raw: m-phenylenediamine → guest: m-CDs	UV	461	703 ms [a]	[76, 77]
	raw-1: polyacrylic acid (PAA)	raw-2: ethylenediamine (EDA) → PCDsI-1	UV	494	658.11 ms [a]	[78]
	host: zeolites AlPO-5	raw: triethylamine → guest: CDs	UV	430	350 ms [a]	[79]
	host-1: urea host-2: biuret	raw: folic acid → guest: N-CDs	UV to blue ligth	440, 500, 518, 625	0.53-1.11 s [a]	[80]
	host: cyanuric acid	raw: m-phenylenediamine → guest: m-CDs	UV	435, 470, 510	>2 h [b]	[81]

	Structure / Material		Excitation	Emission (nm)	Lifetime	Ref.
Nanoparticles	host: melamine	raw: borane dimethylamine → guest: BN-GQDs	UV	435/ 560/ 618	14.8-125.5 ms [a]/ 3.0/ 28.5/ 4.9 s [b]	[82]
	raw: 2-amino-thiophenol → guest: SN-GQDs	raw: p-phenylenediamine → guest: N-GQDs				
Organic-inorganic hybrids	Ionic crystals: TSP		UV	447	168.4 ms [a]	[83]
	Perovskites: $(C_4H_6N_3O)_2InCl_5 \cdot H_2O$		UV	~500	15000 s [b]	[84]
	Perovskites: PA4InCl7 and PA6InCl9		UV	~466	1.03-1.22 s [a]	[85]
	Metal halide hybrids: $(Ph_4P)_2Cd_2Br_6$		UV	500	0.82 s [a]	[86]
	Metal halide hybrids: $CdCl_2$-4HP		UV	416	103.12 ms [a]	[87]
	Metal halide hybrids: $PBA_2[ZnBr_4]$		Blue light: 415 nm	577, 616	100 s [b]	[88]
	Metal halide hybrids: Sb-2DMAP and Sb/In-4DMAP		UV/ UV to blue ligth	405/627	1.63 ms [a]/ 6.94 μs [a]	[89]
	Metal halide hybrids: $(Ph_3S)_2ZrCl_6$:0.1 M (M = NA, Sb, and Bi)		UV	510, 545	186.41-198-75 ms [a]	[90]

Organic-inorganic hybrids						
	Metal halide hybrids: BAPPZn$_2$Cl$_8$		UV	~550	124.73-229.30 ms [a]	[91]
	Metal halide hybrids: BAPPIn$_{1.996}$Sb$_{0.004}$Cl$_{10}$		UV: 254/365	560/ 440, 560	>20 ms [a]	[92]
	Metal halide hybrids: [DDPACDBFDP]$_2$Cu$_4$I$_4$		X-ray	515	3.5-15.0 μs [a]	[93]
	MOFs: Zn-IPA unit		UV	484	1321 ms [a]	[94]
	MOFs: PM1 unit	dopant: Rhodamine B (RB) → PM6	UV	520/ 630	PM1: 765 ms [a]/ PM6: 363 ms [a]	[95, 96]
	host: TPP	guest: BINAP-CuX	UV	503, 535	>3h [b]	[97]
	host: DOBA	guest: R-DPXZAu	UV	492	156 ms at 77 K [a]/ 42 ms at 300 K [a]	[98]

a) Measured by time-correlated single photon counting method (lifetime).

b) Measured by photomultiplier tube (decay time).

c) Measured by spectroradiometer (>0.1 μW·sr^{-1}·m^{-2}, decay time).

d) Measured by *vivo* imaging system in bioluminescence mode (decay time).

1.1.1.1 Single-Component Crystals or Amorphous Powders

Compared to multi-component PersL materials, single-component crystals or amorphous powders simplify afterglow optimization by eliminating the need for miscibility and doping concentration adjustments, while also requiring simpler preparation conditions.[17] Based on the corresponding afterglow mechanism, designing such materials should meet two key prerequisites: (1) the functional groups that accelerate n-π^* transitions and populate triplet excited states, and (2) Effective intermolecular interactions that stabilize generated triplet excitons and inhibit non-radiative decay processes.

Prof. An *et al.,* demonstrated a design rule to modulate the lifetimes of various luminescent molecules by effectively stabilizing triplet excited states through intense coupling in *H*-aggregated organics.[28] The phosphorescence lifetime achieved up to 1.35 seconds under ambient conditions. The incorporation of nitrogen, oxygen and phosphorus atoms promotes triplet exciton formation, while alkyl/aromatic substituents support *H*-aggregate formation to stabilize the triplet states. This strategy was also used to realize bright UOP under visible light.[29] Halogen atoms were incorporated as substituents to modify the molecular packing forms and accelerate the spin-forbidden transition. Prof. Wang *et al.,* developed halogen-atom-containing metal-free organic phosphors that displayed efficient X-ray chargeable luminescence.[32] The iodine atoms were incorporated to enhance triplet exciton harvesting and promote intersystem crossing. The resulting organic phosphors showed strong luminescence under both UV light and X-ray excitation, with radioluminescence displaying significantly enhanced phosphorescence compared to the photoluminescence. The organic phosphor with iodine substitution (*o*-ITC) exhibited a remarkably low detection limit of 33 nGy/s.

1.1.1.2 Host-Guest Complexes or Blend Films

1.1.1.2.1 Afterglow from Spin-Forbidden Transitions

In theory, afterglow can be achieved by reducing non-radiative decay and exciton quenching within a rigid host matrix, particularly when the triplet states contain an adequate number of electrons.[17] However, it is highly challenging to develop a host-guest system with emissive phosphorescent guests and an efficient host that can block moisture and oxygen while limiting non-radiative vibrations. First, the host and guest molecules should be highly compatible to ensure the guest molecules are dispersed in the host matrix as single molecules. Second, the host's lowest triplet and singlet energy levels should be higher than those of the phosphorescent guest to prevent energy transfer from the luminescent guest to the non-luminous host.

Prof. Liu's group explored how trace isomeric impurities in commercial carbazole (Cz) influence the properties of synthesized organic functional materials.[42] The authors found that highly pure Cz, synthesized in the lab, exhibited a blueshifted fluorescence and lacks phosphorescence observed in commercial Cz samples. Through HPLC analysis, they identified the impurity as the Cz isomer 1*H*-benzo[*f*]indole (Bd), present at concentrations below 0.5 mol%. The presence of Bd impurity is responsible for the ultralong phosphorescence reported in various Cz derivatives. They show that adding just 0.1 mol% of Bd to the pure Cz can recover the phosphorescence, indicating that these isomeric impurities are important to the photophysical properties of organic functional molecules derived from commercial Cz. They also developed organic persistent mechanoluminescence (ML) materials using an isostructural doping strategy.[43] The researchers designed a range of piezoelectric host molecules and their isostructural guest counterparts. By strategically modifying the host and guest molecules, they successfully developed a variety of multicolor and efficient persistent ML materials with long lifetimes ranging from 18.8-384.1 ms. Furthermore, the researchers made stress-sensing devices to showcase the promising prospects of these persistent ML materials. Prof. Pan and coauthors developed a crystalline aggregates, carboxypyridinium salt@curcubit[8]uril (LIFM-HG1), which exhibited highly efficient PersL under various excitation methods, including one-photon excitation, two-photon

excitation, and X-ray irradiation.[45] The rigid environment created by the numerous weak interactions and dense stacking structures in the aggregates effectively inhibited non-radiative deactivation pathways and blocks external quenchers, leading to the robust triplet energy levels and efficient intersystem crossing in the guest molecules. As a result, LIFM-HG1 exhibited impressive multichannel excited PersL properties, outstanding lysosomal targeting and limited cytotoxicity.

1.1.1.2.2 Persistent Luminescence from Charge Separation States or Trap States

We must recognize that the lifetime of triplet electrons generated in a single molecule is limited. If these triplet electrons do not undergo radiative transition to the ground singlet state within a short time, they are likely prone to non-radiative dissipation. Therefore, the lifetime based on spin-forbidden transitions is typically on the order of seconds, which cannot compare to that of inorganic PersL materials.[26] A feasible strategy is to endow the host material with charge carrier transport capabilities, allowing the delocalization of charge carriers at the emissive molecule site or their transfer to other molecules. This prolongs the recombination time of electron and hole, thereby extending PersL lifetime.

The breakthrough of purely organic LPL materials was achieved in 2017. Prof. Adachi and Prof. Kabe developed an LPL system based on a blend of two simple organic small molecules, *N,N,N',N'*-tetramethylbenzidine and 2,8-bis(diphenylphosphoryl)dibenzo [b,d]thiophene (TMB@PPT).[23] In contrast to earlier organic PersL systems that necessitated high excitation energies and extremely low temperatures, the reported LPL system is capable of being excited by a low-energy white LED and can emit PersL for an extended period over one hour, even at temperatures surpassing 370 K. The LPL emission was produced from the charge recombination process of the intermediate charge-separated states. Furthermore, they demonstrated that the exciplexes can transfer energy to another doping emitters, enabling wide-range color modification to cover nearly whole visible region.[47] The dopants enhanced the brightness, emission purity, and emission duration of the LPL

system. Moreover, Prof. Zhang and Guo *et al.,* realized a visible-light-activated LPL with 10-fold increase in duration by incorporating a MR-TADF emitter *v*-DABNA into an exciplex system.[48] The MR-TADF molecule, with its inherent charge separation characteristics, facilitates a stepwise charge transfer that enhances the formation of the charge separation state responsible for LPL. Prof. Zheng's group realized 20-40 minutes LPL by using a two-photon ionization (TPI) process.[51] By carefully selecting and optimizing the doped molecules in a dibenzo[*b,d*]thiophen-2-yldiphenyl phosphine oxide (DBTSPO) host, the PersL can be easily tuned.

In 2020, Prof. Tang's group synthesized and characterized organic quaternary phosphonium bromide salts that exhibited observable afterglow for up to 7 hours.[52] They used the ionic phosphonium core as an electron trap, which allowed for energy storage and slow release. Detailed photophysical studies and computational modeling revealed that the charge-transfer characteristics and strong spin-orbital coupling of the phosphonium-bromide system facilitated efficient intersystem crossing and charge separation, enabling the long-lived triplet state that was crucial for PersL. In 2022, Prof. Adachi's group reported the development of p-type LPL systems which could be charged by visible light and exhibit PersL in air.[53] The key innovations were the use of cationic photoredox catalysts serving as electron-accepting dopants within a neutral electron-donor host, and the help of hole-trapping molecules to extend the PersL decay duration. These systems overcame the limitations of previous LPL materials, which required inert gas conditions and ultraviolet excitation. In 2024, I and coauthors discovered TIP mechanism in organic trapping-detrapping system, where the trap depth can be controlled from 0.11 to 0.56 eV, enabling different PersL emission at wavelengths from 507 to 669 nm.[24] The TIP phenomenon in a typical 4-(6-(4-(diphenylamino)phenyl)-1,3-dioxo-1*H*-benzo[*de*]isoquinolin-2(3*H*)-yl)benzonitrile @ 1,3,5-Tris(1-phenyl-1*H*-benzimidazol-2-yl)benzene (TN@TPBi) film maintains for more than 1 day, with additional energy stored at room temperature (RT) for over 1 week. The trap depth is found to be proved by the energy gap between the lowest

unoccupied molecular orbitals (LUMO) of the radical anions of the host and guest molecules. After electrical excitation, TIP was also observed, highlighting the potential for utilizing the semiconductor properties of the organic hosts. Based on this study, the significant role of trap state in organic PersL can be clearly certified.

1.1.1.3 Polymers

Polymer-based PersL materials have garnered increasing interest because of their remarkable properties, like excellent flexibility, easy fabrication, low cost, and good thermal stability. Additionally, polymers have high weight and long chains, that act as rigid matrices that reduce nonradiative decay, thereby facilitating facilitate efficient afterglow emission.[25]

1.1.1.3.1 Nondoped Polymers

In nondoped PersL polymers, the afterglow emission originates from the polymer itself, with phosphors chemically grafted onto the main or side chains of the polymer. Prof. Xu's group reported the development of a metal-free nonconjugated copolymer, polyethyleneimine-acrylic acid (PEI-PAA), that exhibited stable photoluminescence and LPL at high temperatures and humidity. The polymer showed bright afterglow lasting over 15 seconds at RT, and the LPL could be induced by a wide range of excitation wavelengths even to near-infrared (NIR) light. The LPL mechanism was ascribed to the effective utilization of charge energy by the copolymer, along with the incorporation of rigid amide bonds. It was used to fabricate alternating current charged light-emitting diodes (AC-LEDs) with significantly reduced flicker. Prof. Kabe's group, for the first time, realized oxygen-tolerant NIR-OLPL in copolymer system, which were formed by attaching a small amount of ionic acceptor (ATPP) to numerous carbazole donors (EMCz) along a polymethyl methacrylate (PMMA) main chain.[60] The copolymers exhibited afterglow with emission wavelengths ranging from 600 to 1000 nm and a decay time exceeding one hour after the cessation of UV to visible light

excitation. The LPL properties and spectra can be changed by regulating dopants.

1.1.1.3.2 Doped Polymers

For doped polymer-based PersL materials, afterglow is primarily achieved through host-guest systems using a physical mixing method. Prof. Ma's group reported the development of efficient blue PersL materials with ultra-wide range tunable lifetimes.[65] By introducing methyl benzoate derivatives to a polyvinyl alcohol (PVA), they achieved lifetimes ranging from 32.8 to 1925.8 ms. The doped films were in the dark blue region, with quantum yields up to 15.4%. The authors attributed the wide range of tunable lifetimes to the modification of the highest occupied molecular orbitals (HOMO)-to-LUMO and singlet-to-triplet energy gaps by the electron-donating ability of the substituent groups, and the non-covalent interactions within the PVA matrix. Prof. Qin's group fabricated flexible and transparent hour-long PersL polymers through a simple doping strategy.[63] The polymer films exhibit PersL for more than 11 hours under air conditions, driven by charge separation and recombination processes, marking the longest PersL duration reported for polymers. Notably, these PersL polymers can be excited by sunlight, with their cyan afterglow visible to the naked eye at RT in air. The PersL color of the transparent and flexible polymer films can also be tuned from cyan to red by using the Förster resonance energy transfer (FRET) process.

1.1.1.4 Nanoparticles

Organic afterglow nanoparticles, with advantages such as without requiring continuous light excitation, reduced autofluorescence, low imaging background, high signal-to-noise ratio, deep tissue penetration, and high sensitivity, make afterglow imaging highly applicable in cell tracking, biosensing, cancer diagnosis, and therapy.[99]

1.1.1.4.1 Block Copolymer Micelles

Prof. Li's group reported a series of organic RTP nanoparticles with both high

quantum yield (up to 43%) and ultra-long lifetimes (up to 25 minutes in aqueous media).[69] The key strategy involves incorporating RTP guest and host molecules together, which results in the creation of a triplet exciplex that enhances the afterglow performance. These reported materials demonstrate excellent time-resolved bioimaging application. Prof. Pu's group reported semiconducting polymer nanoparticles (SPNs) as biodegradable PersL probes for bioimaging.[70] The authors first investigated the mechanism behind SPN PersL, discovering that the afterglow involved light-induced formation of unstable chemical intermediates. They then proposed a strategy to redshift the afterglow emission and demonstrated its application for high-contrast lymph node and tumor imaging. Finally, they developed an afterglow probe that can detect the drug hepatotoxicity in living mice.

1.1.1.4.2 Carbon dots

Carbon dots (CDs) with multiple emission modes are desirable in the fields of data encryption, anti-counterfeiting, and bioimaging. Prof. Jiang *et al.,* prepared afterglow nanoparticles by fixing CDs into colloidal nano-silica ($nSiO_2$) using covalent bonds.[76] The resulting $CDs@nSiO_2$ composite shows an ultralong afterglow in water, with a lifetime up to 0.703 s and limited effects from dissolved oxygen. The afterglow is found to be predominantly due to delayed fluorescence, with a portion of phosphorescence. The covalent fixation of the CDs onto $nSiO_2$ is key to stabilizing the triplet excitons and enabling the afterglow in both solid and aqueous forms. Additionally, the unstable chemical bonds on the surface of CDs can react with O_2, preventing the triplet excitons from quenching. However, most afterglow CDs do not exhibit any afterglow when dispersed in liquid or exposed to oxygen.[3] Typically, long-lasting phosphorescence or delayed fluorescence is achieved by embedding CDs in small molecule or polymer matrices, or in the form of polymer dots. These afterglow CDs systems usually synthesis as amorphous powders, which, in a certain sense, cannot be classified as nanomaterials. For example, Prof. Yang *et al.,* presented new metal-free polymer CDs (PCDs) that exhibit RTP properties.[78] The PCDs are synthesized through hydrothermal

method by taking polyacrylic acid and ethylenediamine as raw molecules. The covalent crosslinking in PCDs can restrict vibrations and rotations, which promotes efficient intersystem crossing and suppresses non-radiative transitions, leading to the observed RTP. The RTP performance of the PCDs can be modified by varying the nitrogen content, with the nitrogen-doped PCDs exhibiting the strongest RTP.

1.1.1.5 Organic-Inorganic Hybrids

Organic-inorganic hybrid structures offer a solution to the limitations of organic PersL materials, which are generally in solid state for strong afterglow properties. First, intermolecular interactions are utilized to enhance molecular rigidity and limit motion or vibration, reduce non-radiative transition of triplet state and increase lifetimes and quantum yields. Additionally, the ordered aggregation properties of hybrid materials enable hybrid films with long PersL lifetime. Lastly, controlling the self-assembly of hybrid structures allows fine-tuning of excited states by regulating intermolecular reactions.[4] Organic-inorganic hybrids encompass a wide range of structures, including ionic crystals, perovskites, metal halide hybrids, metal-organic frameworks (MOFs), host-guest systems (guest: metal complexes), *etc*.

1.1.1.5.1 Organic-Ionic Crystals

Prof. Ye *et al.,* presented a straightforward chemical approach to realizing high-performance afterglow phosphors involves confining isolated chromophores within ionic crystals.[83] The cations of the ionic crystals formed high-density ionic bonds with the carboxyl groups of the chromophores, resulting in a molecular arrangement where the interactions between chromophores are negligible. By modifying the charged chromophores and their counterions, the phosphorescence can be tuned from blue to deep blue, with a maximum phosphorescence efficiency up to 96.5%. Additionally, these phosphorescent materials can extend the application range like display.

1.1.1.5.2 Perovskites and Metal Halide Hybrids

The spin-orbit coupling is important to photophysical properties of molecular hybrid systems. By introducing heavy atoms into a molecular system, it is helping to alter its photophysical and photochemical properties, a phenomenon recognized as the heavy-atom effect.[100]

Hybrid perovskites, which integrate organic and inorganic semiconductors at the molecular level, have gained great interests due to their exceptional luminescence efficiency and carrier mobility.[101] For instance, 2D layered hybrid perovskites exhibit strong water and thermal stability.[102] Additionally, the rigid inorganic layers in perovskites help regulate energy transfer from Wannier excitons to triplet excitons, promoting phosphorescence in the organic components. Prof. Zhang *et al.,* realized LPL in an hybrid halide perovskite, $(C_4H_6N_3O)_2InCl_5 \cdot H_2O$.[84] The perovskite displayed numerous luminescent centers, which can be seen with different excitation wavelength. The $(C_4H_6N_3O)_2InCl_5 \cdot H_2O$ single crystals exhibit an ultralong PersL decay time of up to ~4.2 hours at RT, which is the longest reported for organic-inorganic hybrid perovskites. The intrinsic defects in perovskites introduced trap states, which can store carriers. The captured carriers can be released into the triplet state of the luminescent centers to give PersL.

Metal halide hybrids have attracted significant attention for their high proton conductivity. Their composition and structure can be easily tuned, allowing for diverse designs in photo-functional materials. By carefully selecting the organic and inorganic components, the dimensionality of metal halide hybrids can be regulated from 3D to 0D.[4] Additionally, the low-temperature synthesis and cost-effective production of metal halide hybrid thin films make them ideal for convenient device fabrication. Prof. Yan's group designed zero-dimensional (0D) metal halide organic-inorganic hybrids, including $(Ph_4P)_2CdX_4$ and $(Ph_4P)_2Cd_2X_6$ (X = Cl or Br), that exhibited ultralong RTP with high efficiency and thermal stability.[86] These materials displayed a unique combination of wide-ranging zero-thermal-quenching, ultralong RTP lifetime (~38 ms), and high RTP efficiency (~63%), which surpasses most RTP systems. The thermal

stability and high RTP efficiency could be attributed to the rigid 0D structure, strong spin-orbit coupling, and effective energy transfer pathways within the hybrid materials. Prof. Fu *et al.,* designed a novel class of metal halide hybrids, $PBA_2[ZnX_4]$ (X = Br or Cl), that exhibited stable LPL emission lasting for minutes at RT.[88] The materials have a unique 2D lamellar structure with $[ZnX_4]^{2-}$ tetrahedron networks sandwiched between organic PBA^+ layers. The LPL mechanism is found to originate from a thermally activated charge-separated state, rather than traditional RTP.

1.1.1.5.3 Metal-Organic Frameworks

Metal-Organic Frameworks (MOFs) are crystalline materials formed by the self-assembly of metal ions or clusters with organic ligands (linkers), creating highly cross-linked structures with tunable chemical porosity and high internal surface area. In MOFs, the coordination of organic afterglow units with metal ions enables afterglow emission through: (1) accelerating spin-orbit coupling by the heavy atom effect to promote triplet excitons, and (2) enhancing molecular rigidity to reduce non-radiative exciton loss and boost phosphorescence emission. Prof. Yan's group firstly developed RTP properties of MOFs by coordinating them with common Zn^{2+} metal ions and terephthalic acid (TPA) ligand.[94] The longest RTP lifetime achieved is 1.3 seconds and the phosphorescence can be modified by varying the metal ions and the stacking modes of the ligands. Dr. Liu *et al.,* realized stable long-wavelength afterglow MOFs by encapsulating organic dyes into the phosphorescent MOFs.[95] The multicolor afterglow can be achieved through efficient energy transfer from green phosphorescent MOFs host to the dye guest.

1.1.1.5.4 Host-Guest Systems

Prof. Zheng's group achieved LPL through melt-casting a triphenylphosphine (TPP) host with CuI complexes (BINAP-CuX, where X = Cl, Br, I).[97] Charge separation was triggered under excitation through coordination with the CuI complex, generating semi-free halide ions and in situ formed CuI cations, which together formed TPP+BINAP-

CuX ion pairs. This allowed the lifetime of the LPL to be easily tuned by different halogen atoms, with afterglow lasting over 3 hours and visible to the naked eye. The ionic solids can also be reprocessed at 100°C without affecting their photophysical properties, indicating their high reprocessability and versatility.

1.1.2 Inorganic Persistent Luminescence Materials

Inorganic PersL materials normally consist of a host matrix, luminescent centers, and traps, all of which have a significant impact on the PersL characteristics. The matrix composition can significantly influence the band structure of materials, including the bandgap width and the relative relationship between the matrix band structure and the luminescent center energy levels, as well as the coordination environment of the luminescent centers, including coordination number, symmetry, and crystal field strength. These factors can alter the excitation wavelength, emission wavelength, and trap depth of the materials. In this part (**1.1.2**), inorganic PersL materials are categorized into four types based on the major compositions of the matrix, including (1) halides, (2) sulfides, (3) oxides, and (4) nitrides. The chemical composition, usable excitation light sources, PersL wavelength (emission peak), and trap depth [or thermoluminescence (TL) peak temperature] of these materials are summarized in Table 1.2. Moreover, a brief review will be conducted on several breakthrough studies involving four different PersL compounds.

In Table 1.2, the trap depth (measured in eV) primarily reflects the storage stability of trapped charge carriers at RT. If the trap depth of a material is not provided in the literature, the peak temperature of the TL (measured in K) is used to indicate the storage stability. Notably, the peak temperature of the thermally stimulated luminescence curve may vary when the same materials are irradiated with light of different wavelengths or when different heating rates are applied after irradiation. Additionally, different estimation methods of the trap depth, including the commonly used methods such as the deconvolution method,[103] initial rise method,[104] Randall-Wilkins method,[105] full width at half maximum method,[106] and trap depth distribution analysis method[107] may yield different estimates of the trap depth for the same TL glow curve.

Table 1.2 Representative inorganic PersL materials and their major properties.

Group	Composition	Ex. source	PersL peak [nm]	Trap depth [eV] or TL peak [K]	Ref.
Halides	BaFX:Eu^{2+} (X=Cl, Br, F)	X-ray	385-405	2.0-2.5 eV	[108, 109]
	BaFCl:Sm^{3+}/ Sm^{2+}	UV	688	3.1 eV	[110-112]
	KBr:In^{+}	X-ray	428, 517	2.1 eV	[113]
	RbBr:Ga^{+}	X-ray	560	1.85 eV	[114]
	Cs$_2$NaYF$_6$:Ce^{3+}	X-ray	360	2.25 eV	[115, 116]
	NaLuF$_4$:Ln^{3+}	X-ray	350-800	0.5-0.9 eV	[117]
	NaYF$_4$:Ln^{3+}	X-ray	480-1060	0.73-1.05 eV	[118]
	NaMgF$_3$:Tb^{3+}	X-ray	488, 548, 584, 621	1.08 eV	[119]
	CsCdCl$_3$:Mn^{2+}, R^{4+} (R=Ti, Zr, Hf, Sn)	X-ray	570-605	1.41 eV	[120]
	KZnF$_3$:Mn^{2+}	X-ray	587	0.52-0.96 eV	[121]
	NaLuF$_4$:Mn^{2+}	X-ray	525	0.75 eV	[122]
	Ba$_2$B$_5$O$_9$Br:Eu^{2+}	X-ray	420	1.19 eV	[123]
	Ca$_{2-x}$Sr$_x$BO$_3$Cl:Eu^{2+}, Dy^{3+}	UV	420, 585	0.6-1.0 eV	[124]
Sulfides	CaS:Eu^{2+}, Sm^{3+}	UV to visible light	643	1.1 eV	[125]
	SrS:Eu^{2+}, Sm^{3+}	UV to visible light	600	1.1 eV	[126]
	Y$_2$O$_2$S:Eu^{3+}, Mg^{2+}, Ti^{4+}	UV	625	0.88 eV	[127, 128]
	CaZnOS (activator/trap=Pr^{3+}, Tb^{3+}, Ho^{3+}, Dy^{3+}, Tm^{3+}, Yb^{3+}, Nd^{3+}, or Er^{3+}) (trap filler= Cu^{+}, Y^{3+}, Pb^{2+})	UV	400-850	~0.68 eV	[129]
Oxides	Lu$_2$O$_3$:Tb^{3+}	UV	550	0.7-1.0 eV	[130]
	Lu$_2$O$_3$:Pr^{3+}, Hf^{4+}	X-ray or UV	621	1.14, 1.69, 2.11 eV	[131]
	Al$_2$O$_3$:C	β-ray or γ-ray	420	460 K	[132, 133]
	MgO:Tb^{3+}	β-ray	550	573 K	[134]
	Ba$_2$SiO$_4$:Eu^{2+}, Ln^{3+} (Ln=Ho, Dy, Tm)	UV	504	0.7-1.0 eV	[135, 136]
	BaSi$_2$O$_5$:Eu^{2+}, Nd^{3+}	UV	515	1.29 eV	[137]
	Sr$_3$SiO$_5$:Eu^{2+}, Dy^{3+}	UV	570	1.05 eV	[138]
	β-Sr$_2$SiO$_4$:Eu^{2+}, Tm^{3+}	UV	470, 540	1.35 eV	[139]
	LiYSiO$_4$:Ce^{3+}	X-ray or UV	405	520 K	[140]
	LiLuSiO$_4$:Ce^{3+}, Tm^{3+}	β-ray or UV	410	0.7 eV	[141]
	Y$_2$GeO$_5$:Pr^{3+}	UV	492, 621	0.9, 1.31 eV	[142]
	Zn$_2$GeO$_4$:Mn^{2+}	UV	536	345 K	[143, 144]
	MgGeO$_3$:Mn^{2+}, Yb^{3+}	UV	677	0.99 eV	[145]
	MgGeO$_3$:Mn^{2+}, Eu^{3+}	UV	677	1.49 eV	[145]
	Mg$_3$Y$_2$Ge$_3$O$_{12}$:Tb^{3+}	UV	382-617	0.91-1.24 eV	[146]

	Material	Excitation	Emission	Trap depth/Temperature	Ref.
	$BaZrGe_3O_9:Pr^{3+}$	UV	615	0.85-0.98 eV	[147]
	$NaLuGeO_4:Bi^{3+}, Cr^{3+}$	UV	400	439 K	[148]
	$LiScGeO_4:Bi^{3+}$	UV	365	408, 521 K	[149]
	Mg_2SnO_4	UV	498	383, 441, 486 K	[150]
	$Mg_2SnO_4:Mn^{2+}$	UV	497	0.71, 0.91 eV	[151]
	$Mg_2SnO_4:Cr^{3+}$	UV to blue light	800	0.5-1.3 eV	[152]
	$CaSnO_3:Bi^{2+}$	UV to NIR	810	0.8, 1.4 eV	[153]
	$CaSnSiO_5:Dy^{3+}$	UV	426, 488, 580, 666	420, 520 K	[154, 155]
	$Sr_2SnO_4:Eu^{3+}, Nd^{3+}$	UV	595	0.65-0.99 eV	[156]
	$Zn_2SnO_4:Cr^{3+}, Eu^{3+}$	UV	800	317, 364, 401 K	[157, 158]
	$12CaO·7Al_2O_3:Eu^{2+}, Mn^{2+}$	UV	444	0.64, 0.86 eV	[159]
	$12CaO·7Al_2O_3:Tb^{3+}$	X-ray or UV	541	0.72, 0.95 eV	[160]
	$LiGa_5O_8:Cr^{3+}$	UV	716	420, 490 K	[161]
	$LiGa_5O_8:Mn^{2+}$	UV	510, 625	0.85-1.27 eV	[162]
	$Zn_{1-2x}Li_xGa_{2+x}O_4:Cr^{3+}$	UV or X-ray	709	0.70-0.72 eV	[163]
	$BaGa_2O_4:Pr^{3+}$	UV	485, 628,651	0.65, 0.75 eV	[164]
	$BaGa_2O_4:Pr^{3+}, Zn^{2+}$	UV	485, 628,651	0.66, 0.70, 0.76 eV	[164]
	$MgGa_2O_4:Fe^{3+}$	UV	703	0.67, 0.95 eV	[165]
	$Zn(Ga_{1-x}Al_x)_2O_4:Cr^{3+}, Bi^{3+}$	UV	695	333-573 K	[166]
	$Y_3Al_{5-x}Ga_xO_{12}:Ce^{3+}, Cr^{3+}$	UV to blue light	525-555	0.41-1.2 eV	[167, 168]
	$Y_3Al_{5-x}Ga_xO_{12}:Ce^{3+}, V^{3+}$	UV to blue light	525-555	1.13-1.62 eV	[169]
	$Y_3Al_{5-x}Ga_xO_{12}:Cr^{3+}$	UV	690	297-545 K	[170]
	$Y_3Al_2Ga_3O_{12}:Pr^{3+}$	UV to visible light	487, 607	1.15, 1.54	[171]
	$Gd_3Al_{5-x}Ga_xO_{12}:Cr^{3+}, Eu^{3+}$	UV	695, 713	355-498 K	[172]
	$Ca_4Ti_3O_{10}:Pr^{3+}, Y^{3+}$	UV to visible light	612	0.9-0.98 eV	[173]
	$CaZrO_3$	UV	410	1.13, 1.55 eV	[174]
	$Ca-Al-Si-O:Ce^{3+}/Tb^{3+}/Pr^{3+}$ glass	NIR laser	B/G/R	-	[175]
	$Zn-Si-B-O:Mn^{2+}$ glass	UV	590	> 360 K	[176]
	$Zn-Si-B-O:Mn^{2+}, Yb^{3+}$ glass	UV	605, 980	0.80, 0.98 eV	[177]
Nitride	$CaAlSiN_3:Eu^{2+}, Tm^{3+}$	UV	635	330-430 K	[178]
	$(Ca_{1-x}Sr_x)_2Si_5N_8:Eu^{2+}, Tm^{3+}$	UV	604-630	0.64, 0.72 eV	[179, 180]
	$SrLiAl_3N_4:Eu^{2+}$	UV	650	0.47, 0.81 eV	[181]
	$CaSi_{10-n}Al_{2+n}O_nN_{16-n}: xEu^{2+}$ (Ca-αSialon:Eu^{2+}, n = 0~1, x = 0.1%~8%)	UV	595	0.65, 0.85 eV	[182]
	$Ba[Mg_2Al_2N_4]:Eu^{2+}, Tm^{3+}$	visible light	710, 800	100-400 K	[183]
	$SrSi_2O_2N_2:Eu^{2+}, Ln^{3+}$ (Ln=Dy, Ho, Er)	UV or blue light	540	0.90-1.18 eV	[184, 185]
	$SrSi_2O_2N_2:Yb^{2+}, Ln^{3+}$ (Ln=Dy, Ho, Er)	UV or blue light	620	0.90-1.17 eV	[184, 185]
	$BaSi_2O_2N_2:Eu^{2+}$	UV	494	0.67-0.82 eV	[186]

YSiO$_2$N:Ce^{3+}, Sm^{3+}	UV	400, 427	1.10 eV	[187]
YSiO$_2$N:Ce^{3+}, Tm^{3+}	UV	400, 427	0.80 eV	[187]
Si$_{6-z}$Al$_z$O$_z$N$_{8-z}$:Eu^{2+} (β-Sialon:Eu^{2+}, 0< z ≤4.2)	UV	537	0.28-1.23 eV	[188]
(Ba$_{1-x}$Sr$_x$)AlSi$_5$O$_2$N$_7$:Yb^{2+}, Yb^{3+}	UV or blue light	664, 985	0.84, 1.32 eV	[189]

1.1.2.1 Halides Persistent Luminescence Materials

Halides (metal halides, *M*F*X*) generally have a large bandgap width, and they are typically excited by using high-energy rays as a light source for energy storage. The stringent excitation conditions make halide-based deep-trap PersL materials primarily applicable in high-end medical and military fields, such as radiation dosimeters and infrared detectors. *M*F*X* is a typical X-ray excited deep-trap PersL material, among which *M* represents one or more alkali-earth metals such as Ba, Sr, or Ca, and *X* represents one or more halogens such as Cl, Br, or F. *M* can be replaced by divalent or trivalent rare-earth elements such as Eu^{2+}, Sm^{2+}, or Sm^{3+} as luminescent centers. The *M*FX crystals, as the main constituent materials of the first-generation X-ray imaging plates, have been widely used in early medical X-ray fluoroscopy, X-ray dosimetry, and crystal structure analysis. They exhibit advantages such as high sensitivity, reusability, and ease of digital integration, but also have drawbacks such as low spatial resolution, rapid signal attenuation, and limited reuse times.[190, 191] As early as 1980s, researchers from Fuji Photo Film Co. Ltd. in Japan embarked on the exploration and investigation of BaF*X*:Eu^{2+} single crystals, focusing on their scanning laser stimulated luminescence (SLSL) studies.[108]

In general, microscale halide polycrystalline materials exhibit a significant scattering effect for light transmission. To suppress the light scattering, Prof. Xie *et al.* reported core-shell encapsulated PersL-enhanced NaYF$_4$:Ln^{3+}@NaYF$_4$ nanoparticles.[118] By introducing different Ln^{3+} ions, the PersL emissions of NaYF$_4$:Ln^{3+}@NaYF$_4$ nanoparticles can be achieved in green (Tb^{3+}), white (Dy^{3+}), red (Ho^{3+}), orange (Eu^{3+}), or NIR (Nd^{3+}). Under X-ray irradiation, high-energy electrons generate numerous

ionized electrons through cascading collisions. The Ln^{3+} (*i.e.*, Tb^{3+}) was recognized as electron traps. Furthermore, different types of optical inks were prepared, each containing well-dispersed PersL nanoparticles with specific Ln^{3+} ions such as Tb^{3+}, Dy^{3+}, and Ho^{3+}. These inks were then utilized to print three images on a sapphire substrate using high-precision inkjet printing technology. The encoded information was readout using wavelength decoding, enabling multidimensional optical information storage. Prof. Zhuang and Prof. Xie also developed another core-shell $NaMgF_3:Tb^{3+}@NaMgF_3$ nanoparticles with nano cubic morphology, outstanding aqueous dispersibility, and optical information storage ability.[119] Tb^{3+} ions can serve as both luminescent center and trap in the $NaMgF_3$ phosphor under X-ray irradiation, with the average trap depth reaching 1.08 eV. These remarkable features make the developed nanoparticles suitable for use in light energy storage and information encryption.

1.1.2.2 Sulfides Persistent Luminescence Materials

Sulfide PersL materials were among the earliest to be discovered and studied. By doping with lanthanide ions or transition metal ions, sulfides with different emission wavelengths and trap depths can be obtained. Zinc sulfide was the most renowned persistent phosphor of the 20th century.[1] In the late 20th century, optical storage and photoluminescent properties of halide and sulfide materials met the requirements for data storage density, data transfer speed, and data erasure speed of computer processors at that time and were used in computer logic and computation design. In 1990s, Jutamulia *et al.* designed a spatial light modulator for parallel Boolean logic operations using $(Ca_xSr_{1-x})S:Eu^{2+}$, Ce^{3+}, Sm^{3+} as the information recording material.[192] They verified 16 kinds of Parallel Boolean logic in a 2×2 plane matrix using ultraviolet light as the write-in beam and NIR light as the read-out beam and achieved a storage density of 40000 bit/cm^2, which was a relatively high value at that time. However, some main drawbacks limit further development of these sulfide PersL materials. Firstly, the luminescent performance (especially the PersL brightness) lags later-developed silicate

or aluminate PersL materials such as $SrAl_2O_4:Eu^{2+}$, Dy^{3+}. Additionally, sulfides lack chemical stability and are prone to oxidation and moisture absorption, making them unsuitable for long-term storage. Moreover, the production process releases harmful gases, posing a significant environmental threat. These issues have led to the gradual replacement of sulfide PersL materials by other categories of materials.

In 1998, Nichia company first discovered most renowned Eu^{3+}-based persistent phosphor, $Y_2O_2S:Eu^{3+}$, Mg^{2+}, Ti^{4+}.[193] Moreover, Prof. Liu *et al.,* reported $Y_2O_2S:Eu^{3+}$, Mg^{2+}, Ti^{4+} nanoparticles with uniformity and well-dispersed distribution ranging from 30 to 50 nm in size.[127] Emission peaks in the spectrum are attributed to Eu^{3+} ions transition, and the trap state formed by doping Mg^{2+} and Ti^{4+} ions.[128] Prof. Wang *et al.,* developed PersL in a wurtzite CaZnOS crystal through synergistic defect engineering.[129] The authors introduce a strategy for deliberate PersL control in a single material system, simultaneously managing luminescent center/trap state and trapping/detrapping processes through multiple doping. This design approach yields a diverse array of luminescent centers with electronic transition processes, including ns^2-to-nsnp, 3d-to-3d, 4f-to-4f, and donor-to-acceptor recombination, and create PersL with unprecedented stimulus-responsive features.

1.1.2.3 Oxides Persistent Luminescence Materials

Compared to fluorides and sulfides, oxide PersL materials typically have a moderately narrow bandgap width. Most oxides can be charged and stored energy through UV radiation and even visible light. Moreover, oxide phosphors also demonstrate good chemical stability, ease of synthesis, preparation, and storage, and are suitable for making ceramic materials.

For aluminate, $SrAl_2O_4:Eu^{2+}$, Dy^{3+} as the ultrabright inorganic PersL materials with longest decay duration has been widely studied in recent years.[194] Yamamoto and Matsuzawa first investigated PersL phenomenon of $SrAl_2O_4:Eu^{2+}$, Dy^{3+} and

CaAl$_2$O$_4$:Eu^{2+}, Nd^{3+} phosphors since 1996.[6, 7] The PersL mechanism has been explained through two models: the Matsuzawa hole capture model, where a hole is trapped by Dy^{3+}, and the electron trap model, where the excited electron of Eu^{2+} is trapped by Dy^{3+}, with the latter being widely accepted based on the 'Dorenbos model'.[195]

In view of silicate, germanate, and stannate, deep-trap PersL materials in silicates are usually achieved by using Eu^{2+} or Ce^{3+} ions as luminescent center and doping another trivalent rare-earth ion as trap centers. Prof. Lin *et al.,* prepared a novel BaSi$_2$O$_5$:Eu^{2+},Nd^{3+} PersL phosphor and further introduced into phosphor-in-glass (PiG) as light-storage materials.[137] PersL nanoparticles, capable of emitting light even after excitation, have gained importance in biomedicine for their ability to eliminate tissue autofluorescence. Prof. Tanabe's group discovered the effect of different trivalent rare-earth ions on the trap distribution of MgGeO$_3$:Mn^{2+}, Ln^{3+}.[145] After co-doping with Yb^{3+} and Eu^{3+}, the peak temperatures of the TL spectra were obtained at 335 K and 502 K, respectively, corresponding to trap depths of 0.99 eV and 1.49 eV, which could be a candidate for the optical stimulation based application. Prof. Li, Prof. Han, and Prof. Qiu *et al.,* reported trap energy up-conversion-like NIR-to-NIR light PersL in Bi^{2+}-doped CaSnO$_3$ phosphors and nanoparticles.[153] These materials demonstrate a unique phenomenon wherein carriers transition from deep traps to shallow traps when excited by NIR photons. This enables repetitive charging of the materials using deep-tissue penetrable NIR photons. The energy trapped in the deep-level traps can be stored for extended periods and then released as afterglow signals in the NIR range. This innovative approach is good for the development of NIR-absorbing and NIR-emitting PersL materials and nanoparticles that can be rejuvenated using non-harmful, deep-tissue penetrable NIR light.

For gallate, ZnGa$_2$O$_4$:Cr^{3+} phosphor possesses excellent NIR PersL characteristics at RT with a trap depth of approximately 0.46 eV. Also, ZnGa$_2$O$_4$:Cr^{3+} phosphor can be easily prepared as nanoparticles and used for surface modification and functional

design.[196-204] Prof. Zhuang *et al.* proposed a band engineering method to control the trap depth by changing the location of the CB in $Zn(Ga_{1-x}Al_x)_2O_4:Cr^{3+}$, Bi^{3+} solid solution.[166] As the molar mass ratio of Al increased, the CB bottom gradually upward shifted, resulting in an increasing energy difference with the energy level of electron traps (positive valence anti-site defects $Ga_{Zn}^{\cdot}$). And the peak temperature of thermal release luminescence in the material increases from 333 (x = 0%) to 573 K (x = 33%).

1.1.2.4 Nitrides Persistent Luminescence Materials

Due to the strong covalency and electron cloud rearrangement effect of, nitride or oxynitride optical materials doped with Eu^{2+} or Ce^{3+} exhibit longer emission wavelength compared to the oxide phosphors with similar structure. Many important red and NIR luminescent materials have been discovered in nitride or oxynitride compounds. Prof. Ueda *et al.* reported a red-light charged NIR PersL $Ba[Mg_2Al_2N_4]:Eu^{2+},Tm^{3+}$ phosphor.[183] Tm^{3+} serves as NIR emission center, expanding the PersL emission band from 600 to 830 nm through energy transfer from Eu^{2+} to Tm^{3+}. Dr. Kitagawa, Prof. Ueda, and Prof. Tanabe reported that $YSiO_2N:Ce^{3+},Ln^{3+}$ (Ln = Sm^{3+} or Tm^{3+}) phosphors increase the intensity of Ce^{3+}:5d-to-4f blue PersL.[187] In the TL glow curves, the sample exhibits two TL peaks related to intrinsic defects and the Ln^{3+} traps. Prof. Smet reported a strong non-destructive ML in $BaSi_2O_2N_2:Eu^{2+}$ phosphor with blue-to-green emission.[205] When irradiated with UV or blue light, this powder showed intense blue-to-green light upon mechanical stimulation. The origin of the ML could be ascribed to the trap-induced PersL of $BaSi_2O_2N_2:Eu^{2+}$ phosphor.

1.2 Applications of Persistent Luminescence Materials

1.2.1 Emergency Signage

PersL materials can absorb ambient light and store light energy. Upon removal of the external light source, the stored energy is gradually released as visible luminescence. This prolonged emission, persisting for even several hours, ensures reliable illumination of emergency indicators during power outages or critical situations, facilitating safe evacuation.[1]
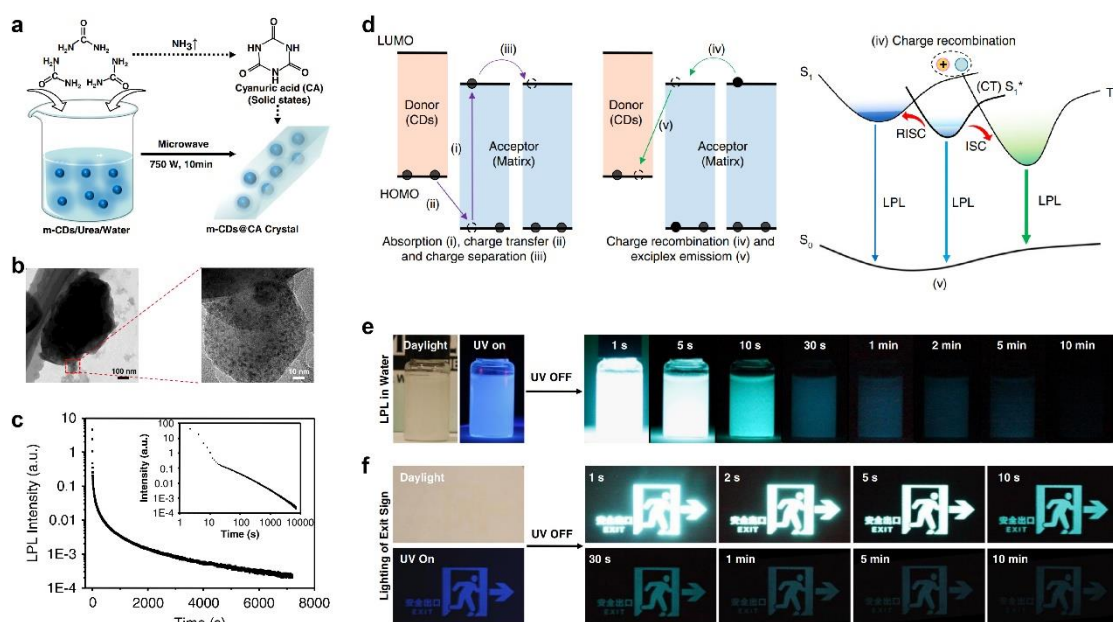
Figure 1.2 Photophysical and emergency signage applications of mCDs@CA-based LPL system. a, Schema of the preparation method of m-CDs@CA. **b**, TEM image. **c**, The PersL decay curve of the m-CDs@CA (Ex.= 365 nm and at RT, insert: log-log plot). **d**, A possible LPL mechanism in m-CDs@CA. **e**, Photographs of the aqueous m-CDs@CA dispersion. **f**, Pictures of a m-CDs@CA-based emergency sign after ceasing UV excitation. Ref. [81]; Copyright © 2022, Springer Nature.

In 2022, Prof. Jiang and I first realized hour level PersL in CDs compounds, breaking

through the lifetime limitation in CDs.[81] As shown in Figure 1.2a, the blend (m-CDs@CA) was easily synthesized by microwave heating of mixture of m-CDs and urea. The uniform incorporation of the m-CDs into cyanuric acid crystals (CA, produced by urea in situ) was confirmed by the TEM images (Figure 1.2b). The long PersL (LPL) was detected by using a photomultiplier tube (PMT) for over 2 h before the signal is attenuated to the noise level (10^{-4}, Figure 1.2c). As shown in Figure 1.2d, the origin of PersL in mCDs@CA can be attributed to the charge-separated (CS) states formed by exciplexes between m-CD and CA under UV irradiation. Moreover, the formation of C-N covalent bonds between m-CD and CA has been proven to play a crucial role in activating PersL. With the assistance of hydrogen bonding and the physical confinement of the CA matrix, the exciplex CS states are effectively stabilized and protected from quenching by water and oxygen (Figure 1.2e). The applications of emergency signs were demonstrated in Figure 1.2f.

1.2.2 Light-Emitting Diodes

1.2.2.1 Organic Light-Emitting Diodes

The great progress has been made in OLEDs field over the past two decades, evolving from fluorescence molecules to phosphorescence molecules.[206-208] In OLEDs, electrically injected electrons and holes recombine to form singlet and triplet excitons in a 25%:75% ratio. The use of phosphorescent metal-organic complexes effectively harnesses the typically non-radiative triplet excitons, thereby enhancing overall electroluminescence efficiency.[209] In 2012, Prof. Adachi's group developed a class of metal-free organic electroluminescent molecules that exhibit highly efficient TADF.[15] These molecules are designed to have a small energy gap (ΔE_{ST}) between the singlet and triplet excited states, which promotes efficient spin up-conversion from non-radiative triplet states to radiative singlet states. This allows both singlet and triplet excitons to be harnessed for electroluminescence from lowest singlet state to ground

state, resulting in an intrinsic efficiency exceeding 90% and an external electroluminescence efficiency (EQE) over 19%. The key to this achievement is the careful molecular design that balances a small energy gap with a fast radiative decay rate to overcome non-radiative transition.
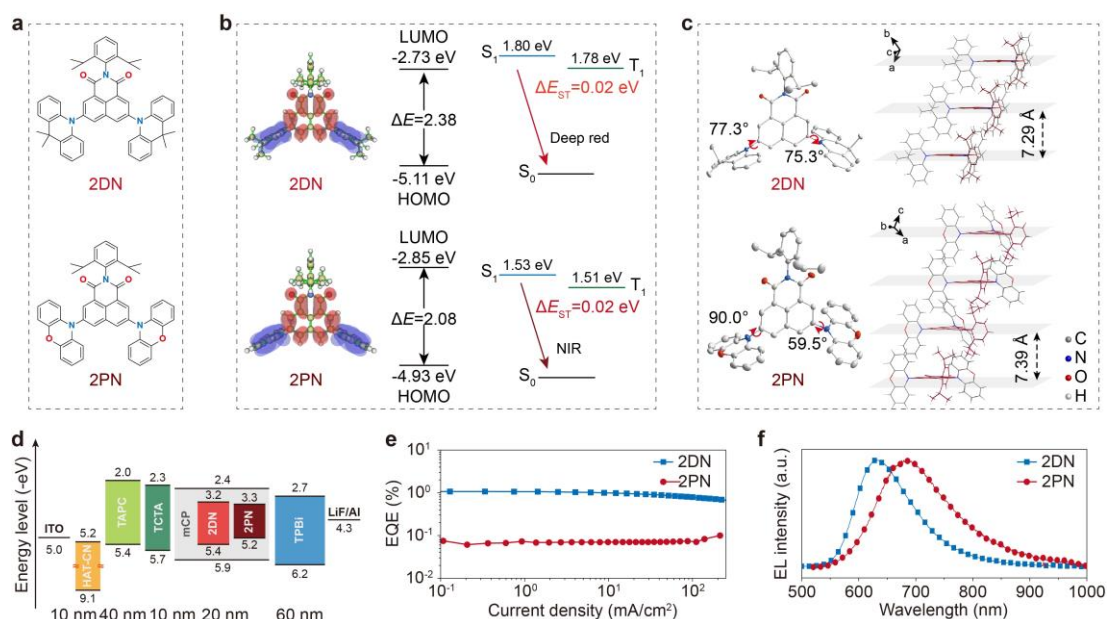
Figure 1.3 Photophysical and OLED properties of DR-NIR TADF emitters. a, Chemical structures of 2DN and 2PN. **b**, Theoretical calculated HOMO, LUMO, S_1, T_1 energy levels, and frontier orbital distributions with optimized ground state structures (blue for HOMO, red for LUMO) at the level of the B3LYP/6-31G(d). **c**, Single-crystal structures of emitters. **d**, Energy level diagram of materials used in the vacuum-deposition OLEDs. **e**. EQE versus current density characteristics for 10 wt% 2DN and 2PN emitters-doped devices. **f**, EL spectra of relevant devices. Ref. [37]; Copyright © 2022, Elsevier B.V.

Deep red to NIR (DR-NIR) organic molecules and OLEDs have extensive promising applications. However, many efforts to achieve TADF typed OLEDs with DR-NIR emission regretfully set up a barrier for their efficiency roll-off. To solve this problem,

I and coauthors developed a series wedge-shape emitters of 1,8-Naphthalimide-derivatives, 2DN and 2PN, which were designed and synthesized by using multiple donor and isopropyl modification strategies (Figure 1.3a).[37] The density functional theory (DFT) calculations show the HOMO are distributed on donor segments (DMAC and PXZ), and LUMO mainly located on the 1,8-Naphthalimide based acceptor (Figure 1.3b). Such significant separations of HOMO and LUMO are reduce ΔE_{ST} for efficient TADF properties. And as shown in Figure 1.3c, the wedge-shape molecular construction of 2DN and 2PN emitters increase planar distance of different molecules (7.29-7.39 Å) and pre-twisted angles between acceptor and donors of a TADF molecule (59.5-90°). These structural characteristics help to realize efficient DR-NIR emission (646-755 nm), small ΔE_{ST}, short DF lifetime (τ_D) and negligible π-π stacking in aggregation states. Accordingly, we fabricated OLEDs showed target DR-NIR electroluminescence in the range 629-701 nm, and greatly reduced efficiency roll-offs. The efficiency roll-offs are 8.4% for 2DN and are near zero for 2PN at 100 cd m^{-2}, which is among the best level of TADF OLEDs with DR-NIR electroluminescence (Figures 1.3d-f).

In 2016, Prof. Hatakeyama's group designed and synthesized of novel organic molecules, which exhibited ultrapure blue TADF emissions [full width at half-maximum (FWHM) = 28 nm].[38] The use of a rigid polycyclic aromatic framework with a boron atom and two nitrogen atoms can effectively separate the HOMO and LUMO (unlike the molecular design principle proposed by Prof. Adachi's group). This approach enabled efficient HOMO-LUMO separation and a small energy gap between the singlet and triplet excited states (ΔE_{ST}), leading to high photoluminescence quantum yields and the ability to fabricate blue OLED devices with high EQE but a serious efficiency roll-off. Furthermore, they developed a new multiple resonance TADF emitter *v*-DABNA, consisting of five benzene rings linked by two boron and four nitrogen atoms, along with two diphenylamino substituents.[39] The unique molecular structure induced important localization of the highest occupied and LUMO on

different atoms. The fabricated OLED device, using *v*-DABNA as the guest in the emission layer, achieved an ultrapure blue light at 469 nm with an FWHM of 18 nm and an extremely high EQE of up to 34.4%.

1.2.2.2 Afterglow Organic Light-Emitting Diodes

Traditional OLEDs (as illustrated in **1.2.2.1**), known for light weight and flexibility, require efficient triplet exciton harvesting. Organic afterglow offers an alternative to traditional devices by producing long-lasting electroluminescence without needing an additional phosphor layer, making them ideal for future lighting.

Prof. Kabe *et al.,* developed a new long-lived phosphorescence host material, 3-(*N*-carbazolyl)androst-2-ene (CzSte) for OLEDs.[54] CzSte consists of a semiconducting carbazole unit and a hydrophobic steroid derivative, offering a rigid environment that reduces nonradiative decay in guest emitters. When CzSte is co-deposited with deuterated *N*,*N*'-bis(3-methylphenyl)-*N*,*N*'-bis(phenyl)-9,9-dimethyl-fluorene (DMFLTPD) as the phosphorescence emitter, the resulting films displayed both blue fluorescence and green phosphorescence under photoexcitation. The integration of this phosphorescence layer into an OLED realized a device that exhibits blue emission under voltage on and green phosphorescence after switching off the applied voltage. Inspired by the proposed phosphorescence mechanism in blend film, they further used a combination of the electron donor 4,4',4-tris[phenyl(*m*-tolyl)amino]triphenylamine (m-MTDATA) and the electron acceptor PPT in OLEDs.[55] The key findings were that the thickness of the emission layer and the doping concentration of guest molecules were important to observe LPL in OLEDs, in contrast to the typical OLED structure.

1.2.2.3 Inorganic Light-Emitting Diodes

White inorganic LEDs powered by direct current (DC) are widely used, requiring

conversion of alternating current (AC) to DC, which introduces heat and noise issues. To address these, AC-driven LEDs (AC-LEDs) have gained attention as they can operate directly from grid power without conversion. However, AC-LEDs can flicker at low frequencies, which may lead to visual discomfort and health issues. Various solutions, including circuit design and using PersL phosphor, have been proposed to reduce flicker by maintaining a steady light output during the AC cycle.[210] Prof. Tanabe's group investigated the use of yellow PersL garnet phosphors to suppress the flicker effect in AC-LED lighting systems. The AC-LED system has advantages such as higher energy efficiency and lower cost, but it causes flicker issues due to rapid fluctuations of the power. The $GdAl_2Ga_3O_{12}$:Ce-Cr PersL phosphor can effectively suppress the flicker effect in AC-LED systems by providing steady PersL even when the LED is not actively emitting light.

1.2.3 Bioimaging

Optical bioimaging is significant for investigating microspecies in living cells, offering a unique method for visualizing tissue morphology with subcellular resolution. By time-resolved observation, PersL can be effectively distinguished from background fluorescence and scattering light, enhancing its utility for bioimaging.[14] Additionally, the decay duration of the afterglow can last for seconds or even hours, facilitating time-resolved luminescence imaging without requiring additional instrumentation.

In 2007, Prof. Scherman *et al.,* first developed PersL nanoparticles (NPs) for in *vivo* imaging.[211] The NPs can be charged before injection and NPs' location can be monitored in real-time for over an hour without the need for external illumination. The NPs were synthesized in a narrow size distribution of 50-100 nm. The NPs exhibited long-lasting afterglow emission in the NIR range, which allowed for improved signal-to-noise ratio and deep tissue imaging compared to traditional fluorescence-based techniques. The authors demonstrated the feasibility of in *vivo* imaging using

subcutaneous and intramuscular injections in mice and showed that the NPs can be surface modified to enable targeting or long blood circulation.

Prof. Pu's group presented a universal method to convert regular optical reagents (including fluorescent polymers, dyes, and inorganic semiconductors) into afterglow luminescent NPs (ALNPs).[73] This method includes cascade light reactions into a single particle, allowing ALNPs to chemically store light energy and spontaneously decay during the energy transfer process. The afterglow distribution of ALNPs can be finely tuned to provide emission from the visible to NIR regions, with their intensity predictable through mathematical models. Representative NIR ALNPs enable rapid tumor detection in living mice with a signal-to-background ratio more than three orders of magnitude higher than NIR fluorescence.

1.2.4 Information Storage

Optical information storage, known for large capacity and low energy use, is crucial in the digital age. While traditional media like CDs and Blu-rays face limits in 2D resolution, new advancements like super-resolution and multiplexing promise higher storage densities. PersL materials (with trap states), capable of storing and emitting photons, offer potential for next-generation optical data storage by enabling data encoding and decoding through photon-based multiplexing.[184]
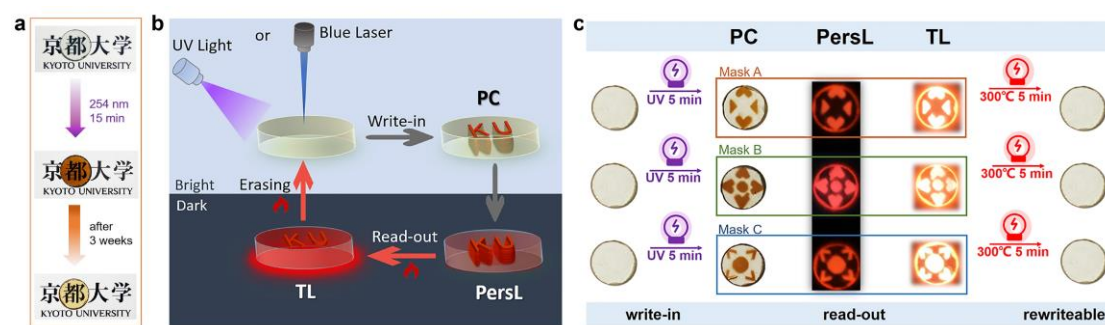
Figure 1.4 Information Storage applications of Y$_3$Al$_2$Ga$_3$O$_{12}$ transparent ceramic.

a, Photographs of the $Y_3Al_2Ga_3O_{12}:Pr^{3+}$ transparent ceramic sample before (top), after 15 minutes of UV ($\lambda ex = 254$ nm) light charging (middle), and three weeks after UV light cessation (bottom), displaying discoloration. **b**, Schematic representation of optical information write-in and read-out processes. **c**, Optical information display demonstrating write-in, read-out, and bleaching through photochromism and PersL in $Y_3Al_2Ga_3O_{12}:Pr^{3+}$ transparent ceramic, achieved by alternating between 254 nm irradiation and a 300°C thermal stimulation. Ref. [171]; Copyright © 2023, Wiley-VCH GmbH.

Dr. Du and Prof. Ueda *et al.* developed Pr^{3+} doped $Y_3Al_2Ga_3O_{12}$ transparent ceramic, with in-line transmittance over 80% at 1800 nm, displays robust PersL after optical up-conversion charging.[171] Two kinds of trap states involving intrinsic oxygen vacancies with varying trap depths were thoroughly investigated. Remarkably, the phosphor also exhibits photochromic characteristics with excellent resistance to fatigue. The excellent fatigue resistance is demonstrated by the reversibility of the color change through alternating optical excitation and thermal stimulation (Figure 1.4a). This work paves the way for future applications in light energy storage (Figures 1.4b-c).

1.2.5 Encryption and Optical Anti-Counterfeiting

In a landscape characterized by pervasive misinformation and exaggerated claims, the prevention of fraud has become imperative, positioning anti-counterfeiting labeling as one of the most effective strategies. Traditional optical anti-counterfeiting systems, relying on luminescent dyes and nanoparticles, face challenges like easy forgery and background noise due to short-lived emissions. Organic PersL materials with long-lived, tunable emissions offer a promising solution, enabling multi-mode encryption and reducing background interference.
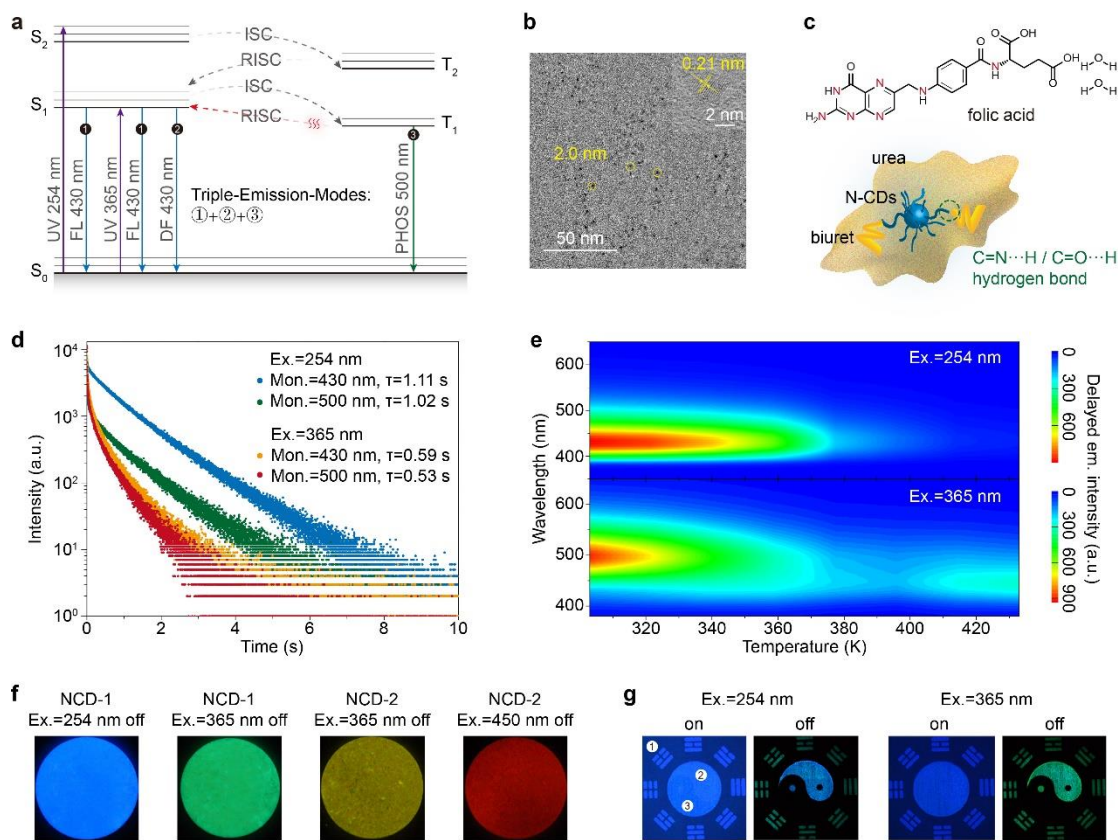
Figure 1.5 Photophysical and anti-counterfeiting applications of NCDs compounds. a, Schematic representation of CDs afterglow. **b**, TEM image. **c**, Structure of folic acid and CDs-based compound. **d**, Afterglow decay curves. **e**, Temperature-dependent afterglow contour mapping by the excitation of 254 nm (top) and 365 nm (bottom). **f**, Afterglow photographs of the samples after turning off the lamps. **g**, Optical anti-counterfeiting applications by inkjet printing. Ref. [80]; Copyright © 2019, The Royal Society of Chemistry.

Some pioneering efforts to trigger good afterglow performance in CDs-based phosphors for advanced anti-counterfeiting, nevertheless, did not perfectly address the problem of printability and color-tunability. I and coauthors developed an encapsulating-dissolving-recrystallization route for CDs-based anti-counterfeiting inks,

and realized full-color and triple-mode emissions from these CDs-based inks (Figure 1.5a).[80] As shown in Figures 1.5b-c, nitrogen-doped CDs (NCD) (~2.0 nm) were synthesized by a hydrothermal reaction, and then encapsulated with biuret and urea. Rich nitrogen doping has large spin-orbit coupling to overcome the spin-forbidden transition between triplet to singlet states. The hydrogen bonds (C=N…H and C=O…H) between NCD and biuret greatly suppress the non-radiative relaxation of the triplet excitons. And the crystallized urea worked as a dense layer to isolate the triplet species from atmospheric O_2 molecules (a typical quencher). As a result, the afterglow lifetime reached up to 1.11 s (Figure 1.5d). Interestingly, as demonstrated in Figure 1.5e, under different excitation wavelengths and at RT, the colors of afterglow are blue and green by the excitation of 254 nm and 365 nm, respectively. The DF emission at ~430 nm under short excitation wavelength mainly occurred through $S_0 \rightarrow S_2 \rightarrow T_2 \rightarrow S_1 \rightarrow S_0$, which could be classified as HLCT mechanism. Besides, with long wavelength excitation, the RTP emission peak significantly shifted to 500 nm *via* $S_0 \rightarrow S_1 \rightarrow T_1 \rightarrow S_0$. The afterglow emissions therefore were greatly dependent on whether the excitation energy is enough to excite the electrons to the S_2 state. Moreover, although with the excitation of 365 nm, the electrons could go through $S_0 \rightarrow S_1 \rightarrow T_1 \rightarrow S_1 \rightarrow S_0$ and showed DF color with extra heating energy (bottom of Figure 1.5e), which belongs to TADF. The triple-modes processes (fluorescence, DF, and RTP) are summarized in Figure 1.5a. Full-color afterglow of NCDs composites were realized according to our universal approach. To the best of our knowledge, there was not yet a report on red afterglow in CDs at that time (Figure 1.5f). With added benefits, the composites could dissolve in kinds of solutions (*i.e.* DMF) to prepare anti-counterfeiting inks and recover afterglow properties on paper by using commercialized ink-jet printers. Figure 1.5g shows the advantages of easy-to-authenticate and hard-to-copy of these afterglow inks in practical applications.

1.2.6 X-ray Luminescence Extension Imaging

X-ray flat-panel detectors are widely used in medical imaging, safety inspections, and industrial detection, relying on two detection methods: direct detection with semiconductor materials and indirect detection with scintillators. Although direct detectors, like those using amorphous selenium, face limitations in carrier transport and sensitivity, indirect detectors dominate due to their higher sensitivity and lower detection limits. Recent advancements in flexible X-ray detectors, particularly those using PersL scintillation materials, offer promising solutions for imaging complex 3D objects and storing image information for extended periods.[212]
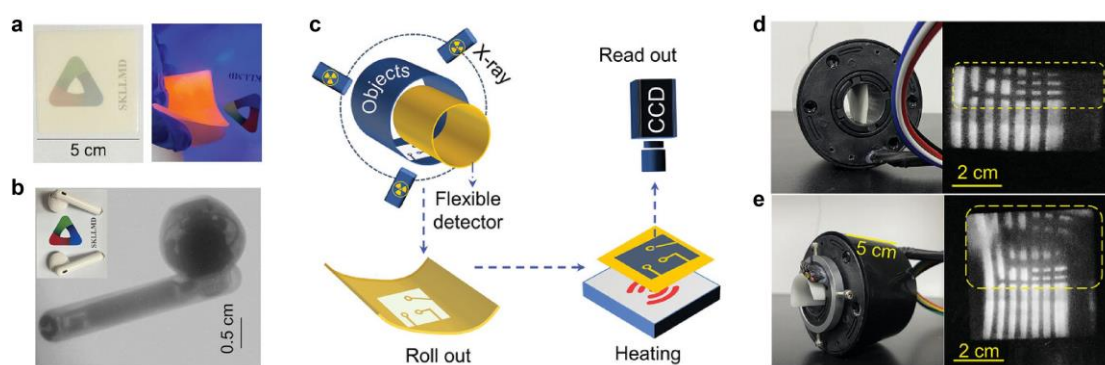
Figure 1.6 a, Photographs of a PMMA-polymer film containing 40 wt% $CsCdCl_3$:5%Mn^{2+},0.1%Zr^{4+} crystals under ambient and UV light conditions. **b**, X-ray images of an earphone, with an inset in the top panel displaying the earphone under ambient light. **c**, A schematic diagram illustrating nondestructive inspection of 3D curved objects facilitated by the PDMS-polymer film containing 10 wt% $CsCdCl_3$:5%Mn^{2+},0.1%Zr^{4+} crystals. The film is initially inserted into the target curved object, and the X-ray source is turned to excite the film, creating a latent image. After turning off the X-rays, the detector is placed on a hot substrate for thermal stimulation and reading the latent images. **d**, Imaging of an annulus electric conduction link using the flat-panel PDMS-polymer film (5 cm × 2.5 cm). **e**, Curved planar reformation of the same object using a highly flexible PDMS-polymer film (5 cm × 5 cm). The image readout temperature is 100 °C. The X-ray operation parameters in these measurements were set to a voltage of 50 kV with a tube current of 0.2 mA, resulting in an X-ray dose

rate of 20.12 mGy s^{-1}. Ref. [120]; Copyright © 2023, Wiley-VCH GmbH.

Prof. Chen and Prof. Liu *et al.,* reported a class of cubic-phase NaLuF$_4$:Ln^{3+} nanoparticles with high spatial resolution of X-ray imaging.[117] NaLuF$_4$:Tb^{3+}@NaYF$_4$ nanoscintillators, consisting of uniform spherical particles with an average size of 27 nm, exhibited enhanced luminescence due to core-shell encapsulation. These nanoparticles demonstrated a detectable strong PersL intensity even after exposure to low-dose irradiation and being stored at RT for 30 days. Moreover, by doping different lanthanide ions into NaLuF$_4$:Ln^{3+}@NaYF$_4$ nanoparticles, it is possible to achieve multicolor radioluminescence regulation ranging from the UV to NIR light. By the elastic collision between high-momentum X-ray photons and small fluorine ions, trap states with trap depths ranging from 0.5 to 0.9 eV were formed. These collisions resulted in the creation of fluoride vacancies as electron traps and interstitials as hole traps. Importantly, NaLuF$_4$:Ln^{3+}@NaYF$_4$ nanoparticles offer several advantages, including extremely low X-ray detection thresholds, high luminescence efficiency, and uniform dispersion in organic matrices such as polydimethylsiloxane (PDMS). These nanoparticles hold great potential for applications in next-generation flexible, highly sensitive, and high spatial resolution X-ray delay imaging, as well as wearable X-ray detection devices. Prof. Xia *et al.,* have rationally designed and synthesized halide perovskite CsCdCl$_3$:Mn^{2+}, R^{4+} (R = Ti, Zr, Hf, and Sn) for use as X-ray PersL phosphors. The storage capability can be significantly enhanced by trap regulation *via* Mn^{2+} site occupation and substitution.[120] Moreover, X-ray imaging with a resolution of 12.5 lp mm^{-1} has been demonstrated in the PMMA-based detector, allowing for three-dimensional X-ray imaging in a delayed mode (Figure 1.6).

1.2.7 Latent Fingerprints Identification

The latent fingerprints (LFP) identification recognition method should encompass

comprehensive details, spanning from Level 1 (overall fingerprint shape, core point, delta, *etc.*) to Level 2 (ending, bifurcation, island, short ridge, *etc.*) and finally to Level 3 (including details such as ridge width, edge shape, pore size, *etc.*).[213] Most optical LFP imaging methods face interference from background noise during excitation, leading to a low signal-to-noise ratio. Developing new imaging technologies with higher signal-to-background ratios and resolution is crucial for enhancing security. PersL materials, capable of emitting light long after excitation, enable time-gated imaging, eliminating background fluorescence and offering clearer, higher-contrast images.
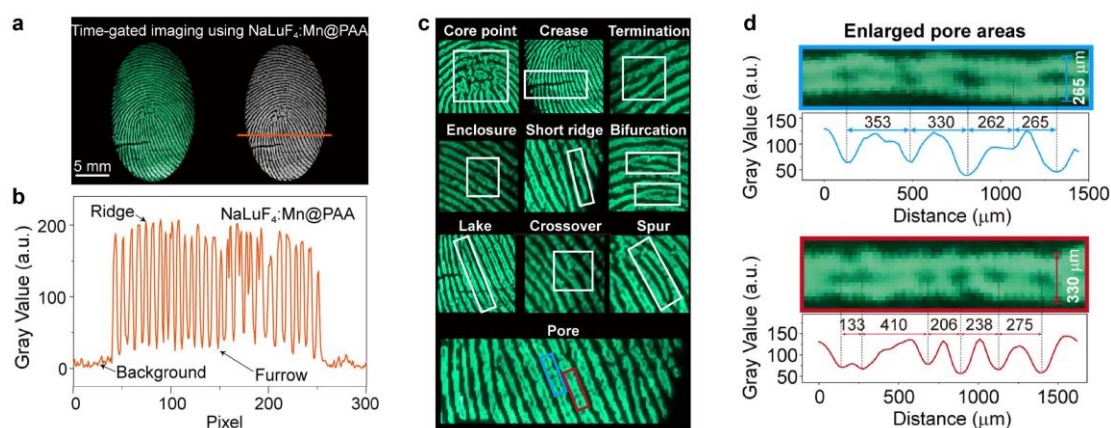
Figure 1.7 Latent Fingerprints Identification applications of NaLuF$_4$:Mn^{2+} nanoparticles. a, Photographs and grayscale images of LFPs deposited on glass by using NaLuF$_4$:Mn@PAA. **b**, The variations in grayscale values along the highlighted straight line in Fig. 5a. **c**, The enlarged details of LFPs, including Level 1, Level 2, and Level 3, developed using the NaLuF4:Mn@PAA nanoparticles. **d**, The enlarged pore areas and their corresponding grayscale value distribution. Ref. [122]; Copyright © 2022, American Chemical Society.

Prof. Zhuang and Prof. Xie *et al.,* reported COOH-bond modified NaLuF$_4$:Mn^{2+} nanoparticles with high PersL intensity for ideal candidate for time-resolved imaging

of LFPs.[122] The nanoparticles exhibited stable chemical reaction with amino acids of fingerprints, giving intense grayscale values either at ridges or at furrows (Figures 1.7a-b). The high signal-to-background ratio allowed for detailed analysis of LFPs, covering details from Level 1 to Level 3 (Figures 1.7c-d).

1.2.8 Sensing

Phosphorescence or delayed fluorescence has become widely recognized for its use in optical sensing applications due to its ability to effectively minimize autofluorescence and scattering light from matrices, resulting in higher sensitivity. The PersL is typically sensitive to oxygen, water, pH, pressure, temperature, *etc.*[17, 214, 215] Prof. Yang's group developed a new class of pure organic materials with dual-emission for ratio and color metrics in oxygen sensing and detection.[216] The researchers chemically modified thianthrene (TA) into intramolecular dimers and dispersed them in a polymer matrix to form films. These TA-based materials exhibited strong RTP emission with long lifetimes. The dimer displayed the largest red-shifted RTP, longest lifetime, and highest RTP efficiency, realizing the highest quenching efficiency and sensitivity for quantitative oxygen detection. Prof. Yuan *et al.,* synthesized Zn_2GeO_4:Mn (ZGO:Mn) PersL nanorods (NRs).[143] PersL intensity and decay duration of the ZGO:Mn NRs can be regulated the reaction pH. The NRs were further applied in autofluorescence-free biosensing. The long PersL of the bioprobes eliminated the interference from serum autofluorescence.

1.2.9 Stress Recording

Prof. Zhuang *et al.,* developed a force-induced charge carrier storage (FICS) effect in trap-typed ML materials, *i.e.*, $(Sr,Ba)Si_2O_2N_2$:Eu^{2+}/Yb^{2+},Dy^{3+}, which enabled storage of mechanical energy (such as grinding or squeezing) in deep traps except for the above-

mentioned optical excitation. The force loading may generate an instantaneous electric field within the crystal through triboelectricity or piezoelectricity, which excites the luminescent centers and stores some of the charge carriers in deep traps. The proposed FICS effect enables distributed stress sensing in a delayed mode, thereby extending the application of deep-trap PersL materials to novel stress recording devices.[105]

1.2.10 Time-Temperature Indicator

The deep-trap PersL phosphor can be extended to a wider application range to time-temperature indicators (TTIs), which have the capability to convert time-temperature history into readily accessible information, enabling the monitoring of the quality of perishable foods, pharmaceuticals, or specialty chemicals throughout the entire transport and storage process.[217, 218] Current TTI technologies, such as diffusion-based TTIs and polymerization-activated TTIs, suffer from limitations in recyclability, sensitivity, and environmental tolerance, which restrict their broad adoption.
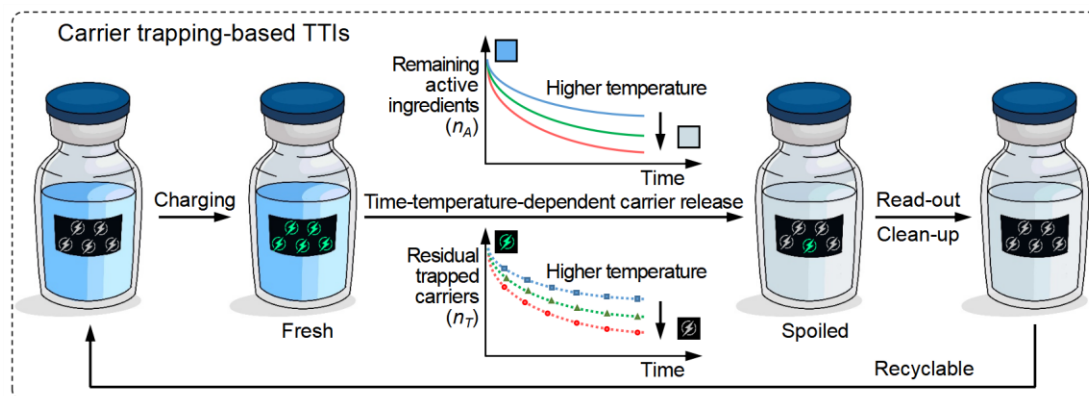
Figure 1.8 Schematics of light storage based TTIs. The release of trapped carriers is closely dependent on the storage temperature and time. The number of residual trapped carriers (n_T) can be read out by using a TL method. The light storage based TTIs are recyclable. The top inset data of remaining active ingredient (n_A) were cited for comparison.[217, 218] Ref. [121]; Copyright © 2023, Wiley-VCH GmbH.

Song *et al.,* developed light-storage-based TTI technology exhibits exceptional recyclability, reliability, and environmental stability.[121] As shown in Figure 1.8, PersL materials serve as the basis for TTI design, relying on the principle that the release rate of light-induced trapped carriers in these materials correlates with storage time and temperature. This correlation allows us to assess product freshness based on the number of residual carriers. The $KZnF_3:Mn^{2+}$ fluoride submicron particles with a broad trap distribution from 0.52 to 0.96 eV were suitable for potential TTI applications.

References

[1] J. Xu, S. Tanabe, *J. Lumin.* **2019**, 205, 581-620.

[2] L. Liang, J. Chen, K. Shao, X. Qin, Z. Pan, X. Liu, *Nat. Mater.* **2023**, 22, 289-304.

[3] W. Zhao, Z. He, B. Z. Tang, *Nat. Rev. Mater.* **2020**, 5, 869-885.

[4] R. Gao, M. S. Kodaimati, D. Yan, *Chem. Soc. Rev.* **2021**, 50, 5564-5589.

[5] J. Hölsä, *Electrochem. Soc. Interface* **2009**, 18, 42-45.

[6] T. Matsuzawa, Y. Aoki, N. Takeuchi, Y. Murayama, *J. Electrochem. Soc.* **2019**, 143, 2670-2673.

[7] H. Yamamoto, T. Matsuzawa, *J. Lumin.* **1997**, 72-74, 287-289.

[8] Y. Lin, Z. Tang, Z. Zhang, *Mater. Lett.* **2001**, 51, 14-18.

[9] Y. Lin, Z. Tang, Z. Zhang, C. W. Nan, *Appl. Phys. Lett.* **2002**, 81, 996-998.

[10] Y. Lin, Z. Tang, Z. Zhang, X. Wang, J. Zhang, *J. Mater. Sci. Lett.* **2001**, 20, 1505-1506.

[11] M. Kasha, *Discuss. Faraday Soc.* **1950**, 9, 14-19.

[12] A. Jablonski, *Nature* **1933**, 131, 839-840.

[13] G. Hong, X. Gan, C. Leonhardt, Z. Zhang, J. Seibert, J. M. Busch, S. Bräse, *Adv. Mater.* **2021**, 33, 2005630.

[14] K. Y. Zhang, Q. Yu, H. Wei, S. Liu, Q. Zhao, W. Huang, *Chem. Rev.* **2018**, 118, 1770-1839.

[15] H. Uoyama, K. Goushi, K. Shizu, H. Nomura, C. Adachi, *Nature* **2012**, 492, 234-238.

[16] Y. Li, M. Gecevicius, J. Qiu, *Chem. Soc. Rev.* **2016**, 45, 2090-2136.

[17] S. Xu, R. Chen, C. Zheng, W. Huang, *Adv. Mater.* **2016**, 28, 9920-9940.

[18] H. Shi, W. Yao, W. Ye, H. Ma, W. Huang, Z. An, *Accounts Chem. Res.* **2022**, 55, 3445-3459.

[19] Q. Li, Y. Tang, W. Hu, Z. Li, *Small* **2018**, 14, e1801560.

[20] Q. Lou, N. Chen, J. Zhu, K. Liu, C. Li, Y. Zhu, W. Xu, X. Chen, Z. Song, C. Liang, et al., *Adv. Mater.* **2023**, 35, e2211858.

[21] C. Ye, L. Zhou, X. Wang, Z. Liang, *Phys. Chem. Chem. Phys.* **2016**, 18, 10818-10835.

[22] W. Li, Y. Pan, L. Yao, H. Liu, S. Zhang, C. Wang, F. Shen, P. Lu, B. Yang, Y. Ma, *Adv. Opt. Mater.* **2014**, 2, 892-901.

[23] R. Kabe, C. Adachi, *Nature* **2017**, 550, 384-387.

[24] C. Lin, Z. Wu, H. Ma, J. Liu, S. You, A. Lv, W. Ye, J. Xu, H. Shi, B. Zha, W. Huang, Z. An, Y. Zhuang, R.-J. Xie, *Nat. Photon.* **2024**, 18, 350-356.

[25] N. Gan, H. Shi, Z. An, W. Huang, *Adv. Funct. Mater.* **2018**, 28, 1802657.

[26] J. Yang, Z. Chen, M. Fang, Z. Li, *Smart Mol.* **2024**, e20240034.

[27] X. Wang, O. S. Wolfbeis, R. J. Meier, *Chem. Soc. Rev.* **2013**, 42, 7834-7869.

[28] Z. An, C. Zheng, Y. Tao, R. Chen, H. Shi, T. Chen, Z. Wang, H. Li, R. Deng, X. Liu, W. Huang, *Nat. Mater.* **2015**, 14, 685-690.

[29] S. Cai, H. Shi, J. Li, L. Gu, Y. Ni, Z. Cheng, S. Wang, W. W. Xiong, L. Li, Z. An, W. Huang, *Adv. Mater.* **2017**, 29, 1701244.

[30] H. Wang, H. Ma, N. Gan, K. Qin, Z. Song, A. Lv, K. Wang, W. Ye, X. Yao, C. Zhou, X. Wang, Z. Zhou, S. Yang, L. Yang, C. Bo, H. Shi, F. Huo, G. Li, W. Huang, Z. An, *Nat. Commun.* **2024**, 15, 2134.

[31] J. Yu, Z. Sun, H. Ma, C. Wang, W. Huang, Z. He, W. Wu, H. Hu, W. Zhao, W. H. Zhu, *Angew. Chem. Int. Ed.* **2023**, 62, e202316647.

[32] X. Wang, H. Shi, H. Ma, W. Ye, L. Song, J. Zan, X. Yao, X. Ou, G. Yang, Z. Zhao, M. Singh, C. Lin, H. Wang, W. Jia, Q. Wang, J. Zhi, C. Dong, X. Jiang, Y. Tang, X. Xie, Y. Yang, J. Wang, Q. Chen, Y. Wang, H. Yang, G. Zhang, Z. An, X. Liu, W. Huang, *Nature Photon.* **2021**, 15, 187-192.

[33] M. Dong, A. Lv, X. Zou, N. Gan, C. Peng, M. Ding, X. Wang, Z. Zhou, H. Chen, H. Ma, L. Gu, Z. An, W. Huang, *Adv. Mater.* **2024**, e2310663.

[34] P. Alam, T. S. Cheung, N. L. C. Leung, J. Zhang, J. Guo, L. Du, R. T. K. Kwok, J. W. Y. Lam, Z. Zeng, D. L. Phillips, H. H. Y. Sung, I. D. Williams, B. Z. Tang, *J. Am. Chem. Soc.* **2022**, 144, 3050-3062.

[35] C. W. Ju, X. C. Wang, B. Li, Q. Ma, Y. Shi, J. Zhang, Y. Xu, Q. Peng, D. Zhao, *Proc. Natl. Acad. Sci.* **2023**, 120, e2310883120.

[36] Q. S. Zhang, S. C. Wang, X. H. Xiong, P. Y. Fu, X. D. Zhang, Y. N. Fan, M. Pan, *Angew. Chem. Int. Ed.* **2022**, 61, e202205556.

[37] C. Lin, Z. Wu, J. Liu, W.-T. Deng, Y. Zhuang, T. Xuan, J. Xue, L. Zhang, G. Wei, R.-J. Xie, *J. Lumin.* **2022**, 243,118683.

[38] T. Hatakeyama, K. Shiren, K. Nakajima, S. Nomura, S. Nakatsuka, K. Kinoshita, J. Ni, Y. Ono, T. Ikuta, *Adv. Mater.* **2016**, 28 (14), 2777-2781.

[39] Y. Kondo, K. Yoshiura, S. Kitera, H. Nishi, S. Oda, H. Gotoh, Y. Sasada, M. Yanai, T. Hatakeyama, *Nature Photonics* **2019**, 13, 678-682.

[40] H. Deng, G. Li, H. Xie, Z. Yang, Z. Mao, J. Zhao, Z. Yang, Y. Zhang, Z. Chi, *Angew. Chem. Int. Ed.* **2024**, 63, e202317631.

[41] X. Zhang, K. C. Chong, Z. Xie, B. Liu, *Angew. Chem. Int. Ed.* **2023**, 62, e202310335.

[42] C. Chen, Z. Chi, K. C. Chong, A. S. Batsanov, Z. Yang, Z. Mao, Z. Yang, B. Liu, *Nat. Mater.* **2021**, 20, 175-180.

[43] Z. Xie, Y. Xue, X. Zhang, J. Chen, Z. Lin, B. Liu, *Nat. Commun.* **2024**, 15, 3668.

[44] H. Wang, C. Peng, M. Chen, Y. Xiao, T. Zhang, X. Liu, Q. Chen, T. Yu, W. Huang, *Angew. Chem. Int. Ed.* **2024**, 63, e202316190.

[45] Q. S. Zhang, X. D. Zhang, J. Y. Zhuang, M. Pan, *Aggregate* **2023**, e456.

[46] W. Xie, W. Huang, J. Li, Z. He, G. Huang, B. S. Li, B. Z. Tang, *Nat. Commun.* **2023**, 14, 8098.

[47] K. Jinnai, R. Kabe, C. Adachi, *Adv. Mater.* **2018**, 30, e1800365.

[48] P. Jin, X. Wei, B. Yin, L. Xu, Y. Guo, C. Zhang, *Adv. Mater.* **2024**, e2400158.

[49] X. Wang, J. Li, Y. Zeng, X. Chen, M. Wu, G. Wang, X. Li, B. Wang, K. Zhang, *Chem. Eng. J.* **2023**, 460, 141916.

[50] W. Li, Z. Li, C. Si, M. Y. Wong, K. Jinnai, A. K. Gupta, R. Kabe, C. Adachi, W. Huang, E. Zysman-Colman, *Adv. Mater.* **2020**, 32, e2003911.

[51] X. Liang, Y. X. Zheng, J. L. Zuo, *Angew. Chem. Int. Ed.* **2021**, 60, 16984-16988.

[52] P. Alam, N. L. C. Leung, J. Liu, T. S. Cheung, X. Zhang, Z. He, R. T. K. Kwok, J. W. Y. Lam, H. H. Y. Sung, I. D. Williams, C. C. S. Chan, K. S. Wong, Q. Peng, B. Z. Tang, *Adv. Mater.* **2020**, 32, e2001026.

[53] K. Jinnai, R. Kabe, Z. Lin, C. Adachi, *Nat. Mater.* **2022**, 21, 338-344.

[54] R. Kabe, N. Notsuka, K. Yoshida, C. Adachi, *Adv. Mater.* **2016**, 28, 655-660.

[55] S. Tan, K. Jinnai, R. Kabe, C. Adachi, *Adv. Mater.* **2021**, 33, e2008844.

[56] G. Xie, J. Wang, X. Xue, H. Li, N. Guo, H. Li, D. Wang, M. Li, W. Huang, R. Chen, Y. Tao, *Appl. Phys. Rev.* **2022**, 9, 031410.

[57] W. Qiu, D. Liu, Z. Chen, Y. Gan, S. Xiao, X. Peng, D. Zhang, X. Cai, M. Li, W. Xie, G. Sun, Y. Jiao, Q. Gu, D. Ma, S.-J. Su, *Matter* **2023**, 6, 1231-1248.

[58] H.-T. Feng, J. Zeng, P.-A. Yin, X.-D. Wang, Q. Peng, Z. Zhao, J. W. Y. Lam, B. Z.

Tang, *Nat. Commun.* **2020**, 11, 2041-1723.

[59] H. Lv, H. Tang, Y. Cai, T. Wu, D. Peng, Y. Yao, X. Xu, *Angew. Chem. Int. Ed.* **2022**, 61, e202204209.

[60] Z. Lin, M. Li, R. Yoshioka, R. Oyama, R. Kabe, *Angew. Chem. Int. Ed.* **2024**, 63, e202314500.

[61] J. Liu, Z. P. Song, J. Wei, J. J. Wu, M. Z. Wang, J. G. Li, Y. Ma, B. X. Li, Y. Q. Lu, Q. Zhao, *Adv. Mater.* **2023**, 36, 2306834.

[62] Y. Miao, F. Lin, D. Guo, J. Chen, K. Zhang, T. Wu, H. Huang, Z. Chi, Z. Yang, *Sci. Adv.* **2024**, 10, e3354.

[63] Y. Zhou, P. Zhang, Z. Liu, W. Yan, H. Gao, G. Liang, W. Qin, *Adv. Mater.* **2024**, e2312439.

[64] Y. Liang, P. Hu, H. Zhang, Q. Yang, H. Wei, R. Chen, J. Yu, C. Liu, Y. Wang, S. Luo, G. Shi, Z. Chi, B. Xu, *Angew. Chem. Int. Ed.* **2024**, e202318516.

[65] L. Zhou, J. Song, Z. He, Y. Liu, P. Jiang, T. Li, X. Ma, *Angew. Chem. Int. Ed.* **2024**, e202403773.

[66] K. Chen, Y. Xiong, D. Wang, Y. Pan, Z. Zhao, D. Wang, B. Z. Tang, *Adv. Funct. Mater.* **2023**, 34, 2312883.

[67] K. Chen, Y. Luo, M. Sun, C. Liu, M. Jia, C. Fu, X. Shen, C. Li, X. Zheng, X. Pu, Y. Huang, Z. Lu, *Angew. Chem. Int. Ed.* **2024**, 63, e202314447.

[68] X. Wang, W. Sun, H. Shi, H. Ma, G. Niu, Y. Li, J. Zhi, X. Yao, Z. Song, L. Chen, S. Li, G. Yang, Z. Zhou, Y. He, S. Qu, M. Wu, Z. Zhao, C. Yin, C. Lin, J. Gao, Q. Li, X. Zhen, L. Li, X. Chen, X. Liu, Z. An, H. Chen, W. Huang, *Nat. Commun.* **2022**, 13, 5091.

[69] Y. Wang, H. Gao, J. Yang, M. Fang, D. Ding, B. Z. Tang, Z. Li, *Adv. Mater.* **2021**, 33, 2007811.

[70] Q. Miao, C. Xie, X. Zhen, Y. Lyu, H. Duan, X. Liu, J. V. Jokerst, K. Pu, *Nat. Biotechnol.* **2017**, 35, 1102-1110.

[71] X. Zhen, C. Xie, K. Pu, *Angew. Chem. Int. Ed.* **2018**, 57, 3938-3942.

[72] S. He, C. Xie, Y. Jiang, K. Pu, *Adv. Mater.* **2019**, 31, e1902672.

[73] Y. Jiang, J. Huang, X. Zhen, Z. Zeng, J. Li, C. Xie, Q. Miao, J. Chen, P. Chen, K. Pu, *Nat. Commun.* **2019**, 10, 2064.

[74] J. Zhu, W. Chen, L. Yang, Y. Zhang, B. Cheng, W. Gu, Q. Li, Q. Miao, *Angew. Chem. Int. Ed.* **2024**, 63, e202318545.

[75] G. S. Zheng, C. L. Shen, C. Y. Niu, Q. Lou, T. C. Jiang, P. F. Li, X. J. Shi, R. W. Song, Y. Deng, C. F. Lv, K. K. Liu, J. H. Zang, Z. Cheng, L. Dong, C. X. Shan, *Nat. Commun.* **2024**, 15, 2365.

[76] K. Jiang, Y. Wang, C. Cai, H. Lin, *Chem. Mater.* **2017**, 29, 4866-4873.

[77] L. Mo, H. Liu, Z. Liu, X. Xu, B. Lei, J. Zhuang, Y. Liu, C. Hu, *Adv. Opt. Mater.* **2022**, 10, 2102666.

[78] S. Tao, S. Lu, Y. Geng, S. A. T. Redfern, Y. Song, T. Feng, W. Xu, B. Yang, *Angew. Chem. Int. Ed.* **2018**, 57, 2393-2398.

[79] J. Liu, N. Wang, Y. Yu, Y. Yan, H. Zhang, J. Li, J. Yu, *Sci. Adv.* **2017**, 3, e1603171.

[80] C. Lin, Y. Zhuang, W. Li, T. Zhou, R.-J. Xie, *Nanoscale* **2019**, 11, 6584-6590.

[81] K. Jiang, Y. Wang, C. Lin, L. Zheng, J. Du, Y. Zhuang, R. Xie, Z. Li, H. Lin, *Light Sci. Appl.* **2022**, 11, 80.

[82] Y. Li, L. Chen, S. Yang, G. Wei, X. Ren, A. Xu, H. Wang, P. He, H. Dong, G. Wang, C. Ye, G. Ding, *Adv. Mater.* **2024**, e2313639.

[83] W. Ye, H. Ma, H. Shi, H. Wang, A. Lv, L. Bian, M. Zhang, C. Ma, K. Ling, M. Gu, Y. Mao, X. Yao, C. Gao, K. Shen, W. Jia, J. Zhi, S. Cai, Z. Song, J. Li, Y. Zhang, S. Lu,

K. Liu, C. Dong, Q. Wang, Y. Zhou, W. Yao, Y. Zhang, H. Zhang, Z. Zhang, X. Hang, Z. An, X. Liu, W. Huang, *Nat. Mater.* **2021**, 20, 1539-1544.

[84] W. Zhu, Z. He, Z. Zhang, *Chem. Eng. J.* **2024**, 493, 152443.

[85] S. Feng, Y. Ma, S. Wang, S. Gao, Q. Huang, H. Zhen, D. Yan, Q. Ling, Z. Lin, *Angew. Chem. Int. Ed.* **2022**, 61, e202116511.

[86] S. Liu, X. Fang, B. Lu, D. Yan, *Nat. Commun.* **2020**, 11, 4649.

[87] B. Zhou, D. Yan, *Angew. Chem. Int. Ed. Engl.* **2019**, 58, 15128-15135.

[88] H. Gong, H. Yu, Y. Zhang, L. Feng, Y. Tian, G. Cui, H. Fu, *Angew. Chem. Int. Ed.* **2023**, 62, e202219085.

[89] B. Zhou, Z. Qi, M. Dai, C. Xing, D. Yan, *Angew. Chem. Int. Ed.* **2023**, 62, e202309913.

[90] Z. Li, M. Cao, Z. Rao, X. Zhao, X. Gong, *Small* **2023**, 19, 2302357.

[91] J. H. Wei, W. T. Ou, J. B. Luo, D. B. Kuang, *Angew. Chem. Int. Ed.* **2022**, 61, e202207985.

[92] J.-H. Wei, J.-F. Liao, L. Zhou, J.-B. Luo, X.-D. Wang, D.-B. Kuang, *Sci. Adv.* **2021**, 7, eabg3989.

[93] N. Zhang, L. Qu, S. Dai, G. Xie, C. Han, J. Zhang, R. Huo, H. Hu, Q. Chen, W. Huang, H. Xu, *Nat. Commun.* **2023**, 14, 2901.

[94] X. Yang, D. Yan, *Adv. Opt. Mater.* **2016**, 4, 897-905.

[95] J. Liu, Y. Zhuang, L. Wang, T. Zhou, N. Hirosaki, R.-J. Xie, *ACS Appl. Mater. Interfaces* **2018**, 10, 1802-1809.

[96] Y. Yang, K.-Z. Wang, D. Yan, *ACS Appl. Mater. Interfaces* **2016**, 8, 15489-15496.

[97] X. Liang, X. F. Luo, Z. P. Yan, Y. X. Zheng, J. L. Zuo, *Angew. Chem. Int. Ed.* **2021**, 60, 24437-24442.

[98] F. H. Yu, R. Jin, X. Chang, K. Li, G. Cui, Y. Chen, *Angew. Chem. Int. Ed.* **2023**, 62, e202312927.

[99] H. Shen, S. Liao, Z. Li, Y. Wang, S. Huan, X. B. Zhang, G. Song, *Chem. Eur. J.* **2023**, 29, e202301209.

[100] K. N. Solov'ev, E. A. Borisevich, *Phys.-Uspekhi* **2005**, 48, 231-253.

[101] J. M. Bermúdez-García, M. Sánchez-Andújar, S. Castro-García, J. López-Beceiro, R. Artiaga, M. A. Señarís-Rodríguez, *Nat. Commun.* **2017**, 8, 15715.

[102] L. Dou, A. B. Wong, Y. Yu, M. Lai, N. Kornienko, S. W. Eaton, A. Fu, C. G. Bischak, J. Ma, T. Ding, N. S. Ginsberg, L.-W. Wang, A. P. Alivisatos, P. Yang, *Science* **2015**, 349, 1518-1521.

[103] Y. Katayama, J. Ueda, S. Tanabe, *J. Lumin.* **2014**, 148, 290-295.

[104] Y. Zhuang, J. Ueda, S. Tanabe, *J. Mater. Chem. C* **2013**, 1, 7849-7855.

[105] Y. Zhuang, D. Tu, C. Chen, L. Wang, H. Zhang, H. Xue, C. Yuan, G. Chen, C. Pan, L. Dai, R.-J. Xie, *Light Sci. Appl.* **2020**, 9, 182.

[106] Y. Wang, L. Wang, *J. Appl. Phys.* **2007**, 101, 053108.

[107] K. Van den Eeckhout, A. J. J. Bos, D. Poelman, P. F. Smet, *Phys. Rev. B* **2013**, 87, 045126.

[108] M. Sonoda, M. Takano, J. Miyahara, H. Kato, *Radiology* **1983**, 148, 833-838.

[109] K. Takahashi, J. Miyahara, Y. Shibahara, *J. Electrochem. Soc.* **2019**, 132, 1492-1494.

[110] H. Riesen, W. A. Kaczmarek, *Inorg. Chem.* **2007**, 46, 7235-7237.

[111] N. Riesen, X. Pan, K. Badek, Y. Ruan, T. M. Monro, J. Zhao, H. Ebendorff-Heidepriem, H. Riesen, *Opt. Express* **2018**, 26, 12266.

[112] H. Riesen, K. Badek, T. M. Monro, N. Riesen, *Opt. Mater. Express* **2016**, 6, 3097.

[113] U. Rogulis, I. Tale, T. Hangleiter, J. M. Spaeth, *J. Phys.: Condens. Matter* **1995**, 7, 3129-3137.

[114] U. Rogulis, S. Schweizer, S. Assmann, J. M. Spaeth, *J. Appl. Phys.* **1998**, 84, 4537-4542.

[115] T. Pawlik, J. M. Spaeth, *J. Appl. Phys.* **1997**, 82, 4236-4240.

[116] T. Pawlik, J. M. Spaeth, M. Otte, H. Overhof, *Radiat. Eff. Defects Solids* **2006**, 135, 49-54.

[117] X. Ou, X. Qin, B. Huang, J. Zan, Q. Wu, Z. Hong, L. Xie, H. Bian, Z. Yi, X. Chen, et al., *Nature* **2021**, 590, 410-415.

[118] Y. Zhuang, D. Chen, W. Chen, W. Zhang, X. Su, R. Deng, Z. An, H. Chen, R. J. Xie, *Light Sci. Appl.* **2021**, 10, 132.

[119] Y. Wang, D. Chen, Y. Zhuang, W. Chen, H. Long, H. Chen, R. J. Xie, *Adv. Opt. Mater.* **2021**, 9, 2100624.

[120] X. Zhou, K. Han, Y. Wang, J. Jin, S. Jiang, Q. Zhang, Z. Xia, *Adv. Mater.* **2023**, 35, e2212022.

[121] Y. Song, J. Du, R. Yang, C. Lin, W. Chen, Z. Wu, H. Lin, X. Chen, Y. Zhuang, R. J. Xie, *Adv. Opt. Mater.* **2023**, 11, 2202654.

[122] W. Chen, Y. Song, W. Zhang, R. Deng, Y. Zhuang, R. J. Xie, *ACS Appl. Mater. Interfaces* **2022**, 14, 28230-28238.

[123] A. Meijerink, G. Blasse, *J. Phys. D: Appl. Phys.* **1991**, 24, 626-632.

[124] J. Cao, S. Ding, Y. Zhou, X. Ma, Y. Wang, *J. Mater. Chem. C* **2022**, 10, 12266-12275.

[125] Y. Tamura, A. Shibukawa, *Jpn. J. Appl. Phys.* **1993**, 32, 3187.

[126] H. Nanto, T. S., M. Miyazaki, A. Imai, H. Komori, Y. Douguchi, E. Kusano, S.

Nasu, A. Kinbara, *Proc. SPIE* **1999**, 3802.

[127] W. Li, Y. Liu, P. Ai, *Mater. Chem. Phys.* **2010**, 119, 52-56.

[128] C. Cui, G. Jiang, P. Huang, L. Wang, D. Liu, *Ceram. Int.* **2014**, 40, 4725-4730.

[129] X. Zhang, H. Suo, Y. Wang, B. Chen, W. Zheng, Q. Wang, Y. Wang, Z. Zeng, S. W. Tsang, D. Tu, et al., *Laser Photonics Rev.* **2023**, 17, 2300132.

[130] E. Zych, J. Trojan-Piegza, D. Hreniak, W. Strek, *J. Appl. Phys.* **2003**, 94, 1318-1324.

[131] A. Wiatrowska, E. Zych, *J. Phys. Chem. C* **2013**, 117, 11449-11458.

[132] M. S. Akselrod, V. S. K., D. J. Kravetsky, V. I. Gotlib, *Radiat. Prot. Dosimetry* **1990**, 32, 15-20.

[133] E. G. Yukihara, V. H. Whitley, J. C. Polf, D. M. Klein, S. W. S. McKeever, A. E. Akselrod, M. S. Akselrod, *Radiat. Meas.* **2003**, 37, 627-638.

[134] A. J. Bos, M. Prokic, J. C. Brouwer, *Radiat. Prot. Dosimetry* **2006**, 119, 130-133.

[135] C. Wang, Y. Jin, Y. Lv, G. Ju, D. Liu, L. Chen, Z. Li, Y. Hu, *J. Mater. Chem. C* **2018**, 6, 6058-6067.

[136] D. Liu, L. Yuan, Y. Jin, H. Wu, Y. Lv, G. Xiong, G. Ju, L. Chen, S. Yang, Y. Hu, *ACS Appl. Mater. Interfaces* **2019**, 11, 35023-35029.

[137] S. Lin, H. Lin, Q. Huang, Y. Cheng, J. Xu, J. Wang, X. Xiang, C. Wang, L. Zhang, Y. Wang, *Laser Photonics Rev.* **2019**, 13, 1900006.

[138] X. Sun, J. Zhang, X. Zhang, Y. Luo, X.-J. Wang, *J. Phys. D: Appl. Phys.* **2008**, 41, 195414.

[139] B. Zhang, X. Yu, T. Wang, S. Cheng, J. Qiu, X. Xu, J. McKittrick, *J. Am. Ceram. Soc.* **2015**, 98, 171-177.

[140] M. J. Knitel, P. Dorenbos, C. W. E. van Eijk, *J. Lumin.* **1997**, 72-74, 765-766.

[141] A. Dobrowolska, A. J. J. Bos, P. Dorenbos, *Radiat. Meas.* **2019**, 127, 106147.

[142] W. Wang, J. Yang, Z. Zou, J. Zhang, H. Li, Y. Wang, *Ceram. Int.* **2018**, 44, 10010-10014.

[143] J. Wang, Q. Ma, W. Zheng, H. Liu, C. Yin, F. Wang, X. Chen, Q. Yuan, W. Tan, *ACS Nano* **2017**, 11, 8185-8191.

[144] Y. Cong, Y. He, B. Dong, Y. Xiao, L. Wang, *Opt. Mater.* **2015**, 42, 506-510.

[145] Y. Katayama, T. Kayumi, J. Ueda, P. Dorenbos, B. Viana, S. Tanabe, *J. Mater. Chem. C* **2017**, 5, 8893-8900.

[146] G. Krieke, G. Doke, A. Antuzevics, I. Pudza, A. Kuzmin, E. Welter, *J. Alloys Compd.* **2022**, 922, 166312.

[147] S. Tian, B. Liu, L. Zhao, Z. Liu, X. Fan, L. Yang, Q. Min, H. Zhang, X. Yu, J. Qiu, et al., *J. Alloys Compd.* **2019**, 800, 224-230.

[148] Z. Zou, X. Tang, C. Wu, D. Wang, J. Zhang, Z. Ci, S. Du, Y. Wang, *Mater. Res. Bull.* **2018**, 97, 251-259.

[149] Y. Zhang, D. Chen, W. Wang, S. Yan, J. Liu, Y. Liang, *Inorg. Chem. Front.* **2020**, 7, 3063-3071.

[150] J. Zhang, M. Yu, Q. Qin, H. Zhou, M. Zhou, X. Xu, Y. Wang, *J. Appl. Phys.* **2010**, 108, 123518.

[151] J. Xue, T. Hu, F. Li, F. Liu, H. M. Noh, B. R. Lee, B. C. Choi, S. H. Park, J. H. Jeong, P. Du, *Laser Photon. Rev.* **2023**, 17, 2200832.

[152] W. Xie, W. Jiang, R. Zhou, J. Li, J. Ding, H. Ni, Q. Zhang, Q. Tang, J. X. Meng, L. Lin, *Inorg. Chem.* **2021**, 60, 2219-2227.

[153] X. Chen, Y. Li, K. Huang, L. Huang, X. Tian, H. Dong, R. Kang, Y. Hu, J. Nie, J. Qiu, G. Han, *Adv. Mater.* **2021**, 33, e2008722.

[154] X. Xu, Q. He, L. Yan, *J. Alloys Compd.* **2013**, 574, 22-26.

[155] X. Xu, L. Yan, X. Yu, H. Yu, T. Jiang, Q. Jiao, J. Qiu, *Mater. Lett.* **2013**, 99, 158-160.

[156] C. Wang, Z. Zheng, Y. Zhang, Q. Liu, M. Deng, X. Xu, Z. Zhou, H. He, *Opt. Express* **2020**, 28, 4249-4257.

[157] Y. Zhang, R. Huang, Z. Lin, J. Song, X. Wang, Y. Guo, C. Song, Y. Yu, *J. Alloys Compd.* **2016**, 686, 407-412.

[158] J. L. Li, J. P. Shi, C. C. Wang, P. H. Li, Z. F. Yu, H. W. Zhang, *Nanoscale* **2017**, 9, 8631-8638.

[159] X. L. Yan, Y. X. Liu, D. T. Yan, H. C. Zhu, C. G. Liu, C. S. Xu, *J. Nanosci. Nanotechnol.* **2011**, 11, 9964-9969.

[160] S. Li, Y. Liu, C. Liu, D. Yan, H. Zhu, C. Xu, L. Ma, X. Wang, *J. Alloys Compd.* **2017**, 696, 828-835.

[161] F. Liu, W. Yan, Y. J. Chuang, Z. Zhen, J. Xie, Z. Pan, *Sci. Rep.* **2013**, 3, 1554.

[162] S. Lin, H. Lin, C. Ma, Y. Cheng, S. Ye, F. Lin, R. Li, J. Xu, Y. Wang, *Light Sci. Appl.* **2020**, 9, 22.

[163] S. Lyu, P. Zhou, J. Du, X. Wang, T. Wang, P. Wang, H. Wang, S. Sun, H. Lin, *J. Mater. Chem. C* **2022**, 10, 18404-18414.

[164] X. Ma, P. Feng, Y. Wang, S. Ding, S. Tian, Y. Wang, *J. Mater. Chem. C* **2022**, 10, 1105-1117.

[165] Z. Zhou, S. Zhang, Y. Le, H. Ming, Y. Li, S. Ye, M. Peng, J. Qiu, G. Dong, *Adv. Opt. Mater.* **2021**, 10, 2101669.

[166] Y. Zhuang, J. Ueda, S. Tanabe, P. Dorenbos, *J. Mater. Chem. C* **2014**, 2, 5502.

[167] J. Ueda, K. Kuroishi, S. Tanabe, *Appl. Phys. Lett.* **2014**, 104, 101904.

[168] J. Ueda, P. Dorenbos, A. J. J. Bos, K. Kuroishi, S. Tanabe, *J. Mater. Chem. C* **2015**, 3, 5642-5651.

[169] W. Li, Y. Zhuang, P. Zheng, T. L. Zhou, J. Xu, J. Ueda, S. Tanabe, L. Wang, R. J. Xie, *ACS Appl. Mater. Interfaces* **2018**, 10, 27150-27159.

[170] J. Xu, J. Ueda, Y. Zhuang, B. Viana, S. Tanabe, *Appl. Phys. Express* **2015**, 8, 042602.

[171] Q. Du, J. Ueda, R. Zheng, S. Tanabe, *Adv. Opt. Mater.* **2023**, 11, 2202612.

[172] J. Xu, J. Ueda, S. Tanabe, *Opt. Mater. Express* **2015**, 5, 963.

[173] B. Wang, X. Li, Y. Chen, Y. Chen, J. Zhou, Q. Zeng, *J. Am. Ceram. Soc.* **2018**, 101, 4598-4607.

[174] X. Liu, J. Zhang, X. Ma, H. Sheng, P. Feng, L. Shi, R. Hu, Y. Wang, *J. Alloys Compd.* **2013**, 550, 451-458.

[175] J. Qiu, K. Miura, H. Inouye, Y. Kondo, T. Mitsuyu, K. Hirao, *Appl. Phys. Lett.* **1998**, 73, 1763-1765.

[176] C. Li, Y. Yu, S. Wang, Q. Su, *J. Non-Cryst. Solids* **2003**, 321, 191-196.

[177] C. Li, J. Wang, H. Liang, Q. Su, *J. Appl. Phys.* **2007**, 101, 113304.

[178] J. Wang, H. Zhang, B. Lei, Z. Xia, H. Dong, Y. Liu, M. Zheng, Y. Xiao, *J. Mater. Chem. C* **2015**, 3, 4445-4451.

[179] J. Wang, H. Zhang, B. Lei, H. Dong, H. Zhang, Y. Liu, N. Lai, Y. Fang, Z. Chen, *Opt. Mater.* **2014**, 36, 1855-1858.

[180] J. Wang, H. Zhang, B. Lei, H. Dong, H. Zhang, Y. Liu, M. Zheng, Y. Xiao, R. J. Xie, *J. Am. Ceram. Soc.* **2015**, 98, 1823-1828.

[181] S. Zhang, Z. Song, S. Wang, Z. Wang, F. Wang, Q. Liu, *J. Mater. Chem. C* **2020**, 8, 4956-4964.

[182] F. Wang, J. Guo, S. Wang, B. Qu, Z. Song, S. Zhang, W.-T. Geng, Q. Liu, *J. Alloys Compd.* **2020**, 821, 153482.

[183] J. Ueda, J. L. Leaño, C. Richard, K. Asami, S. Tanabe, R.-S. Liu, *J. Mater. Chem. C* **2019**, 7, 1705-1712.

[184] Y. Zhuang, L. Wang, Y. Lv, T.-L. Zhou, R.-J. Xie, *Adv. Funct. Mater.* **2018**, 28, 1705769.

[185] Y. Zhuang, Y. Lv, L. Wang, W. Chen, T. L. Zhou, T. Takeda, N. Hirosaki, R. J. Xie, *ACS Appl. Mater. Interfaces* **2018**, 10, 1854-1864.

[186] H. Song, R. Zhang, Z. Zhao, X. Wu, Y. Zhang, J. Wang, B. Li, *ACS Appl. Mater. Interfaces* **2022**, 14, 45562-45572.

[187] Y. Kitagawa, J. Ueda, S. Tanabe, *Phys. Stat. Solidi A* **2022**, 219, 2100670.

[188] S. Wang, X. Liu, B. Qu, Z. Song, Z. Wang, S. Zhang, F. Wang, W.-T. Geng, Q. Liu, *J. Mater. Chem. C* **2019**, 7, 12544-12551.

[189] Y. Lv, L. Wang, Y. Zhuang, T.-L. Zhou, R.-J. Xie, *J. Mater. Chem. C* **2017**, 5, 7095-7101.

[190] K. Takahashi, *J. Lumin.* **2002**, 100, 307-315.

[191] S. Schweizer, *Phys. Status Solidi A* **2001**, 187, 335-393.

[192] S. Jutamulia, G. M. Storti, J. Lindmayer, W. Seiderman, *Appl. Opt.* **1990**, 29, 4806-4811.

[193] J. Ueda, *Bull. Chem. Soc. Jpn.* **2021**, 94, 2807-2821.

[194] R. E. Rojas-Hernandez, F. Rubio-Marcos, M. Á. Rodriguez, J. F. Fernandez, *Renew. Sustainable Energy Rev.* **2018**, 81, 2759-2770.

[195] J. Ueda, T. Nakanishi, Y. Katayama, S. Tanabe, *Phys. Status Solidi C* **2012**, 9, 2322-2325.

[196] T. Maldiney, A. Bessiere, J. Seguin, E. Teston, S. K. Sharma, B. Viana, A. J. Bos, P. Dorenbos, M. Bessodes, D. Gourier, D. Scherman, C. Richard, *Nat. Mater.* **2014**, 13, 418-426.

[197] Z. Li, Y. Zhang, X. Wu, L. Huang, D. Li, W. Fan, G. Han, *J. Am. Chem. Soc.* **2015**, 137, 5304-5307.

[198] J. Shi, X. Sun, J. Zhu, J. Li, H. Zhang, *Nanoscale* **2016**, 8, 9798-9804.

[199] J. Wang, Q. Ma, X. X. Hu, H. Liu, W. Zheng, X. Chen, Q. Yuan, W. Tan, *ACS Nano* **2017**, 11, 8010-8017.

[200] X. H. Lin, L. Song, S. Chen, X. F. Chen, J. J. Wei, J. Li, G. Huang, H. H. Yang, *ACS Appl. Mater. Interfaces* **2017**, 9, 41181-41187.

[201] Z. Zhou, W. Zheng, J. Kong, Y. Liu, P. Huang, S. Zhou, Z. Chen, J. Shi, X. Chen, *Nanoscale* **2017**, 9, 6846-6853.

[202] J. Wang, J. Li, Y. Yu, H. Zhang, B. Zhang, *ACS Nano* **2018**, 12, 4246-4258.

[203] J. M. Liu, D. D. Zhang, G. Z. Fang, S. Wang, *Biomaterials* **2018**, 165, 39-47.

[204] Y. Lv, D. Ding, Y. Zhuang, Y. Feng, J. Shi, H. Zhang, T. L. Zhou, H. Chen, R. J. Xie, *ACS Appl. Mater. Interfaces* **2019**, 11, 1907-1916.

[205] J. Botterman, K. V. d. Eeckhout, I. D. Baere, D. Poelman, P. F. Smet, *Acta Mater.* **2012**, 60, 5494-5500.

[206] M. Pope, H. P. Kallmann, P. Magnante, *J. Chem. Phys.* **1963**, 38, 2042-2043.

[207] C. Adachi, M. A. Baldo, M. E. Thompson, S. R. Forrest, *J. Appl. Phys.* **2001**, 90, 5048-5051.

[208] M. A. Baldo, S. Lamansky, P. E. Burrows, M. E. Thompson, S. R. Forrest, *Appl. Phys. Lett.* **1999**, 75, 4-6.

[209] M. A. Baldo, D. F. O'Brien, Y. You, A. Shoustikov, S. Sibley, M. E. Thompson,

[196] T. Maldiney, A. Bessiere, J. Seguin, E. Teston, S. K. Sharma, B. Viana, A. J. Bos, P. Dorenbos, M. Bessodes, D. Gourier, D. Scherman, C. Richard, *Nat. Mater.* **2014**, 13, 418-426.

[197] Z. Li, Y. Zhang, X. Wu, L. Huang, D. Li, W. Fan, G. Han, *J. Am. Chem. Soc.* **2015**, 137, 5304-5307.

[198] J. Shi, X. Sun, J. Zhu, J. Li, H. Zhang, *Nanoscale* **2016**, 8, 9798-9804.

[199] J. Wang, Q. Ma, X. X. Hu, H. Liu, W. Zheng, X. Chen, Q. Yuan, W. Tan, *ACS Nano* **2017**, 11, 8010-8017.

[200] X. H. Lin, L. Song, S. Chen, X. F. Chen, J. J. Wei, J. Li, G. Huang, H. H. Yang, *ACS Appl. Mater. Interfaces* **2017**, 9, 41181-41187.

[201] Z. Zhou, W. Zheng, J. Kong, Y. Liu, P. Huang, S. Zhou, Z. Chen, J. Shi, X. Chen, *Nanoscale* **2017**, 9, 6846-6853.

[202] J. Wang, J. Li, Y. Yu, H. Zhang, B. Zhang, *ACS Nano* **2018**, 12, 4246-4258.

[203] J. M. Liu, D. D. Zhang, G. Z. Fang, S. Wang, *Biomaterials* **2018**, 165, 39-47.

[204] Y. Lv, D. Ding, Y. Zhuang, Y. Feng, J. Shi, H. Zhang, T. L. Zhou, H. Chen, R. J. Xie, *ACS Appl. Mater. Interfaces* **2019**, 11, 1907-1916.

[205] J. Botterman, K. V. d. Eeckhout, I. D. Baere, D. Poelman, P. F. Smet, *Acta Mater.* **2012**, 60, 5494-5500.

[206] M. Pope, H. P. Kallmann, P. Magnante, *J. Chem. Phys.* **1963**, 38, 2042-2043.

[207] C. Adachi, M. A. Baldo, M. E. Thompson, S. R. Forrest, *J. Appl. Phys.* **2001**, 90, 5048-5051.

[208] M. A. Baldo, S. Lamansky, P. E. Burrows, M. E. Thompson, S. R. Forrest, *Appl. Phys. Lett.* **1999**, 75, 4-6.

[209] M. A. Baldo, D. F. O'Brien, Y. You, A. Shoustikov, S. Sibley, M. E. Thompson,

S. R. Forrest, *Nature* **1998**, 395, 151-154.

[210] K. Asami, J. Ueda, S. Tanabe, *J. Sci. Technol. Lighting* **2018**, 41, 89-92.

[211] Q. le Masne de Chermont, C. Chaneac, J. Seguin, F. Pelle, S. Maitrejean, J. P. Jolivet, D. Gourier, M. Bessodes, D. Scherman, *Proc. Natl. Acad. Sci.* **2007**, 104, 9266-9271.

[212] N. Zhang, R. Zhang, X. Xu, F. Wang, Z. Sun, S. Wang, S. Wu, *Adv. Opt. Mater.* **2023**, 11, 202300187.

[213] Y.-L. Wang, C. Li, H.-Q. Qu, C. Fan, P.-J. Zhao, R. Tian, M.-Q. Zhu, *J. Am. Chem. Soc.* **2020**, 142, 7497-7505.

[214] X. Yang, G. I. N. Waterhouse, S. Lu, J. Yu, *Chem. Soc. Rev.* **2023**, 52, 8005-8058.

[215] K. Jiang, Y. Wang, Z. Li, H. Lin, *Mater. Chem. Front.* **2020**, 4, 386-399.

[216] H. Liu, G. Pan, Z. Yang, Y. Wen, X. Zhang, S. T. Zhang, W. Li, B. Yang, *Adv. Opt. Mater.* **2022**, 10, 202102814.

[217] W. A. M. McMinn, T. R. A. Magee, *Food Bioprod. Process.* **1997**, 75, 223-231.

[218] R. K. Singh, D. B. Lund, F. H. Buelow, *J. Food Sci.* **2006**, 48, 939-944.

Chapter 2

Theoretical Background

2.1 Theory of Persistent Luminescence in Organic Materials

Persistent luminescence (PersL) in inorganic materials arises from the recombination of electrons and holes stored in luminescent centers and traps, respectively, as will be detailed in **Section 2.2**. However, for traditional organic afterglow materials, the charge carrier trapping-detrapping mechanism does not apply. Organic excitons, whether in singlet or triplet states, exhibit high binding energies (several hundred meV) as their Frenkel exciton nature, making it not easy to separate bound excitons into free electrons and holes at room temperature (RT), unlike Wannier-Mott excitons with binding energies around 0.01 eV in inorganic phosphors.[1] Consequently, the PersL in traditional organic afterglow materials primarily results from the slow radiative transition of long-lasting triplet excitons. The excited excitons in organics are typically highly unstable, featuring efficient intersystem crossing (ISC) and reverse intersystem crossing (RISC). In **Sections 2.1.1-2.1.2**, the phosphorescence and delayed fluorescence arise from spin-forbidden transitions from the triplet state to the singlet state, and the lifetimes usually occur over hundreds of microseconds.[2-4] Importantly, charge separation and recombination strategies have been developed to realize hours-level long PersL (LPL) from an organic host-guest system (**Section 2.1.3**).[5-8] In 2024, we provided the first evidence of trap states in low-doped host-guest organic systems, breaking the theoretical boundary between organic and inorganic materials (**Section 2.1.4**).[9] Additionally, a general method has been reported to convert traditional fluorescent chemicals into long-lived afterglow nanoparticles. This method relies on a chemical cascade photoreaction in the nanoparticles to store light energy (**Section 2.1.5**).[10]

73

Before formally introducing types of organic PersL, the basic concepts of photophysical processes in organic luminescent materials, as all types of organic afterglow involve these photoelectronic processes. Organic molecules typically consist of multiple atoms, each with numerous atomic orbitals exhibiting high levels of degeneracy and abundant electrons, making quantum mechanical calculations highly challenging. To simplify practical analysis, molecular orbital theory was introduced.[11] Molecular orbitals are formed by the combination of atomic orbitals from several atoms. The theory can be summarized as follows: (1) The movement of an electron in the molecule is illustrated by the wave function Ψ. The nuclei create a potential field, and each electron in the molecule also generates its own potential field, resulting in a combined average potential field that influences electron movement. (2) Molecular orbitals are linear combinations of atomic orbitals, with a fixed number of valence bond orbitals. The energy levels of these orbitals differ, creating bonding and anti-bonding orbitals. (3) The electron arrangement within molecular orbitals adheres to the principles of the minimum energy principle, Pauli exclusion principle, and Hund's rule. (4) To form molecular orbitals, atomic orbitals with similar energy levels, optimal overlap, and compatible symmetry are required. According to Pauli's principle and Hund's rule, each molecular orbital can accommodate only two electrons with opposite spins. When two or more molecular orbitals have the same energy, electrons will occupy separate orbitals with parallel spins. The process of filling bonding orbitals generates the highest occupied molecular orbital (HOMO) and the lowest unoccupied molecular orbital (LUMO), commonly referred to as frontier molecular orbitals (FMO).

In ground state, electrons follow the above principles of electron configuration, resulting in the molecule having the lowest energy. According to Pauli's principle, any pair of electrons in the same orbital must be spin-paired, meaning that all ground-state configurations exist in a singlet state (S_0). When a molecule is excited, electrons transition from a ground state to a higher energy excited state. If the two electrons in the excited state retain opposite spins, the molecule remains in a singlet state, denoted

S_n (n≥1). If an electron undergoes spin-flip, resulting in two electrons with the same spin direction, the molecule's spin multiplicity becomes M=2s+1=2×1+1=3 (s=1), putting it in a triplet state, represented as T_n (n≥1).[2] The excited state is unstable and high in energy, returning to the ground state by releasing energy through radiative or non-radiative transitions. The actual transition process is complex, so researchers apply certain assumptions to simplify analysis. When the transition to the S_0 state involves luminescence, it generally follows the Franck-Condon principle.[12] The radiative transitions typically occur between the lowest vibrational level of the S_0 state and a high vibrational level of the S_n/T_n state. When a molecule undergoes a significant structural change, vibrational relaxation can lead to substantial energy loss and be accompanied by a large Stokes shift. Molecules with a large Stokes shift are predicted to have a lower photoluminescence quantum yield. Luminescent molecules with high quantum yield generally possess rigid structures, limiting molecular deformation even upon excitation. Consequently, they lose less energy due to molecular distortion post-excitation. Such molecules have closely aligned vibrational levels in both ground and excited states, often producing absorption and emission spectra that are nearly mirror images of each other.

When an organic molecule is excited by external light and subsequently returns to its S_0 state by emitting a photon, the radiative transition is known as photoluminescence. Jablonski energy diagram provides a detailed depiction of radiative transitions within the excited states (Figure 2.1).[13] During the decay process in the excited state, not only do radiative transitions occur, but non-radiative transitions facilitated through vibrational relaxation (VR) could also be significant. The generation and decay of excited states represent two distinct dynamic processes, each with unique formation times and lifetimes. Under normal environmental conditions, a molecule typically resides in its ground state with minimal vibrational energy. Upon absorbing a photon with sufficient energy, the molecule transitions to a higher vibrational level within the excited state, a process that takes approximately 10^{-15} s.[14] Over the next 10^{-14}-10^{-11} s,

the molecule undergoes vibrational relaxation, decaying to a lower vibrational level and subsequently returning to the lowest singlet state S_1 *via* internal conversion (IC), releasing energy as heat to the surroundings. Internal conversion, which transfers energy between states with the same spin multiplicity, occurs only between S_n/T_n states. To emit fluorescence, the $S_1 \rightarrow S_0$ transition must occur *via* radiative decay. However, this process can also proceed through internal conversion back to S_0, dissipating energy as heat into the environment. Additionally, for phosphorescence emission, the molecule requires a significant spin-orbit coupling (SOC) coefficient, enabling it to transition to the first excited triplet state T_1 *via* ISC process. When the molecule is in a rigid, low-temperature environment that restricts vibrational and rotational motion, T_1 can return to the S_0 through radiative decay, emitting phosphorescence ($T_1 \rightarrow S_0$);[3, 4] or return to S_1 via RISC process to give delayed fluorescence ($T_1 \rightarrow S_1 \rightarrow S_0$).[15, 16] However, the strict conditions for triplet-state emissions make it challenging to achieve, so molecules typically lose this energy through non-radiative transitions. An excited-state excitons can return to the ground state through various pathways. Besides the transition processes mentioned above, energy can also be dissipated through interactions between excitons and the external environment, as well as through solvent-solute interactions. These processes include the formation of exciplexes and excimers,[17, 18] chemical reactions,[19, 20] Förster energy transfer,[21-23] Dexter energy transfer.[24]
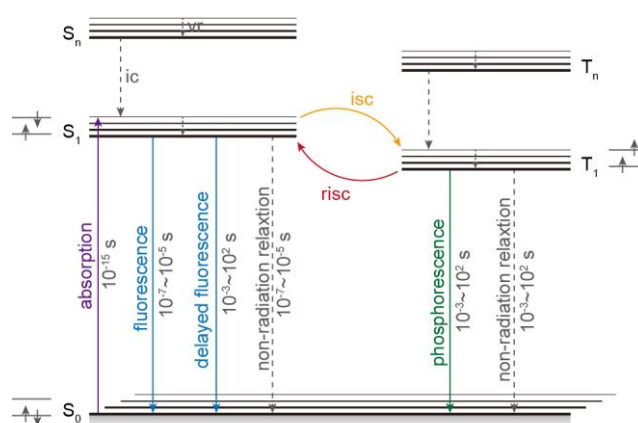
Figure 2.1 Jablonski energy level diagram. The diagram is prepared based on the proposed mechanism in Ref [1].

2.1.1 Phosphorescence

As shown in Figure 2.2, phosphorescent molecules under optical excitation involve two spin-flip processes: (1) The molecule in S_0 state is excited by a photon and the transition to the S_1 state occurs, with the T_1 state typically formed from S_1 through ISC; (2) Subsequently, T_1 relax to the lowest energy S_0 state *via* radiative or non-radiative transitions (also a RISC process). Since the $T_1 \rightarrow S_0$ transition is spin-forbidden, the transition rate from T_1 to S_0 are generally much slower than their S_1 to S_0 counterparts. Thus, the phosphorescence emission process competes with a series of excited state decay processes. The efficiency of phosphorescence can be expressed as:[25]

$$\phi_p = \phi_{isc} \frac{k_p}{k_p + k_{nr} + k_q} \quad \text{(Equation 2.1)}$$

where ϕ_p is the phosphorescent quantum yield, ϕ_{isc} represents the ISC efficiency from S_1 to T_1, k_p indicates the radiative transition rate of triplet excitons, k_{nr} refers to the non-radiative transition rate of triplet excitons, and k_q signifies the quenching rate of triplet excitons by the environment. From the Equation 2.1, to achieve efficient phosphorescence, it is necessary to enhance spin-orbit coupling (increasing ϕ_{isc} and k_p), while simultaneously reducing the non-radiative transitions and quenching rates of triplet excitons (decreasing k_{nr} and k_q).
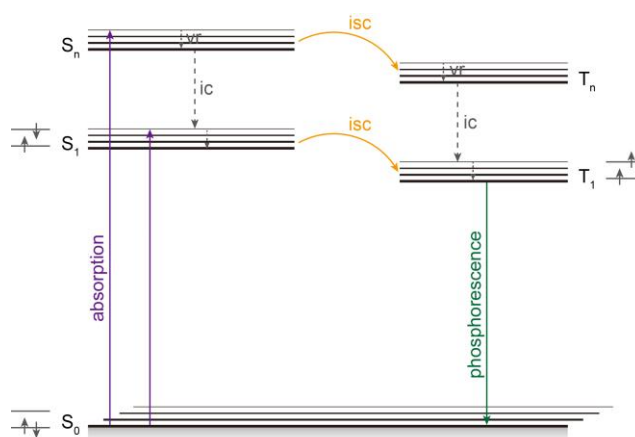

Figure 2.2 Energy level diagram of phosphorescence. The diagram is prepared based

on the proposed mechanism in Ref [1].

2.1.1.1 Increasing Spin-Orbit Coupling

On the one hand, it is necessary to enhance ISC. ϕ_{isc} can be expressed as:[26]

$$\phi_{isc} = \frac{k_{isc}}{k_f + k_{ic} + k_{isc}} \quad \text{(Equation 2.2)}$$

where k_{isc} denotes the rate constant for ISC from S_1 to T_1, k_f represents the rate constant for the radiative transition of singlet excitons, and k_{ic} refers to the rate constant for internal conversion from S_n to S_1. According to Equation 2.2, to achieve a higher ϕ_{isc}, the condition $k_{isc} > k_f$ must be satisfied. k_f can be expressed as:

$$k_f \approx \bar{v}_0^2 f = \bar{v}_0^2 \frac{8\pi m_e \bar{v}}{3he^2} \left\langle \varphi_0^{1(0)} \middle| r \middle| \varphi_1^{1(0)} \right\rangle^2 \quad \text{(Equation 2.3)}$$

where f denotes the oscillator strength for fluorescence emission, $\bar{v}$ represents the fluorescence energy, r represents the transition dipole length for fluorescence emission, m_e is the electron mass, h is Planck's constant, and $\varphi_0^{1(0)}$ and $\varphi_1^{1(0)}$ are the electronic wave functions at the zero vibrational levels of S_0 and S_1, respectively. The Equation 2.3 indicates that a smaller overlap between $\varphi_0^{1(0)}$ and $\varphi_1^{1(0)}$ results in a reduced value of k_f, which is beneficial for achieving a high ϕ_{isc}. And k_{isc} can be expressed as:

$$k_{isc} = \sum_n k_{isc}^n \quad \text{(Equation 2.4)}$$

$$k_{isc}^n = \frac{2\pi}{\hbar} \left\langle \varphi_1^{1(0)} \middle| H_{SO} \middle| \varphi_n^{3(0)} \right\rangle^2 \times FCWD = f_s \times FCWD \quad \text{(Equation 2.5)}$$

$$FCWD = \frac{1}{\sqrt{4\pi\lambda kT}} \sum_v \exp(-S) \frac{S^v}{v!} \exp\left[-\frac{\Delta G}{4\lambda kT}\right] \quad \text{(Equation 2.6)}$$

$$\Delta G = (\Delta E + \mu\hbar\omega + \lambda)^2 \quad \text{(Equation 2.7)}$$

Here, $\varphi_n^{3(0)}$ refers to the electronic wave function of the vibrational level 0 for T_n, H_{SO}

denotes the SOC operator between S_1 and T_n, *FCWD* represents the Franck-Condon weighted density for non-radiative transitions from S_1 to T_n, λ indicates the Marcus reorganization energy, ΔE signifies the energy difference when both S_1 and T_n are at vibrational level 0, $\hbar\omega$ refers to the energy of the non-classical vibrational modes involved in the transition, k is the Boltzmann constant, and S represents the relevant Huang-Rhys factor. From these equations (Equations 2.4-2.7), it is evident that as the energy of T_n approaches that of S_1, the value of k_{isc} increases. Additionally, based on El-Sayed's rules, when the transition from S_1 to T_n occurs between a charge transfer excited state (^1CT) and a localized excited state (^3LE), or between ^1LE and ^3CT, where S_1 and T_n have different transition types, the value of $\left\langle \varphi_1^{1(0)} \middle| H_{SO} \middle| \varphi_n^{3(0)} \right\rangle$ increases.[27] This enhancement facilitates a larger SOC coefficient between S_1 and T_n, thereby promoting the ISC process and leading to efficient phosphorescence.

On the other hand, it is necessary to improve RISC, which refers to the radiative transition efficiency of phosphorescence. k_p can be expressed as:[2]

$$k_p \approx \bar{v}_0^2 f = \bar{v}_0^2 \frac{8\pi m_e \bar{v}}{3he^2} \left| \overline{\mu_{T_1 \to S_0}} \right|^2 \quad \text{(Equation 2.8)}$$

$$\overline{\mu_{T_1 \to S_0}} = \sum_n \lambda_n \times \mu_{S_n \to S_0} + \sum_n \lambda_n' \times \mu_{T_n \to T_1} \quad \text{(Equation 2.9)}$$

$$\lambda_n = \frac{\left\langle \varphi_1^{3(0)} \middle| H_{SO} \middle| \varphi_n^{1(0)} \right\rangle}{^3E_1 - {}^1E_n} \quad \text{(Equation 2.10)}$$

$$\lambda_n' = \frac{\left\langle \varphi_n^{3(0)} \middle| H_{SO} \middle| \varphi_n^{1(0)} \right\rangle}{^3E_n - {}^1E_0} \quad \text{(Equation 2.11)}$$

Here, f denotes the oscillator strength for the transition from T_1 to S_0, $\mu_{T_1 \to S_0}$ represents the transition dipole moments for the phosphorescent transition from T_1 to S_0, $\mu_{S_n \to S_0}$ represents the transition dipole moments for the fluorescence transition from S_n to S_0. $^3E_1 - {}^1E_n$ and $^3E_n - {}^1E_0$ refer to the energy differences between S_n and T_1, as well as between T_n and S_0, respectively. From the above equations (Equations

[2.8-2.11](), when the energy difference between S_n and T_1 is minimal, $\left\langle \varphi_1^{3(0)} \middle| H_{SO} \middle| \varphi_n^{1(0)} \right\rangle$ increases, leading to an enhancement in k_p, which can be realized by introducing heavy atoms into the system. Furthermore, the introduction of heavy atoms can easily satisfy the condition $k_p > k_q$, as k_q is independent of $\left\langle \varphi_1^{3(0)} \middle| H_{SO} \middle| \varphi_n^{1(0)} \right\rangle$.[27] However, it is important to note that while the introduction of heavy atoms increases k_p, it also raises k_{nr}. Therefore, the incorporation of heavy atoms represents a trade-off between enhancing the phosphorescent radiative rate to achieve an increase in ϕ_p and the non-radiative transition rate, which may lead to luminescence quenching.

2.1.1.2 Decreasing Non-Radiative Transitions and Quenching

For decreasing non-radiative transitions, it is necessary to decrease k_{nr}, which can be defined as:[2]

$$k_{nr} = \sum_n k_{nr}^n = \frac{2\pi}{\hbar} \left\langle \varphi_1^{3(0)} \middle| H_{SO} \middle| \varphi_n^{1(v)} \right\rangle^2 \times FCWD' = F_s \times FCWD' \quad \text{(Equation 2.12)}$$

$$FCWD' = \sum_v F_V F_E \quad \text{(Equation 2.13)}$$

$$F_V = \exp\left(-S'\right) \frac{{S'}^v}{v!} \infty \exp\left(-\frac{\Delta E'}{\hbar \omega}\right) \quad \text{(Equation 2.14)}$$

$$F_E = \frac{1}{\sqrt{4\pi \lambda' kT}} \exp\left[-\frac{(\Delta E' + v\hbar\omega + \lambda')^2}{4\lambda' kT}\right] \quad \text{(Equation 2.15)}$$

Here, F_V and F_E represent the forbidden factors for the nuclei and electrons, respectively. λ' refers to the Marcus reorganization energy for the transition from T_1 to S_0, $\Delta E'$ denotes the energy difference between the zero-vibrational level of T_1 and that of S_0, $\hbar\omega$ signifies the energy associated with non-classical vibrational modes involved in the transition, and S' is the Huang-Rhys factor related to the T_1 to S_0 transition. According to the equations ([Equations 2.12-2.15]()), to achieve a high ϕ_p, it is generally necessary to reduce k_{nr} while maintaining k_p constant. This can be accomplished through deuteration of the molecules, which decreases $\hbar\omega$ and

consequently reduces F_V. Additionally, positioning the system at liquid nitrogen temperatures or within a rigid matrix can significantly diminish k_{nr}, enhancing the overall efficiency of the phosphorescent process.[3]

Besides, to effectively reduce the quenching of triplet excitons, it is essential to understand the quenching pathways, which include energy transfer quenching, thermal motion quenching, oxygen quenching, and aggregation-induced quenching. (1) Energy transfer quenching occurs when the energy of the triplet state of the guest material is higher than that of the corresponding host material.[28] To minimize this energy transfer quenching, it is advisable to utilize hosts with higher triplet state energies. (2) Thermal motion quenching is primarily due to the enhanced diffusion of oxygen, water, and impurities within the system as the temperature rises.[29] Therefore, placing the phosphorescent material in a rigid environment with minimal molecular interactions can significantly reduce thermal quenching effects on the triplet state. (3) According to molecular orbital theory, molecular oxygen contains two parallel spins in its two unpaired electrons, making ground-state oxygen a triplet state ($^3O_2$).[30] To mitigate the impact of oxygen quenching, environments devoid of moisture and oxygen are typically employed, or crystalline and rigid matrices are used to limit oxygen permeability. While water itself does not intrinsically quench triplet excitons, the high oxygen content in water can lead to significant quenching. (4) Increased concentration of phosphorescent molecules often exacerbates quenching effects.[31] Higher concentrations can lead to the formation of lower-energy dark triplet states (T_1^*), which readily capture triplet excitons and result in their deactivation. A common strategy to counteract this effect involves embedding phosphorescent molecules in rigid hosts to reduce their concentration and prevent aggregation, thus suppressing quenching phenomena.

2.1.2 Delayed Fluorescence

Compared to phosphorescence, delayed fluorescence (DF) involves RISC process from the T_n to S_n, followed by the radiative transition to the S_0 state ($T_n \rightarrow S_n \rightarrow S_0$, Figures 2.2-2.5). As a result, DF exhibits nearly the same emission color as fluorescence. However, because the RISC process from the triplet to the singlet state is also spin-forbidden, it results in a longer excited-state lifetime compared to fluorescence. Notably, because the excitation and ISC processes for DF are similar to those in phosphorescence, achieving efficient DF requires conditions that favor efficient phosphorescence, such as enhancing spin-orbit coupling and preventing non-radiative decay and quenching of the triplet excitons (refer to **Section 2.1.1**). These statements will not be repeated here.

Additionally, the RISC process is crucial for DF ($T_n \rightarrow S_n \rightarrow \ldots \rightarrow S_1 \rightarrow S_0$, n≥1), and it competes with the formation of phosphorescence ($T_1 \rightarrow S_0$). When considering all decay processes, including fluorescence, DF, phosphorescence, and non-radiative transitions, the decay rates of the S_1 and T_1 states can be expressed as follows:

$$\frac{d[S_1]}{d[t]} = -(k_r^S + k_{nr}^S + k_{isc})[S_1] + k_{risc}[T_1] \quad \text{(Equation 2.16)}$$

$$\frac{d[T_1]}{d[t]} = -(k_r^T + k_{nr}^T + k_{risc})[T_1] + k_{isc}[S_1] \quad \text{(Equation 2.17)}$$

where k_r^S and k_r^T represent the radiative transition rate of the S_1 and T_1 states, respectively. k_{nr}^S and k_{nr}^T denote the non-radiative transition rates of the S1 and T_1 states, respectively. k_{isc} and k_{risc} are the transition rates of ISC and RISC processes, respectively. Notably, the emission from the S_1 state encompasses both fluorescence and DF, which can be expressed as follows:

$$[S_1] = C_1 \exp(k_f t) + C_2 \exp(k_{df} t) \quad \text{(Equation 2.18)}$$

where k_f and k_{df} are the transition rate of fluorescence and DF, respectively. Assuming that the radiative and non-radiative transitions of T_1 can be neglected, and that k_r^S, k_{nr}^S, and k_{isc} are much larger than k_{risc}, the rate constants for k_f and k_{df}

can be simplified as follows:

$$k_f = k_r^S + k_{nr}^S + k_{isc} \quad \text{(Equation 2.19)}$$

$$k_{df} = (1 - \frac{k_{isc}}{k_r^S + k_{nr}^S + k_{isc}})k_{risc} \quad \text{(Equation 2.20)}$$

Correspondingly, ϕ_f and ϕ_{df} can be expressed as:

$$\phi_f = \frac{k_r^S}{k_r^S + k_{nr}^S + k_{isc}} = \frac{k_r^S}{k_f} \quad \text{(Equation 2.21)}$$

$$\phi_{df} = \frac{\phi_{isc}\phi_{risc}}{1 - \phi_{isc}\phi_{risc}}\phi_f \quad \text{(Equation 2.22)}$$

Where ϕ_{isc} and ϕ_{risc} (assuming equal to 1) represent the efficiencies of ISC and RISC, respectively. ϕ_{isc} can be expressed as followed:

$$\phi_{isc} = \frac{k_{isc}}{k_r^S + k_{nr}^S + k_{isc}} = \frac{k_{isc}}{k_f} \quad \text{(Equation 2.23)}$$

The values of ϕ_f, ϕ_{df}, the instantaneous lifetime of the TADF process (τ_f), and the delayed lifetime (τ_{df}) can be experimentally determined.

$$k_f = \frac{\phi_f}{\tau_f} \quad \text{(Equation 2.24)}$$

$$k_{df} = \frac{\phi_{df}}{\tau_{df}} \quad \text{(Equation 2.25)}$$

Consequently, k_{isc} can be measured and obtained:

$$k_{isc} = \frac{\phi_{df}}{\phi_f + \phi_{df}}k_f \quad \text{(Equation 2.26)}$$

Moreover, based on Equations 2.20 and 2.23, k_{risc} can be measured and expressed as:

$$k_{risc} = \frac{k_{df}\phi_{risc}}{1 - \phi_{isc}\phi_{risc}} = \frac{k_{df}}{k_{isc}}\frac{\phi_{df}}{\phi_f} \quad \text{(Equation 2.27)}$$

At this point, we can obtain k_{risc} through experimental testing, which can be used to analyze and design efficient DF materials.

2.1.2.1 Thermally Activated Delayed Fluorescence

Thermally activated delayed fluorescence (TADF) involves a single T_1 exciton undergoing RISC *via* heating to form a S_1 exciton (Figure 2.3).[15] In 1961, this phenomenon was first observed in tetrabromofluorescein (Eosin), also referred to as E-type delayed fluorescence.[32] According to the following Boltzmann distribution:[33]

$$k_{risc} \propto \exp\left(\frac{\Delta E_{ST}}{k_B T}\right) \quad \text{(Equation 2.28)}$$

where k_{risc} is the rate constant of RISC, k_B is Boltzmann's constant and T is the temperature. From Equations 2.28, it can be observed that the magnitude of k_{risc} is related to ΔE_{ST}; the smaller ΔE_{ST}, the larger k_{risc}. According to quantum chemistry, the energies of S_1 and T_1 can be divided into three components: orbital energy (E), electron repulsion energy (K), and exchange energy (J). Since the electrons that compose S_1 and T_1 are from the same pair, these three energy terms are identical for both S_1 and T_1. The energies of S_1 and T_1 can be expressed as:

$$E_S = E + K + J \quad \text{(Equation 2.29)}$$

$$E_T = E + K - J \quad \text{(Equation 2.30)}$$

Since T_1 is composed of two electrons with the same spin, its energy is lower than that of S_1. The energy difference ΔE_{ST} between the singlet and triplet states can be expressed as:

$$\Delta E_{ST} = E_S - E_T = 2J \quad \text{(Equation 2.31)}$$

Since the two electrons composing either S_1 and T_1 are distributed in the HOMO and LUMO of the material, the exchange integral J can be expressed as:

$$J = \iint \phi_L(1)\phi_H(2)\left(\frac{e^2}{r_1 - r_2}\right)\phi_L(2)\phi_H(1)dr_1 dr_2 \quad \text{(Equation 2.32)}$$

The exchange integral J depends on the overlap between the HOMO (ϕ_L) and LUMO (ϕ_H) wavefunctions, with e representing the charge number. From Equation 2.32, it is evident that the exchange integral is proportional to the overlap between the HOMO

and LUMO orbitals. Therefore, to achieve a small ΔE_{ST} and efficient RISC process, it is crucial for the HOMO and LUMO orbitals of the organic material to be as spatially separated as possible. In the design of TADF molecules, it is common to incorporate electron-withdrawing and electron-donating groups at different functional sites within the same molecule. This strategy effectively creates a charge-transfer (CT) state by promoting electron density transfer between the electron-withdrawing and electron-donating groups. The resulting CT character enhances the energy separation between the S_1 and T_1 states.[34]
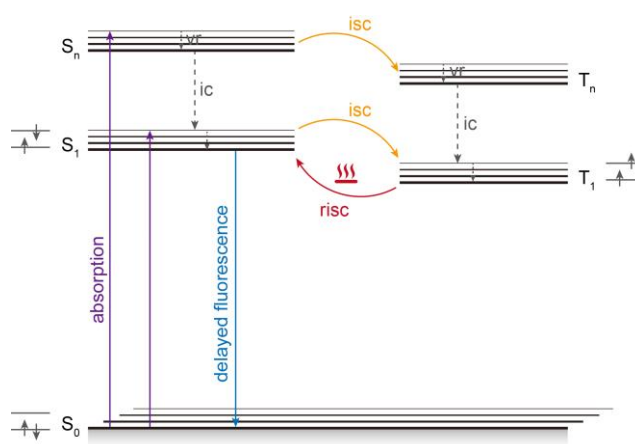

Figure 2.3 Energy level diagram of thermally activated delayed fluorescence. The diagram is prepared based on the proposed mechanism in Ref [15].

2.1.2.2 Triplet-Triplet Annihilation

Triplet-Triplet Annihilation-based photon upconversion (TTA-UC) is a bimolecular process in which two T_1 exciton collide, resulting in the annihilation of one S_1 exciton (Figure 2.4).[35] The energy transfer process begins with the excitation with a low-energy photon within the sensitizer, which rapidly populates its first T_1 state *via* ISC. The initial energy transfer step involves triplet energy transfer (TET) from the sensitizer's triplet excited state to a ground-state annihilator, leading the generation of

a triplet-excited annihilator. In the second energy transfer step, two triplet-excited annihilators undergo TTA. During TTA, the triplet energies are combined, leading to the formation of a singlet-excited annihilator. The singlet-excited annihilator then returns to the ground state, emitting a photon in the process (DF). Overall, this sequence converts two low-energy photons into one higher-energy photon. TTA-UC leverages prolonged triplet states to temporarily store photon energy. However, because O_2 efficiently quenches T_n states in atmosphere, it is essential to thoroughly degas TTA-UC systems to ensure optimal performance.
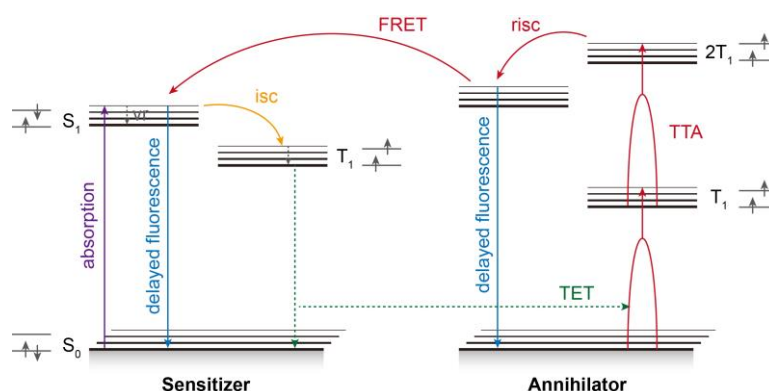

Figure 2.4 Energy level diagram of triplet-triplet annihilation. The diagram is prepared based on the proposed mechanism in Ref [35].

In a TTA-UC system, the sensitizer is important to absorb photons and transfer the light energy to the T_n state of an annihilator. Ideal sensitizers meet the following criteria:[36] (1) The sensitizer should exhibit strong absorption over a broad wavelength range, ensuring efficient photon absorption and lowering the threshold intensity. (2) The sensitizer should exhibit an efficient ISC process, ideally resulting in near-quantitative triplet yield. (3) The triplet excited states of the sensitizer should have long lifetimes. (4) A small singlet-triplet splitting minimizes energy losses, facilitating efficient energy transfer. (5) The emission spectrum of the sensitizer should have

minimal overlap with the emission spectrum of the annihilator to prevent the reabsorption of the upconverted emission. In addition to these considerations for the sensitizer, there are key aspects to consider when choosing an annihilator:[36] (1) The annihilator's triplet energy needs to be lower than that of the sensitizer to confirm efficient triplet-to-triplet energy transfer. (2) The energy of the annihilator's first excited triplet state should be larger than half of its first excited singlet state energy. (3) The annihilator should possess a high emission quantum yield to maximize photon emission during the down-conversion process.

2.1.2.3 Hybridized Local and Charge-Transfer

The formation of a CT state includes the electron transfer from a segment of the molecule with stronger electron-donating ability (donor) to a segment with stronger electron-accepting ability (acceptor), ultimately resulting in a CT excited state composed of two moieties bearing partial positive and negative charges. This type of excited state has a larger dipole moment, making its energy more sensitive to the surrounding polar environment. Because of the partial charge carrier character of the CT state, it is a state with relatively weak exciton binding energy, positioned between the Wannier-Mott excitons (weak bounding) and the Frenkel excitons (strong bounding).

The key design principle for TADF materials focuses on constructing strong CT emitting states (**Section 2.1.2.1**). However, the electron-donating and electron-accepting moieties in the CT state are relatively independent, leading to a small overlap integral and consequently low vibrational intensity when the molecule is under excitation, which negatively impacts the quantum yield.[37] The strategy of designing hybrid locally-emissive and charge-transfer (HLCT) states involves incorporating locally emissive (LE) components into the CT emitting state to address the issue of low quantum yield in CT states.[38] This approach is characterized by two main requirements (Figure 2.5): (1) The high-energy excited state must exhibit significant CT

characteristics, ensuring a sufficiently small energy gap between S_{CT} and T_{CT}, which allows for an effective RISC process. (2) There needs to be a sufficiently large energy gap between T_{LE} and T_{CT} to suppress the competing internal conversion process from T_{CT} to S_{CT}.
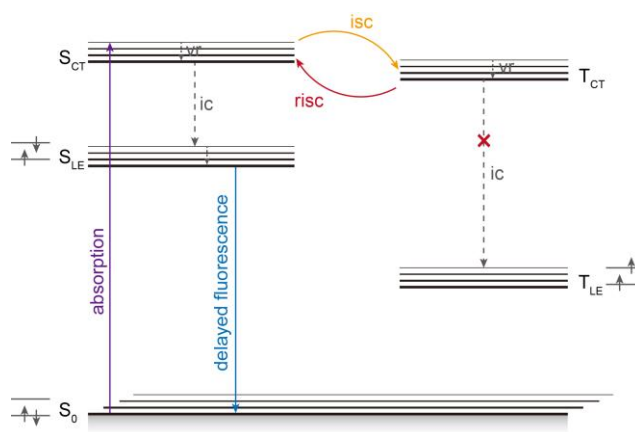

Figure 2.5 Energy level diagram of hybridized local and charge-transfer. The diagram is prepared based on the proposed mechanism in Ref [38].

In 2012, Prof. Ma first constructed a deep blue light-emitting material using triphenylamine and phenylimidazole as functional groups (TPA-PPI).[39] TPA served as a highly effective electron donor, where the lone pair of electrons on the nitrogen atom's p_z orbital engages in strong p-π conjugation with the π electron clouds of the three benzene rings. This interaction stabilized the nitrogen's hybridization state to a planar sp^2 configuration, resulting in a stable propeller-like structure. And the bonding configurations of the two nitrogen atoms in the PPI moiety differed significantly: one was connected entirely by single bonds, with its p_z orbital occupied by a lone pair of electrons, exhibiting electron-donating properties; while the other featured a double bond, with an empty p_z orbital that acted as an electron acceptor. Consequently, the PPI moiety displayed 'bipolarity', making it suitable for both donor and acceptor roles. The direct connection between the TPA and PPI groups facilitated CT interactions.

Importantly, the HOMO levels of TPA and PPI are quite close, allowing for effective π conjugation and the formation of favorable localized states. The localized state components ensure a relatively high vibrational intensity in the excited state, while the CT state components enhance the utilization of electrically generated triplet states.

2.1.3 Long Persistent Luminescence

2.1.3.1 Electron Transporting Model

PersL from organic molecules is usually referred to as phosphorescence or delayed fluorescence (**Sections 2.1.1-2.1.2**); however, in most cases, this lasts for less than a second, and in the best scenarios, only for a few minutes, which makes it less competitive compared to inorganic PersL phosphors. This limitation arises from the instability of triplet-state electrons, which are easily quenched by the environment, leading to non-radiative transitions. Clearly, utilizing the spin-forbidden transition mechanism imposes a theoretical limit on achieving ultralong afterglow lifetimes. When light is used to generate ionized states (photo-induced ionized states) and charge-separated states (photo-induced charge-separated states), exceptionally long lifetimes can be achieved.[40] However, this typically requires a strategy involving high-intensity two-photon absorption. Inspired by organic photovoltaics, blend films of electron donors and electron acceptors provide a means to form charge-separated states even under weak photo-irradiation.[41] In 2017, Prof. Adachi and Prof. Kabe employed a melt-casting method to prepare host-guest exciplexes, accelerating charge separation under weak excitation sources, thereby achieving PersL on the order of hours at RT for the first time.[5] This work marks a new chapter in the field of ultra-long organic PersL , leading to a surge of research efforts that continuously break records for decay durations.[7, 8, 42-46] See **Chapter 1-Section 1.1.1.2.2** for details.

The electron transporting model is illustrated in Figure 2.6. During the photoexcitation process, electrons transfer from the HOMO of the donor to the HOMO of the acceptor, forming a charge-transfer state (process 1-2). Subsequently, the radical anion of the acceptor diffuses to separate the cation of the donor group and the anion of the acceptor group, generating a charge-separated state (process 3). The slow recombination of the radical anion and cation (process 4) results in the emission of an exciplex, with a transition from the LUMO of the acceptor to the HOMO of the donor

(process 5). The charge recombination produces an exciplex in a 25% singlet-state and 75% triplet-state excitions. The small energy gap between the S_1 and T_1 states of the exciplex promotes RISC through thermal activation.
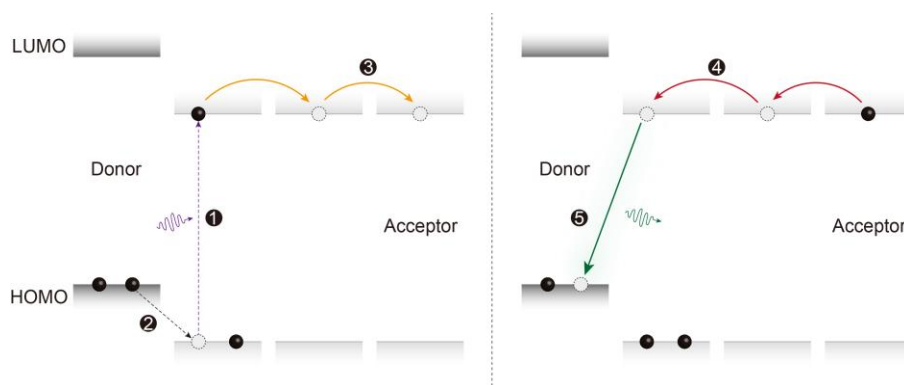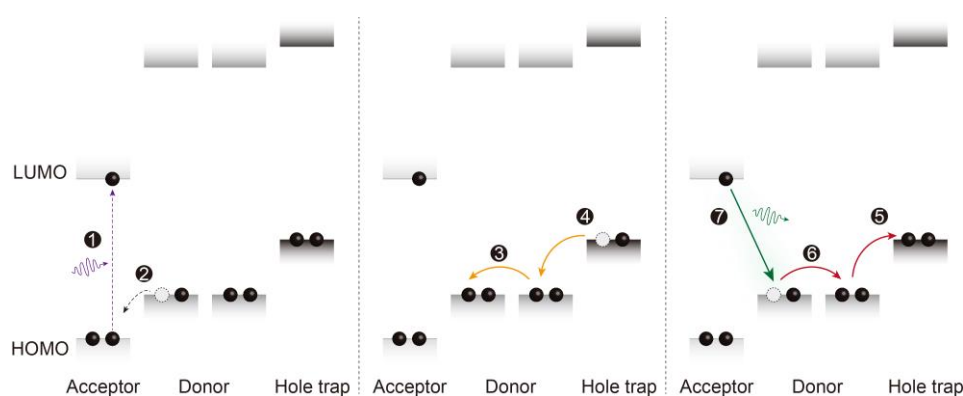

Figure 2.6 Energy level diagram of LPL's electron transporting model. Abbreviations and labels: excitation (purple line), emission (green line), electrons (black balls), holes (white balls), arrows direction (electron movement), and the terms 'donor' and 'acceptor' are used in relation to electrons. The diagram is prepared based on the proposed mechanism in Ref [5].

2.1.3.2 Hole Transporting Model

Water and oxygen stability has always been a significant challenge for organic persistent luminescence materials. This issue persists in LPL systems for two main reasons: (1) The recombination of charge carriers involves radiative transitions from triplet to singlet states ($T_1 \rightarrow S_0$) or RISC ($T_1 \rightarrow S_1$), but the triplet state electrons are less environmentally tolerant; (2) The radical anions formed during electron transport (n-type organic semiconductors) are unstable in air and easily quenched. In fact, the PersL composite crystals developed by Prof. Tang and Prof. Li's research groups effectively address the issue of poor water and oxygen tolerance.[7, 43, 47] However, the crystalline structure significantly challenges the application of these materials in areas such as

bioimaging and optoelectronic devices. The p-type OLPL system, in which the diffusion of radical cations occurs, is expected to exhibit greater stability against oxygen. By adjusting the LUMO energy level to be deeper than the reduction potential of oxygen (-3.5 eV), oxygen-stable organic transistors were achieved. Based on this, Prof. Adachi's research group introduced cationic electron acceptors (organic photoredox catalysts) into the LPL system and constructed energy level traps to capture separated holes, achieving air-stable near-infrared (NIR) PersL excitable in the range of UV-to-visible-light.[6]

The hole transporting model is illustrated in Figure 2.7, and the process can be divided into seven main steps. Under low-power excitation, charge transfer and separation between the donor and acceptor can occur (Processes 1-2). The generated radical cations (holes) then diffuse among the electron donor molecules at high concentration (Process 3) and form a long-lived charge-trapped state (Process 4). During this process, oxygen with a reduction potential is less likely to quench the diffused holes through photoreaction. Furthermore, thermal detrapping from the trap state regenerates donor radical cations, which then recombine with acceptor radical anions to give PersL (Processes 5-7).

Figure 2.7 Energy level diagram of LPL's hole transporting model. Abbreviations and labels: excitation (purple line), emission (green line), electrons (black circles), holes (white circles), arrows indicating the direction of electron movement (with the

directions of hole and electron movement being opposite), and the terms 'donor' and 'acceptor' as used in relation to electrons. The diagram is prepared based on the proposed mechanism in Ref [6].

2.1.4 Trap-Induced Persistent Luminescence

In inorganic PersL materials, lattice-based charge traps are demonstrated to play a significant role in luminescent performance, with the PersL properties effectively tunable through precise control of trap types.[48] For the hour-scale organic LPL mechanism proposed by Prof. Kabe and other scientific researchers, a fundamental question arises to me: if charge carriers are not captured by physical entities akin to 'trap states', their transport through the medium would occur rapidly, making it improbable for them to delay recombination and return to the 'luminescent centers' over several hours to sustain luminescence. Inspired by the trap-induced PersL mechanisms in inorganic systems, I first proved trap states in organic host-guest phosphors, achieving record-setting PersL emission intensities and storage durations at RT.[9] Currently, this work has been highlighted by journals of *Science Bulletin* and *Smart Molecules*.[49, 50] It is important to note, however, that trap-induced PersL (TIP) theory should be viewed as complementary rather than opposed to the aforementioned hour-scale PersL mechanism (**Section 2.1.3**). Moving forward, I will provide a more in-depth introduction to this mechanism and its performance characteristics.

The charge carrier migration model is illustrated in Figure 2.8, and the process can be divided into four main steps. First, an electron from the HOMO of a guest molecule is excited to the LUMO of the host molecule (Process 1, excitation). This excited electron then separates among the LUMOs of the host molecules. Next, the separated electron may pair with another distant guest molecule, forming a metastable radical anion, or 'trap state' (Process 2, trapping). To escape from this trap, the electron requires sufficient energy to leave the radical anion and transition back to another host molecule (Process 3, detrapping). This escape energy, determined by the trap depth ε, can be measured *via* thermoluminescence (TL). Finally, the escaped electron recombines with the remaining hole at the luminescent center, generating persistent luminescence (PersL) (Process 4, emission).
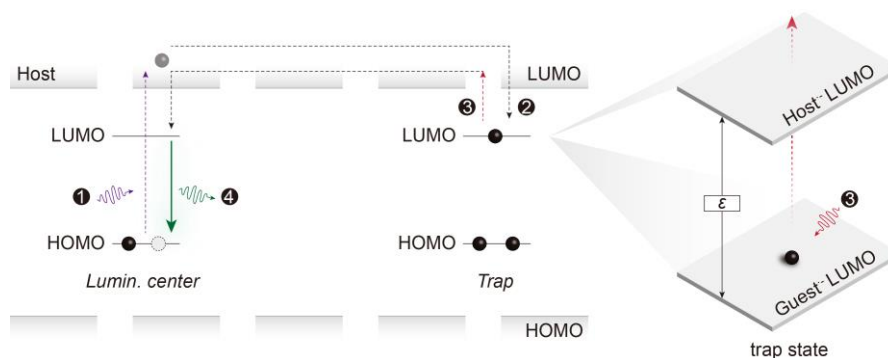
Figure 2.8 Energy level diagram of trap-induced persistent luminescence. Abbreviations and labels: trap depth (ε), excitation (purple line), emission (green line), electrons (black balls), holes (white balls), the LUMO level of host radical anion (Host$^{\bullet-}$), the LUMO level of guest radical anion (Guest$^{\bullet-}$), and the arrows indicate the direction of electron movement. The diagram is prepared based on the proposed mechanism in Ref [9].

Notably, the charge separation process could be achieved either through two-photon ionization by the guest molecules (UV-to-visible light) or direct excitation of the host (UV light). As illustrated in Figure 2.9a, the guest molecule exhibits two-photon absorption under visible light excitation, leading to electron delocalization from the luminescent center.[45] The separated electrons are then transferred through host molecules. We speculate that similar effects occur under UV excitation (type-1, Figure 2.9b). Additionally, we believe that there is a simultaneous direct transition of electrons from HOMO to LUMO of TPBi host, followed by charge separation (type-2, Figure 2.9b). It's noteworthy that the holes on the HOMO of host would transfer to lower energy levels (the HOMO of guest). Hence, the luminescent center remains the guest molecule, implying equivalence between type-1 and type-2 for PersL emission. In the theoretical model depicted in Figure 2.8, we have simplified the charge separation process.
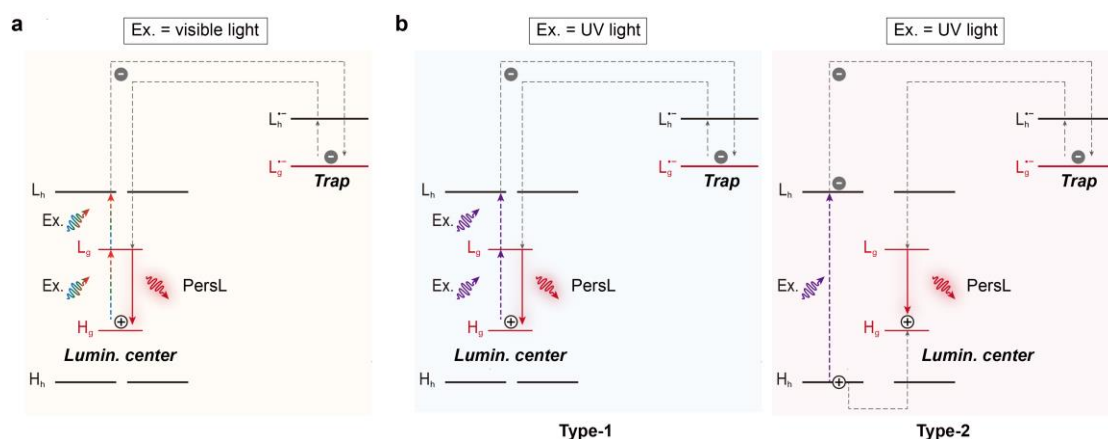
Figure 2.9 Schematic illustrations of the possible PersL mechanism through electron transitions in the hosts and in the guests under visible light (a) and UV light (b) excitation. Abbreviations and labels: LUMO of host (L_h), HOMO of host (H_h), LUMO of guest (L_g), HOMO of guest (H_g), LUMO of the host racial anion ($L_h^{\bullet-}$), LUMO of the guest racial anion ($L_g^{\bullet-}$), electron (grey ball), hole (white ball), colorful fold and dashed lines (visible light excitation), purple fold and dashed lines (UV light excitation), and red fold and solid lines (PersL emission).

2.1.5 Chemiluminescent Afterglow

Molecular endoperoxide (MEPO) with heterocyclic peroxides (-O-O-) has demonstrated significant potential for disease diagnosis and treatment.[20, 51] As shown in Figure 2.10, it is predominantly formed through the [4 + 2] or [2 + 2] cycloaddition reactions of singlet oxygen ($^1O_2$) with aromatic or vinylene substrates, respectively (Processes 1-3). MEPOs with 1,2-dioxetanes can thermally decompose into excited carbonyl products. This decomposition may follow a synergistic cyclic mechanism or/and a diradical mechanism. In the concerted mechanism, C-C and O-O bonds are cleaved simultaneously, while in the diradical mechanism, O-O bond cleavage occurs first, generating a diradical intermediate that rapidly undergoes C-C bond cleavage.[52] These decomposition pathways yield primarily carbonyl products along with luminescence emissions (chemiluminescence, Process 4), making them suitable for bioimaging applications. Process 5 involves considering whether to add other organic fluorophores based on the wavelength of the chemiluminescence and its compatibility with the requirements. Although chemiluminescence occurs post-excitation and resembles traditional afterglow phenomena, the two processes are fundamentally different. For examples of the bioimaging applications of this process, please refer to **Chapter 1-Section 1.1.1.4**.
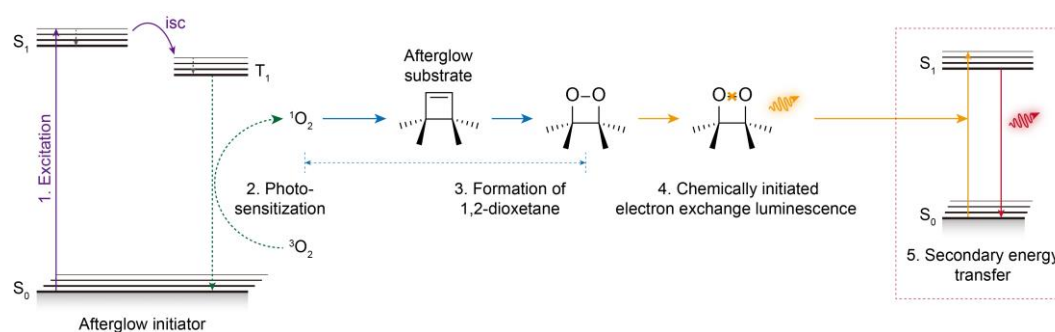
Figure 2.10 Schematic diagram of photoreaction processes resulting in chemiluminescent PersL. The diagram is prepared based on the proposed mechanism in Ref [10].

97

2.2 Theory of Persistent Luminescence in Inorganic Materials

Great progress has been made in understanding the mechanism behind the PersL phenomenon in inorganic phosphors.[53-56] There are generally two key types of activation centers: luminescent centers and traps. Luminescent centers often include lanthanide ions (*e.g.*, Ce^{3+}, Eu^{2+}, Pr^{3+}, Tb^{3+}) involved in 5d-to-4f or 4f-to-4f transitions, transition metal ions (*e.g.*, Cr^{3+}, Mn^{2+}, Mn^{4+}, Ni^{2+}) with d-to-d transitions, and main group or post-transition metal ions (*e.g.*, Pb^{2+}, Bi^{3+}) with p-to-s transitions. Traps may consist of lattice or intrinsic defects (*e.g.*, oxygen vacancies, *F*-centers, anti-site defects), impurities (*e.g.*, Cu^+, Co^{2+}, Ti^{3+}), or doped aliovalent or isovalent co-dopants (*e.g.*, Dy^{3+} in $SrAl_2O_4:Eu^{2+}$, Nd^{3+} in $CaAl_2O_4:Eu^{2+}$, Cr^{3+} in $Y_3Al_2Ga_3O_{12}:Ce^{3+}$). Notably, some luminescent centers (*e.g.*, Cr^{3+} or Bi^{3+}) can also function as trap centers. It is widely accepted that the PersL in most inorganics originates from thermodynamically metastable states formed when excited charge carriers are trapped by point defects in the materials. These metastable states should overcome a certain energy gap to release the charge carriers, and the activation energy is defined as trap depth. This metastable state typically releases charge carriers *via* thermal activation or light excitation. Both luminescent centers and traps are situated within the band gap and typically have trap depths of a few electron volts (eV), just lower than the conduction band (CB) for electron traps or just higher than the valence band (VB) for hole traps. Various models, including electron trapping model, hole trapping model, quantum tunneling model, and intrinsic defect model, have been proposed to explain this phenomenon. Among them, Prof. Dorenbos's work on energy level diagrams of host materials and the energy levels of activation centers has enabled better explanations and predictions of PersL and electron/hole trapping phenomena. In the following sections, we will explore specific mechanisms of PersL, like electron trapping-detrapping models (**Section 2.2.1**) and hole trapping-detrapping models (**Section 2.2.2**). Additionally, we will introduce the concept of 'two zigzag curves' and discuss 'bandgap engineering' strategies informed

by host-referred binding energy (HRBE) and vacuum-referred binding energy (VRBE) diagrams within the context of 'electron trapping-detrapping model' (**Section 2.2.1**).

2.2.1 Electron Trapping-Detrapping Model

Figure 2.11 represents the typical electron transition path. The excitation process can originate from band-to-band excitation in the host, where the electrons are directly excited from the VB to the CB, or start from luminescent centers, where electrons are charged from the ground state of the luminescent centers to an excited state and then transferred to the CB. After the electrons in the CB are captured by trap states, they could return to the CB through thermal activation, and finally recombine with the luminescent centers and emit PersL. Especially, if the traps in the materials are deeper than 1.0 eV, the electrons stored in the deep traps would not be energetic to overcome the energy barrier and escape from the traps at RT. In this case, only under high-energy-oriented excitation, such as intense photo-stimulation (photon energy greater than 1.0 eV) or higher temperature thermal activation (typically above 200 °C), can endow the electrons with enough energy to release from the traps.
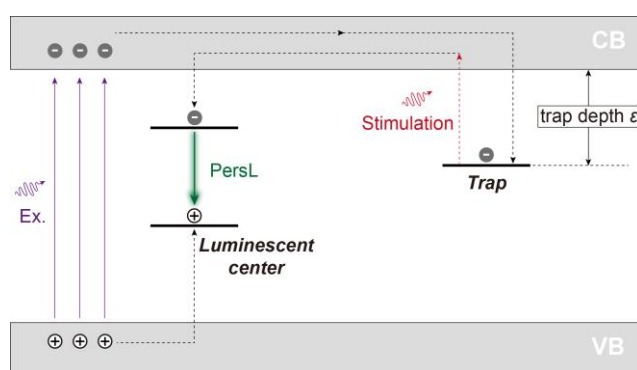
Figure 2.11 Semantics of electron trapping-detrapping model of inorganic PersL materials. Abbreviations and labels: trap depth (ε), excitation (purple line), emission (green line), electrons (black balls), holes (white balls) and the arrows indicate the

direction of electron movement. Notably, electrons can also be excited from the ground state of the luminescence center to CB. The diagram is prepared based on the proposed mechanism in Ref [53].

In 2005, amidst a decade-long debate regarding the mechanism of $SrAl_2O_4:Eu^{2+}$-Dy^{3+}, Prof. Dorenbos introduced a seminal energy level scheme for the $SrAl_2O_4$ host, characterized by two zigzag curves indicating the ground states of divalent and trivalent lanthanide ions.[57] The HRBE diagram indicates that Eu^{2+} serves as a luminescent center, and trivalent ions like Nd^{3+}, Dy^{3+}, Ho^{3+}, and Er^{3+} serve as electron traps, given that the ground states of their divalent counterparts reside lower than the CB with certain trap depths. This framework led to the proposal of an enhanced electron trapping-detrapping mechanism involving the electrons ionization from Eu^{2+} 5d excited state to the CB, followed by capturing by Dy^{3+} (the Eu^{2+}-Dy^{3+}/Eu^{3+}-Dy^{2+} couple). The diagram enables predictions regarding[53]: (1) the excitation process *via* electron and/or hole transfer; (2) the possibility of luminescent centers and traps for PersL, even in the co-doping system. For instance, Eu^{2+} typically functions as luminescent center because of their good preference for hole trapping, since there is a large energy gap between Eu^{2+} ground state and the top of the VB. Conversely, Dy^{3+}, Ho^{3+}, and Er^{3+} are recognized as effective electron traps, benefiting from enough trap depths that facilitate electron detrapping at RT. In contrast, Eu^{3+} and Yb^{3+} are not suitable as co-doping electron traps, as their divalent ground states are significantly below the CB, necessitating high heating energy to overcome the energy gap at elevated temperatures compared to RT; (3) this framework aids in predicting the delocalization energy of charge carrier, thereby enabling rapid identification of the charging energy for specific persistent phosphors.

Trap depth engineering by selecting suitable trivalent lanthanide co-dopants as traps in host material has been proved to be a useful strategy to obtain certain trap depths in PersL phosphor. Prof. Zhuang *et al.,* reported controlling method of the trap depth in Ln^{2+}/Ln^{3+}-doped $SrSi_2O_2N_2$ (Ln^{2+} = Yb^{2+}, Eu^{2+}, and Ln^{3+} = Dy^{3+}, Ho^{3+}, Er^{3+}). The

HRBE scheme in the SrSi$_2$O$_2$N$_2$ host was firstly established, in which Dy^{3+}, Ho^{3+}, Er^{3+}, Tm^{3+}, and other trivalent lanthanide ions were designed to be the electron trap centers with a depth more than 0.6 eV.[58] As illustrated in the Figure 2.12, the initial state of the electron trap is trivalent lanthanide ions (Ln$^{\cdot}_{Sr}$), and then divalent lanthanide ions (Ln$^{\times}_{Sr}$) were formed after capturing an electron. The established HEBE schemes displayed the energy-level of the rare-earth ions in SrSi$_2$O$_2$N$_2$ phosphors. The trap depth is determined by the energy difference between the ground state of the Ln$^{\times}_{Sr}$ and the bottom of the CB. The trap depths were calculated as 1.17, 1.04, 0.90, and 1.55 eV by co-doping with Dy^{3+}, Ho^{3+}, Er^{3+}, and Tm^{3+}, respectively in SrSi$_2$O$_2$N$_2$ host according to TL measurements, which matched well with the predictions of the HRBE model.[59] These results demonstrated that the HRBE model could provide a valuable guidance to modulate the trap depth in certain material systems.
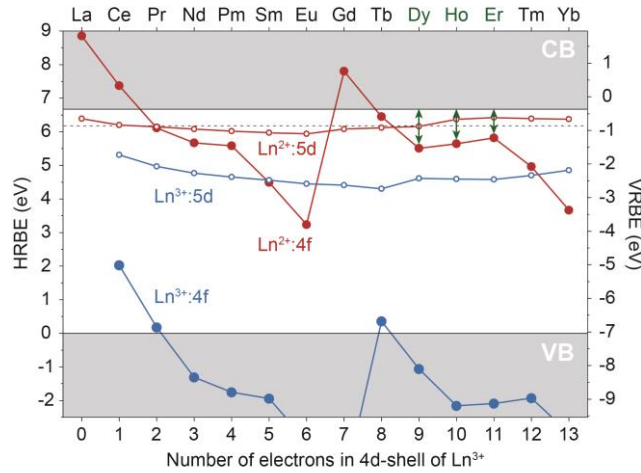
Figure 2.12 HRBE (left ordinate) and VRBE (right ordinate) schemes of Ln^{2+}/Ln^{3+}-doped SrSi$_2$O$_2$N$_2$. The 4f ground states (Ln^{2+}:4f) and the lowest 5d excited states (Ln^{2+}:5d) of Ln^{2+} are labeled by red dots and hollow circles. The 4f ground states (Ln^{3+}:4f) and the lowest 5d excited states (Ln^{3+}:5d) of Ln^{3+} are labeled by blue dots and hollow circles. The estimated trap depths are labeled by green double arrow line. The diagram is prepared based on the proposed mechanism in Ref [58].

Bandgap engineering has also been employed in inorganic PersL materials to modulate trap depths. Prof. Ueda *et al.* developed yellow persistent phosphor of $Y_3Al_{5-x}Ga_xO_{12}:Ce^{3+}$, Cr^{3+} that could be charged by blue-light (460 nm) and UV excitations.[60, 61] By varying the molar mass ratio of Ga, the peak temperature of the TL glow curve could be regulated from 150 to 400 K, and the related trap depths increased from 0.41 to 1.2 eV. A larger trap depth was reported by Prof. Zhuang *et al.* in $Y_3Al_{5-x}Ga_xO_{12}:Ce^{3+}$, V^{3+} fluorescent particles-based PiG films.[62] As the molar mass ratio of Ga decreased from 3 to 0, the peak temperature of the TL glow curve increased from 410 to 545 K. Thanks to the bandgap engineering effect, as shown in Figure 2.13, the trap depth in the phosphors state and PiG film states can be regulated from 1.13 to 1.62 eV by changing the energy gap between the electron trap and the bottom of the CB.[63]
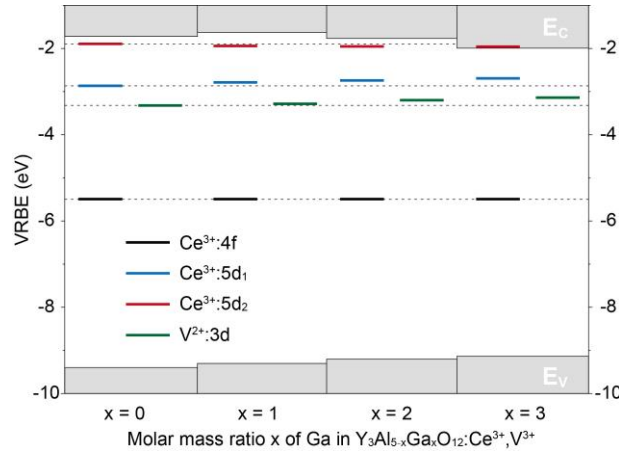
Figure 2.13 Stacked vacuum-referred binding energy (VRBE) diagrams of $Y_3Al_{5-x}Ga_xO_{12}:Ce^{3+}$, V^{3+} (x = 0, 1, 2, and 3). The bottom of the conduction band (E_C) rose from 0 to 1 and dropped down from 1 to 3. The top of valence band (E_V) monotonously moved upward when x increased. The diagram is prepared based on the proposed mechanism in Ref [62].

2.2.2 Hole Trapping-Detrapping Model

 Similarly, holes can be released from the hole trapping centers and recombine with electrons at the luminescent center through the VB. This mechanism is referred to as the 'hole trapping-detrapping model' (Figure 2.14). Under excitation, electrons and holes are generated. The hole can migrate through the VB and be captured by the hole traps, while the separated electron is captured by the excited state at the luminescent center. Then, if the thermal activation energy exceeds the trap depth between the top of the VB and the hole trapping state, the captured hole can be released from the trap state *via* the VB. Finally, the hole captured in the ground state and the electron in the excited state recombine, resulting in PersL emission.

 Limited reports on the hole trapping-detrapping process arise from challenges in identifying hole trapping centers and characterizing their trap depths. It is crucial to determine the trapping level's position relative to the top of VB and to differentiate between hole release from the VB and electron release from CB at specific temperatures.[53] The VRBE diagram facilitates comparisons of binding energies at the VB top and CB bottom across different compounds on a consistent energy level. Notably, the $4f$ ground states of all lanthanides show minimal dependence on compound type, allowing for fine-tuning of hole trap depths by adjusting the VRBE at the VB top. For example, Prof. Dorenbos investigated hole trapping-detrapping processes in Bi^{3+} and lanthanide-doped rare earth orthophosphates.[64] Utilizing a VRBE diagram, they demonstrated that Bi^{3+} can function as both a deep electron trap and a shallow hole trap, depending on the choice of co-dopants. When paired with shallow hole traps like Tb^{3+} or Pr^{3+}, Bi^{3+} served as a deep electron trap and luminescent center. Conversely, when combined with deep electron traps such as Tm^{3+}, Sm^{3+}, Yb^{3+}, or Eu^{3+}, Bi^{3+} acted as a shallow hole trap, with holes released from Bi^{4+} recombining with electrons trapped at the lanthanide ions through the VB. Additionally, the study revealed that introducing Lu^{3+} into YPO₄ can adjust the VB energy and regulate the hole trap depth of Bi^{3+}. Prof. Ueda developed new rare-earth (RE) based phosphors with red PersL emission

[RE_2O_2S (RE = La, Gd, Y, Lu) doped with Eu^{3+}-Pr^{3+} and Eu^{3+}-Tb^{3+}].[65] Among the doped elements, Eu^{3+} served as a luminescent center, and Pr^{3+} and Tb^{3+} ions acted as hole traps. The trap depth of Pr^{3+} deeper than that of Tb^{3+}, and can be changed with RE host. This phenomenon could be ascribed to the nephelauxetic effect by using VRBE diagram.
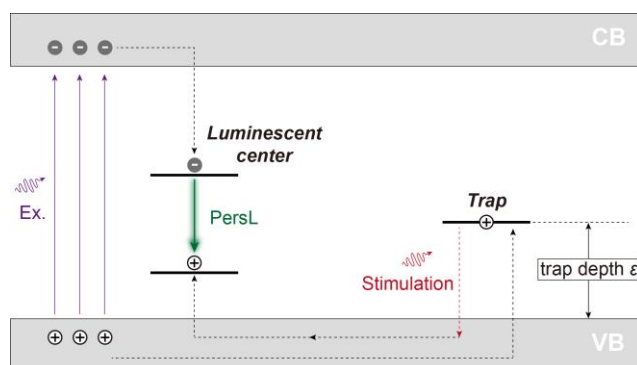
Figure 2.14 Semantics of hole trapping-detrapping model of inorganic PersL materials. Abbreviations and labels: trap depth (ε), excitation (purple line), emission (green line), electrons (black balls), holes (white balls) and the arrows indicate the direction of electron movement. Notably, electrons can also be excited from the ground state to excited state in the luminescence center. Correspondingly, holes can also transition directly from the ground state of the luminescence center to the VB. The diagram is prepared based on the proposed mechanism in Ref [53].

2.3 Theory of Stimulation in Persistent Luminescence

Stimulation refers to the process in which charge carriers escape from trap states back to the luminescent center after the excitation has ended, specifically in trap-induced PersL materials (Figure 2.15a). Currently, the reported forms of stimulation include thermal stimulation, optical stimulation, force stimulation, electrical stimulation, and magnetic stimulation (**Sections 2.3.1-2.3.5**). Notably, the luminescence intensity enhancement associated with certain stimulation forms is not a new type of emission; it fundamentally remains PersL. Almost all inorganic PersL materials are induced by trap states, and research on corresponding stimulation forms is relatively extensive and in-depth.[53] In the case of organic PersL materials, traditional phosphorescence or delayed fluorescence based on triplet state spin-forbidden transition lack trap states, and thus do not exhibit stimulated response characteristics. While the LPL material systems do not explicitly describe the nature of traps, Prof. Adachi's team has discovered phenomena related to optical and magnetic excitation;[66] we have explored thermal and photonic excitation in depth after confirming the nature of the traps.[9]

Since stimulation accelerates the release of holes or electrons stored in the traps, the PersL intensity at the moment can even exceed that at the end of excitation, depending on the trap depth and storage temperature (Figure 2.15b). However, it can be observed that after repeated pulsed excitations under the same stimulation conditions, the intensity of the PersL increases less and less, and the decay slope becomes steeper. This indicates that the stimulated response is not derived from 'excitation'. It also reflects that the remaining holes or electrons stored in the traps are decreasing, leading to a higher decay rate. Due to these characteristics, pulsed excitation curves are widely used to determine whether a material exhibits stimulated response characteristics to a certain stimulation form. Additionally, they can be employed in organic systems to distinguish whether the target afterglow originates from triplet-state-based emission or from trap-induced PersL.
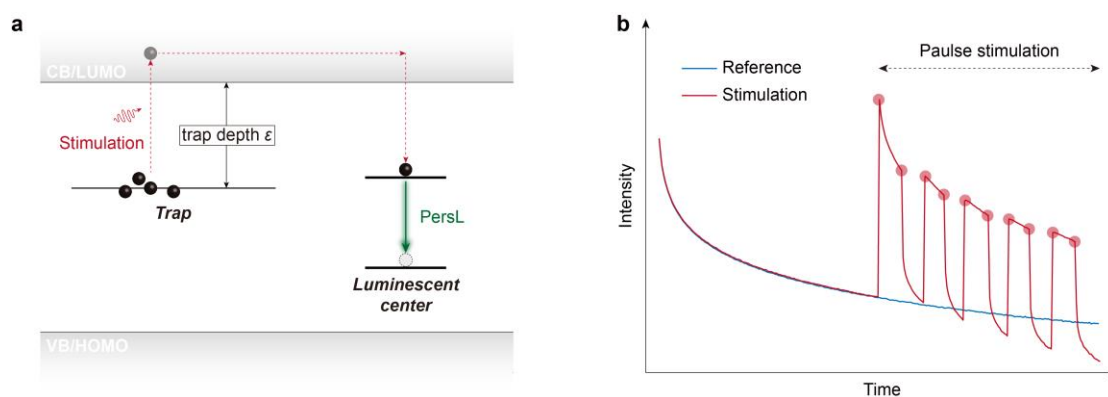
Figure 2.15 a, Semantics of stimulation process in organic/inorganic PersL materials (taking electron trapping model as an example). **b**, PersL decay curves with stimulation in a pulsed mode (repeating on and off after initial decay time, red line) and without stimulation (reference, blue line). Abbreviations and labels: trap depth (ε), emission (green line), electrons (black balls), holes (white balls) and the arrows indicate the direction of electron movement. The diagram is prepared based on the proposed mechanism in Ref [9].

2.3.1 Thermal Stimulation

TL is light emitted when a solid is heated to below incandescence after being exposed to radiation, and the heat serves merely as a trigger.[67] TL measurement is sensitive to material defects, and has been widely accepted as a useful tool for studying trap depth in trap-induced PersL materials.[56] In the inorganic domain, nearly all studies on trap states employ TL methods, which will not be elaborated upon here. In contrast, reports concerning TL in the organic realm are notably sparse.[9, 68] It is essential to distinguish between TL and TADF. The latter exhibits a blue shift in emission peak position under thermal influence; however, due to thermally activated non-radiative transitions, the emission intensity continues to decay.[69] In this section, we focus on how to utilize the Randall-Wilkins model to calculate trap depths.

The probability of holes or electrons escaping from traps because of the thermal stimulation can be quantified using the Arrhenius equation. Specifically, the probability per unit time, α, for the release of an electron from a trap is given by:

$$\alpha = s \exp\left(-\frac{\varepsilon}{k_B T}\right) \quad \text{(Equation 2.33)}$$

The pre-exponential factor is often referred to as the frequency factor or attempt-to-escape factor (s). This factor is independent of temperature and generally takes on values in the order of vibration frequency. ε is the trap depth (or activation energy). k_B is Boltzmann's constant (8.617×10^{-5} eV/K), and T is the absolute temperature. The values of ε and s determine carriers escaping at a given temperature T. When $\varepsilon \gg kT_0$ (where T_0 is the temperature during excitation), trapped carriers remain immobilized for extended periods, resulting in a substantial population of trapped carriers even after radiation exposure. Additionally, since separated electrons and holes are generated in pairs, the same population of trapped relative carriers will exist in the luminescent center. Raising the temperature above T_0 accelerates the return to equilibrium, increasing the probability of detrapping. However, it is crucial to note that not every detrapping results in light emission, and non-radiative transitions may also occur.

Randall and Wilkins model is assumed to be no quenching or re-trapping process, meaning all charge carriers detrapped to the CB contribute to recombination and PersL.[67] n (m^{-3}) is the concentration of trapped electrons and m (m^{-3}) is the concentration of trapped holes. The TL intensity $I(t)$, measured in photons per unit volume and per unit time (m^{-3} s^{-1}), at any time t during heating is proportional to the rate of recombination of holes and electrons at luminescent center:

$$I(t) = -\frac{dm}{dt} = -\frac{dn}{dt} = n\alpha = ns \exp\left(-\frac{\varepsilon}{k_B T}\right) \quad \text{(Equation 2.34)}$$

Typically, thermoluminescence is observed as temperature T increases linearly with time according to:

$$T(t) = T_0 + \beta t \quad \text{(Equation 2.35)}$$

where β (K s^{-1}) represents a constant heating rate and T_0 indicates the initial temperature at time $t = 0$. By substituting this temperature profile into Equation 2.35 and solving it, one arrives at the Randall-Wilkins equation (Equation 2.36), which describes the relationship between TL intensity and temperature:

$$I(T) = -\frac{1}{\beta}\frac{dn}{dt} = n_0 \frac{s}{\beta} \exp\left(-\frac{\varepsilon}{k_B T}\right) \exp\left[-\frac{s}{\beta} \int_{T_0}^{T} \exp\left(-\frac{\varepsilon}{k_B T'}\right) dT'\right] \quad \text{(Equation 2.36)}$$

where n_0 represents the total number of trapped electrons at $t = 0$ and T' serves as a dummy variable. This equation characterizes the shape of a TL peak. As temperature rises, the intensity begins to increase due to the detrapping of charge carriers and the subsequent recombination that triggers luminescence. Following this, the intensity increases to a maximum before declining as the available electrons are detrapped. The shape of the TL grow curve and position of the peak temperature are determined by the trap parameters s and the heating rate β. The intensity I_m at the temperature of the peak temperature of the TL glow curve (T_m) can be described by:

$$I_m(T_m) = n_0 \frac{\beta \varepsilon}{k_B T^2} \exp\left(-g_m\right) \quad \text{(Equation 2.37)}$$

with $g_m = g\left(\frac{\varepsilon}{k_B T_m}\right)$ and $g = g\left(\frac{\varepsilon}{k_B T}\right)$, an exponential integral with a value very close to unity for $T = T_m$ is shown. The ratio $\frac{\varepsilon}{T_m}$ is almost constant, so $I_m \sim \frac{n_0}{T_m}$. The temperature at which the maximum intensity occurs can be determined by setting the derivative of Equation 2.37 to 0. This condition yields:

$$\frac{\beta \varepsilon}{k_B T_m^2} = s \cdot \exp\left(\frac{-\varepsilon}{k_B T_m}\right) \quad \text{(Equation 2.38)}$$

In Equation 2.38, s is not a constant and varies across different material systems. To eliminate the influence of s, we can take the logarithm of both sides of Equation 2.38:

$$\ln \frac{T_m^2}{\beta} = \varepsilon \frac{-1}{k_B \cdot T_m} + \ln \frac{\varepsilon}{s k_B} \quad \text{(Equation 2.39)}$$

In Equation 2.39, let $\ln \frac{T_m^2}{\beta}$ be x and $\frac{-1}{k_B \cdot T_m}$ be y; then ε represents the slope of the function. By varying the heating rate β, we can identify different T_m values, thereby

determining the trap depth ε.

2.3.2 Optical Stimulation

To enable re-excitation of PersL phosphors using low-energy light sources, methods such as photo-stimulation are frequently employed. These techniques facilitate the repeated generation of enhanced PersL using low-energy photo-stimulation light, specifically red-to-NIR region. Notably, low-energy light sources for optical stimulation involve both intrinsic energies, where longer wavelengths may be insufficient for excitation from the VB of the host material or the ground state of the luminescent center to the CB; and optical power, which may not be adequate for achieving up-conversion luminescence. Optical excitation is not the same as optical stimulation mentioned here. However, the precise mechanisms underlying photo-stimulation remain a topic of ongoing debate. Some researchers suggest that the heat generated during photo-stimulation may accelerate the return of electrons from traps to the luminescent center, akin to TL (**Section 2.3.1**). In our study, we will characterize this process using thermal imaging and absorption spectroscopy, positing that the free radical anions of the trap molecules exhibit absorption in the red-to-NIR region, facilitating the transportation of charge carrier back to the luminescent center (**Section 2.1.4** and **Chapter 3**).[9]

Optical stimulation holds significant promise for PersL-based bioimaging applications, as longer wavelength light is more capable of penetrating human tissue to reach target indicators, enabling effective 'recharge'. For instance, Prof. Lv developed a novel core-shell nanoplatform, termed ZGGO@ZIF-8, which integrates chromium-doped zinc gallogermanate (ZGGO) as the core with NIR PersL nanoparticles, and zeolitic imidazolate framework-8 (ZIF-8) as the shell.[70] The ZGGO cores provided NIR PersL suitable for no autofluorescence bioimaging, while the ZIF-8 shells possessed a high loading properties for the anticancer drug doxorubicin and exhibited

pH-responsive drug release, accelerating in the acidic environment typical of tumors. By using 661 nm red-light to re-excite the ZGGO@ZIF-8 nanoparticles, the PersL intensity can be effectively restored. This restoration occurred because red-light irradiation facilitated the further distribution of electrons from deep-level traps to shallow-level traps, thereby enhancing PersL at RT.

2.3.3 Force Stimulation

Two distinct excitation processes for mechanoluminescence (ML) are inferred from experimental observations.[71, 72] The first involves the release of carriers from traps (Figure 2.18a). ML generated by the force diminishes or may vanish once enough carriers have been stimulated, a phenomenon currently elucidated through the 'piezoelectricity-induced carrier detrapping model'.[73] Furthermore, under force conversion, PersL persists regardless of the frequency of application within the mechanical fatigue limits. The latter is not the process we refer to as force stimulation. The interplay of the two mentioned processes at the microscopic level culminates in macroscopic emission, observable as 'piezoluminescence', resulting from material deformation within the elastic limit. Notably, force stimulation typically reside in deeper traps, whereas thermal stimulation holes are found in shallower ones. Consequently, an PersL from the ML material is also observable at RT.[72] Prof. Smet reported strong non-destructive mechanoluminescent properties in $BaSi_2O_2N_2$:Eu phosphor with blue-green PersL.[74] When exposed to UV or blue light, this phosphor emits intense blue-green light under mechanical stimulation. The peak of the ML emission band occurs at 498 nm, showing a slight redshift compared to the photoluminescence. By comparing the PersL emission of the $BaSi_2O_2N_2$:Eu phosphor, they concluded that ML was caused by the same traps as PersL. In the realm of organic materials, ML is predominantly associated with luminescence arising from crystal fracturing.[75] Reports detailing reversible force-induced afterglow are exceedingly rare,

let alone those that explicitly highlight trap-induced enhancement of this phenomenon.[76]

2.3.4 Electrical Stimulation

In 2024, Prof. Seto and Prof. Wang first investigated the use of an external electric field to enhance the PersL properties of the $SrAl_2O_4$:Eu^{2+},Dy^{3+} phosphor, which is currently the most widely used PersL material.[77] Through in-situ direct current (DC) electric field measurements using a layered structure composed of phosphor and electrodes, they found that the increase in PersL intensity was attributed to a phenomenon called 'external electric field stimulated enhancement of initial brightness of afterglow'. During the long afterglow emission process, electrons trapped in a super shallow trap at 0.022 eV can be accelerated by the external electric field through the CB, returning to the luminescent center. At a voltage of 6 V, the afterglow intensity reached 0.538 cd/m^2. Notably, the stored electrons are still generated through light excitation, as the $SrAl_2O_4$:Eu^{2+},Dy^{3+} powder is an insulating material and cannot be driven at such low voltages. his form of stimulation response has not yet been reported in organic systems.

2.3.5 Magnetic Stimulation

Prof. Tachikawa and Prof. Kabe first reported the discovery of optically and magnetically stimulated luminescence in organic melt-cast films, which is consist of electron-donating molecule, electron-accepting molecule, and trap or emitter molecule.[66] The blend films can store energy using UV light as the input and release it as visible light upon NIR light irradiation (optical stimulation). This organic photo stimulation exhibited outstanding repeatability, color tunability, and even could response to weak external magnetic fields. Under an external magnetic field, the PersL

intensity would be significantly reduced, exhibiting a negative magnetic field effect. This magnetic field effect may originate from the recombination of the charge-separated state into the luminescent state *via* spin entanglement. In contrast, the undoped trap/emitter system may not exhibit a significant magnetic field effect due to the shorter charge separation distance and faster spin relaxation. This mode of stimulation response has not been reported in the field of inorganic phosphors.

References

[1] S. Xu, R. Chen, C. Zheng, W. Huang, *Adv. Mater.* **2016**, 28, 9920-9940.

[2] W. Zhao, Z. He, B. Z. Tang, *Nat. Rev. Mater.* **2020**, 5, 869-885.

[3] R. Gao, M. S. Kodaimati, D. Yan, *Chem. Soc. Rev.* **2021**, 50, 5564-5589.

[4] X. Yang, G. I. N. Waterhouse, S. Lu, J. Yu, *Chem. Soc. Rev.* **2023**, 52, 8005-8058.

[5] R. Kabe, C. Adachi, *Nature* **2017**, 550, 384-387.

[6] K. Jinnai, R. Kabe, Z. Lin, C. Adachi, *Nat. Mater.* **2022**, 21, 338-344.

[7] P. Alam, N. L. C. Leung, J. Liu, T. S. Cheung, X. Zhang, Z. He, R. T. K. Kwok, J. W. Y. Lam, H. H. Y. Sung, I. D. Williams, B. Z. Tang, *Adv. Mater.* **2020**, 32, e2001026.

[8] K. Jiang, Y. Wang, C. Lin, L. Zheng, J. Du, Y. Zhuang, R. Xie, Z. Li, H. Lin, *Light Sci. Appl.* **2022**, 11, 80.

[9] C. Lin, Z. Wu, H. Ma, J. Liu, S. You, A. Lv, W. Ye, J. Xu, H. Shi, B. Zha, W. Huang, Z. An, Y. Zhuang, R.-J. Xie, *Nat. Photon.* **2024**, 18, 350-356.

[10] Q. Miao, C. Xie, X. Zhen, Y. Lyu, H. Duan, X. Liu, J. V. Jokerst, K. Pu, *Nat. Biotechnol.* **2017**, 35, 1102-1110.

[11] N. J. Hestand, F. C. Spano, *Chem. Rev.* **2018**, 118, 7069-7163.

[12] J. L. Bredas, D. Beljonne, V. Coropceanu, J. Cornil, *Chem. Rev.* **2004**, 104, 4971-5004.

[13] A. Jablonski, *Nature* **1933**, 131, 839-840.

[14] Q. Li, Y. Tang, W. Hu, Z. Li, *Small* **2018**, 14, e1801560.

[15] Z. Yang, Z. Mao, Z. Xie, Y. Zhang, S. Liu, J. Zhao, J. Xu, Z. Chi, M. P. Aldred, *Chem. Soc. Rev.* **2017**, 46, 915-1016.

[16] M. Y. Wong, E. Zysman-Colman, *Adv. Mater.* **2017**, 29, 1605444.

[17] K. Goushi, C. Adachi, *Appl. Phys. Lett.* **2012**, 101, 023306.

[18] M. Chapran, I. Sahalianov, N. N. Karaush-Karmazin, G. Wiosna-Salyga, I. Glowacki, B. Luszczynska, P. Pander, G. V. Baryshnikov, *ACS Appl. Electron. Mater.* **2023**, 5, 1489-1501.

[19] Y. Chen, A. J. Spiering, S. Karthikeyan, G. W. Peters, E. W. Meijer, R. P. Sijbesma, *Nat. Chem.* **2012**, 4, 559-562.

[20] Z. Gao, Y. Zhang, Q. Liu, D. Ding, *MedMat* **2024**, 1, 27-39.

[21] P. Jin, X. Wei, B. Yin, L. Xu, Y. Guo, C. Zhang, *Adv. Mater.* **2024**, e2400158.

[22] L. Mo, H. Liu, Z. Liu, X. Xu, B. Lei, J. Zhuang, Y. Liu, C. Hu, *Adv. Opt. Mater.* **2022**, 10, 2102666.

[23] K. Stavrou, L. G. Franca, A. Danos, A. P. Monkman, *Nat. Photonics* **2024**, 18, 554-561.

[24] H. H. Cho, D. G. Congrave, A. J. Gillett, S. Montanaro, H. E. Francis, V. Riesgo-Gonzalez, J. Ye, R. Chowdury, W. Zeng, M. K. Etherington, J. Royakkers, O. Millington, A. D. Bond, F. Plasser, J. M. Frost, C. P. Grey, A. Rao, R. H. Friend, N. C. Greenham, H. Bronstein, *Nat. Mater.* **2024**, 23, 519-526.

[25] H. Shi, W. Yao, W. Ye, H. Ma, W. Huang, Z. An, *Acc. Chem. Res.* **2022**, 55, 3445-3459.

[26] K. Schmidt, S. Brovelli, V. Coropceanu, D. Beljonne, J. Cornil, C. Bazzini, T. Caronna, R. Tubino, F. Meinardi, Z. Shuai, J.-L. Brédas, *J. Phys. Chem. A* **2007**, 111, 10490-10499.

[27] M. A. El-Sayed, *J. Chem. Phys.* **1963**, 38, 2834-2838.

[28] C. Adachi, R. C. Kwong, P. Djurovich, V. Adamovich, M. A. Baldo, M. E. Thompson, S. R. Forrest, *Appl. Phys. Lett.* **2001**, 79, 2082-2084.

[29] K. Horie, I. Mita, *Chem. Phys. Lett.* **1982**, 93, 61-65.

[30] J. Yang, M. Fang, Z. Li, *Accounts Mater. Res.* **2021**, 2, 644-654.

[31] X. Yan, H. Peng, Y. Xiang, J. Wang, L. Yu, Y. Tao, H. Li, W. Huang, R. Chen, *Small* **2021**, 18, e2104073.

[32] C. A. Parker, C. G. Hatchard, *Trans. Faraday Soc.* **1961**, 57, 1894.

[33] Y. Tao, K. Yuan, T. Chen, P. Xu, H. Li, R. Chen, C. Zheng, L. Zhang, W. Huang, *Adv. Mater.* **2014**, 26, 7931-7958.

[34] H. Uoyama, K. Goushi, K. Shizu, H. Nomura, C. Adachi, *Nature* **2012**, 492, 234-238.

[35] C. Ye, L. Zhou, X. Wang, Z. Liang, *Phys. Chem. Chem. Phys.* **2016**, 18, 10818-10835.

[36] V. Gray, K. Moth-Poulsen, B. Albinsson, M. Abrahamsson, *Coord. Chem. Rev.* **2018**, 362, 54-71.

[37] Y. Im, M. Kim, Y. J. Cho, J.-A. Seo, K. S. Yook, J. Y. Lee, *Chem. Mater.* **2017**, 29, 1946-1963.

[38] W. Li, Y. Pan, L. Yao, H. Liu, S. Zhang, C. Wang, F. Shen, P. Lu, B. Yang, Y. Ma, *Adv. Opt. Mater.* **2014**, 2, 892-901.

[39] W. Li, D. Liu, F. Shen, D. Ma, Z. Wang, T. Feng, Y. Xu, B. Yang, Y. Ma, *Adv. Funct. Mater.* **2012**, 22, 2797-2803.

[40] H. Ohkita, W. Sakai, A. Tsuchida, M. Yamamoto, *Macromolecules* **1997**, 30, 5376-5383.

[41] S. Gélinas, A. Rao, A. Kumar, S. L. Smith, A. W. Chin, J. Clark, T. S. van der Poll, G. C. Bazan, R. H. Friend, *Science* **2014**, 343, 512-516.

[42] W. Li, Z. Li, C. Si, M. Y. Wong, K. Jinnai, A. K. Gupta, R. Kabe, C. Adachi, W. Huang, E. Zysman-Colman, I. D. W. Samuel, *Adv. Mater.* **2020**, 32, e2003911.

[43] P. Alam, T. S. Cheung, N. L. C. Leung, J. Zhang, J. Guo, L. Du, R. T. K. Kwok, J. W. Y. Lam, Z. Zeng, D. L. Phillips, H. H. Y. Sung, I. D. Williams, B. Z. Tang, *J. Am. Chem. Soc.* **2022**, 144, 3050-3062.

[44] Z. Lin, M. Li, R. Yoshioka, R. Oyama, R. Kabe, *Angew. Chem. Int. Ed.* **2024**, 63, e202314500.

[45] X. Liang, Y. X. Zheng, J. L. Zuo, *Angew. Chem. Int. Ed.* **2021**, 60, 16984-16988.

[46] X. Liang, X. F. Luo, Z. P. Yan, Y. X. Zheng, J. L. Zuo, *Angew. Chem. Int. Ed.* **2021**, 60, 24437-24442.

[47] Y. Wang, H. Gao, J. Yang, M. Fang, D. Ding, B. Z. Tang, Z. Li, *Adv. Mater.* **2021**, 33, e2007811.

[48] L. Liang, J. Chen, K. Shao, X. Qin, Z. Pan, X. Liu, *Nat. Mater.* **2023**, 22, 289-304.

[49] T. Chen, D. Yan, *Science Bull.* **2024**, 69, 1806-1808.

[50] J. Yang, Z. Chen, M. Fang, Z. Li, *Smart Mol.* **2024**, e20240034.

[51] D. Chen, T. Zhang, A. Jiao, X. Mou, X. Dong, Y. Cai, *Coord. Chem. Rev.* **2025**, 523, 216258.

[52] M. Vacher, I. Fdez. Galván, B.-W. Ding, S. Schramm, R. Berraud-Pache, P. Naumov, N. Ferré, Y.-J. Liu, I. Navizet, D. Roca-Sanjuán, W. J. Baader, R. Lindh, *Chem. Rev.* **2018**, 118, 6927-6974.

[53] J. Xu, S. Tanabe, *J. Lumin.* **2019**, 205, 581-620.

[54] J. Ueda, *Bull. Chem. Soc. Jpn.* **2021**, 94, 2807-2821.

[55] J. Shi, X. Sun, L. Song, M. Hong, Q. Yuan, Y. Zhang, *Prog. Mater. Sci.* **2024**, 142, 101246.

[56] Y. Li, M. Gecevicius, J. Qiu, *Chem. Soc. Rev.* **2016**, 45, 2090-2136.

[57] P. Dorenbos, *J. Electrochem. Soc.* **2005**, 152, H107.

[58] P. Dorenbos, *J. Lumin.* **2013**, 136, 122-129.

[59] Y. Zhuang, Y. Lv, L. Wang, W. Chen, T. L. Zhou, T. Takeda, N. Hirosaki, R. J. Xie, *ACS Appl. Mater. Interfaces* **2018**, 10, 1854-1864.

[60] J. Ueda, K. Kuroishi, S. Tanabe, *Appl. Phys. Lett.* **2014**, 104, 101904.

[61] J. Ueda, P. Dorenbos, A. J. J. Bos, K. Kuroishi, S. Tanabe, *J. Mater. Chem. C* **2015**, 3, 5642-5651.

[62] W. Li, Y. Zhuang, P. Zheng, T. L. Zhou, J. Xu, J. Ueda, S. Tanabe, L. Wang, R. J. Xie, *ACS Appl. Mater. Interfaces* **2018**, 10, 27150-27159.

[63] I. I. Vrubel, R. G. Polozkov, I. A. Shelykh, V. M. Khanin, P. A. Rodnyi, C. R. Ronda, *Crystal Growth & Design* **2017**, 17, 1863-1869.

[64] T. Lyu, P. Dorenbos, *J. Mater. Chem. C* **2018**, 6, 6240-6249.

[65] A. Hashimoto, J. Ueda, Y. Aoki, P. Dorenbos, S. Tanabe, *J. Phys. Chem. C* **2023**, 127, 15611-15619.

[66] M. Sakurai, R. Kabe, M. Fuki, Z. Lin, K. Jinnai, Y. Kobori, C. Adachi, T. Tachikawa, *Commun. Mater.* **2021**, 2, 74.

[67] A. J. J. Bos, *Materials (Basel)* **2017**, 10, 1357.

[68] K. Jinnai, N. Nishimura, C. Adachi, R. Kabe, *Nanoscale* **2021**, 13, 8412-8417.

[69] C. Lin, Y. Zhuang, W. Li, T. Zhou, R.-J. Xie, *Nanoscale* **2019**, 11, 6584-6590.

[70] Y. Lv, D. Ding, Y. Zhuang, Y. Feng, J. Shi, H. Zhang, T. L. Zhou, H. Chen, R. J. Xie, *ACS Appl. Mater. Interfaces* **2019**, 11, 1907-1916.

[71] Y. Zhuang, R. J. Xie, *Adv. Mater.* **2021**, 33, e2005925.

[72] Z. Huang, B. Chen, B. Ren, D. Tu, Z. Wang, C. Wang, Y. Zheng, X. Li, D. Wang, Z. Ren, S. Qu, Z. Chen, C. Xu, Y. Fu, D. Peng, *Adv. Sci.* **2023**, 10, e2204925.

[73] J.-C. Zhang, X. Wang, G. Marriott, C.-N. Xu, *Prog. Mater. Sci.* **2019**, 103, 678-

742.

[74] J. Botterman, K. V. d. Eeckhout, I. D. Baere, D. Poelman, P. F. Smet, *Acta Mater.* **2012**, 60, 5494-5500.

[75] Y. Xie, Z. Li, *Chem* **2018**, 4, 943-971.

[76] J. Chen, F. Lin, D. Guo, T. Tang, Y. Miao, Y. Wu, W. Zhai, H. Huang, Z. Chi, Y. Chen, Z. Yang, *Adv. Mater.* **2024**, 2409642.

[77] X. Ma, Y. Wang, T. Seto, *Light Sci. Appl.* **2024**, 13, 165.

Chapter 3

Deep Trap Management in Organic Persistent Luminescence for Multi-Mode Optical Information Storage

Note: This work resulted in a manuscript titled "Deep Trap Management in Organic Persistent Luminescence for Multi-Mode Optical Information Storage" for *Advanced Optical Materials* and still under revision, presented here.

3.1 Abstract

The global data explosion has heightened the demand for advanced optoelectronic information storage technologies but developing multidimensional and deep-trap persistent luminescence (PersL) in organic storage media remains a significant challenge. Herein, donor-acceptor-donor wedge-shape thermally activated delayed fluorescence emitter 2,5-bis(4-(diphenylamino)phenyl)-7-oxo-7*H*-benzo[*de*]benzo[4,5]imidazo[2,1-*a*] isoquinoline-10,11-dicarbonitrile (TCN) was designed for PersL host/guest system, enabling multi-mode excitation and stimulation forms, ~0.72 eV deep trap depth, 6.1% aggregation-induced quenching effect. UV, visible light (425-630 nm), and X-ray efficiently triggered deep traps with nearly identical depth values, deviating less than 0.04 eV from density functional theory calculations. The thermoluminescence peak T_m at 385 K (heating rate at 50 K/min), coupled with near-infrared (NIR) stimulation wavelengths extending to 1300 nm, greatly exceeds room temperature storage capacities, ensuring consistent intensity for over 1 month of information retention. The multi-mode optical information storage and retrieval capability of this PersL media extended its application scope to include blue-laser direct writing, X-ray time-lapse imaging, and NIR electronic signatures. This

study on deep-trap PersL storage media significantly advances our understanding of the molecular design and luminescent mechanisms in organic semiconductors, with broad implications for enhancing their energy storage applications in diverse scenarios.

3.2 Introduction

The demand for information storage is rapidly increasing, with annual data production in the zettabyte scale doubling every two years since 2000.[1] The optoelectronic information storage surpasses magnetic and solid-state storages with its superior rewritability, reduced noise, extensive capacity, low energy consumption, and advanced design capability.[2] However, 2D planar optical data storage technology is hindered by intense optical diffraction, limiting its storage capacity and lagging behind other mainstream data storage technologies.[3] Recently, significant research efforts have focused on developing next-generation supercapacity optical data storage technologies by enhancing information dimensions, including spatial coordination,[4, 5] intensity,[6, 7] wavelength,[8, 9] polarization,[10, 11] angular momentum,[12, 13] and time gating[14, 15].

Persistent luminescence (PersL) materials, also referred to charge-carrier-trapping materials, have been utilized for information storage and high-energy radiation dosimetry since the early 1980s.[16, 17] Importantly, luminescence by the recombination process with carriers released under thermal or optical stimulation can carry operable optical information, such as emission intensity and wavelength, enabling PersL materials with multi-dimensional optical information storage capabilities.[18] To prevent charge carriers from escaping the traps and achieve high information retention rates at room temperature (RT), PersL materials generally need to exhibit trap depths with ~0.8 eV.[19] To date, great progress has been made in both mechanism and application behind the deep-trap inorganic PersL materials, including $NaLuF_4:Tb^{3+}$, $ZnGa_2O_4:Cr^{3+}$, $CsCdCl_3:Mn^{2+}$, Zr^{4+}, and $YAG:Ce^{3+}$.[20-24] However, this system not only requires doping with metal ions to construct deep traps but also exhibits a relatively singular high energy excitation form (primarily UV or X-ray). Organic afterglow phosphors offer advantages like form flexibility, excitation tunability, compositional variety, and semiconducting properties.[25-30] However, phosphorescence and thermally activated delayed fluorescence (TADF) from organic molecules typically stem from spin-

forbidden transitions between triplet and singlet states, lacking inherent energy storage properties.[31, 32] Inspired by charge trapping/detrapping model in inorganic phosphor, recent advances in trap-induced PersL (TIP) mechanism have extended durations to hour-levels and enabled organic optical information storage, while molecular design for trap depth remains unclear.[33, 34]

Herein, to achieve deep trap depth in organic TIP host/guest systems, a novel electron-accepting naphthalimide modified with two cyan groups was designed and introduced into the guest molecule. The 2,5-dibromo-7-oxo-7*H*-benzo[*de*]benzo[4,5]imidazo[2,1-*a*]isoquinoline-10,11-dicarbonitrile (CN) electron acceptor enables UV, visible light, and X-ray excitation (Figures 3.1a-b), while forming radical anions with low LUMO, lowest unoccupied molecular orbital, energy levels to construct deep trap depths for information storage applications. The incorporation of two triphenylamine (TPA) segments on the side chains of CN acceptor prevents aggregation-induced quenching (ACQ). Additionally, the separation of the frontier molecular orbitals of electron acceptor and donors promotes TADF properties, achieving nearly 100% exciton utilization when trapped electrons return to the luminescent center under thermal or photo-stimulation (Figures 3.1a and 1c).[35] The developed organic TIP film exhibited PersL durations exceeding 5 hours and storage stability of over 45 days at RT. A molecular design principle for TADF guest molecules in organic TIP systems is anticipated to significantly broaden the scope of optical information storage applications.
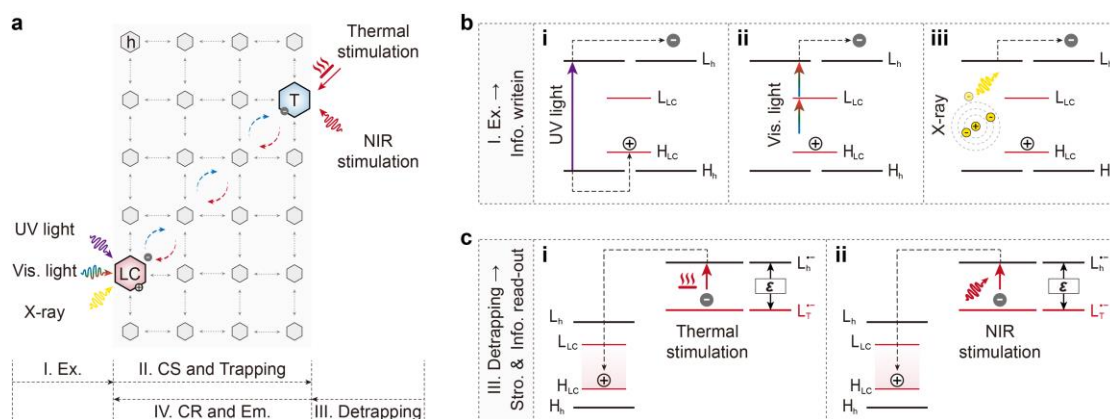
Figure 3.1 PersL in TCN@TPBi host-guest molecular system. **a**, Schematic illustration of the possible PersL mechanism and electron migration in a host-guest molecular system. Briefly, electrons from luminescent center can be excited under irradiation of UV light, visible light, and X-ray (Step I), and captured by traps (Step II). The trapped electrons are released under thermal and NIR stimulation (Step III), recombine with the luminescent center and finally give PersL(Step IV). **b**, Proposed energy level diagram of PersL under different excitation sources, including UV light (**i**), visible light (**ii**), and X-ray (**iii**). **c**, Proposed energy level diagram of PersL under different detrapping methods, including thermal stimulation (**i**) and optical stimulation (**ii**). Abbreviations and labels: host (H, grey hexagon), electrons (grey solid balls), luminescence center (L, red hexagon), trap (T, blue hexagon), the LUMO of the host (L_H), the HOMO of the host (H_H), LUMO of the guest (L_G), HOMO of the guest (H_G), LUMO of the host radical anion ($L_H^{\cdot-}$), LUMO of the guest radical anion ($L_G^{\cdot-}$). charge separation (CS), charge recombination (CR), and trap depth (ε).

3.3 Experimental Procedure

3.3.1 Materials and Characterizations

Unless otherwise noted, all reagents used in the experiments were purchased from commercial sources without further purification. 2,5-bis(4-(diphenylamino)phenyl)-7-oxo-7*H*- benzo[*de*]benzo[4,5]imidazo[2,1-*a*] isoquinoline-10,11- dicarbonitrile (TCN) was synthesized in three steps including dehydration reaction and palladium catalyzed Suzuki cross-coupling reaction, followed by characterizations of nuclear magnetic resonance (NMR) spectroscopy (Advance III 500 MHz NMR, Bruker). 1,3,5-tris(1-phenyl-1*H*- benzimidazol-2-yl)benzene (TPBi) was obtained from Xi'an Polymer Light Technology Corp.

Synthesis of S₁
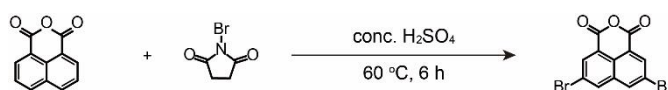
Scheme 3.1 Synthetic route of 5,8-dibromo-1*H*,3*H*-benzo[*de*]isochromene-1,3-dione (S₁).

A mixture of 1,8-naphthalic anhydride (99%) (35.2 g, 178 mmol) and 1-bromopyrrolidine-2, 5-dione (99%) (NBS, 77.8 g, 435 mmol) in concentrated sulfuric acid (250 mL) was stirred at 60 °C for 6 h. After cooling down to ambient temperature, the mixture was poured into ice water (1000 mL). The precipitate was collected by filtration, washed successively with water (1000 mL) and acetonitrile (1000 mL). The crude product was obtained by recrystallization with *N,N*-Dimethylformamide to give S₁ as a pale pink solid (12.72g, yield = 20.1%). ^{1}H NMR (400 MHz, CDCl₃) δ 8.66 (d, *J* = 1.7 Hz, 1H), 8.37 (d, *J* = 1.7 Hz, 1H).

Synthesis of CN
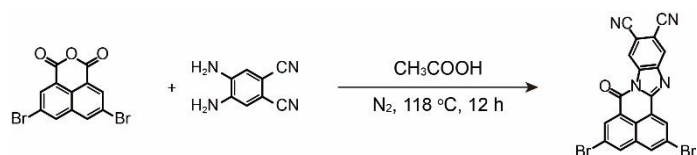
Scheme 3.2 Synthetic route of 2,5-dibromo-7-oxo-7*H*-benzo[*de*]benzo[4,5]imidazo[2,1-*a*]isoquinoline- 10,11-dicarbonitrile (**CN**).

A mixture of S_1 (889.5mg, 2.5mmol) and 4,5-Diamino-1,2-Benzenedicarbonitrile (98%) (316.3mg, 2 mmol) in acetic acid (40 mL) was stirred at 118 ºC for 12 h in nitrogen atmosphere. After allowed to cool to ambient temperature, the mixture was poured into ice water (40 mL) and dichloromethane (30ml). The crude product was filtered and washed with dichloromethane (15 mL), followed by vacuum-dry at 100 ºC. The product was obtained to give **CN** as a yellow solid (776.2mg, yield = 84.2%). ^{1}H NMR (400 MHz, CDCl$_3$) δ 9.01, 8.99, 8.98, 8.90, 8.89, 8.67, 8.66, 8.45, 8.44, 8.37, 8.37, 8.35, 8.34, 8.30.

Synthesis of TCN
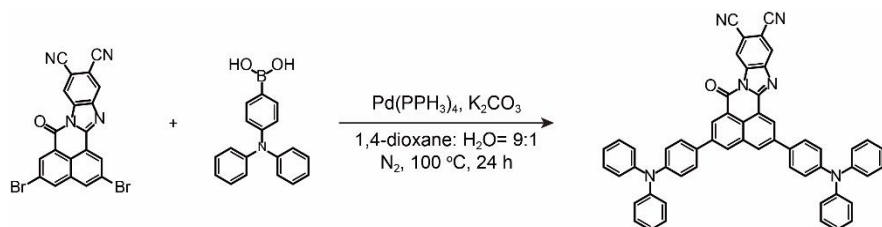
Scheme 3.3 Synthetic route of 2,5-bis(4-(diphenylamino)phenyl)-7-oxo-7*H*-benzo[*de*]benzo[4,5]imidazo[2,1-*a*] isoquinoline-10,11-dicarbonitrile (**TCN**).

CN (478 mg, 1.0 mmol), (4-(diphenylamino)phenyl)boronic acid (636.1 mg, 2.2 mmol) and tetrakis(triphenylphosphine)palladium(0) (231.1 mg, 0.2 mmol), potassium carbonate (828.3 mg, 6 mmol), 1,4-dioxane and distilled water (50 mL, 9:1, v/v) were added. The mixture was heated to 100 °C under a nitrogen atmosphere for 24 h. After cooling to room temperature, the mixture was extracted with dichloromethane, and the organic layer was washed with sodium chloride water and then dried over anhydrous MgSO$_4$ and concentrated. The crude product was firstly purified by column

chromatography on silica gel (petroleum ether/dichloromethane = 1:1-1:5, v/v). Then this compound was purified by temperature-gradient sublimation under vacuum at 370 °C. By exploiting the solubility disparity and employing a high-temperature concentration method, impurities can be dissolved in dichloromethane, while TCN can be further precipitated to obtain a reddish-brown solid (655.7 mg, yield = 40.7%). ^{1}H NMR (400 MHz, CDCl$_3$) δ 9.05 (s, 1H), 9.00 (d, J = 8.6 Hz, 2H), 8.48 (s, 1H), 8.38 (s, 1H), 8.23 (s, 1H), 7.68 (t, J = 8.6 Hz, 4H), 7.31 (t, J = 7.8 Hz, 8H), 7.24-7.13 (m, 12H), 7.09 (t, J = 7.2 Hz, 4H).

3.3.2 Fabrication of TCN@TPBi Film

A mixture of TCN emitter and TPBi (totally ~1 mmol) was heated to 350°C on a quartz substrate inside a glovebox. After melting, the mixture was stirred thoroughly, and then cooled rapidly to room temperature. It was finally encapsulated in a quartz glass case with a size of 2×2 cm^2 by using an ultraviolet-cured epoxy resin. The fabrication of the melt-casting films was performed under a nitrogen atmosphere inside the glovebox.

3.3.3 Characterizations of Photophysical Properties

Emission spectra and lifetime decay curves were collected in a spectrometer (FLS980, Edinburgh; and QE-Pro, Ocean Photonics). The absorption spectra were measured by an ultraviolet/visible/near-infrared spectrophotometer (UV-3600Plus, Shimadzu). The electron spin resonance (ESR) spectra were obtained using an X-band EPR spectrometer (EMX-10/12, Bruker). The experimental HOMO and LUMO energy were measured with cyclic voltammetry standardized against ferrocene/ferrocenium (PalmSens 4 electrochemical workstation, Pt = working electrode, platinum wire = auxiliary electrode, and Ag wire = reference electrode). After deoxygenation, the reduction and oxidation potentials were measured in anhydrous CH$_2$Cl$_2$ solutions containing 0.1 M tetrabutylammonium hexafluorophosphate (n-Bu$_4$NPF$_6$) as supporting electrolyte at a scan rate of 0.1 V s^{-1}. The radical cations and anions of the

host and guest were obtained through electrochemical oxidation or reduction reactions, with the host and guest dissolved in dichloromethane containing 0.1 M TBAPF$_6$. Thermogravimetric analyse (TGA) was carried out on a thermal analyzer (SDT-Q600) at a heating rate of 10 °C min^{-1} from 25 to 800 °C under a nitrogen atmosphere. Photographs and videos of the samples were taken using digital cameras (α7SIII, SONY). The ISO, F-number, and exposure time of the videos were ISO 80000-409600, f/1.2, and 1/4 s, respectively. And photography parameters were ISO 65535, f/1.2, and 1/25-5 s. Due to the extended exposure time, the photographs exhibit enhanced clarity.

3.3.4 Characterizations of PersL and TL in Organics

The PersL decay curve, PersL spectra, and TL glow curve spectra were recorded using a self-built measurement system. Briefly, the sample was placed on a cooling-heating stage (THMS600E, Linkam Scientific Instruments) with a controllable temperature ranging from 100 to 600 K. The sample chamber was filled in dry nitrogen gas, and the top of the chamber was installed with quartz glass. The sample was excited through the quartz glass by UV or visible LEDs for 5 min. The excitation power density of 365, 440, 520 and 620 nm is 37.5, 41.3, 21.0 and 16.6 mW/cm^2, respectively. A filter-attached PMT (R928P, Hamamatsu photonics), a multimeter (2400, Keithley) and a high voltage power supply (HVC1800, Zolix) were used to monitor the PersL intensity (or TL emission, PersL decayc curves) after ceasing the excitation source. The PersL spectra were recorded at the same time using a multichannel spectrometer (QE-Pro, Ocean Optics) during the TL measurements. In TL measurements, the samples were first cooled to 100 K and excited by the excitation source (UV, visible light, or X-ray) for 5 min. After trunning off the excitation source for 20 s, the sample was heated to 400 K at a certain heating rate (*i.e.*, 50, 20, 10, 5 and 2 K/min), and the emission intensity was recorded in real time. The above measurement system was driven by LabVIEW-based computer programs. The PersL excitation spectra were obtained by high-energy broadly tunable lasers (NT342, Ekspla) with monochromatic light with a power density of ~37.5 mW/cm^2. The PersL intensity was measured after ceasing the

excitation source for 30 s. The excitation wavelength was sequentially changed from 700 to 425 nm with a wavelength increment of 5 nm and a time interval of 5 min between two tests.

3.3.5 Theoretical Calculations of Crystallographic Configuration and Electronic structures

The excitation energies were evaluated using the time-dependent density functional theory (TD-DFT) method based on the equilibrium configuration of the ground state (S_0) at the B3LYP/def2-SVP level. Additionally, the HOMO and LUMO levels were calculated using the Gaussian 16 package. To ensure stable equilibrium geometries in the S_0, all neutral molecules were optimized at the B3LYP/def2-SVP level using the Gaussian 16 program. The geometries of the anions and cations were derived from these neutral S_0 structures. Molecular orbitals were depicted for both closed-shell and open-shell systems.

3.4 Results and Discussion

To construct deep traps for energy storage, a novel TADF emitter 2,5-bis(4-(diphenylamino)phenyl)-7-oxo-7*H*-benzo[*de*]benzo[4,5]imidazo[2,1-*a*] isoquinoline-10,11-dicarbonitrile (TCN) with strong electron-accepting properties was designed (see Figure 3.2a for the chemical structure, Experimental Section of Supporting Information, and Figures S3.1-3.3). By modifying the 1,8-naphthalimide electron acceptor with two cyan electron-withdrawing functional groups (CN acceptor), the LUMO energy level of TCN was significantly lowered, facilitating the formation of a lower LUMO energy level for the TCN radical anion after electron capture.[36] As shown in Figure 3.2b and Figure S3.4, the density functional theory (DFT) calculated LUMO energy level was -3.15 eV, which matched well with that obtained from cyclic voltammetry measurements (-3.32 eV). Moreover, CN acceptor used a significantly large and planar backbone to suppress the nonradiative transition and enhance thermal stability (T_d up to 497.3 ℃, corresponding to 5% weight loss, Figure S3.5). And two bulky TPA were employed as electron donors on the side chain of CN segment, resulting in enlarged plane-to-plane distance (d_{p-p}) from 3.69 to 4.18 Å in the molecular packing groups (Figure 3.2c).[37] The twisted donor-acceptor-donor (D-A-D) connection pattern caused by steric hindrance mitigated ACQ when TCN functions as a luminescent center in the PersL molecular system.[38] We obtained nearly unchanged photoluminescence (PL) lifetimes of TCN in toluene and in neat film, which were 15.53 and 15.77 ns, respectively (Figure S3.6). Only a 6.1% decrease in quantum efficiency was observed in atmosphere from TCN in its monodispersed state to its aggregated state (25.6% in toluene, and 19.5% in neat film). Furthermore, the highest occupied molecular orbital (HOMO) and LUMO of TCN are predominantly localized on electron donor and acceptor segments, respectively (Figure 3.2b). Thereby, TCN molecule exhibited a small energy gap (ΔE_{ST}) of ~0.03 eV between the lowest excited singlet (670 nm) and triplet (680 nm) states (Figure S3.7a). The intensity of the delayed fluorescent emission increased with the temperature variation from 77 to 300 K, confirming the TADF feature (Figure S3.7b).[39]

This characteristic enabled for relatively high exciton harvesting capability when the trapped charge carriers were released and recombined with the luminescent center.
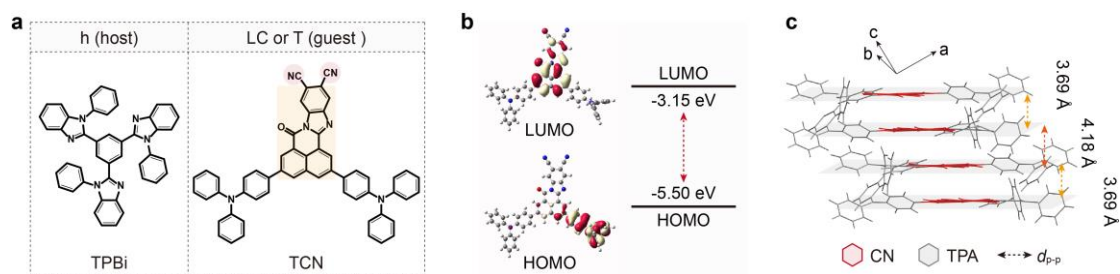
Figure 3.2 Molecular design of TCN guest. **a**, Chemical structure of TPBi as the host molecule (left) and TCN as the guest molecule (right). **b**, Theoretical calculated HOMO, LUMO, and frontier orbital distributions with optimized ground state structures of TCN. **c**, Molecular packing mode of TCN.

To ensure full excitation of the sample, a 5-minutes excitation time was chosen (Figure S3.8). First, a guest/host ratio of 1 wt% was optimized for the TCN doped into electron transporting molecule 1,3,5-tris(1-phenyl-1*H*- benzimidazol-2-yl)benzene (TPBi) based on PersL decay measurements (Figure S3.9). Thanks to its resistance to ACQ effect, the TCN@TPBi film exhibited RT PersL durations reaching up to hour-level across doping concentrations ranging from 0.1 to 5 wt% after cessation of 365 nm UV lamp irradiation. As shown in Figure 3.3a, the intense absorption bands around 260-450 nm can be attributed to the localized π-π* transitions of the conjugated skeletons, while the moderate absorption bands over 450 nm are due to intramolecular and intermolecular charge transfer transitions, with peaks at 480 nm for TCN in toluene and 520 nm for TCN in neat film.[40, 41] A redshift (from ~615 to 670 nm) was also observed in the PL spectra of TCN from monomer state to and aggregate state. The TCN@TPBi melt-cast film exhibited a broad emission centered at ~640 nm under excitation of 365 nm. By comparing the PL and phosphorescence spectra of TPBi, the emission deviated

from the emission of TCN molecules, which was ascribed to the synergistic effect of TCN molecular aggregation and TPBi polarization (Figure S3.10). Notably, the melt-casting method was crucial for forming TCN aggregates in TPBi even at a low doping ratio (1 wt%), broadening the cut-off wavelength of the intermolecular charge transfer absorption to around 630 nm. The PersL excitation spectra of the TCN@TPBi were acquired by measuring the luminescence intensity at 30 s after ceasing the monochromatic excitation light (whose wavelength was switched from 650 to 425 nm with a step of 5 nm) (Figure 3.3b). The long-lasting luminescence excitation spectra covered almost the entire visible light region, consistent with the trend of the absorption spectrum. As shown in Figure 3.3c and Figure S3.11, the time resolved PersL spectra could be detected for over 5 h after continuous excitation for 5 min. The emission spectra taken at 1 minute after excitation, with a peak at 640 nm, are consistent with the PL spectra. Moreover, as shown in Figure 3.3d, the X-ray absorption spectra of host and guest molecules were simulated using the photon cross-section database (TPBi, $Z_{max} = 7$, $K_\alpha = 0.392$ keV; TCN, $Z_{max} = 8$, $K_\alpha = 0.525$ keV).[42] By using X-ray as the excitation source, the PersL could be detected by a photomultiplier tube (PMT) detector for over 10 min before the photon signals attenuated to the noise level (Figure 3.3e). In brief, UV light, visible light, and X-rays are efficient excitation sources for triggering charge separation from the luminescent center to the trap state.

In PersL materials, thermoluminescence (TL) intensity is recorded during the subsequent heating process after charging at a certain temperature. As expected, after 10 minutes of natural decay at room temperature, the emission intensity of the TCN@TPBi film increased rapidly by factors of 1.5, 30.6, and 118.0 when the temperature was raised to 300 K, 350 K, and 400 K, respectively (Figure 3.3f). This increase aligns well with the thermodynamic model of thermal activation of charge carriers from traps.[33] The intensity-wavelength-temperature (3D-plot) TL diagrams of the TCN@TPBi film after UV irradiation was collected. As shown in Figure 2g, a broad band from 275 to 400 K with a peak temperature (T_m) at 387 K was observed, indicating

that the long-lasting emission is due to charge carriers released from traps under thermal stimulation. Due to the TADF property, the TL spectra shifted from dominant phosphorescence at 665 nm to fluorescence emission at 640 nm as the temperature increased from 100 to 400 K, confirming that the emission throughout the thermal stimulation originated from the same luminescent center (Figure S3.12). Furthermore, additional experiments were conducted to explore the effect of NIR (980 nm) photo-stimulation on the emission decay (Figure 3.3h). After natural decay for 5 minutes at RT, the emission intensity was enhanced by 90.1 times with a faster decay rate when NIR light was projected onto the TCN@TPBi film. Moreover, the intensity could be periodically regulated by pulsing the NIR light on and off every 30 s. Therefore, we conclude that the PersL is due to the recombination of charge carriers released from the trap state by thermal or optical stimulation.
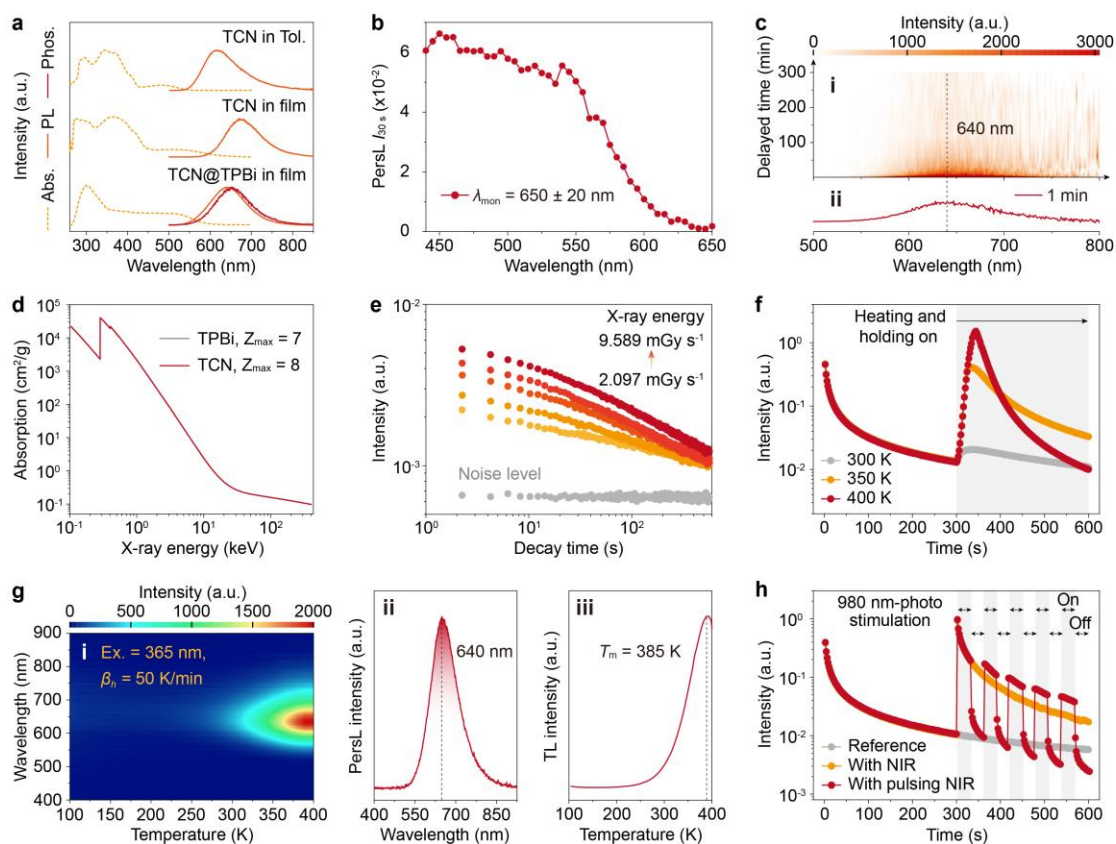
Figure 3.3 Excitation and stimulation properties of 1 wt% TCN@TPBi host-guest

molecular system. a, Absorption and PL spectra (λ_{ex} = 365 nm) of TCN in toluene (1×10^{-5} mol L^{-1}), TCN in neat-film, TCN@TPBi in melt-casting film. **b**, PersL excitation spectra at RT. The sample was charged with monochromatic light with a power density of ~37.5 mW/cm^2 for 1 min in advance for each excitation wavelength. The PersL intensity at 30 s after ceasing the excitation source (I_{30s}, λ_{mon} = 650±20 nm) was recorded and plotted with the excitation wavelength. The excitation wavelength was switched from 700 to 430 nm with a step of 5 nm and an interval time of 1 min was set between two tests. **c**, Intensity-time-wavelength diagram (3D plot) of PersL (i, decay time from 1 min to 5 h) and 1 min PersL spectra (ii) at RT after ceasing UV irradiation (λ_{ex} = 365 nm, t_{ex} = 5 min). **d**, X-ray absorption spectra of TPBi and TCN measured as a function of X-ray energy. The attenuation coefficient was obtained from the photon cross-section database. **e**, Log-log plot of PersL decay curves at RT under different energy of X-ray irradiation (2.098, 4.406, 6.715, 7.928, and 9.589 mGy s^{-1}). The TCN@TPBi was charged by X-ray for 300 s, and the PersL intensity was continuously monitored for 10 min. The grey curve shows the noise level of the PMT detector. **f**, PersL decay curves under different thermal simulation conditions. The excited TCN@TPBi phosphor was initially kept at RT for 5 min, and then heated to 300, 350, and 400 K with a heating rate of 50 K/min. **g**, Intensity-wavelength-temperature diagram (3D plot) of TL (i). The film was charged by light at 365 nm prior to the TL tests. The heating rate was fixed at 50 K/min. The TL spectrum was monitored at 387 K (ii), and the TL glow curve was monitored at 640 nm (iii). **h**, PersL decay curves with 980 nm NIR photo-stimulation in a continuous output mode, NIR photo-stimulation in a pulsed mode (repeating on and off every 30 s), and without NIR photo-stimulation.

In a further set of experiments, the trap depth ε, defined as the activation energy required for the charge carriers to escape from the traps, was estimated by using the Randall-Wilkins model,[43]

$$\frac{\beta\varepsilon}{k_B \cdot T_m^2} = s \cdot \exp\left(\frac{-\varepsilon}{k_B \cdot T_m}\right) \quad \text{(Equation 3.1)}$$

where β (K/s) is the applied heating rate, k_B is the Boltzmann constant, T_m is obtained from TL glow curves, and s (s^{-1}) is the frequency factor. As expected, the peak temperature T_m shifted to the lower-temperature side with decreasing the heating rate β (Figure 3.4a). The trap depth ε of the TCN@TPBi, derived by plotting $\ln(T_m^2/\beta)$ against $1/(k_B \cdot T_m)$, were 0.71 ± 0.01 eV, 0.71 ± 0.01 eV, 0.72 ± 0.02 eV, 0.72 ± 0.02 eV, and 0.69 ± 0.02 eV after charging with light at 365 nm, 420 nm, 520 nm, 620 nm, and X-ray, respectively (Figure 3.4b and Figures S3.13-3.16). Therefore, irrespective of the excitation source, whether visible light, UV light, or X-ray, the TCN@TPBi could efficiently charge through the same traps, ultimately resulting in deep red PersL emissions. The existence of a deep trap depths impedes the facile recombination of dissociated charge carriers with the luminescent center at ambient conditions, necessitating thermal activation as a potent approach. Importantly, the TCN@TPBi film exhibited high photostability, including under high-power and prolonged UV and X-ray irradiation, providing a solid foundation for accurately determining trap depth (Figures S3.17-3.18). Notably, in comparison to the TL signals from pure TCN or TPBi melt-cast films at a heating rate of 50 K/min, where TCN displayed no TL peak and TPBi exhibited a peak in the shallow trap region around 160 K, the TCN@TPBi film showed a TL peak at ~380 K (Figures S3.19-3.20). This suggested that the deep traps were not exclusively derived from either the host or the guest molecules.

In pursuit of uncovering the nature of NIR stimulation, we measured the difference of absorption (Δabsorption) in the TCN@TPBi before and after light irradiation at 365 nm (Figure 3.4c and Figure S3.21). The recorded positive signals indicated the formation of new metastable radicals of the host or guest, with absorption spanning from 400 nm to 1300 nm (Figures S3.22-3.23). Notbaly, the intensity increase observed in Figure 2h primarily arised from NIR-light-induced electron transitions from trap states to luminescent centers, rather than thermal effects, as thermal accumulation with 5 minutes of optical stimulation is negligible (<1 K, Figure S3.24). This result aligned

well with the femtosecond transient absorption (fs-TA) spectroscopy of the excited-state absorption (ESA) bands in the TCN@TPBi film by using a 365 nm femtosecond laser as the pump source (as shown the visible region in Figure S25, and NIR region in Figures 3.4d-3.4e). In the range of 450-700 nm, the positive ESA signal in TCN@TPBi film can be attributed to the absorption of TPBi radical anions or cations (Figures S3.25-3.26). However, signal variations arose due to the negative ground-state bleaching signals of TCN at 475 nm and 560 nm, alongside the negative stimulated emission signal at 640 nm (Figure S3.27). In the NIR region from 800 to 1300 nm, the ESA signal of TCN@TPBi originated from the superposition of the ESA signals of TPBi and TCN. The main peak of TPBi was ~950 nm (Figure S3.28), while that of TCN is around 1200 nm (Figures 3.4d-3.4e). This overlapping absorption allowed the PersL system to be further excited by NIR light after excitation cessation, thereby facilitating electron escape from the trap state. Notably, weak intermolecular charge transfer between TCN molecules may lead to the formation of radical cations and anions in the guest, but these species had very short lifetimes of only 7 ps (Figure 3.3a, and Figures 3.4d-3.4f). However, once separated carriers are captured, the guest radicals, serving as both trap and luminescent center, became relatively stable with lifetimes extending to 0.82 ns.

The presence of radical cations and radical anions was further confirmed by electron spin resonance (ESR) measurements. As shown in Figure 3.4g, an ESR signal appeared at g-factor around 2.0032 in TCN@TPBi film after UV irradiation, indicating the formation of species containing unpaired electrons.[44] The ESR signal recorded after excitation at 300 K was weaker than that at 110 K, as a greater number of trapped electrons were thermally released at elevated temperatures, thus resulting in a low concentration of radical anions. Notably, the ESR signal was slowly quenched over the initial 10 days but remained nearly unchanged and detectable for additional 45 days at RT, which could be attributed to the deep trap depth in TCN@TPBi film. Furthermore, the orbital configurations and energy levels in the relevant radical anions (TPBi$^{\bullet-}$ and TCN$^{\bullet-}$) were examined by utilizing DFT calculations at B3LYP/def2-SVP level of

theory (Figure 3.4h and Table S3.1). The average energy difference between the LUMO of TPBi$^{\bullet-}$ and TCN$^{\bullet-}$ was ~0.73 eV (including four components of 0.53, 0.66, 0.79, and 0.92 eV when considering two different densities of electrons with spin α and spin β in an open-shell system), showing an energy deviation less than 0.04 ± 0.01 eV (Table S3.2). The energy difference value is in good agreement with the experimental result of trap depth ~0.72 eV by TL analysis, indicating that the electronic transitions between the LUMO of TCN$^{\bullet-}$ are TPBi$^{\bullet-}$ are probably responsible for the charge trapping and detrapping processes in the host-guest system.

Based on the above results, a possible mechanism for the trap-induced PersL in organics is proposed in four steps (see diagram in Figures 3.1a-3.1c and Figure 3.4h):

[i] Excitation:

$$\text{TCN}_{LC} + \text{TPBi} \xrightarrow{UV,VIS,or\ X-ray} \text{TCN}^*_{LC} + \text{TPBi} \quad \text{(Equation 3.2)}$$
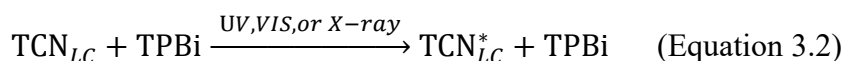
[ii] Charge separation (CS) and Charge trapping:
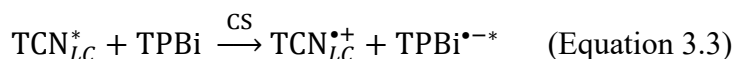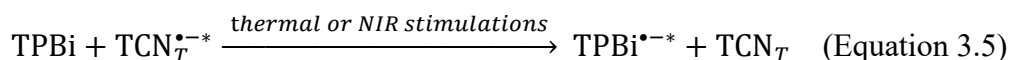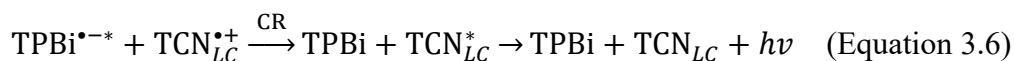
$$\text{TCN}^*_{LC} + \text{TPBi} \xrightarrow{CS} \text{TCN}^{\bullet+}_{LC} + \text{TPBi}^{\bullet-*} \quad \text{(Equation 3.3)}$$

$$\text{TPBi}^{\bullet-*} + \text{TCN}_T \xrightarrow{trapping} \text{TPBi} + \text{TCN}^{\bullet-*}_T \quad \text{(Equation 3.4)}$$

[iii] Charge detrapping:

$$\text{TPBi} + \text{TCN}^{\bullet-*}_T \xrightarrow{thermal\ or\ NIR\ stimulations} \text{TPBi}^{\bullet-*} + \text{TCN}_T \quad \text{(Equation 3.5)}$$

[iv] Charge recombination (CR) and emission:

$$\text{TPBi}^{\bullet-*} + \text{TCN}^{\bullet+}_{LC} \xrightarrow{CR} \text{TPBi} + \text{TCN}^*_{LC} \rightarrow \text{TPBi} + \text{TCN}_{LC} + h\nu \quad \text{(Equation 3.6)}$$

where the asterisk denotes that the active site contains an electron in the LUMO state, and the subscripts LC and T denote that the TCN molecules work as the luminescent center and trapping center, respectively. The proposed mechanism indicates that under UV light, visible-light or X-ray irradiation an electron is excited and separated from the

TCN guest (TCN_{LC}), forming two metastable radical species of $TCN_{LC}^{\bullet+}$ and TPBi$^{\bullet-}$. The excited electron is mobile within the host due to the excellent electron-transporting property of the TPBi, and eventually captured by another TCN molecule (TCN_T). The energy gap between the LUMO level of $pTAP_T^{\bullet-}$ and TPBi$^{\bullet-}$ creates an energy barrier that the electron needs to absorb heating or NIR energy and cross (ε) to recombine with the original luminescent center, resulting in PersL (hv) with distinct thermal activation characteristics.
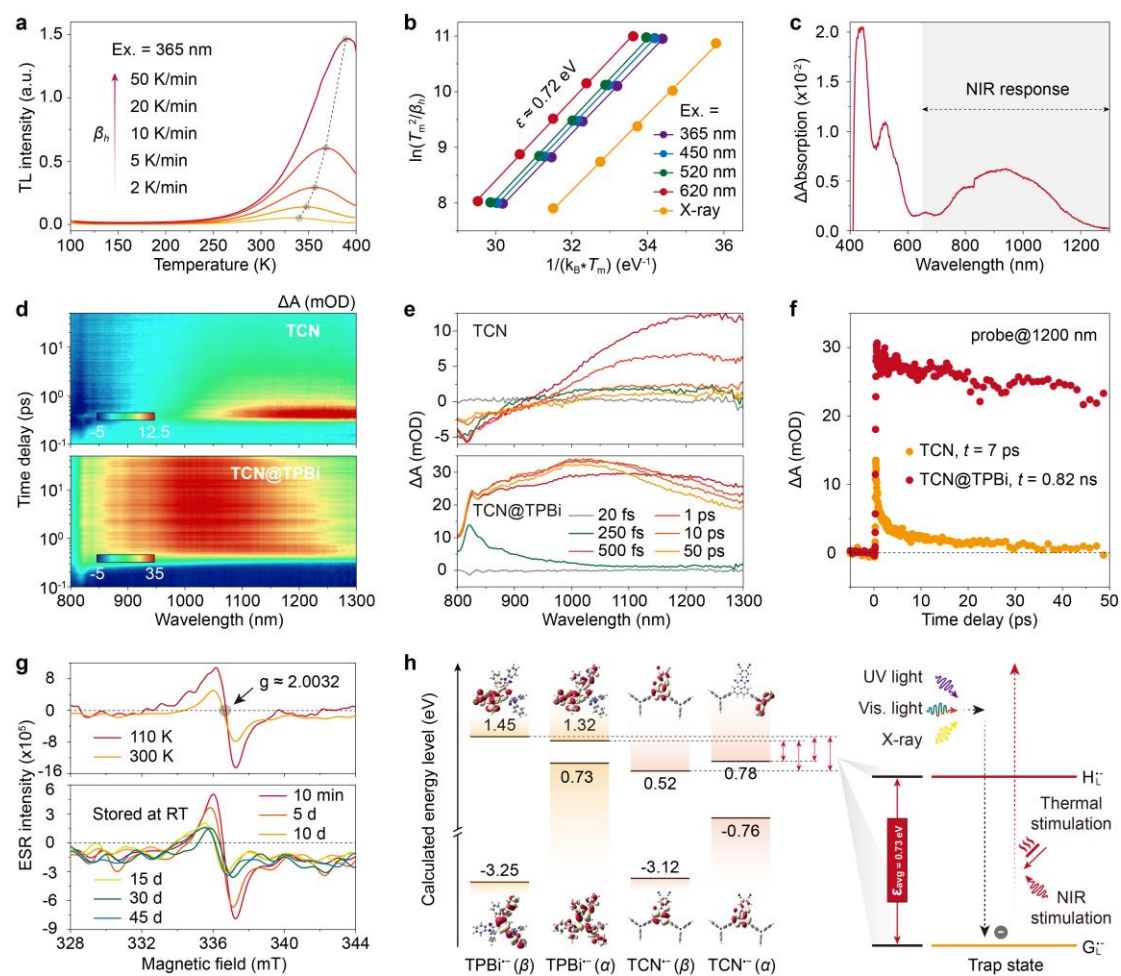
Figure 3.4 Trap profiles for PersL of the TCN@TPBi film. a, TL glow curves with different heating rates from 2, 5, 10, 20, to 50 K/min after charged by light at 365 nm. The charging time was 5 min, and the charging temperature was 100 K. **b**, Estimation of the trap depth using the Randall-Wilkins model by charging the sample at UV light

(365 nm), visible light (450, 520, and 620 nm), and X-ray (9.589 mGy s^{-1}). **c**, Self-absorption spectra obtained by the differences in absorptions of TCN@TPBi after and before the 365 nm excitation. **d**, Pseudo-color transient absorption plot of the TCN@TPBi with 365 nm pump source. **e**, Transient absorption spectra at different delay times from 20 fs to 50 Ps. **f**, Decay dynamics of transient absorption at different wavelengths. **g**, ESR spectra recorded after UV irradiation at 110 and 300 K (top) and after 365 nm excitation at different storage time (bottom, from 10 minutes to 45 days). **h**, Schematics of the orbital configurations of TPBi$^{\bullet-}$ and TCN$^{\bullet-}$ by obtained using DFT calculations at the B3LYP/def2-SVP level of theory. The energy levels of the HOMO and LUMO are labeled in the diagram. There are two different densities of electrons with spins α and spin β in an open-shell system. The energy differences (ε, red double arrow) between the LUMO levels of TPBi$^{\bullet-}$ and TCN$^{\bullet-}$. The charge -trapping (detrapping) process corresponds to an electronic transition from TPBi$^{\bullet-}$ to TCN$^{\bullet-}$ (and vice versa).

Leveraging the proposed TADF guest molecular configuration, we have designed deep-trap organic phosphors stable at RT ($\varepsilon = 0.72$ eV, $T_m = 385$ K at 50 K/min heating rate), significantly advancing the development of multi-modal integrated information storage and retrieval applications. First, as shown in Figures 3.5a-3.5c, we applied a blue laser direct-writing method to record information in PersL film ("Information Storage" text and world map). The luminescence intensity that is a read-out process of the stored optical information exhibited a natural decay at RT for over 1 h, followed by an information reproduction at higher temperature. Besides, we used X-ray irradiation to store information for items obscured by leather or enclosed in a black box onto the TCN@TPBi sample (Figures 3.5d-3.5e). Similarly, after a period of attenuation for several seconds, the information from the items can still be easily reproduced by heating, greatly expanding the application potential of organic materials in the field of X-ray time-lapse imaging. As another example, we utilized a UV lamp to store energy across

the entire film and NIR stimulation to read specific information, employing methods such as templating or laser pen writing (Figures 3.5g-3.5i). This reading process can be reproduced by heating the unread sections. The developed organic deep-trap phosphors offer diverse excitation and stimulation methods, allowing the switching of information storage and retrieval modes based on practical applications.
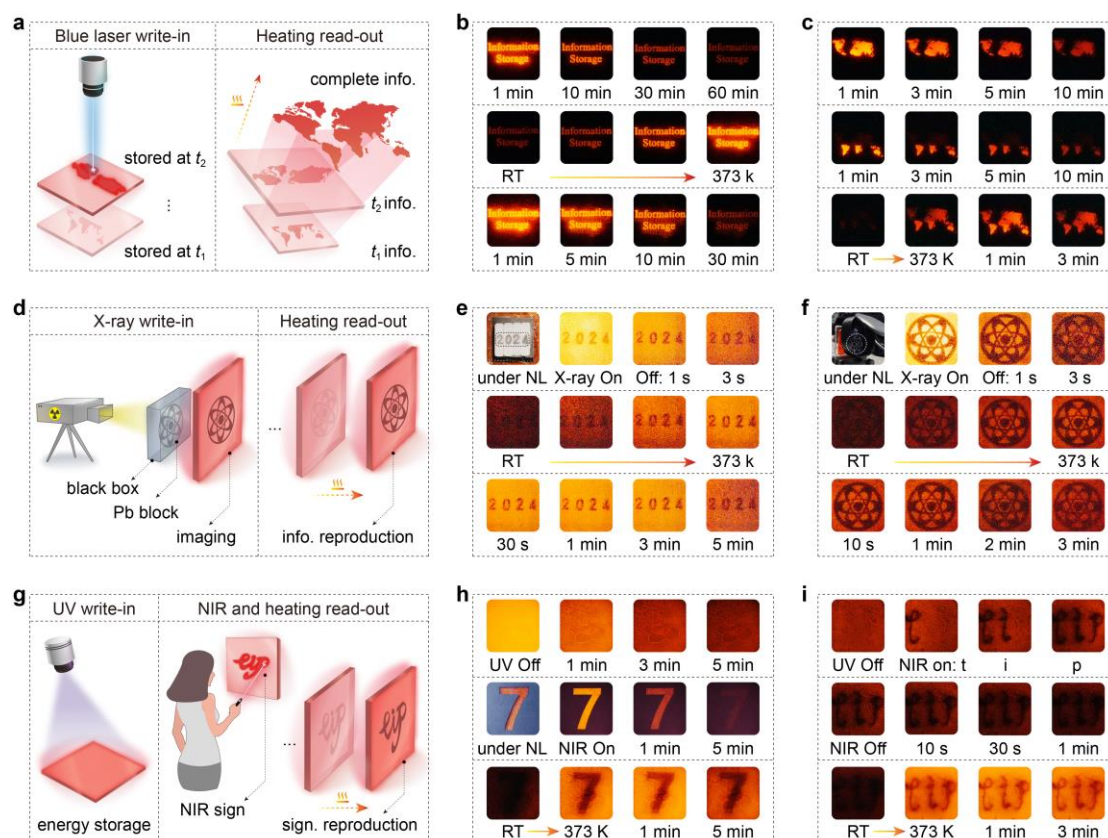
Figure 3.5 Multi-modal integrated optical information storage application. a-c, Blue-laser write-in and heating read-out information storage application. The northern and southern halves of the world map were written into the TCN@TPBi film in two interval time. After natural decay at RT, the recorded whole world map could be simultaneously retrieved by heating the sample to 373 K (**a**). The information storage and retrieval of the corresponding single information ("Information Storage" text, **b**) and double information (northern and southern parts of the world map, **c**). **d-f**, X-ray write-in and heating read-out information storage application. The lead (Pb) block in

the black box formed an image on the TCN@TPBi film and stored optical energy through X-ray irradiation. After natural decay at RT, the imaging information could be reproduced through heating the sample to 373 K (**c**). The X-ray imaging, information storage, and reproduction of digital information through leather and plastic (**e**), and the image information in the black box (**f**). **g-i**, UV write-in and NIR/heating read-out information storage application. After energy storage by UV light, the part of stored information in TCN@TPBi film was completely released using a NIR laser pointer. Following natural decay at RT, the information read by NIR could be reproduced through heating, such as an electronic signature (**g**). The NIR stimulated information reading and reproduction through template method (digit "7", **h**) and sign method ("tip" letters, **i**). Abbreviations: natural light (NL), information (info.), and signature (sign.).

3.5 Conclusion

In conclusion, we propose a molecular design principle utilizing planar CN as strong electron acceptors to ensure TCN@TPBi PersL film possess deep trap depth up to 0.72 eV, alongside employing a D-A-D wedge-shaped molecular configuration to enhance exciton utilization and minimize ACQ in TADF luminescent centers. The trap depth remains unaffected by the type of excitation source, including UV, visible light, and X-ray. Analysis through Δabsorption spectra, fs-TA spectra, ESR spectra, TL growing curves, and TD-DFT calculations revealed that the depth is primarily governed by the LUMO energy difference between the radical anions of host and guest molecules. Remarkably, TIP in a typical TCN@TPBi film lasted for more than 5 hours and stored additional energy for over 45 days at RT. Importantly, the multi-mode optical information storage and retrieval capability of this PersL media extended its application scope to include blue-laser direct writing, X-ray time-lapse imaging, and NIR electronic signatures.

3.6 Reference

[1] M. Gu, Q. Zhang, S. Lamon, *Nat. Rev. Mater.* **2016**, 1*,* 16070.

[2] M. Gu, X. Li, Y. Cao, *Light Sci. Appl.* **2014**, 3, e177.

[3] Y. Liu, Y. Lu, X. Yang, X. Zheng, S. Wen, F. Wang, X. Vidal, J. Zhao, D. Liu, Z. Zhou, C. Ma, J. Zhou, J. A. Piper, P. Xi, D. Jin, *Nature* **2017**, 543, 229-233.

[4] J. F. Heanue, M. C. Bashaw, L. Hesselink, *Science* **1994**, 265, 749-752.

[5] B. H. Cumpston, S. P. Ananthavel, S. Barlow, D. L. Dyer, J. E. Ehrlich, L. L. Erskine, A. A. Heikal, S. M. Kuebler, I. Y. S. Lee, D. McCord-Maughon, J. Qin, H. Röckel, M. Rumi, X.-L. Wu, S. R. Marder, J. W. Perry, *Nature* **1999**, 398, 51-54.

[6] C. Zhang, H. P. Zhou, L. Y. Liao, W. Feng, W. Sun, Z. X. Li, C. H. Xu, C. J. Fang, L. D. Sun, Y. W. Zhang, C. H. Yan, *Adv. Mater.* **2010**, 22, 633-637.

[7] D. L. Kallepalli, A. M. Alshehri, D. T. Marquez, L. Andrzejewski, J. C. Scaiano, R. Bhardwaj, *Sci. Rep.* **2016**, 6, 26163.

[8] H. H. Pham, I. Gourevich, J. K. Oh, J. E. N. Jonkman, E. Kumacheva, *Adv. Mater.* **2004**, 16, 516-520.

[9] E. Heydari, J. R. Sperling, S. L. Neale, A. W. Clark, *Adv. Funct. Mater.* **2017**, 27, 1701866.

[10] O. Wilson, G. J. Wilson, P. Mulvaney, *Adv. Mater.* **2002**, *14*, 1000-1004.

[11] X. Li, Y. Cao, M. Gu, *Opt. Lett.* **2011**, 36, 2510-2512.

[12] N. Bozinovic, Y. Yue, Y. Ren, M. Tur, P. Kristensen, H. Huang, A. E. Willner, S. Ramachandran, *Science* **2013**, 340, 1545-1548.

[13] H. Ren, X. Li, Q. Zhang, M. Gu, *Science* **2016**, 352, 805-809.

[14] Y. Lu, J. Zhao, R. Zhang, Y. Liu, D. Liu, E. M. Goldys, X. Yang, P. Xi, A. Sunna, J. Lu, Y. Shi, R. C. Leif, Y. Huo, J. Shen, J. A. Piper, J. P. Robinson, D. Jin, *Nat. Photon.*

2013, 8, 32-36.

[15] H. Sun, S. Liu, W. Lin, K. Y. Zhang, W. Lv, X. Huang, F. Huo, H. Yang, G. Jenkins, Q. Zhao, W. Huang, *Nat. Commun.* **2014**, 5, 3601.

[16] J. Xu, S. Tanabe, *J. Lumin.* **2019**, *205*, 581-620.

[17] L. Liang, J. Chen, K. Shao, X. Qin, Z. Pan, X. Liu, *Nat. Mater.* **2023**, 22, 289-304.

[18] Y. Li, M. Gecevicius, J. Qiu, *Chem. Soc. Rev.* **2016**, 45, 2090-2136.

[19] Y. Zhuang, L. Wang, Y. Lv, T.-L. Zhou, R.-J. Xie, *Adv. Funct. Mater.* **2018**, 28, 1705769.

[20] X. Ou, X. Qin, B. Huang, J. Zan, Q. Wu, Z. Hong, L. Xie, H. Bian, Z. Yi, X. Chen, Y. Wu, X. Song, J. Li, Q. Chen, H. Yang, X. Liu, *Nature* **2021**, 590, 410-415.

[21] Z. Pan, Y. Y. Lu, F. Liu, *Nat. Mater.* **2011**, 11, 58-63.

[22] X. Zhou, K. Han, Y. Wang, J. Jin, S. Jiang, Q. Zhang, Z. Xia, *Adv. Mater.* **2023**, 35, 2212022.

[23] Z. Hu, J. Guan, S. Zheng, Z. Chai, S. Wu, D. Liu, J. Su, F. Shi, C. Duan, Y. Wang, K. Xia, *Laser Photon. Rev.* **2024**, 2301024.

[24] Y. Zhuang, D. Chen, W. Chen, W. Zhang, X. Su, R. Deng, Z. An, H. Chen, R.-J. Xie, *Light Sci. Appl.* **2021**, 10, 132.

[25] R. Kabe, C. Adachi, *Nature* **2017**, 550, 384-387.

[26] Z. An, C. Zheng, Y. Tao, R. Chen, H. Shi, T. Chen, Z. Wang, H. Li, R. Deng, X. Liu, W. Huang, *Nat. Mater.* **2015**, 14, 685-690.

[27] L. Zhou, J. Song, Z. He, Y. Liu, P. Jiang, T. Li, X. Ma, *Angew. Chem. Int. Ed*. **2024**, e202403773.

[28] H. Deng, G. Li, H. Xie, Z. Yang, Z. Mao, J. Zhao, Z. Yang, Y. Zhang, Z. Chi, *Angew. Chem. Int. Ed*. **2024**, 63, e202317631.

[29] H. Lv, H. Tang, Y. Cai, T. Wu, D. Peng, Y. Yao, X. Xu, *Angew. Chem. Int. Ed*. **2022**, 61, e202204209.

[30] Q. S. Zhang, S. C. Wang, X. H. Xiong, P. Y. Fu, X. D. Zhang, Y. N. Fan, M. Pan, *Angew. Chem. Int. Ed*. **2022**, 61, e202205556.

[31] W. Zhao, Z. He, B. Z. Tang, *Nat. Rev. Mater.* **2020**, 5, 869-885.

[32] R. Gao, M. S. Kodaimati, D. Yan, *Chem. Soc. Rev.* **2021**, 50, 5564-5589.

[33] C. Lin, Z. Wu, H. Ma, J. Liu, S. You, A. Lv, W. Ye, J. Xu, H. Shi, B. Zha, W. Huang, Z. An, Y. Zhuang, R.-J. Xie, *Nat. Photon.* **2024**, 18, 350-356.

[34] C. Lin, Z. Wu, J. Ueda, R. Yang, S. You, A. Lv, W. Deng, Q. Du, R. Li, Z. An, J. Xue, Y. Zhuang, R.-J. Xie, *Adv. Mater.* **2024**, e2401000.

[35] H. Uoyama, K. Goushi, K. Shizu, H. Nomura, C. Adachi, *Nature* **2012**, 492, 234-238.

[36] Y. Im, M. Kim, Y. J. Cho, J.-A. Seo, K. S. Yook, J. Y. Lee, *Chem. Mater.* **2017**, 29, 1946-1963.

[37] J. X. Chen, W. W. Tao, W. C. Chen, Y. F. Xiao, K. Wang, C. Cao, J. Yu, S. Li, F. X. Geng, C. Adachi, C. S. Lee, X. H. Zhang, *Angew. Chem. Int. Ed*. **2019**, 58, 14660-14665.

[38] Y. Yuan, Y. Hu, Y.-X. Zhang, J.-D. Lin, Y.-K. Wang, Z.-Q. Jiang, L.-S. Liao, S.-T. Lee, *Adv. Funct. Mater.* **2017**, 27, 1700986.

[39] S. Wang, X. Yan, Z. Cheng, H. Zhang, Y. Liu, Y. Wang, *Angew. Chem. Int. Ed*. **2015**, 54, 13068-13072.

[40] J. Xue, Q. Liang, R. Wang, J. Hou, W. Li, Q. Peng, Z. Shuai, J. Qiao, *Adv. Mater.* **2019**, 31, 1808242.

[41] J. Xue, J. Xu, J. Ren, Q. Liang, Q. Ou, R. Wang, Z. Shuai, J. Qiao, *Sci. China Chem.* **2021**, 64, 1786-1795.

[42] X. Wang, H. Shi, H. Ma, W. Ye, L. Song, J. Zan, X. Yao, X. Ou, G. Yang, Z. Zhao, M. Singh, C. Lin, H. Wang, W. Jia, Q. Wang, J. Zhi, C. Dong, X. Jiang, Y. Tang, X. Xie, Y. Yang, J. Wang, Q. Chen, Y. Wang, H. Yang, G. Zhang, Z. An, X. Liu, W. Huang, *Nat. Photon.* **2021**, 15, 187-192.

[43] A. J. J. Bos, *Materials* **2017**, 10, 1357.

[44] Y. Wang, W. Zhu, W. Du, X. Liu, X. Zhang, H. Dong, W. Hu, *Angew. Chem. Int. Ed*. **2018**, 57, 3963-3967.

3.7 Supporting Information
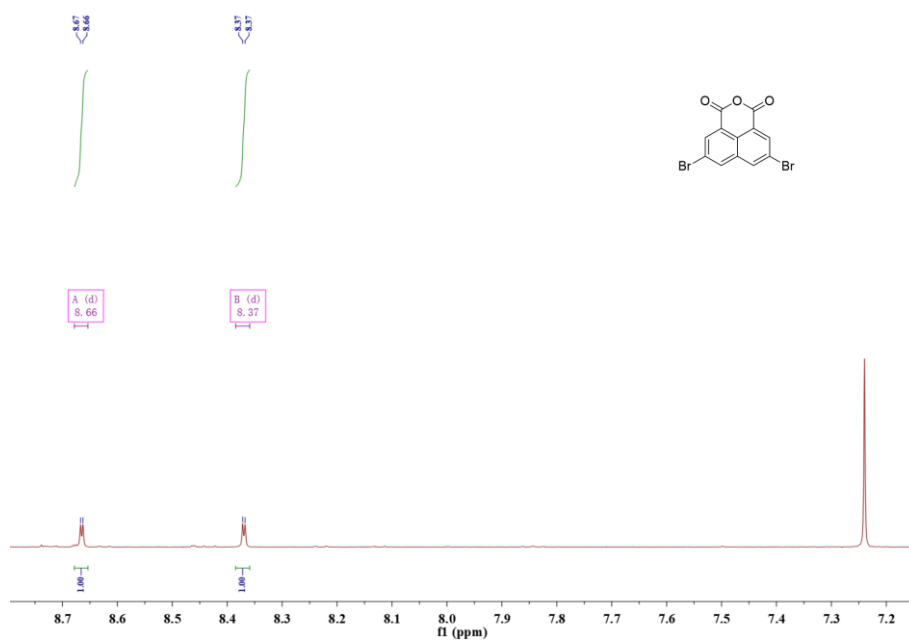
Figure S3.1 ^{1}H-NMR spectra of S[1].
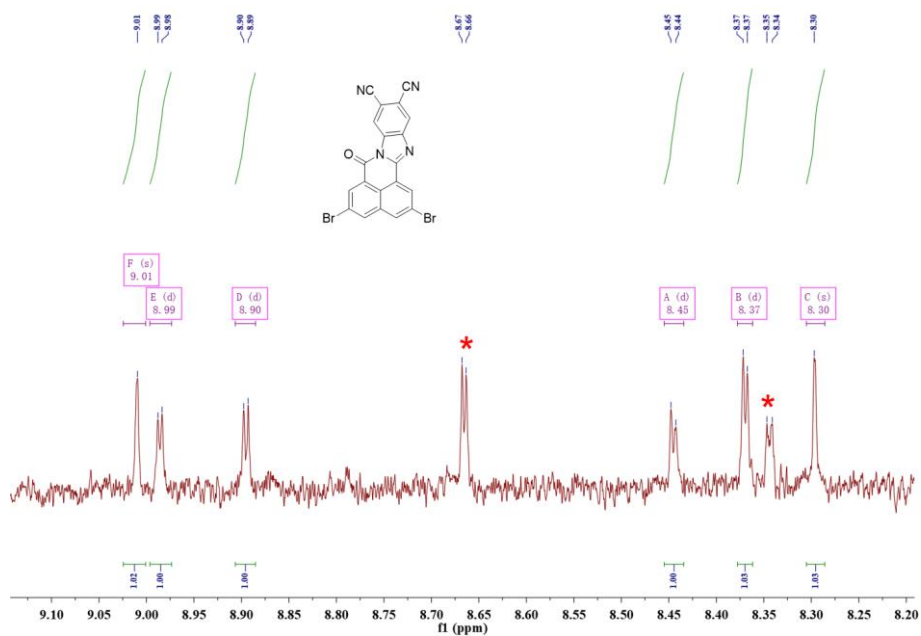
Figure 3.2 ^{1}H-NMR spectra of CN. The solubility of CN is extremely low, resulting in low intensity of ^{1}H-NMR. By comparing the ^{1}H-NMR spectrum of S[1], it can be

determined that the main impurity belongs to S_1 (marked with *).
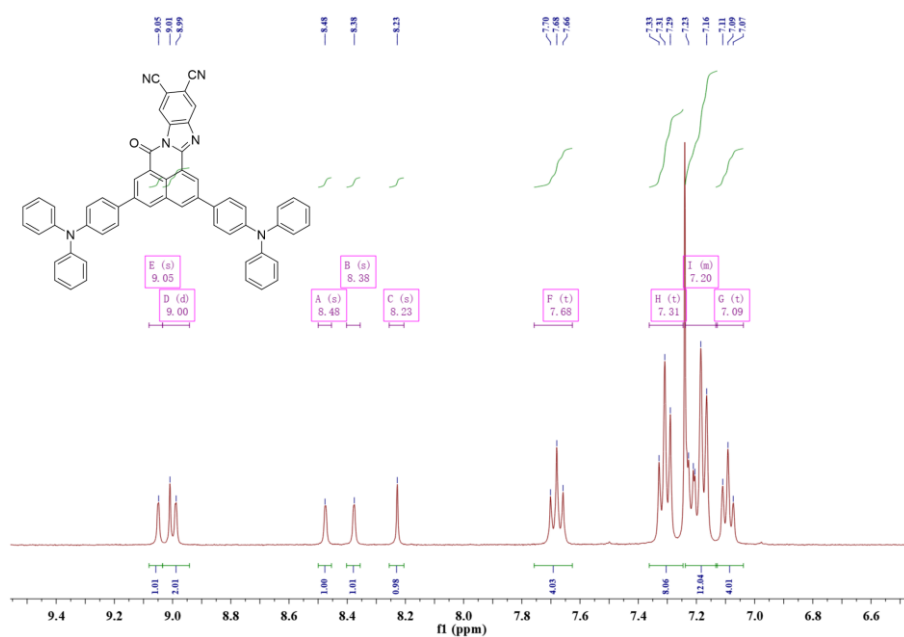
Figure S3.3 ^{1}H-NMR spectra of TCN.
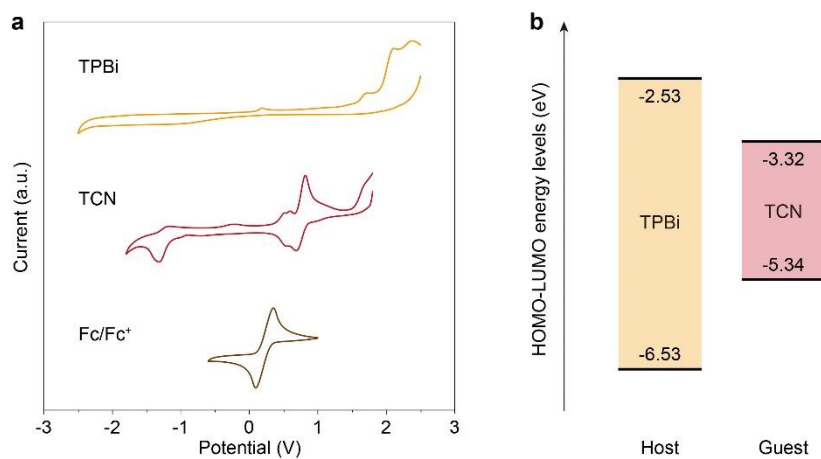
Figure S3.4 Cyclic voltammograms of TCN recorded versus Fc/Fc$^+$ at 298 K under a N$_2$ atmosphere.
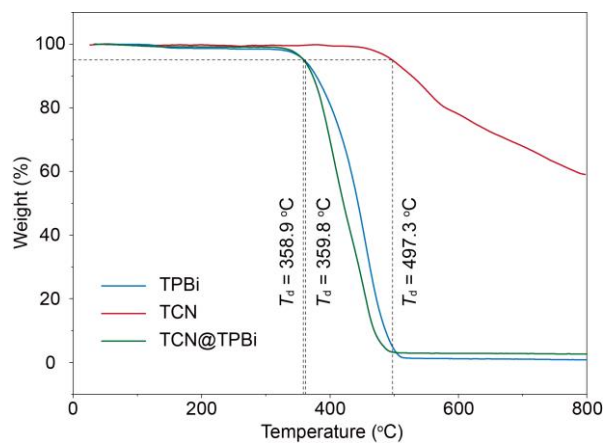
Figure S3.5 Thermogravimetric analysis (TGA) of TCN, TPBi, and 1 wt% TCN@TPBi phosphors.
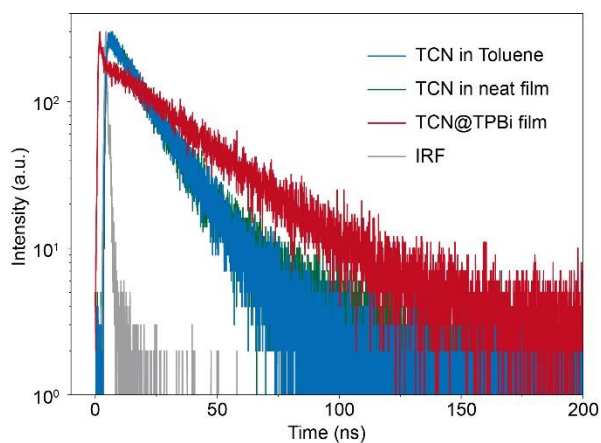
Figure S3.6 Prompt fluorescence decay curves of TCN in toluene, in neat film and doped at TPBi melt-cast film.
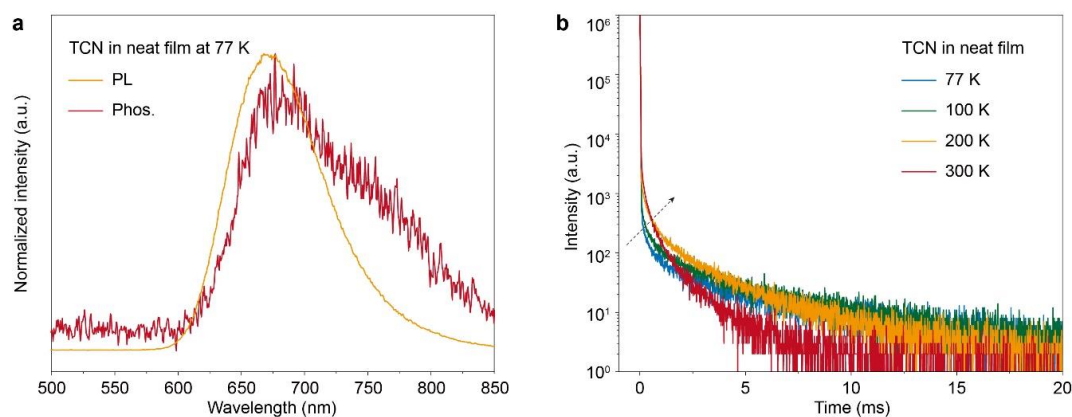
Figure S3.7 a, Normalized photoluminescence and phosphorescence spectra at 77 K of a TCN neat film. **b**, Phosphorescence decay curves of the emission at 640 nm in the temperature range from 77 to 300 K.

As shown in Figure S3.7a, the energy difference between the S_1 or T_1 state and the S_0 state in TCN was ~1.85 (ΔE_{S1-S0}) and 1.82 eV (ΔE_{T1-S0}), respectively, which was estimated according to the peak wavelength of the photoluminescence and phosphorescence spectra of the TCN neat film. Thus, the energy gap between the singlet and triplet states (ΔE_{ST}) should be ~0.03 eV. The TADF lifetime measured 4.66 ms at 77 K. As the temperature increased from 77 K to 300 K, the TADF emission intensity gradually rose, suggesting enhanced lowest excited triplet state (T_1) to lowest excited singlet state (S_1) up-conversion with rising temperature (Figure S3.7b).
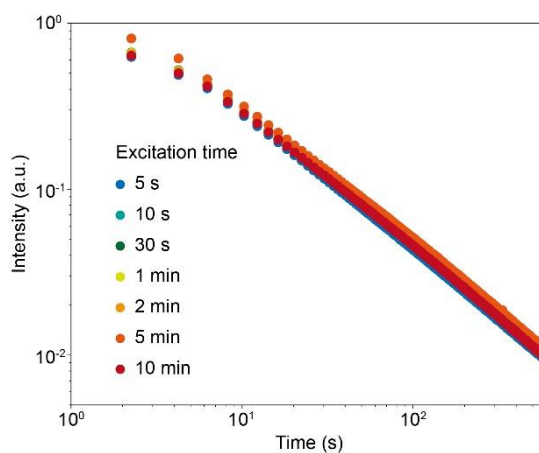
Figure S3.8 PersL decay profiles of TCN@TPBi with different excitation time (excitation temperature and recoding temperature = RT, excitation wavelength = 365 nm).
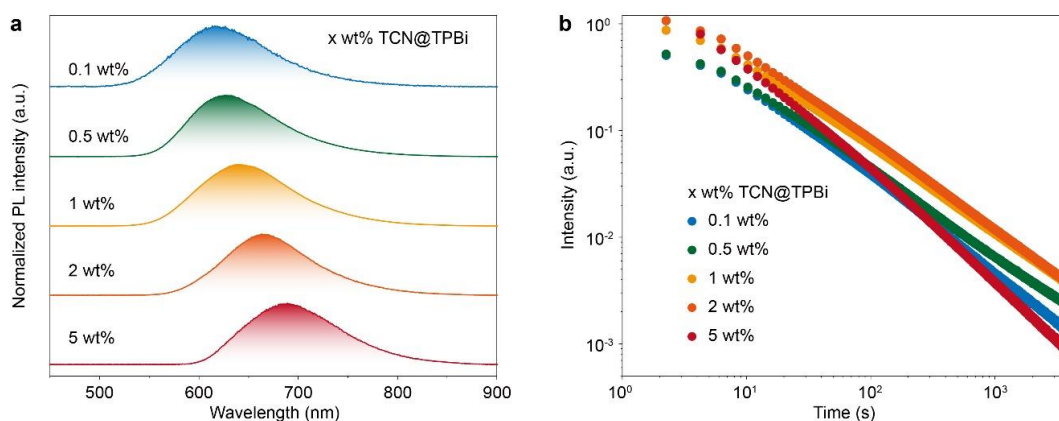
Figure S3.9 a, Fluorescence spectra of x wt% (x = 0.1, 0.5, 1, 2, and 5 wt%) TCN@TPBi with different doping concentration (excitation wavelength = 365 nm). **b**, PersL decay profiles of x wt% TCN@TPBi with different doping concentrations of TCN (excitation temperature and recoding temperature = RT, excitation wavelength = 365 nm, excitation time = 300 s).
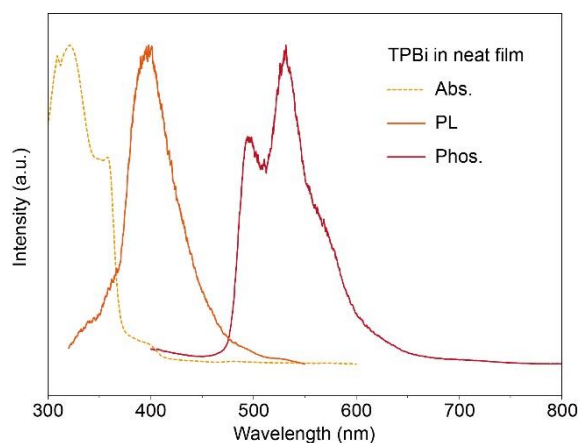
Figure S3.10 Ultraviolet-visible absorption (Abs.), photoluminescence (PL, λ_{ex} = 300 nm, at 77 K), and phosphorescence (Phos., λ_{ex} = 365 nm, delayed time 8 ms, at 77 K) spectra of TPBi in a neat film.
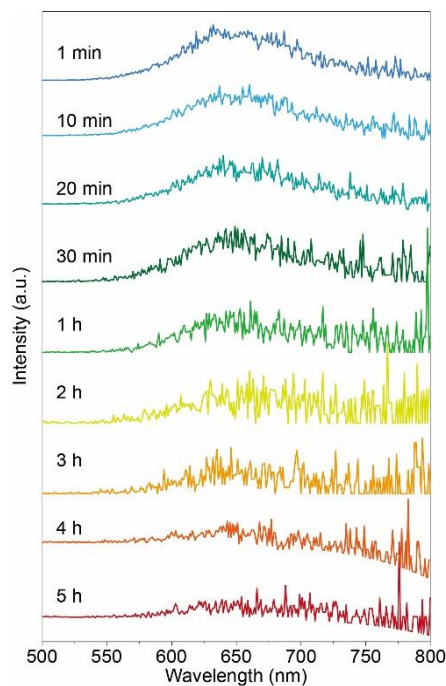
Figure S3.11 Time-resolved emission spectra of the TCN@TPBi film recorded at 1 min, 10 min, 20 min, 30 min, 1 h, 2 h, 3 h, 4 h, and 5 h after ceasing the UV excitation light (redraw from Fig. 2c).
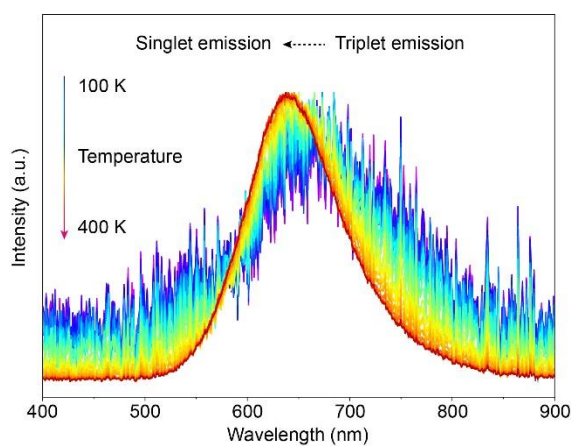
Figure S3.12 Normalized emission spectra at different temperature extracted from the contour mapping of TL with a heating rate of 50 K/min (redraw from Fig. 2g).
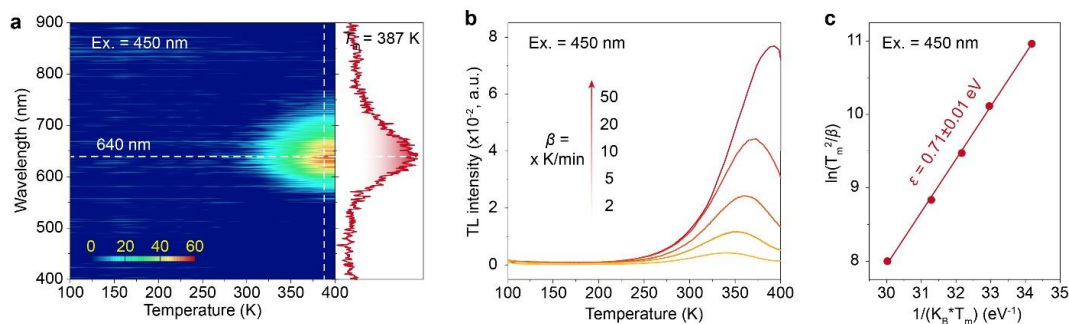
Figure S3.13 TL feature of the 1 wt% TCN@TPBi film after blue light (450 nm) charging. a, Intensity-wavelength-temperature TL glow graph (3D-plot) with a heating rate of 50 K/min. PersL spectra (right part) are obtained from the 3D-plot. **b**, TL glow curves with different heating rates from 2, 5, 10, 20 to 50 K/min (excitation time 5 min, excitation temperature 100 K, scanning range 100 to 400 K). **c**, Estimation of the trap depth by using the Randall-Wilkins model.
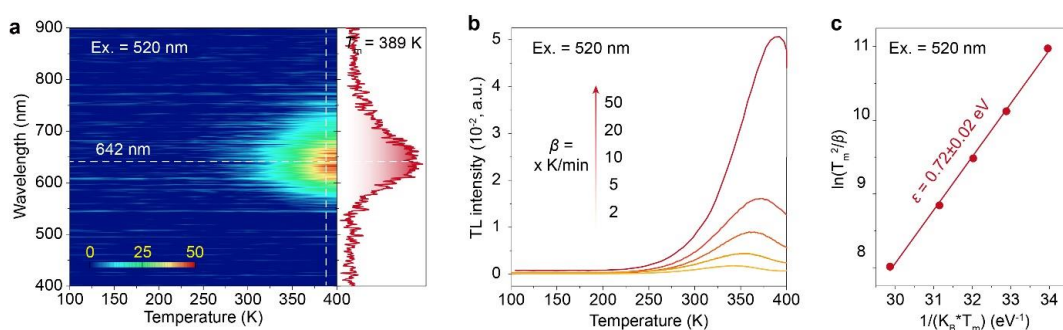
Figure S3.14 TL feature of the 1 wt% TCN@TPBi film after green light (520 nm) charging. a, Intensity-wavelength-temperature TL glow graph (3D-plot) with a heating rate of 50 K/min. PersL spectra (right part) are obtained from the 3D-plot. **b**, TL glow curves with different heating rates from 2, 5, 10, 20 to 50 K/min (excitation time 5 min, excitation temperature 100 K, scanning range 100 to 400 K). **c**, Estimation of the trap depth by using the Randall-Wilkins model.
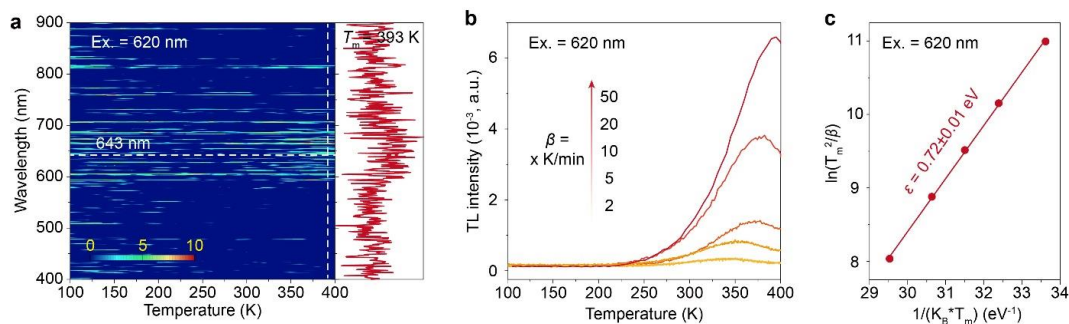
Figure S3.15 TL feature of the 1 wt% TCN@TPBi film after red light (620 nm) charging. a, Intensity-wavelength-temperature TL glow graph (3D-plot) with a heating rate of 50 K/min. PersL spectra (right part) are obtained from the 3D-plot. **b**, TL glow curves with different heating rates from 2, 5, 10, 20 to 50 K/min (excitation time 5 min, excitation temperature 100 K, scanning range 100 to 400 K). **c**, Estimation of the trap depth by using the Randall-Wilkins model.
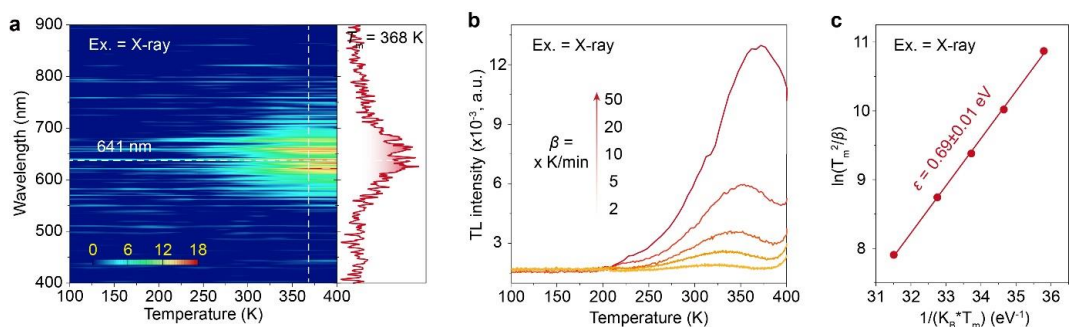
Figure S3.16 TL feature of the 1 wt% TCN@TPBi film after X-ray charging. a, Intensity-wavelength-temperature TL glow graph (3D-plot) with a heating rate of 50 K/min. PersL spectra (right part) are obtained from the 3D-plot. **b**, TL glow curves with different heating rates from 2, 5, 10, 20 to 50 K/min (excitation time 5 min, excitation temperature 100 K, scanning range 100 to 400 K). **c**, Estimation of the trap depth by using the Randall-Wilkins model.
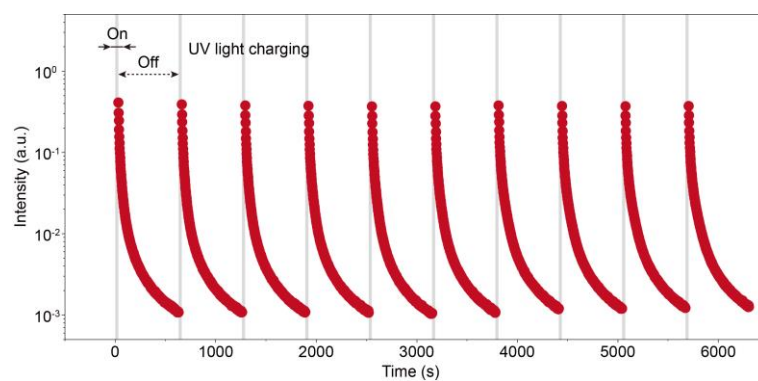
Figure S3.17 PersL decay curves of the TCN@TPBi film under intermittent UV charging (temperature, RT; charging time, 30 s; recording time, 10 min in 1 cycle).
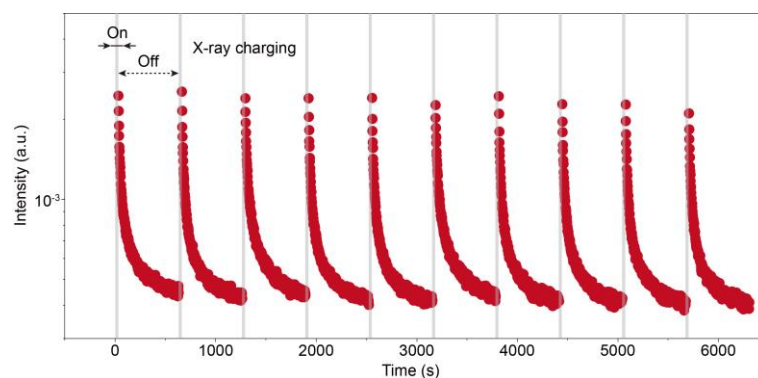
Figure S3.18 PersL decay curves of the TCN@TPBi film under intermittent X-ray charging (temperature, RT; charging time, 30 s; recording time, 10 min in 1 cycle).
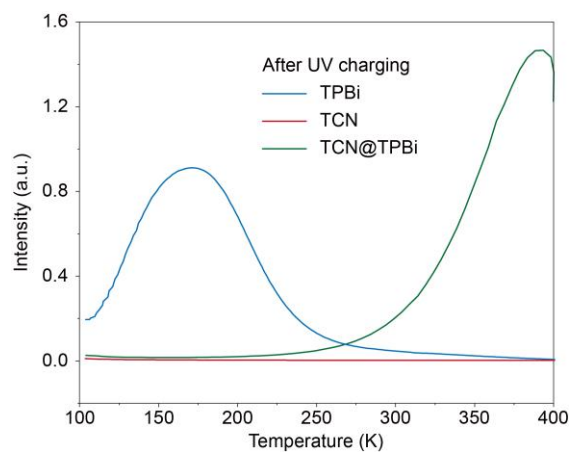
Figure S3.19 TL feature comparison of pure TCN, pure TPBi, and 1 wt% TCN@TPBi

film after UV light charging.
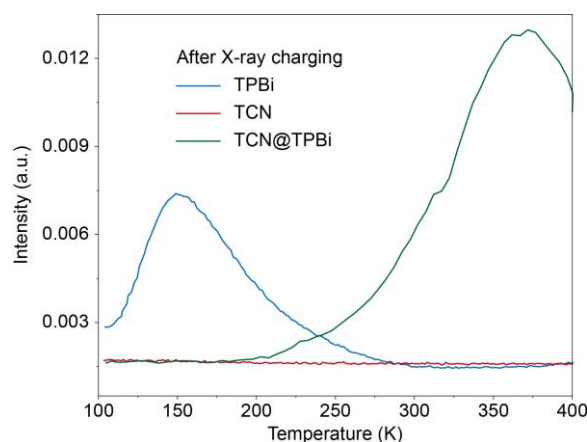
Figure S3.20 TL feature comparison of pure TCN, pure TPBi, and 1 wt% TCN@TPBi film after X-ray charging.
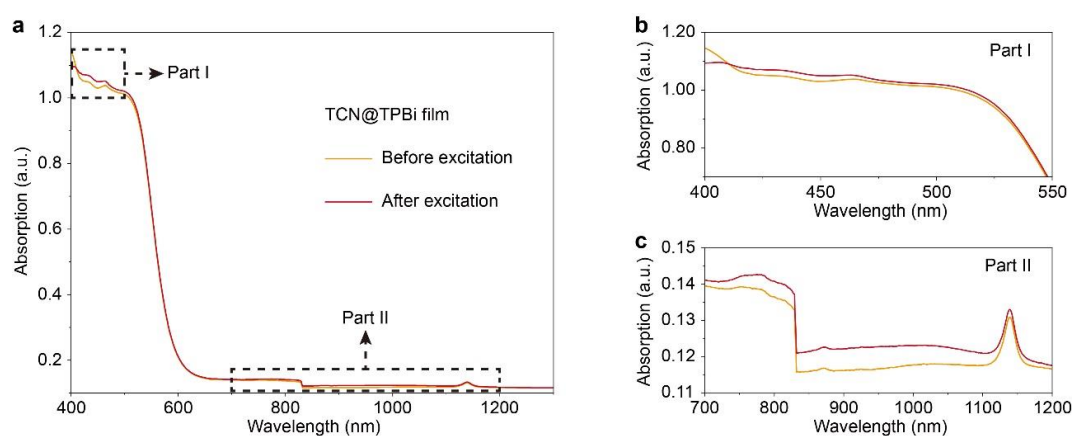
Figure S3.21 a, Absorption spectra of TCN@TPBi film after and before 365 nm excitation. **b**, Enlarged view with absorption wavelength of 400-550 nm. **c**, Enlarged view with absorption wavelength of 700-1200 nm. The sample before excitation was wrapped with the tinfoil and placed in a dark environment for 24 h (redraw from Fig. 3c).
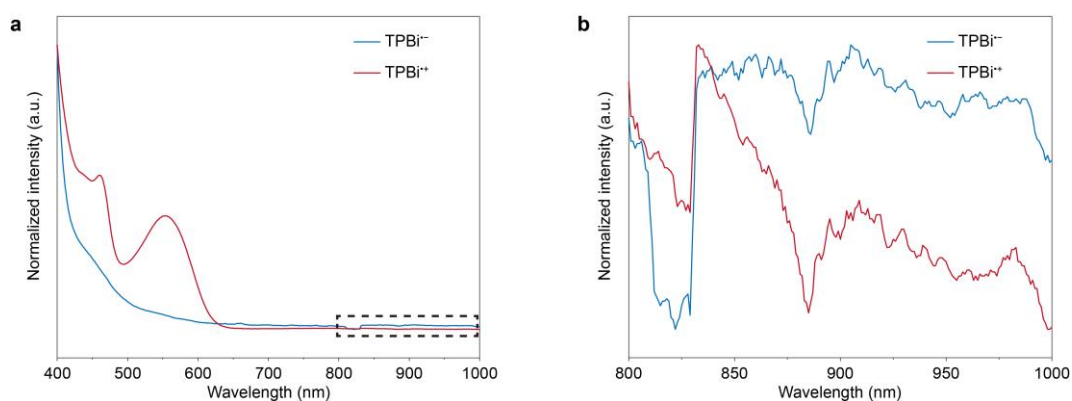
Figure S3.22 The normalized absorption spectra of TPBi radical cation (TPBi$^{\bullet+}$) and TPBi radical anions (TPBi$^{\bullet-}$) in dichloromethane (**a**) in the range of 400-1000 nm and (**b**) in the range of 800-1000 nm.[3]
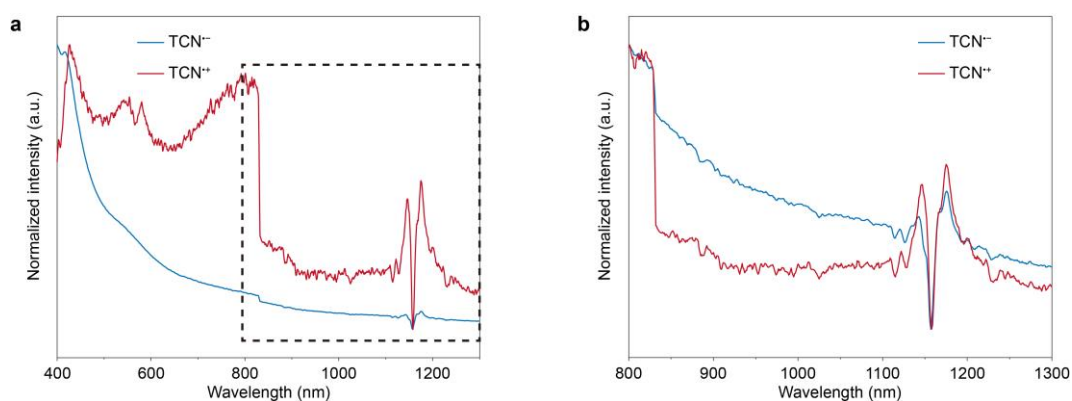
Figure S3.23 The normalized absorption spectra of TCN radical cation (TCN$^{\bullet+}$) and TCN radical anions (TCN$^{\bullet-}$) in dichloromethane (**a**) in the range of 400-1300 nm and (**b**) in the range of 800-1300 nm.
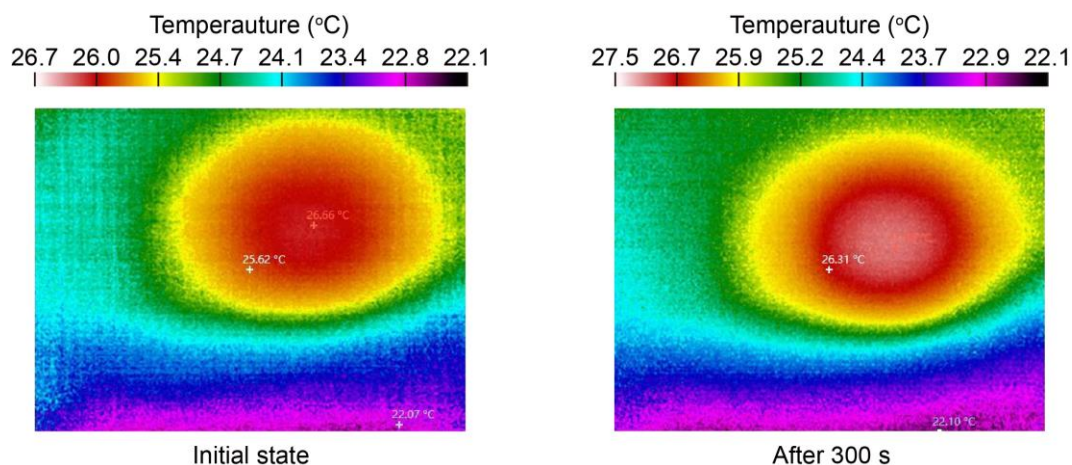
Figure S3.24 Change in temperature distribution from 0 to 300 s when a 980 nm light source was irradiated on TCN@TPBi.
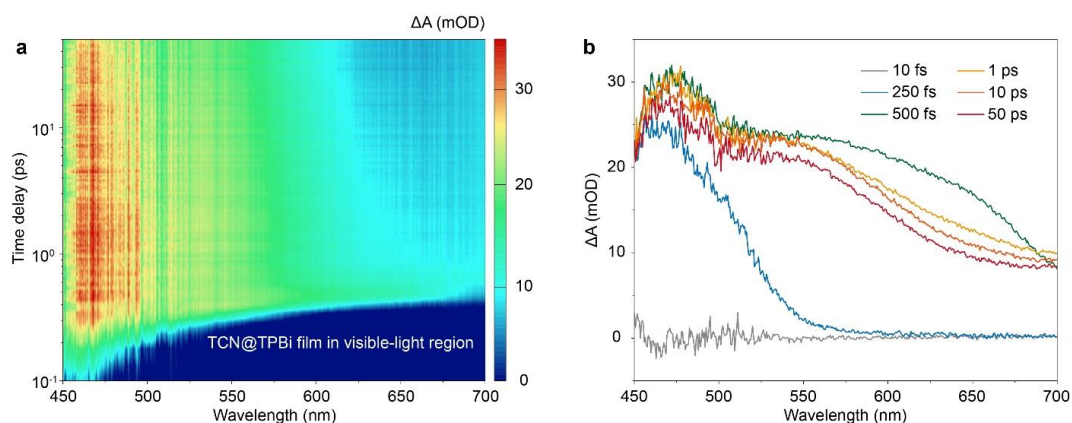
Figure S3.25 TA spectra of the TCN@TPBi film under 365 nm pump laser excitation. a, Pseudo-color TA plot. **b**, TA spectra with a delay time from 10 fs to 50 ps.
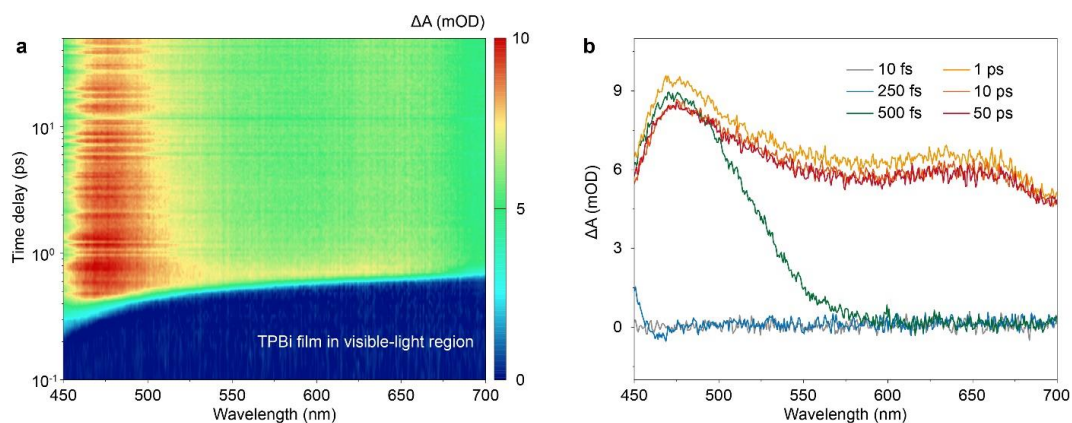
Figure S3.26 TA spectra of the TPBi film under 365 nm pump laser excitation. a,
Pseudo-color TA plot. **b**, TA spectra with a delay time from 10 fs to 50 ps.
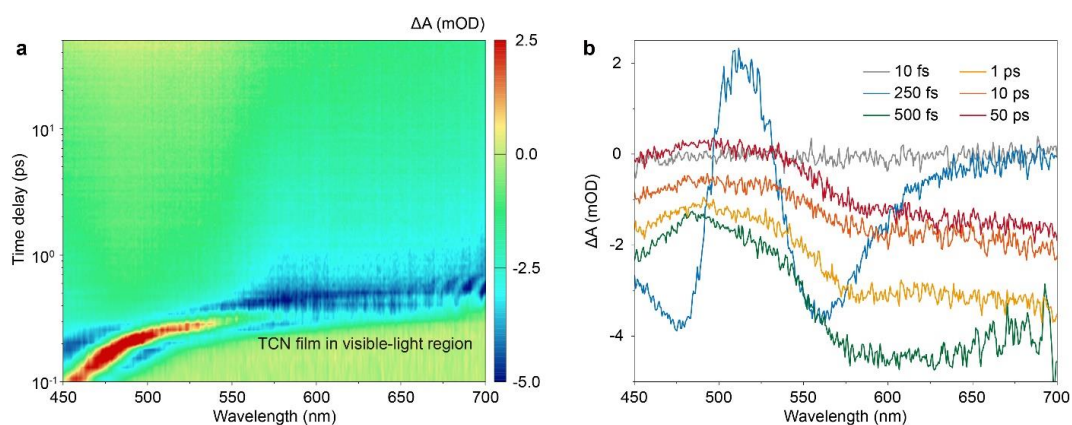
Figure S3.27 TA spectra of the TCN film under 365 nm pump laser excitation. a,
Pseudo-color TA plot. **b**, TA spectra with a delay time from 10 fs to 50 ps.
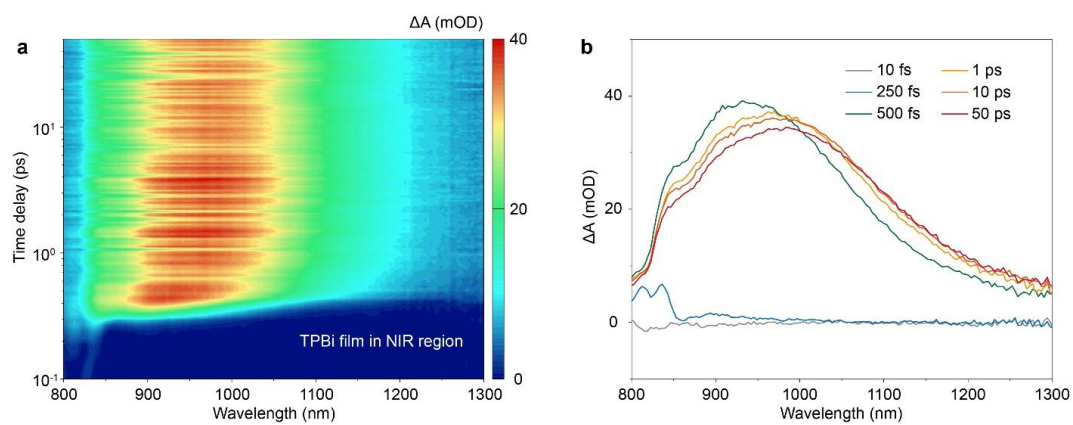
Figure S3.28 TA spectra of the TPBi film under 365 nm pump laser excitation. a, Pseudo-color TA plot. **b**, TA spectra with a delay time from 10 fs to 50 ps.

Table S3.1 Schematic diagrams showing the chemical structure and TD-DFT-calculated energy levels and main orbital configurations of TPBi and TCN molecules and that of radical cations and anions.
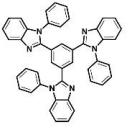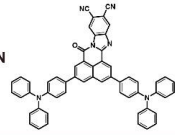
Name	Structure	Calculated LUMO and HOMO distribution (eV)				
		Molecule	Radical cation (α)	Radical cation (β)	Radical anion (α)	Radical anion (β)
TPBi		-1.89 / -6.02	-4.00 / -8.86	-8.10 / -8.42	1.32 / 0.73	1.45 / -3.25
TCN		-3.15 / -5.50	-5.07 / -8.57	-8.17 / -8.37	0.78 / -0.76	0.52 / -3.12

Table S3.2 Summaries of trap depth in TCN@TPBi film.

Guest@TPBi	Ex. (nm)	$\varepsilon_{cal.}$ (eV)[a]				A$\varepsilon_{cal.}$ (eV)[b]	ε_{MV} (eV)[c]	$\Delta\varepsilon$ (eV)[d]
		$\alpha_H - \beta_G$	$\alpha_H - \alpha_G$	$\beta_H - \alpha_G$	$\beta_H - \beta_G$			
TCN@TPBi	365						1.15 ± 0.01	0.15 ± 0.01
	450						1.17 ± 0.03	0.13 ± 0.03
	520	0.79	0.53	0.66	0.92	0.73	1.16 ± 0.01	0.14 ± 0.01
	620						1.15 ± 0.01	0.15 ± 0.01
	X-ray						1.15 ± 0.01	0.15 ± 0.01

[a] Calculated trap depth from the D-value between the LUMO of TPBi host radical anion and that of TCN guest radical anion at the B3LYP/def2-SVP level of theory.

[b] Average calculated trap depth.

[c] Measured trap depth value from plotting $\ln(T_m^2/\beta_h)$ against $1/(k_B \cdot T_m)$ under TL

measurement using the Randall-Wilkins model.

[d] Difference in of $\varepsilon_{cal.}$ and ε_{MV}.

Chapter 4

Enabling Visible-Light-Charged Near-Infrared Persistent Luminescence in Organics by Intermolecular Charge Transfer

4.1 Abstract

Visible light is a versatile and user-friendly excitation source; however, leveraging it to achieve persistent luminescence (PersL) in materials remains a significant challenge. Here, the concept of intermolecular charge transfer (xCT) is applied to a typical host-guest molecular system, significantly reducing the energy requirements for charge separation. This enables efficient charging of near-infrared (NIR) PersL in organics using visible light (425-700 nm). Notably, the NIR PersL in organics is achieved by trapping electrons from charge transfer aggregates (CTAs) into trap states with depths ranging from 0.63 to 1.17 eV. These trapped electrons are then released through thermal stimulation, resulting in a unique light-storage effect and PersL lasting up to 4.6 hours at room temperature. By tuning the xCT absorption range through varying the electron-donating ability of a series of acenaphtho[1,2-b]pyrazine-8,9-dicarbonitrile-based CTAs, the organic PersL emission was adjusted from 681 to 722 nm. This study on NIR PersL induced by xCT interactions in organic materials represents a significant step toward understanding the underlying luminescence mechanisms of organic

semiconductors. These findings are expected to advance their applications in optoelectronics, energy storage, and medical diagnostics.

4.2 Introduction

The discovery of luminescence with lifetimes that are orders of magnitude longer than those of traditional fluorescence has led to several important breakthroughs in luminescence theory and has driven an enormous revolution in lighting, bioimaging, and information technologies over the past few decades.[1-5] Specifically, long-lasting near-infrared (NIR) luminescence has found promising applications in next-generation bioimaging and advanced anti-counterfeiting owing to its deep tissue penetration, high signal-to-noise ratio, and excellent anti-interference performance.[6-11] To date, the best luminescence performances (in terms of duration and afterglow brightness) have mainly been observed in inorganic compounds, including $SrAl_2O_4:Eu^{2+}/Dy^{3+}$, $ZnGa_2O_4:Cr^{3+}$, and $NaYF_4:Tb^{3+}$, which are attributed to persistent luminescence (PersL) using traps to capture and release charge carriers.[12-18] In contrast, the long-lasting luminescence reported in organics is mostly based on spin-forbidden transitions in the molecular orbitals (*i.e.,* room-temperature phosphorescence [RTP]) or thermally activated delayed fluorescence (TADF) *via* triplet states.[19-23] Consequently, it is extremely difficult to achieve luminescence lasting for minutes or even longer in organics based on classical theoretical models, despite the attractive advantages of low toxicity, excellent biocompatibility, and intrinsic flexibility over their inorganic counterparts.[24] It was only recently that hour-level long-lasting luminescence was demonstrated in organic systems, such as exciplexes and cocrystals, based on charge separation.[25-28] These exciting findings will undoubtedly open new avenues for the application of long-lasting organic luminescence in optoelectronics.

Visible light is the main component of common light sources, such as sunlight, white-light-emitting diodes (white LEDs), and xenon-lamp radiation. Nevertheless, long-lasting luminescence in materials is generally stimulated by ultraviolet (UV) light or X-rays because high photonic energies are required to separate the charge carriers from their initial states in wide-bandgap semiconductor compounds. It is highly preferable to use visible-light irradiation instead of UV light or X-rays as it is inherently milder

and safer for human skin, eyes, and tissues.[29,30] However, the use of visible light to charge long-lasting luminescence in materials is currently very challenging.

Herein, to achieve visible-light-charged long-lasting luminescence in organics, the concept of intermolecular charge transfer (xCT) is introduced to host–guest molecular systems to drive charge separation and trapping. Compared to the intramolecular charge transfer (iCT) mechanism in monomers, the xCT interaction occurring in charge-transfer aggregates (CTAs) should reduce the energy of the excited states and, more importantly, weaken the Frenkel exciton binding energy (Figure 4.1a).[31] This eventually leads to a significant redshift in absorption and much lower energy for charge separation when CTAs are doped as luminescent centers.[32,33] Meanwhile, the host–guest system consists of an electron-transporting material as the host and CTA molecules as the guest (Figure 4.1b), which promotes the diffusion and trapping of the separated charge carriers.[34] These charge carriers are subsequently released from the trap states with an adjustable trap depth (ε) by thermal stimulation, and recombine with the CTAs to generate PersL (Figure 4.1c). As a result, we obtained visible-light-charged long-lasting NIR luminescence in organics with an hour-level duration. The chargeable wavelength for the developed materials covers almost the entire visible spectrum (425-700 nm) and is wider than that of inorganic PersL materials.[6,7] A new understanding of the charge separation and trapping processes in organic materials is expected to greatly expand the scope and applications of organic luminescent materials.
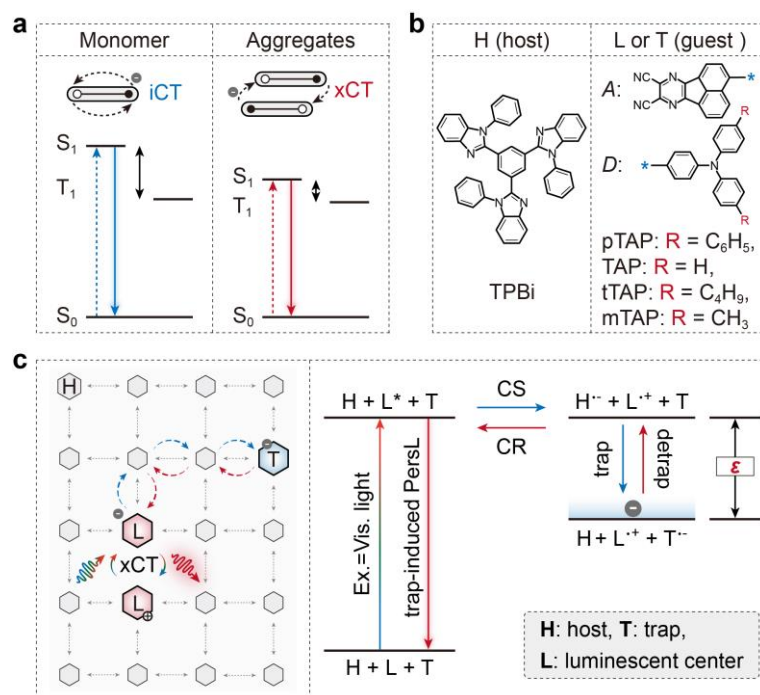
Figure 4.1 PersL based on the xCT process in a host–guest molecular system. a, Schematic of the energy levels of guest monomers (left) and CTAs (right). The energy difference between the excited state (S_1/T_1) and ground state (S_0) is lower in CTAs than the monomers due to the xCT process, which allows for efficient charge separation under light irradiation at a longer wavelength. **b**, Chemical structure of 1,3,5-tris(1-phenyl-1*H*-benzimidazol-2-yl)benzene (TPBi) as the host molecule (left) and AP-based TADF molecules as the guest (right). Four TADF emitters were studied in this work, including 3-(4-(di([1,1'-biphenyl]-4-yl)amino)phenyl)acenaphtho[1,2-*b*]pyrazine-8,9-dicarbonitrile (pTAP, R = C_6H_5), 3-(4-(diphenylamino)phenyl)acenaphtho[1,2-*b*]pyrazine-8,9-dicarbonitrile (TAP, R = H), 3-(4-(bis(4-(*tert*-butyl)phenyl)amino)phenyl)acenaphtho[1,2-*b*]pyrazine-8,9-dicarbonitrile (tTAP, R = C_4H_9), and 3-(4-(di-*p*-tolylamino)phenyl)acenaphtho[1,2-*b*]pyrazine-8,9-dicarbonitrile (mTAP, R = CH_3). **c**, Schematic of the possible PersL mechanism in organics based on xCT interaction. Left: electron migration in a host–guest structural model; right: electron migration described by a proposed energy-level diagram. Briefly, electrons from CTAs can be excited under irradiation with visible light and captured by trap states. The trapped electrons are released under thermal stimulation, recombine with the CTAs,

and finally produce PersL. Abbreviations and labels: ground state (S_0), singlet/triplet excited state (S_1/T_1), host (H, gray hexagon), luminescence center (L, red hexagon), trap (T, blue hexagon), AP-based electron-accepting segment of guest (A), tribenzamine derivative-based electron-donating segments of guest (D), excited state of luminescent center (L^*), radical anion of host ($H^{\bullet-}$), radical cation of luminescence center ($L^{\bullet+}$), radical anion of trap ($T^{\bullet-}$), charge separation (CS), charge recombination (CR), trap depth (ε), and electrons (gray solid balls).

4.3 Experimental Procedure

4.3.1 Materials and Chemicals

1,3,5-Tris(1-phenyl-1*H*-benzimidazol-2-yl)benzene (TPBi) was obtained from Xi'an Polymer Light Technology Corp without additional purification. The pTAP 3-(4-(di([1,1'-biphenyl]-4-yl)amino)phenyl)acenaphtho[1,2-*b*]pyrazine-8,9-dicarbonitrile (pTAP), 3-(4-(diphenylamino)phenyl)acenaphtho[1,2-*b*]pyrazine-8,9-dicarbonitrile (TAP), 3-(4-(bis(4-(*tert*-butyl)phenyl)amino)phenyl)acenaphtho[1,2-*b*]pyrazine-8,9-dicarbonitrile (tTAP) and 3-(4-(di-*p*-tolylamino)phenyl)acenaphtho[1,2-*b*]pyrazine-8,9-dicarbonitrile (mTAP) were synthesized according to reference (*Sci. China Chem.* **2021**, 64, 1786-1795).

4.3.2 Fabrication of TADF@TPBi Films

A mixture of TADF emitters (TAP, mTAP, tTAP, and pTAP) and TPBi (~1 mmol) was heated to 350°C on a quartz substrate inside an anaerobic glovebox. After melting, the mixture was thoroughly stirred and rapidly cooled to RT (25 °C). Finally, the mixture was encapsulated in a quartz glass case with an area of 2×2 cm^2 using an ultraviolet-cured epoxy resin. Melt-cast films were fabricated under a nitrogen atmosphere inside a glovebox. The doping concentration of the TADF emitters was varied as required. We selected pTAP@TPBi and its derivatives as the emitters investigated in this study based on their NIR emission, high PLQY, and xCT-induced long-wavelength absorption, as described above.

4.3.3 Characterization of Photophysical Properties

Emission spectra were collected using a spectrometer (FLS980, Edinburgh and QE-Pro, Ocean Photonics). Absorption spectra were measured using an ultraviolet/visible/near-infrared spectrophotometer (UV-3600Plus, Shimadzu). ESR spectra were obtained using an X-band electron paramagnetic resonance spectrometer (EMX-10/12, Bruker). Photographs and videos of the samples were taken using digital

cameras (Canon EOS 5D Mark II and SONY α7SIII).

4.3.4 Transient Absorption Measurements

Ultrafast femtosecond transient absorption (fs-TA) measurements were conducted under ambient conditions with a femtosecond pump-probe system in addition to an amplified laser system, which consisted of a mode-locked Ti:sapphire seed laser (Spectra Physics, Maitai) directed into a regenerative amplifier (Spitfire Pro, Spectra Physics) and a high-power laser (Empower, Spectra Physics) used for pumping and amplification. The amplified 800 nm output was divided into two parts, and a pump pulse with tunable wavelengths was generated from a major part of the beam (~85%) after an optical parametric amplifier (TOPAS prime, Spectra Physics). A white light continuum probe and reference pulses (400-600 nm) were generated from the remainder of the beam passing through an optical delay line followed by a CaF_2 crystal. The probe beam traveled through the sample, and the reference beam was sent directly to the reference spectrometer. A chopper was used to modulate the pump pulses and alternately obtain the fs-TA spectra with and without the pump pulse. An optical fiber coupled to a multichannel spectrometer with a complementary metal oxide semiconductor sensor was used to record the pump-induced fluctuation in the probe/reference beam intensity while adjusting the optical delay line (maximum of ~3 ns). The spectral profiles were further processed using Surface Xplorer and Glotaran software.

4.3.5 Characterization of PersL and TL in the Organics

The PersL decay curve, PersL spectra, and TL glow curve spectra were recorded using a custom-made measurement system. Briefly, the sample was placed on a cooling-heating stage (THMS600E, Linkam Scientific Instruments) with a controllable temperature range from 100 to 600 K. The sample chamber was filled with dry nitrogen gas, and the top of the chamber was covered with quartz glass. The sample was excited through a quartz glass using UV or visible LEDs for 5 min. The excitation power

densities at 365, 440, 520, and 620 nm were 37.5, 41.3, 21.0, and 16.6 mW/cm^2, respectively. A filtered PMT (R928P, Hamamatsu Photonics), multimeter (2400, Keithley), and high-voltage power supply (HVC1800, Zolix) were used to monitor the PersL intensity (or TL emission, PersL decay curves) after switching off the excitation source. PersL spectra were recorded simultaneously using a multichannel spectrometer (QE-Pro, Ocean Optics) during the TL measurements. For a typical TL measurement, the sample was cooled to 100 K and irradiated with an excitation source for 5 min. After creasing the excitation source for 20 s, the sample was heated to 400 K at a certain heating rate (*i.e.*, 50, 20, 10, 5 and 2 K/min), and the emission intensity was recorded in real time. The above measurement system was driven by LabVIEW-based computer programs. The PersL excitation spectra were obtained by high-energy broadly tunable lasers (NT342, Ekspla) with monochromatic light with a power density of ~37.5 mW/cm^2. The PersL intensity was measured after ceasing the excitation source for 30 s. The excitation wavelength was sequentially changed from 700 to 425 nm with a wavelength increment of 5 nm and a time interval of 5 min between two tests.

4.3.6 Estimation of Trap Depth

The trap depth is estimated, assuming the first order kinetics, by using the following Randall-Wilkins model:

$$\ln\frac{T_m^2}{\beta} = \varepsilon \cdot \frac{1}{k_B T_m} + \ln\frac{\varepsilon}{s k_B} \quad \text{(Equation 4.1)}$$

Here, β (K/s) represents the heating rate, ε (eV) stands for the trap depth, k_B denotes the Boltzmann constant, T_m (K) is the peak temperature derived from the TL glow curves, and s (s^{-1}) corresponds to the frequency factor. The trap depth ε (*i.e.,* the slope of the fitting line) can be determined by plotting $\ln(T_m^2/\beta)$ against $1/(k_B \cdot T_m)$.

4.3.7 Theoretical Calculations of Crystallographic Configuration and Electronic Structures

The equilibrium configuration and the frontier molecular orbitals (HOMO and

LUMO) of the ground states (S_0), as well as the excitation energies of the lowest excited states (S_1), were performed at the (TD)B3LYP/def2-TZVP level implemented in the Gaussian 09 package. Frontier molecular orbitals have open shells and closed shells in their equilibrium geometry. The electronic structures of different configurations (D1, D2 and D3) from crystals for the pTPA dimer were evaluated by using the approach of time-dependent density functional theory (TD-DFT).

4.4 Results and Discussion

To validate the proposed scheme, a series of TADF emitters consisting of a strong electron-drawing acceptor [acenaphtho[1,2-*b*]pyrazine-8,9-dicarbonitrile (AP)] and an electron donor with modifiable groups (-R) were used as guests (see the chemical structures in Figure 4.1b and Table S4.1). This type of TADF emitter is used in organic LEDs and has shown high external quantum efficiency of NIR luminescence.[35] Here, we took a melt-casting film with the composition of pTAP (R = C_6H_5 in Figure 4.1b) doped into TPBi, namely, pTAP@TPBi, to investigate its photophysical properties. According to cyclic voltammetry (CV) measurements, the highest occupied molecular orbital (HOMO) and the lowest unoccupied molecular orbital (LUMO) of pTAP are located inside the energy gap between those of TPBi, which is different from typical exciplex systems with an interlaced energy-level configuration (Figure S4.1).[25-28] The doping concentration of the guest was optimized to 1 wt% according to the long-lasting luminescence spectra and decay curves (Figure S4.2). Compared to the photoluminescence (PL) spectra of TPBi and pTAP, the PL spectra of 1 wt% pTAP@TPBi exhibited a broadband emission centered at 683 nm (Figure 4.2a and Figure S4.3), which is ascribed to the synergistic effect of pTAP molecular aggregation and TPBi polarization. At a delay time of 25 ms, pTAP@TPBi showed RTP with a peak at ~747 nm. Impressively, the NIR long-lasting luminescence peak at ~696 nm was recorded using a spectrometer after ceasing light with excitation wavelength (λ_{ex}) at 365 nm for 30 min (Figure 4.2a). This suggests the existence of a different long-lasting luminescence mechanism other than RTP in pTAP@TPBi.

The excitation spectra of long-lasting luminescence in pTAP@TPBi were acquired by measuring the luminescence intensity after ceasing monochromatic excitation for 30 s (the wavelength was changed from 700 to 425 nm in steps of 5 nm; Figure 4.2b). Notably, the excitation spectra covered almost the entire visible light region, overlapping with the emission spectra of commercial white LEDs. Using blue light (450 nm) as the excitation source, long-lasting luminescence was detected by a

photomultiplier tube (PMT) detector for ~4.6 h before the photon signal attenuated to the noise level (Figure 4.2c). The effectiveness of other visible light sources (monochromatic light at 520 and 620 nm or light from white LEDs) in generating PersL is further demonstrated in Figures S4.4 and S4.5.

In this study, thermoluminescence (TL) was used to reveal the mechanism of the observed long-lasting luminescence.[36] In general, after charging with visible light at a certain temperature, the TL intensity is recorded during the subsequent heating process.[2] As shown in Figures 4.2d and 4.2e, the TL glow bands indicate that the hour-level long-lasting luminescence in pTAP@TPBi is a type of trap-induced PersL with typical characteristics of thermally stimulated luminescence. Specifically, the 3D intensity-wavelength-temperature TL plots show a TL glow band ranging from 250 to 400 K (with a peak at ~375 K) after charging at 365 or 620 nm (Figure 4.2d). The two TL spectra extracted from the 3D-plot diagrams present nearly identical peaks at ~695 nm, suggesting that the same luminescent center is involved in charge recombination (Figure 4.2d, right). Furthermore, the trap depth ε, defined as the activation energy required for the charge carriers to escape from the traps, was estimated using the following Randall-Wilkins model,[37]

$$\frac{\beta\varepsilon}{k_B \cdot T_m^2} = s \cdot \exp\left(\frac{-\varepsilon}{k_B \cdot T_m}\right) \qquad \text{(Equation 4.2)}$$

where β (K/s) is the applied heating rate, k_B is Boltzmann's constant, T_m (K) is the peak temperature obtained from TL glow curves, and s (s^{-1}) is the frequency factor. As expected, T_m shifts to lower temperatures with decreasing β (Figure 4.2e). The ε of pTAP@TPBi, derived by plotting $\ln(T_m^2/\beta)$ against $1/(k_B \cdot T_m)$, is 1.15 ± 0.01, 1.17 ± 0.03, and 1.16 ± 0.01 eV after charging with 365, 420 and 620 nm irradiation, respectively (Figure 4.2f and Figure S4.6). Therefore, regardless of whether visible light (from blue to red light) or UV light is used as the excitation source, pTAP@TPBi is efficiently charged through the same traps and finally generates NIR PersL.
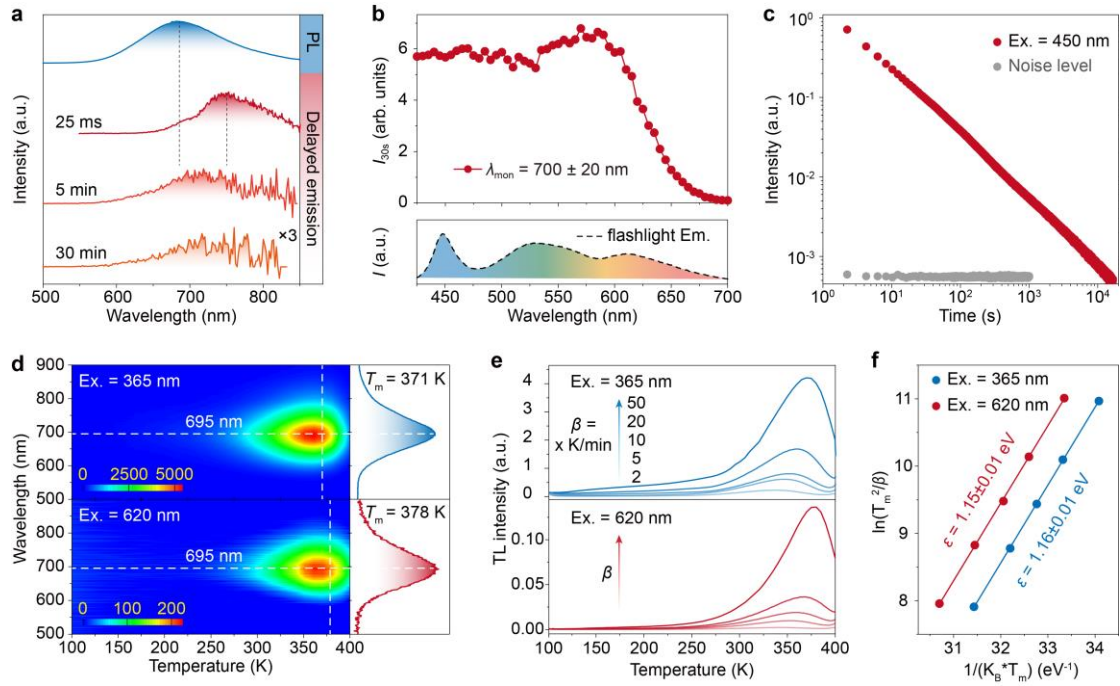
Figure 4.2 Photophysical properties of a 1 wt% pTAP@TPBi melt-casting film. a, PL (λ_{ex} = 365 nm, steady-state excitation), RTP (λ_{ex} = 365 nm, delay time of 25 ms), and PersL spectra (λ_{ex} = 365 nm, delay times of 5 and 30 min) of the pTAP@TPBi film. **b**, PersL excitation spectra (top). The sample was charged with monochromatic light with a power density of ~37.5 mW/cm^2 for 1 min in advance for each excitation wavelength. The PersL intensity at 30 s after ceasing the excitation source (I_{30s}, λ_{mon} = 700 ± 20 nm) was recorded and plotted with λ_{ex}. The λ_{ex} was switched from 700 to 425 nm with a step of 5 nm, and an interval time of 5 min was set between the two tests. The emission spectrum of a white LED is given at the bottom for comparison. **c**, Log–log plot of PersL decay curves. The pTAP@TPBi was charged by 450 nm blue light for 300 s, and the PersL intensity was continuously monitored for 6 h. The gray curve shows the noise level of the PMT detector. The measurements giving the results in **a-c** were performed at RT. **d**, 3D intensity-wavelength-temperature TL plot. The film was charged by light at 365 nm (top) and 620 nm (bottom) before the TL tests. The heating rate was fixed at 50 K/min. Right: TL spectra extracted from the 3D plot, which shows nearly identical spectra after charging at 365 and 620 nm. **e**, TL glow curves with different heating rates (2, 5, 10, 20, or 50 K/min) after charging with light at 365 nm

(top) and 620 nm (bottom) for 5 min. The charging temperature was 100 K for **d, e**. **f**, Estimation of the trap depth using the Randall-Wilkins model. The trap depths were similar for charging at 365 and 620 nm. The five points in **f** are derived from the five curves in **e**.

To reveal the electronic transition of the visible-light charging process in pTAP@TPBi, we first investigated the absorption of TPBi and pTAP dispersed in toluene and solid melt-cast films. As shown in Figure 4.3a, the absorption of TPBi in both solution and film states was almost negligible in the visible region. pTAP dispersed in toluene (*i.e.,* monomer state) showed a broad absorption peak at ~500 nm, which is due to a typical iCT transition from an electron donor to an acceptor in the pTAP monomer.[38] Compared to the solution state, the absorption of pTAP in melt-cast films shifted towards longer wavelengths, suggesting a different energy-level structure. A redshift (from ~ 625 to 800 nm) was also observed in the emission spectra of pTAP in solution state to film state (Figure S4.7). An absorption redshift was also observed in the pTAP@TPBi melt-cast films, displaying a gradual shift of the peak wavelength from ~510 to 600 nm as the doping concentration of pTAP increases from 0.01 to 5 wt% (dashed curves in Figure 4.3b). Notably, the melt-casting method was important for the formation of pTAP aggregates in TPBi with low pTAP concentrations (Figure S4.8). According to the literature, the absorption redshift in pTAP@TPBi melt-cast films with different guest doping concentration is attributed to the intense xCT process due to the aggregation of pTAP molecules.[39] Correspondingly, the peak wavelength of PL in pTAP@TPBi varied from ~620 to 725 nm depending on the doping level (solid curves in Figure 4.3b), verifying the decrease in irradiation energy from S_1 to S_0. Electron spin resonance (ESR) measurements were performed to investigate the electron-pair states of the samples. As shown in Figure 4.3c, an ESR signal is observed at g ~2.0035 for pTPA and 1 wt% pTAP@TPBi after UV irradiation in air. Similar signals with higher intensities are observed for pTAP@TPBi after irradiation at 450, 530, and 620 nm under

oxygen-free conditions. A comparison of the two conditions verified the necessity of oxygen-free conditions to inhibit radical quenching.[26] These ESR signals indicate the generation of radical cations or anions (containing unpaired electrons) from closed-shell neutral molecules under light irradiation, providing important evidence to support the xCT mechanism.[40]

The intermolecular interactions in the aggregates were further studied using a structural model of pTAP single crystals.[35] As depicted in Figure S4.9, three types of dimer configurations, denoted as D1, D2, and D3, form intermolecular bonds between the adjacent pTAP molecules. The lengths of C-H⋯ hydrogen bonds and C-H⋯π interactions in D1 and D2 dimers are 2.654 and 3.144 Å, respectively. The length of the C-H⋯N hydrogen bond is 2.844 Å and that of the π⋯π interaction is 3.683 Å in D3 dimers. It was reported that a short intermolecular bond length (typically less than 3.7 Å) is favorable for electron delocalization of dimers under light irradiation.[41,42] Therefore, close interactions between adjacent pTAP molecules could be effective in generating xCT in aggregates. The electronic structures of the pTAP dimers were analyzed using time-dependent density functional theory (TD-DFT) (Figure 4.3d). The HOMO and LUMO of the dimers are predominantly distributed on different pTAP molecules. The separation of the frontier molecular orbitals (FMOs) is also favorable for xCT in aggregates. Among the three dimers, D1 shows the longest HOMO-LUMO distance (d_{H-L}) of 12.26 Å. A portion of the LUMO is located in the original molecule, indicating a relatively weak xCT interaction. In contrast, for D2 and D3, the FMOs are completely separated, giving d_{H-L} values of 5.34 and 4.28 Å, respectively. Using the Gaussian 09 package at the (TD)B3LYP/def2-TZVP level, an energy difference between S_1 and S_0 of 2.06 eV in D1 was calculated, which was smaller in D2 and D3 dimers (1.98 and 1.85 eV, respectively; Figure 4.3e). These results indicate that the short d_{H-L} in the pTAP aggregates reduces the S_1 energy level. This also explains the redshift of the absorption and emission in the pTAP@TPBi films with increasing pTAP concentration (Figure 4.3b and Figure S4.2).
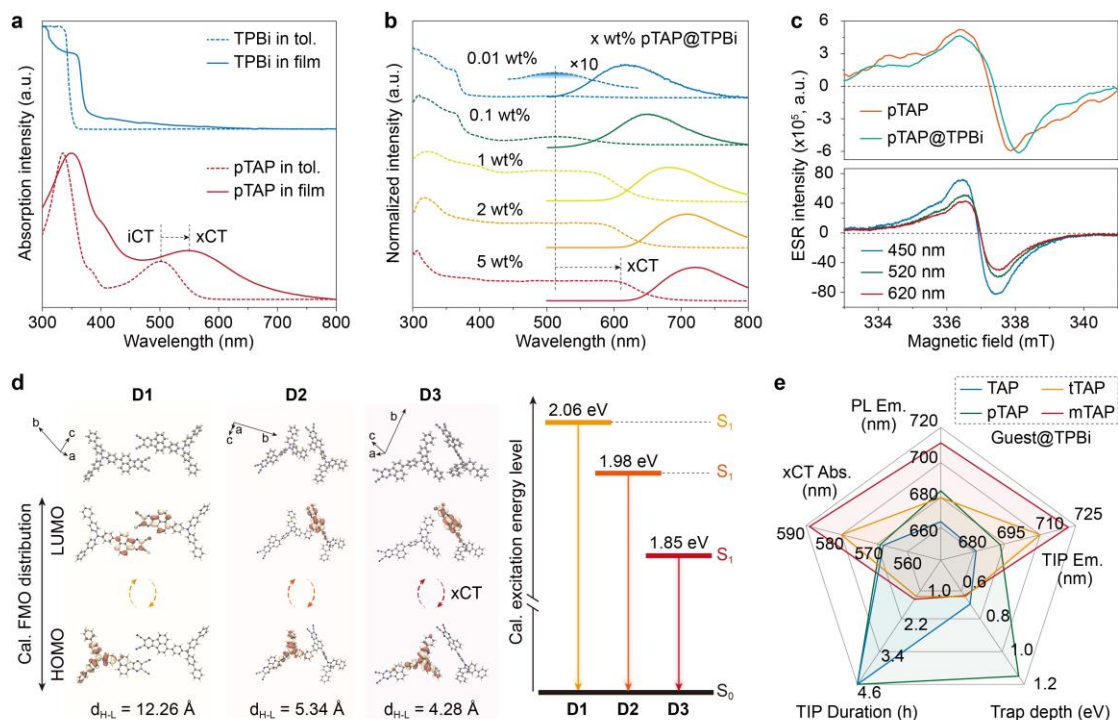
Figure 4.3 Electronic transition of the xCT interaction in host-guest molecular systems. a, Absorption spectra of TPBi and pTAP dispersed in toluene (tol.) solutions (1×10^{-5} mol L^{-1}) and as melt-cast films. **b**, Absorption (dashed line) and PL (solid line) spectra of the pTAP@TPBi in melt-cast films (pTAP concentration x = 0.01, 0.1, 1, 2, and 5 wt%). **c**, ESR signals of pTAP and 1 wt% pTAP@TPBi after 365 nm irradiation in an ambient atmosphere (top) and those of the pTAP@TPBi after visible light irradiation at 450, 520, and 620 nm in an anaerobic atmosphere (bottom). The comparison between the two tests indicates that oxygen has a significant quenching effect on the ESR signals. **d**, Calculated crystallographic configurations and FMO distributions of three representative pTAP dimers (D1, D2, and D3) calculated (Cal.) using the TD-DFT approach. **e**, Energy level diagrams of three types of pTAP dimers. The difference between the S_1 and S_0 levels varies in the three dimers. The Gaussian 09 package at the (TD)B3LYP/def2-TZVP level was used in the calculation. **f**, Summary of the main photophysical properties of TAP@TPBi, pTAP@TPBi, tTAP@TPBi, and mTAP@TPBi. The doping concentration of the guest was kept at 1 wt%.

To understand the origin of the charge-trapping process under xCT, we measured the difference in absorption (Δabs.) in the pTAP@TPBi melt-cast films before and after light irradiation at 450 nm (Figure 4.4a-top; original absorption spectra are shown in Figure S4.10). Compared with the absorption spectra of pTAP and TPBi in the oxidized and reduced states obtained by a deliberate electrochemical reaction (Figure 4a-middle and bottom, respectively), the presence of various radicals was verified in pTAP@TPBi after irradiation, including TPBi anion (TPBi$^{\bullet-}$ at 432 nm), TPBi cation (TPBi$^{\bullet+}$ at 461 and 555 nm), pTAP anion (pTAP$^{\bullet-}$ at 686 nm) and pTAP cation (pTAP$^{\bullet+}$ at 759 and 866 nm) radicals. In addition, the ESR signals of the pTAP@TPBi film after blue-light irradiation were monitored at room temperature (RT) for a period of time (Figure 4.4b). Notably, the ESR signals at g ~2.0036 were still detected after 30 d, although their intensity decreased with increasing storage time. These results indicate that the generated radicals with unpaired electrons are partially retained at RT, and their numbers exhibit a decreasing trend similar to that of the PersL intensity. Furthermore, femtosecond transient absorption spectroscopy was used to study the dynamics of the photoinduced charge-carrier transitions. With a 450-nm femtosecond laser as the pump source, the transient absorption in TPBi is almost negligible, and the negative signals recorded in pTAP (wavelength range of 550-625 nm and time domain of 20 fs to 3 ns) are attributed to the ground-state bleaching effect (Figure 4.4c and Figures S4.11 and S4.12).[43] In contrast, we detected clear excited-state absorption (ESA) bands from pTAP@TPBi at approximately 677, 778, and 835 nm (Figures 4d-f and Figures S4.13 and S4.14). These ESA bands are well matched with the absorption spectra of pTAP$^{\bullet-}$ and pTAP$^{\bullet+}$ (Figure 4.4a), confirming the formation of the two radical species. More importantly, the ESA signals from pTAP@TPBi under femtosecond-pulse excitation exhibit a decay duration of 1.75-2.58 ns (Figure 4.4f). This is much longer than that of the weak ESA signals from pTAP (0.10-0.21 ns; Figure S4.12). Notably, the ESA signals from pTAP@TPBi between 550 and 570 nm are attributed to the absorption of

178

TPBi after receiving one electron or hole. This is verified by the absorption spectra of the TPBi radical anion and cation (Figure 4.4a) and transient absorption spectra of TPBi using a 365 nm pump source (Figure S4.15). Transient absorption dynamics indicated that the duration of the generated radicals was significantly prolonged in pTAP@TPBi, probably because of the interaction between the host and guest molecules.

The orbital configurations and energy levels in the relevant radical species (TPBi$^{•+}$, TPBi$^{•-}$, pTAP$^{•+}$, and pTAP$^{•-}$) were examined by DFT calculations (Tables S4.2 and S4.3). Notably, the average energy difference between the LUMOs of TPBi$^{•-}$ and pTAP$^{•-}$ is ~1.30 eV (including four components of 1.25, 1.26, 1.34, and 1.35 eV when considering two different densities of electrons with spins α and β in an open-shell system; Figures 4g and 4h). The energy difference is in good agreement with the experimental ε of ~1.16 eV determined by TL analysis, indicating that the electronic transitions between the LUMOs of pTAP$^{•-}$ and TPBi$^{•-}$ are probably responsible for the charge trapping and detrapping processes in pTAP@TPBi.

Based on the above results, a mechanism for visible-light-charged PersL in organic compounds is proposed. Taking pTAP@TPBi as an example, the generation of trap-induced PersL involves four steps.

[i] Excitation and charge separation (CS):
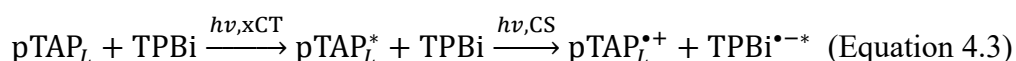
$$\text{pTAP}_L + \text{TPBi} \xrightarrow{h\nu,\text{xCT}} \text{pTAP}_L^* + \text{TPBi} \xrightarrow{h\nu,\text{CS}} \text{pTAP}_L^{•+} + \text{TPBi}^{•-*} \quad \text{(Equation 4.3)}$$

[ii] Charge trapping

$$\text{TPBi}^{•-*} + \text{pTAP}_T \xrightarrow{\text{trapping}} \text{TPBi} + \text{pTAP}_T^{•-*} \quad \text{(Equation 4.4)}$$

[iii] Charge detrapping

$$\text{TPBi} + \text{pTAP}_T^{•-*} \xrightarrow{\text{detrapping}} \text{TPBi}^{•-*} + \text{pTAP}_T \quad \text{(Equation 4.5)}$$

[iv] Charge recombination (CR) and emission

$$\text{TPBi}^{\bullet-*} + \text{pTAP}_L^{\bullet+} \xrightarrow{\text{CR}} \text{TPBi} + \text{pTAP}_L^* \rightarrow \text{TPBi} + \text{pTAP}_L + h\nu \quad \text{(Equation 4.6)}$$
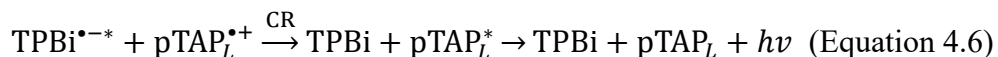
where the asterisk denotes that the active site contains an electron in the LUMO state, and the subscripts L and T denote that the pTAP molecules act as luminescent and trapping centers, respectively. The proposed mechanism indicates that an electron from pTAP$_L$ is first excited (pTAP$^*_L$) under visible-light irradiation and is further excited and transferred to TPBi through a two-photon absorption process,[44-46] forming two metastable radical species, $\text{pTAP}_L^{\bullet+}$ and $\text{TPBi}^{\bullet-}$. The excited electron is mobile within the host owing to the excellent electron-transport properties of TPBi, and is eventually captured by another pTAP molecule (pTAP$_T$). The energy gap between the LUMO levels of $\text{pTAP}_T^{\bullet-}$ and $\text{TPBi}^{\bullet-}$ creates the energy barrier (ε) that the electron needs to cross to recombine with the original luminescent center, resulting in PersL with distinct thermal-activation characteristics.
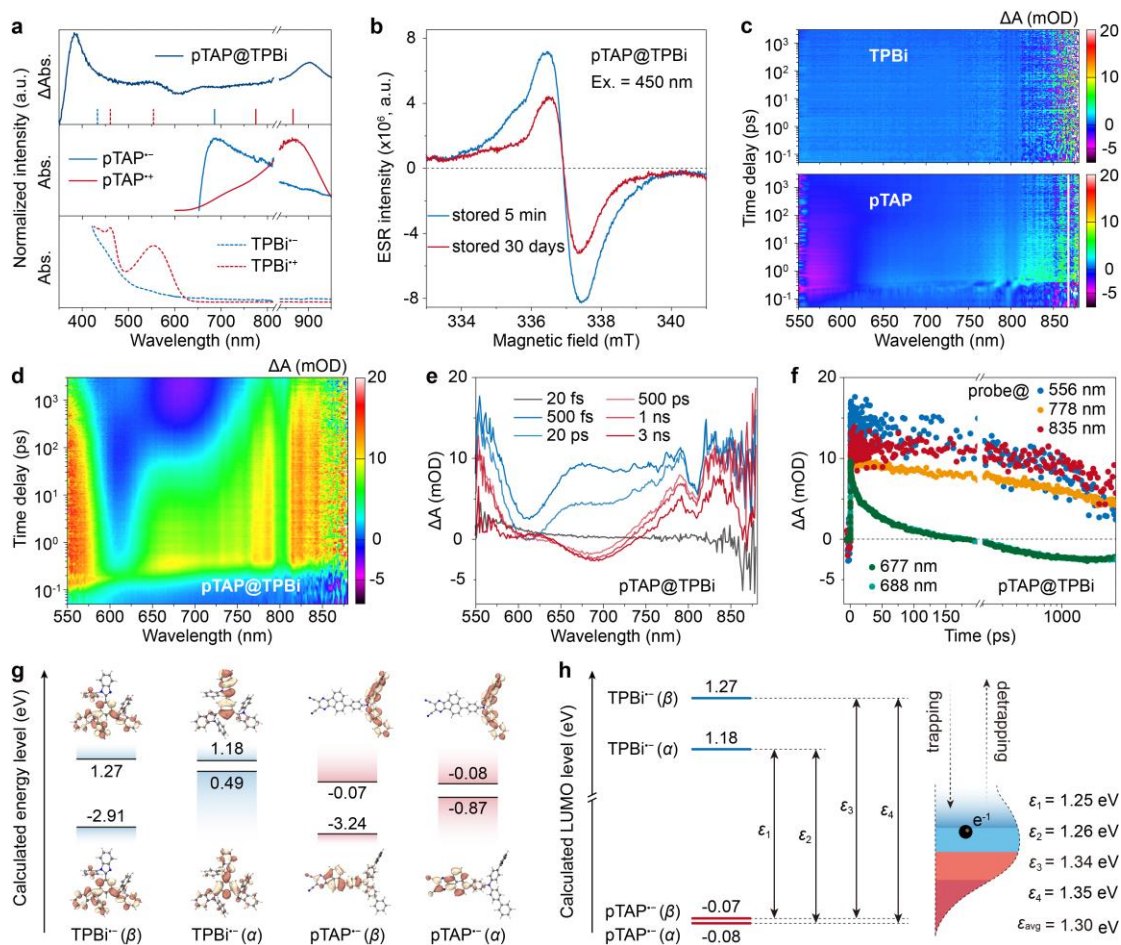
Figure 4.4 Charge separation and charge trapping in pTAP@TPBi. a, Difference in absorption (Δabs.) of the 1 wt% pTAP@TPBi before and after light irradiation at 450 nm (top). Reference absorption spectra of the (middle) pTAP radical cation (pTAP$^{\bullet+}$) and anion (pTAP$^{\bullet-}$), and (bottom) TPBi radical cation (TPBi$^{\bullet+}$) and anion (TPBi$^{\bullet-}$) obtained in a dichloromethane solution containing 0.1 M TBAPF$_6$ under electrochemical oxidation and reduction reactions. The spectra are noisy in the region of 815-835 nm due to photodetector switching. **b**, ESR spectra of the pTAP@TPBi after light irradiation at 450 nm. **c**, Pseudo-color transient absorption plots of TPBi (top) and pTAP (bottom). A 450-nm fs-laser was used as the pump source. The transient absorption spectra and decay dynamics are given in Figures S4.11 and S4.12. **d**, Pseudo-color transient absorption plot of the pTAP@TPBi with 450 nm pump source. **e**, Transient absorption spectra at different delay times from 20 fs to 3 ns. **f**, Decay dynamics of transient absorption at different wavelengths. The positive signals (ΔA) at

~556, 677, 778, and 835 nm indicate ESA in pTAP@TPBi. The negative signals at ~688 nm are attributed to stimulated emission bands. **g**, Schematics of the orbital configurations of TPBi$^{\bullet-}$ and TN$^{\bullet-}$ obtained using DFT calculations at the B3LYP/def2-SVP level of theory. The energy levels of the HOMO and LUMO are labeled in the diagram. It should be noted that there are two different densities of electrons with spins α and β in an open-shell system. **h**, Energy differences (ε_1, ε_2, ε_3, and ε_4) between the LUMO levels of TPBi$^{\bullet-}$ and pTPA$^{\bullet-}$. The average energy difference was ~1.30 eV. The charge-trapping(detrapping) processes correspond to an electronic transition from TPBi$^{\bullet-}$ to pTPA$^{\bullet-}$ (and vice versa).

In further experiments, we selected a series of AP-based TADF emitters with different electron-donating abilities of the donor units for use as guest molecules (Figure 4.2b). These molecules include TAP (R = H), tTAP (R = C$_4$H$_9$), and mTAP (R = CH$_3$). Their chemical structures and calculated energy levels are presented in Table S4.1. As anticipated, all TAP@TPBi, tTAP@TPBi, and mTAP@TPBi melt-cast films exhibited trap-induced PersL at RT after charging under 450 nm light, which lasted for ~4.6, 1.2 and 1.3 h, respectively, after switching off the excitation source (Figure S4.16). As the electron-donating ability of the triphenylamine unit increases from TAP to tTAP to mTAP,[47] a redshift of the xCT absorption is observed, and the peak wavelength of the PL shifts from 664 to 680 to 711 nm, respectively (Figure S4.17). The PersL excitation spectra of the three samples covered the entire visible light region (up to 650 nm). And a redshift of the PersL excitation spectra was observed from TAP, tTAP, to mTAP, which was similar to that of the absorption spectra (Figure S4.18). According to the 3D plot of the TL measurements, the PersL spectra of TAP@TPBi, tTAP@TPBi, and mTAP@TPBi showed broad bands at 681, 710, and 722 nm, respectively (Figures S4.19-S4.21), giving corresponding ε values of 0.70 ± 0.02, 0.64 ± 0.01 and 0.63 ± 0.01 eV, respectively. These estimated ε values are close to the average energy differences between the LUMO levels of TPBi$^{\bullet-}$ and AP-based radical anions by DFT calculations

(*i.e.*, 0.73, 0.69, and 0.69 eV; Table S4.3). The main photophysical properties of the four samples studied in this work, including their ε values, emission wavelengths, and afterglow durations, are summarized in Figure 4.3e and Tables S4.2 and S4.3. AP-acceptor-based TADF emitters and their derivatives were used as typical model samples. Other TADF molecules that simultaneously exhibit NIR luminescence, high photoluminescence quantum yield, and xCT-induced long-wavelength absorption can be considered as an extension of this system. We believe that the design route based on xCT and charge-trapping processes in host-guest molecular systems may contribute to the development of more visible-light-chargeable and emission-tunable organic PersL materials.

Owing to the fundamental differences in the long-lasting emission mechanism of RTP, trap-induced PersL in organics allows the development of new applications in light-storage technologies. First, we compared the light-storage abilities of the 1 wt% pTAP@TPBi and $ZnGa_2O_4{:}0.5\%Cr^{3+}$ phosphors. The latter is a well-known inorganic compound showing excellent NIR PersL properties with a peak wavelength of ~696 nm, which is highly anticipated for *in vivo* bioimaging and anti-counterfeiting applications.[6,7,48] As shown in Figure 4.5a, using the same light source, the TL intensity of $ZnGa_2O_4{:}Cr^{3+}$ was higher than that of pTAP@TPBi after charging at 365 nm. In contrast, when charged with visible light at 450, 520, or 620 nm, pTAP@TPBi exhibited superior light-storage capacity (*i.e.,* higher TL intensity) than its inorganic counterpart. This may be attributed to the fact that the xCT interaction facilitates efficient charge separation and trapping in organic emitters under low-energy light excitation (Figures 4.1a and 4.2b).

Because charge detrapping is a temperature-dependent process (see Equation 4.1), trap-induced PersL must be correlated with the working temperature of the material, which facilitates optical anti-counterfeiting applications.[49,50] As a demonstration, pTAP@TPBi was formed into a patterned logo and charged with white LEDs using a mobile phone (Figures 4.5b and 4.c). PersL showed a natural decay at RT (process 2 in

Figure 4.5c). When the temperature increased to 400 K, the PersL intensity increased (process 3) and then decayed at an accelerated rate (process 4). As another example, we applied a laser direct-writing method to prepare a pattern using pTAP@TPBi. Similarly, the intensity of the luminous pattern exhibited a natural decay at RT, followed by an accelerated decay at higher temperatures (Figure 4.5d). Additionally, we wrote different optical information onto pTAP@TPBi films in separate steps. Owing to its light-storage characteristics, all of the recorded information, which was almost quenched at RT, was retrieved by high-temperature thermal stimulation (Figure 4.5e).

Finally, although visible-light-charged NIR PersL can be achieved through xCT interactions and charge-trapping strategies, the materials investigated in this work are sensitive to moisture and oxygen. Therefore, bioimaging applications were not demonstrated in this study. Nevertheless, we believe that this work will inspire further research on high-performance NIR PersL materials and their future applications, such as the realization of longer emission wavelengths, improved moisture/oxygen resistance, and favorable biocompatibility.
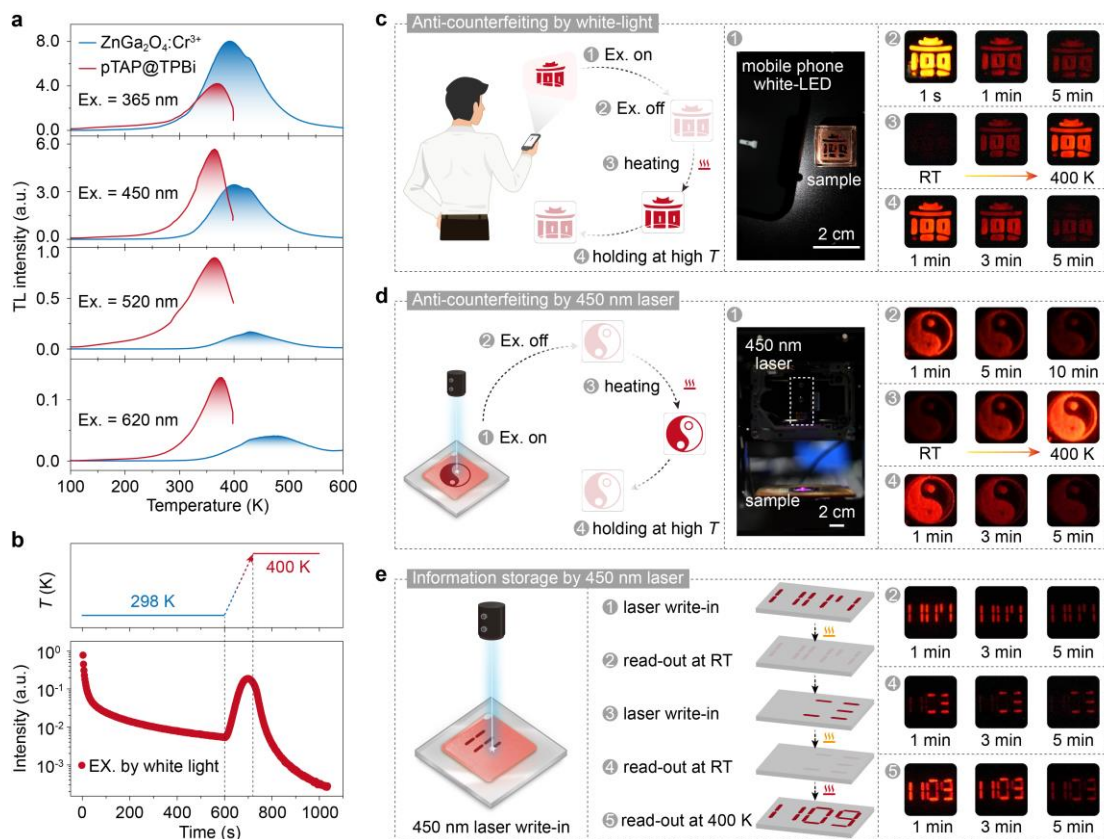
Figure 4.5 Applications of the pTAP@TPBi as light-storage materials. a, Comparison of the TL glow curves of 1 wt% pTAP@TPBi and $ZnGa_2O_4$:0.5% Cr^{3+}. The two samples were charged by the same light sources at 365, 450, 520, and 620 nm before TL recording. **b**, PersL decay curve of the pTAP@TPBi at various temperatures. The top panel shows the three-step temperature history: (i) holding at RT for 10 min, (ii) heating to 400 K at a rate of 50 K/min, and (iii) holding at 400 K for 5 min. **c**, Anti-counterfeiting application based on the storage of white light. A patterned logo of pTAP@TPBi exhibited long-lasting PersL at RT after charging with white light (Processes 1 and 2). After natural decay, the almost-quenched pattern was recovered by heating (Process 3) and showed a new decay at high temperature (Process 4). **d**, Anti-counterfeiting application based on the storage of blue laser light. A pattern was created on the pTAP@TPBi film by laser direct writing at 450 nm, which exhibited long-lasting PersL at RT after writing (Processes 1 and 2). After natural decay, the almost-quenched pattern was recovered by heating (Process 3) and showed a new decay at high

temperature (Process 4). **e**, Information storage application. Vertical bars and horizontal bars were written into the pTAP@TPBi film in two separate steps (Processes 1 and 3). After natural decay at RT (Processes 2 and 4), the recorded information was retrieved by heating the sample to 400 K (Process 5). Note that the color of the photos with high brightness might deviate from the original deep red to yellow because of brightness oversaturation of the applied camera (especially for the red channel).

4.5 Conclusion

In conclusion, we developed a series of visible light-charged PersL organics with hour-level NIR emission durations from host–guest molecular systems. The absorption and ESR spectra, and TD-DFT simulation results confirmed that the strong xCT interaction in the guest CTAs resulted in effective charge separation under low-energy light excitation and a significant redshift in the emission peaks. The TL measurements, thermally stimulated decay curves, transient absorption spectra, and constructed energy-level diagrams indicate that the hour-level emission of the host–guest molecules is attributed to charge trapping and detrapping processes. The emission wavelength, trap depth, and afterglow duration can be tuned by controlling the electronic structures of the host/guest molecules and their radical anions. Considering the large differences in the long-lasting mechanism and emission duration from RTP, organic NIR PersLs may offer great opportunities for the application of organic semiconductors in optoelectronic fields, such as optical anti-counterfeiting, optical information storage, and biological imaging technologies.

4.6 Reference

[1] J. Xu, S. Tanabe, *J. Lumin.* **2019**, 205, 581-620.

[2] L. Liang, J. Chen, K. Shao, X. Qin, Z. Pan, X. Liu, *Nat. Mater.* **2023**, 22, 289-304.

[3] W. Zhao, Z. He, B. Z. Tang, *Nat. Rev. Mater.* **2020**, 5, 869-885.

[4] Y. Wei, C. Gong, M. Zhao, L. Zhang, S. Yang, P. Li, Z. Ding, Q. Yuan, Y. Yang, *J. Rare Earths* **2022**, 9, 1333-1342.

[5] Y. Li, M. Gecevicius, J. Qiu, *Chem. Soc. Rev.* **2016**, 45, 2090-2136.

[6] T. Maldiney, A. Bessiere, J. Seguin, E. Teston, S. K. Sharma, B. Viana, A. J. Bos, P. Dorenbos, M. Bessodes, D. Gourier, D. Scherman, C. Richard, *Nat. Mater.* **2014**, 13, 418-426.

[7] Z. Pan, Y. Y. Lu, F. Liu, *Nat. Mater.* **2011**, 11, 58-63.

[8] Y. Jiang, J. Huang, X. Zhen, Z. Zeng, J. Li, C. Xie, Q. Miao, J. Chen, P. Chen, K. Pu, *Nat. Commun.* **2019**, 10, 2064.

[9] L. Liang, N. Chen, Y. Jia, Q. Ma, J. Wang, Q. Yuan, W. Tan, *Nano Res.* **2019**, 12, 6, 1279-1292.

[10] R. Zou, S. Gong, J. Shi, J. Jiao, K. L. Wong, H. Zhang, J. Wang, Q. Su, *Chem. Mater.* **2017**, 29, 9, 3938-3946.

[11] S. K. Sun, H. F. Wang, X. P. Yan, *Acc. Chem. Res.* **2018**, 51, 1131-1143.

[12] P. Dorenbos, *Phys. Stat. Sol. (b)* **2005**, 242, 1, 7-9.

[13] J. J. Joos, K. Korthout, L. Amidani, P. Glatzel, D. Poelman, P. F. Smet, *Phys. Rev. Lett.* **2020**, 125, 033001.

[14] T. Maldiney, A. Lecointre, B. Viana, A. Bessiere, M. Bessodes, D. Gourier, C. Richard, D. Scherman, *J. Am. Chem. Soc.* **2011**, 133, 11810-11815

[15] T. Matsuzawa, Y. Aoki, N. Takeuchi, Y. Murayama, *J. Electrochem. Soc.* **2019**, 143, 2670-2673.

[16] X. Ou, X. Qin, B. Huang, J. Zan, Q. Wu, Z. Hong, L. Xie, H. Bian, Z. Yi, X. Chen, Y. Wu, X. Song, J. Li, Q. Chen, H. Yang, X. Liu, *Nature* **2021**, 590, 410-415.

[17] F. Yang, X. Wu, H. Cui, Z. Ou, S. Jiang, S. Cai, Q. Zhou, B. G. Wong, H. Huang, G. Hong, *Sci. Adv.* **2022**, 8, eabo6743.

[18] D. Dutczak, T. Jüstel, C. Ronda, A. Meijerink, *Phys. Chem. Chem. Phys.* **2015**, 17, 15236-15249.

[19] Z. An, C. Zheng, Y. Tao, R. Chen, H. Shi, T. Chen, Z. Wang, H. Li, R. Deng, X. Liu, W. Huang, *Nat. Mater.* **2015**, 14, 685-690.

[20] B. Ding, L. Ma, Z. Huang, X. Ma, He Tian, *Sci. Adv.* **2021**, 7, eabf9668.

[21] J. Liu, N. Wang, Y. Yu, Y. Yan, H. Zhang, J. Li, J. Yu, *Sci. Adv.* **2017**, 3, e1603171.

[22] B. Zhou, D. Yan, *Angew. Chem. Int. Ed.* **2019**, 58, 15128-15135.

[23] H. Lv, H. Tang, Y. Cai, T. Wu, D. Peng, Y. Yao, X. Xu, *Angew. Chem. Int. Ed.* **2022**, e202204209.

[24] R. Gao, M. S. Kodaimati, D. Yan, *Chem. Soc. Rev.* **2021**, 50, 5564-5589.

[25] R. Kabe, C. Adachi, *Nature* **2017**, 550, 384-387.

[26] K. Jinnai, R. Kabe, Z. Lin, C. Adachi, *Nat. Mater.* **2022**, 21, 338-344.

[27] K. Jiang, Y. Wang, C. Lin, L. Zheng, J. Du, Y. Zhuang, R. J. Xie, Z. Li, H. Lin, *Light. Sci. Appl.* **2022**, 11, 80.

[28] P. Alam, N. L. C. Leung, J. Liu, T. S. Cheung, X. Zhang, Z. He, R. T. K. Kwok, J. W. Y. Lam, H. H. Y. Sung, I. D. Williams, C. C. S. Chan, K. S. Wong, Q. Peng, B. Z. Tang, *Adv. Mater.* **2020**, 32, 2001026.

[29] S. Cai, H. Shi, J. Li, L. Gu, Y. Ni, Z. Cheng, S. Wang, W. W. Xiong, L. Li, Z. An,

W. Huang, *Adv. Mater.* **2017**, 29, 1701244.

[30] Y. Fan, S. Liu, M. Wu, L. Xiao, Y. Fan, M. Han, K. Chang, Y. Zhang, X. Zhen, Q. Li, Z. Li, *Adv. Mater.* **2022**, 34, 2201280.

[31] H. Nakanotani, T. Furukawa, K. Morimoto, C. Adachi, *Sci. Adv.* **2016**, 2, 1501470.

[32] N. J. Hestand, F. C. Spano, *Chem. Rev.* **2018**, 118, 7069-7163.

[33] J. H. Kim, A. Liess, M. Stolte, A. M. Krause, V. Stepanenko, C. Zhong, D. Bialas, F. Spano, F. Wurthner, *Adv. Mater.* **2021**, 33, 2100582.

[34] C. Lin, Z. Wu, H. Ma, J. Liu, S. You, A. Lv, W. Ye, J. Xu, H. Shi, B. Zha, W. Huang, Z. An, Y. Zhuang, R. J. Xie, *Nat. Photon.* **2024**, 18, 350-356.

[35] J. Xue, J. Xu, J. Ren, Q. Liang, Q. Ou, R. Wang, Z. Shuai, J. Qiao, *Sci. China Chem.* **2021**, 64, 1786-1795.

[36] F. Daniels, C. A. Boyd, D. F. Saunders, *Science* **1953**, 117, 343-349.

[37] A. J. J. Bos, *Materials* **2017**, 10, 1357.

[38] Q. Zhang, H. Kuwabara, W. J. Potscavage, Jr., S. Huang, Y. Hatae, T. Shibata, C. Adachi, *J. Am. Chem. Soc.* **2014**, 136, 18070-18081.

[39] J. Zhang, B. He, Y. Hu, P. Alam, H. Zhang, J. W. Y. Lam, B. Z. Tang, *Adv Mater* **2021**, 33, e2008071.

[40] W. Zhu, L. Zhu, Y. Zou, Y. Wu, Y. Zhen, H. Dong, H. Fu, Z. Wei, Q. Shi, W. Hu, *Adv. Mater.* **2016**, 28, 5954-5962.

[41] L. Sun, W. Zhu, W. Wang, F. Yang, C. Zhang, S. Wang, X. Zhang, R. Li, H. Dong, W. Hu, *Angew. Chem. Int. Ed.* **2017**, 56, 7831-7835.

[42] Y. Xie, Y. Ge, Q. Peng, C. Li, Q. Li, Z. Li, *Adv. Mater.* **2017**, 29, 1606829.

[43] W. Zhang, H. Song, J. Kong, Z. Kuang, M. Li, Q. Guo, C. F. Chen, A. Xia, *J. Phys. Chem. C* **2019**, 123, 19322-19332.

[44] H. Ohkita, W. Sakai, A. Tsuchida, M. Yamamoto, *J. Phys. Chem. B*,**1997**, 101, 10241.

[45] W. Li, Z. Li, C. Si, M. Y. Wong, K. Jinnai, A. K. Gupta, R. Kabe, C. Adachi, W. Huang, E. Zysman-Colman, I. D. W. Samuel, *Adv. Mater.* **2020**, 2003911.

[46] X. Liang, Y. X. Zheng, J. L. Zuo, *Angew. Chem. Int. Ed.* **2021**, 60, 16984-16988.

[47] H. Wang, J. X. Chen, L. Zhou, X. Zhang, J. Yu, K. Wang, X. H. Zhang, *Mater. Horiz.* **2023**, 10, 2997-3004.

[48] Y. Zhuang, J. Ueda, S. Tanabe, P. Dorenbos, *J. Mater. Chem. C* **2014**, 2, 5502-5509.

[49] S. Liu, X. Fang, B. Lu, D. Yan, *Nat. Commun.* **2020**, 11, 4649.

[50] S. Peng, L. Liu, L. Wang, R. Rong, L. Song, W. You, J. Shi, Y. Zhang, *J. Rare Earths* **2022**, 9, 1417-1423.

4.7 Supporting Information
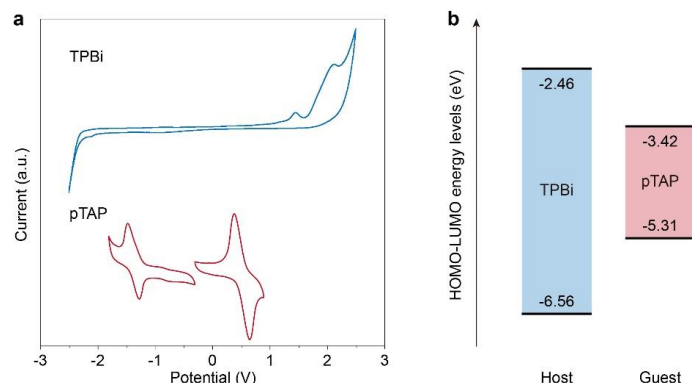
Figure S4.1 a, Cyclic voltammograms of TPBi and pTAP in dried DCM with TBAPF$_6$ recorded versus Fc/Fc$^+$ at 298 K under a N$_2$ atmosphere. **b**, Estimated energy levels of HOMO and LUMO of TPBi and pTAP.

We performed the cyclic voltammetry (CV) measurements of pTAP and TPBi to estimate the energy levels. As shown in Figure S1, the energy levels of HOMO and LUMO are -6.56 and -2.46 eV for TPBi, and -5.31 and -3.42 eV for pTAP, respectively. Both the two levels of pTAP are located inside the energy gap between the HOMO and LUMO levels of TPBi, which is different from the typical exciplex systems with an interlaced energy level configuration.
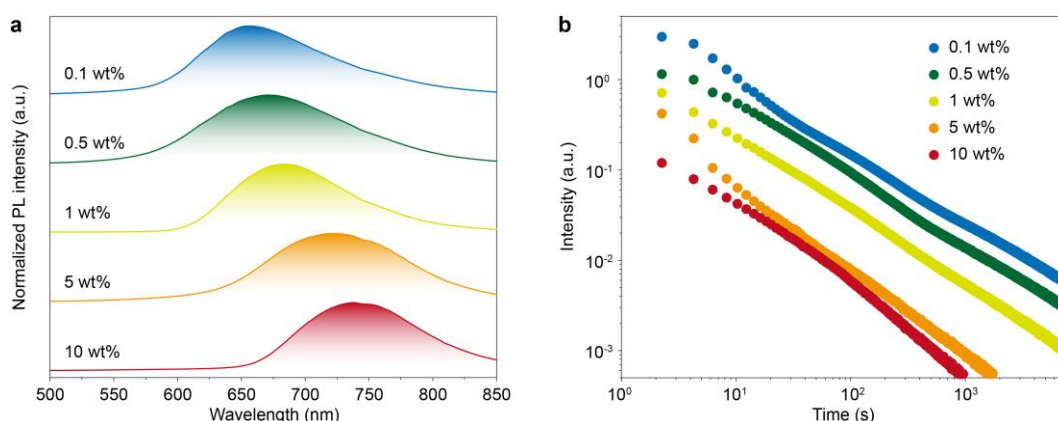
Figure S4.2 Photophysical properties of the pTAP@TPBi films with different doping concentrations. a, Photoluminescence (PL) spectra of the x wt% pTAP@TPBi.

The excitation wavelength is 365 nm. **b**, Trap-induced PersL decay curves of the x wt% pTAP@TPBi. The excitation (charging) wavelength is 450 nm. The excitation temperature and recording temperature are both 298 K (room temperature). The excitation (charging) time is 300 s. The doping concentration x = 0.1, 0.5, 1, 5, and 10 wt%.
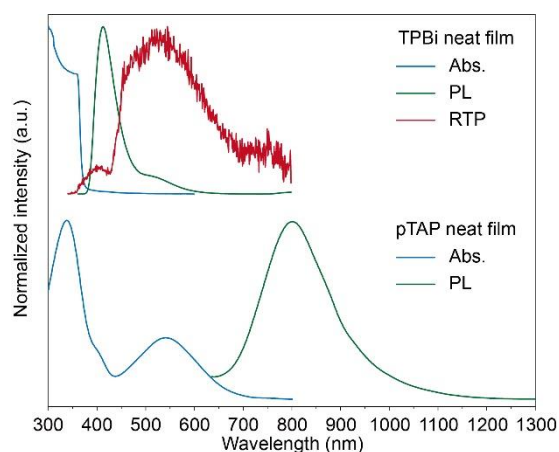
Figure S4.3 Photophysical properties of TPBi and pTAP. Ultravioletvisible absorption spectra (Abs., blue curves) and photoluminescence spectra (PL, green curves), and room temperature phosphorescence spectra (RTP, red curve) of the TPBi (top) and pTAP (bottom) samples. The TPBi and pTAP samples were prepared into a neat melt-casting film (with ~100 wt% purity).[3,5]
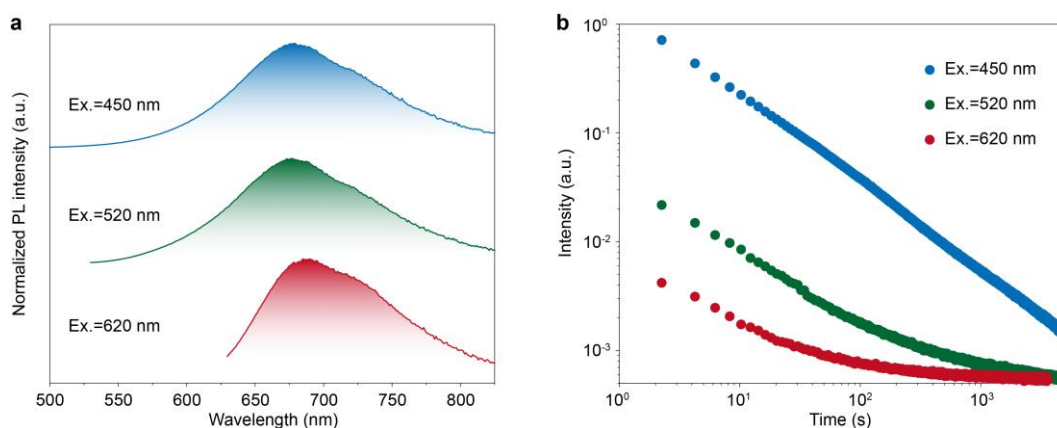
Figure S4.4 Photophysical properties of pTAP@TPBi under different excitation wavelengths. a, PL spectra of 1 wt% pTAP@TPBi under different excitation wavelengths at 450, 520, and 620 nm. **b**, Log-log plot of trap-induced PersL decay curves. The excitation (charging) wavelength is 450, 520 and 620 nm for the blue, green and red curves, respectively. The excitation time is 300 s. The PersL intensity after charging is monitored for 2 h at room temperature.
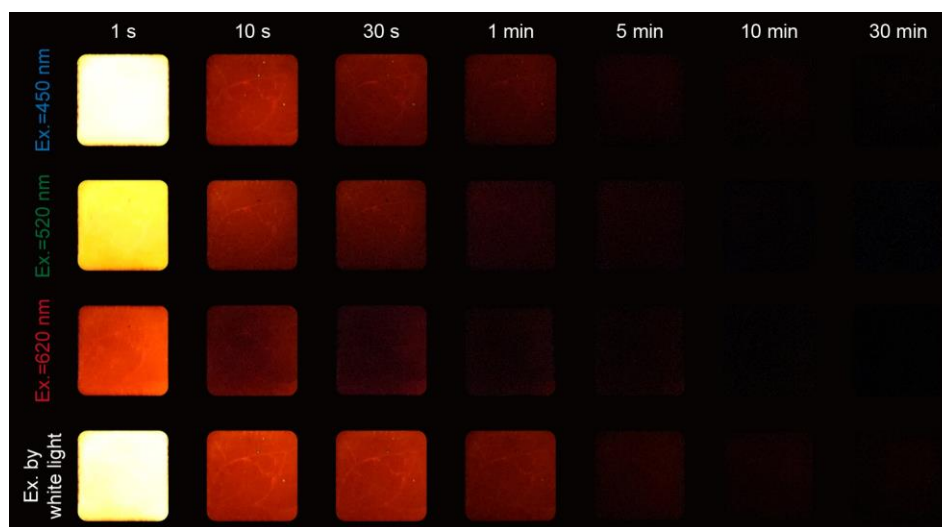
Figure S4.5 Photographs of the 1 wt% pTAP@TPBi melt-casting film after charging with different visible light. From top to bottom, monochromatic lights peaked at 450, 520, 620 nm and white light from a white-LED are used as the excitation (charging) light sources. The delay time is 1 s to 30 min from the left to right. The working temperature is 298 K (room temperature). The exposure time for the photograph is kept constant of 5 min. The used commercial digital camera (α7SIII, Sony) has a weak sensitivity in the NIR region (> 650 nm).
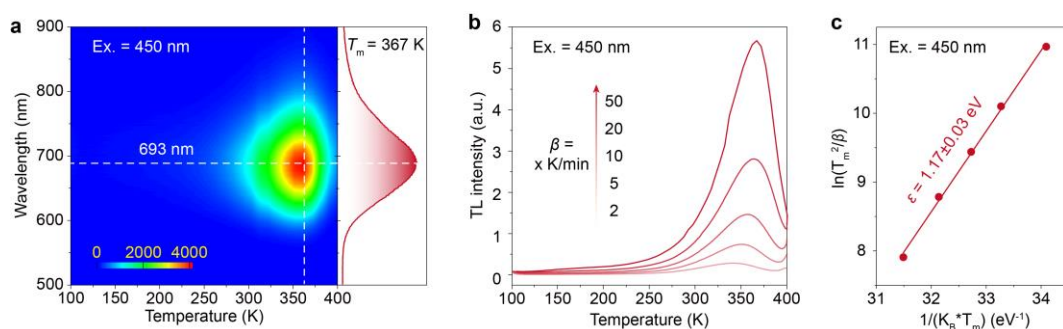
Figure S4.6 TL feature of the 1 wt% pTAP@TPBi film after blue light (450 nm) charging. a, Intensity-wavelength-temperature TL glow graph (3D-plot) with a heating rate of 50 K/min. PersL spectra (right part) are obtained from the 3D-plot. **b**, TL glow curves with different heating rates from 2, 5, 10, 20 to 50 K/min (excitation time 5 min, excitation temperature 100 K, scanning range 100 to 400 K). **c**, Estimation of the trap depth by using the Randall-Wilkins model. The results in Figure 2d and Figure S6 indicate that the estimated trap depth is basically independent on the excitation wavelength.
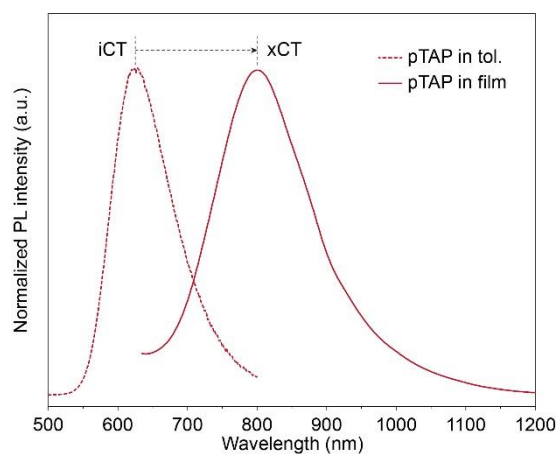
Figure S4.7 PL spectra of pTAP dispersed in toluene solutions (1×10^{-5} mol L^{-1}) and that of pTAP prepared in melt-casting films.[3]
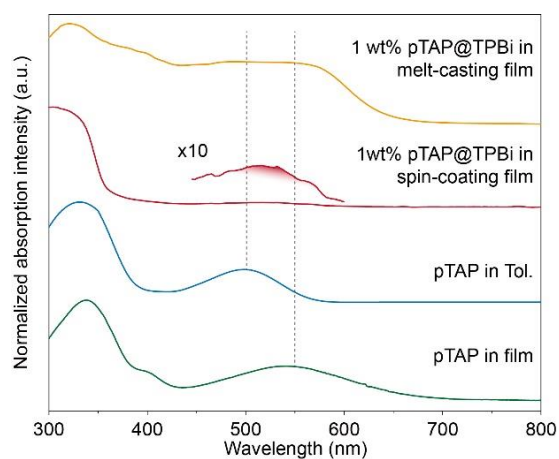
Figure S4.8 Absorption spectra of 1 wt% pTAP@TPBi prepared in melt-casting film (yellow), 1 wt% pTAP@TPBi prepared in spin-coating film (red), pTAP dispersed in toluene solutions (1×10^{-5} mol L^{-1}, blue), and pTAP prepared in pure melt-casting film (green).
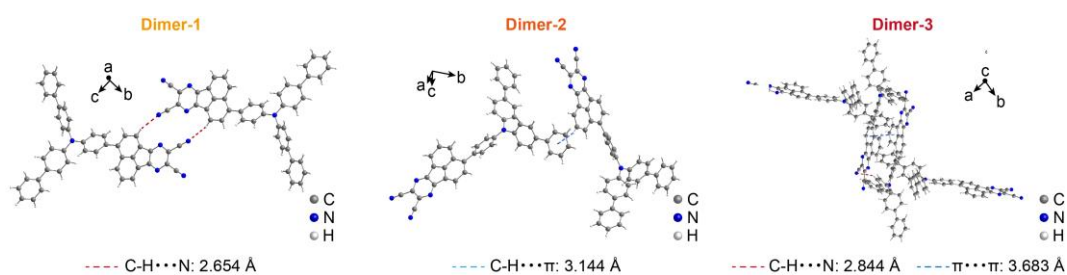
Figure S4.9 Intermolecular force of the dimers D1, D2 and D3 based on the pTAP crystal structure model.
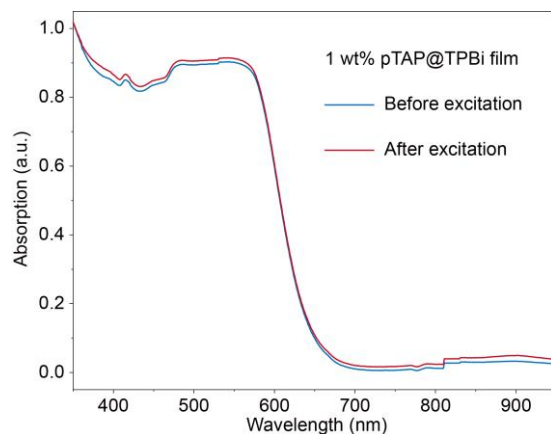
Figure S4.10 Absorption spectra of 1 wt% pTAP@TPBi melt-casting film before and after 450 nm excitation.
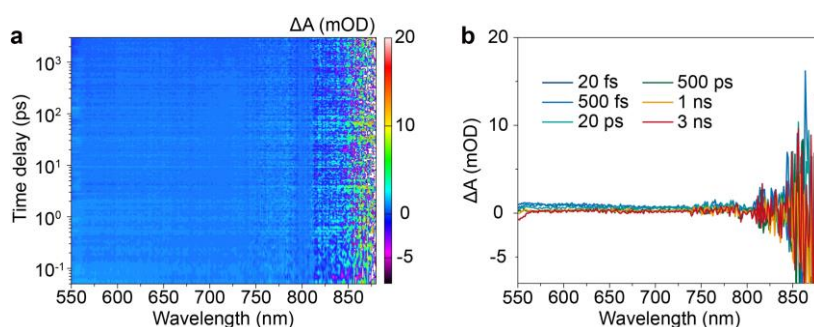
Figure S4.11 Transient absorption (TA) spectra of the TPBi melt-casting film under 450 nm pump laser excitation. a, Pseudo-color TA plot. **b**, TA spectra with a delay time from 20 fs to 3 ns.
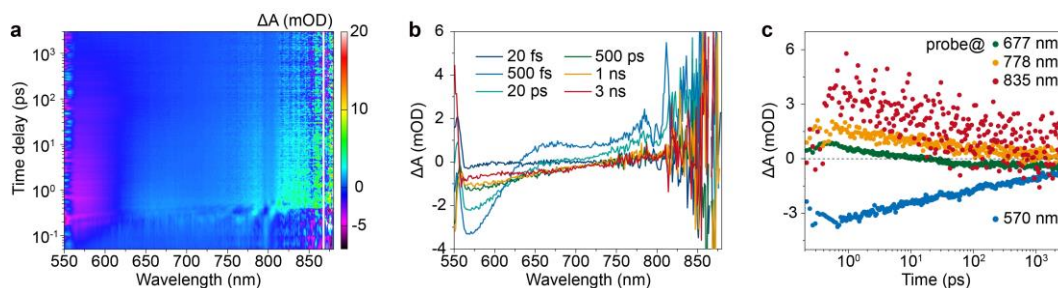
Figure S4.12 TA spectra of the pTAP melt-casting film under 450 nm pump laser excitation. a, Pseudo-color TA plot. **b**, TA spectra with a delay time from 20 fs to 3 ns.

c, The decay dynamics of excited-state absorption probed at 677, 778, and 835 nm and ground-state bleach probed at 570 nm.
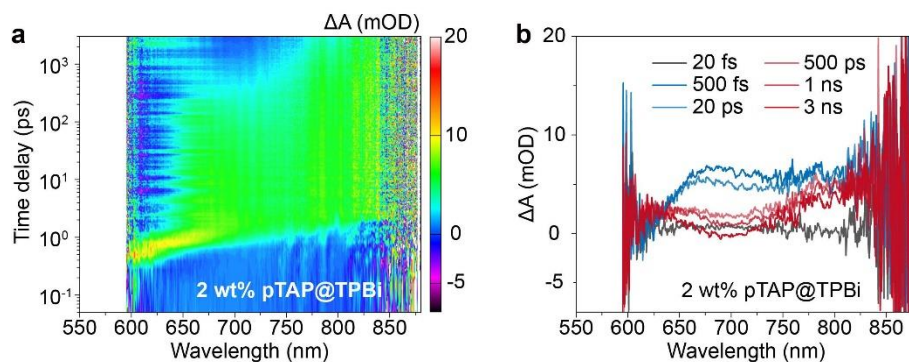
Figure S4.13 TA spectra of the 2 wt% pTAP@TPBi melt-casting film under 450 nm pump laser excitation. a, Pseudo-color TA plot. **b**, TA spectra with a delay time from 20 fs to 3 ns.
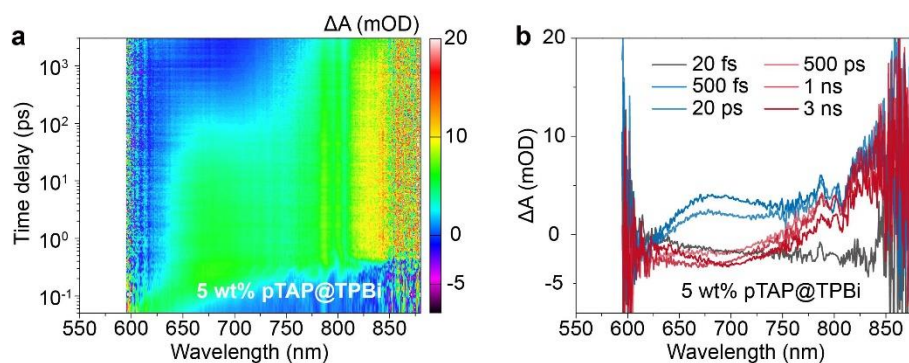
Figure S4.14 TA spectra of the 5 wt% pTAP@TPBi melt-casting film under 450 nm pump laser excitation. a, Pseudo-color TA plot. **b**, TA spectra with a delay time from 20 fs to 3 ns.
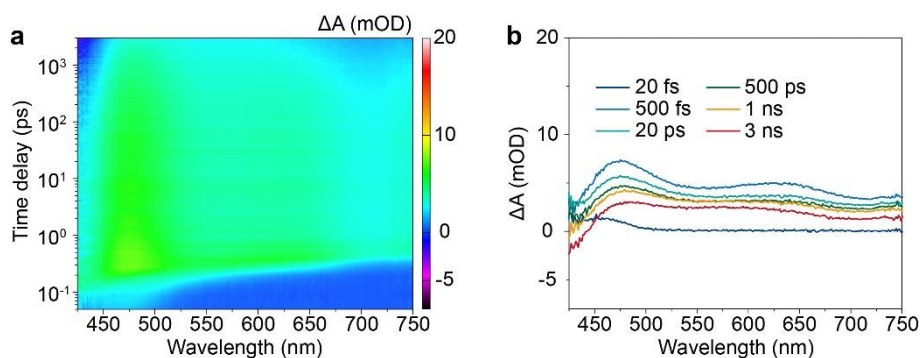
Figure S4.15 Transient absorption (TA) spectra of the TPBi melt-casting film under 365 nm pump laser excitation. a, Pseudo-color TA plot. **b**, TA spectra with a delay time from 20 fs to 3 ns.
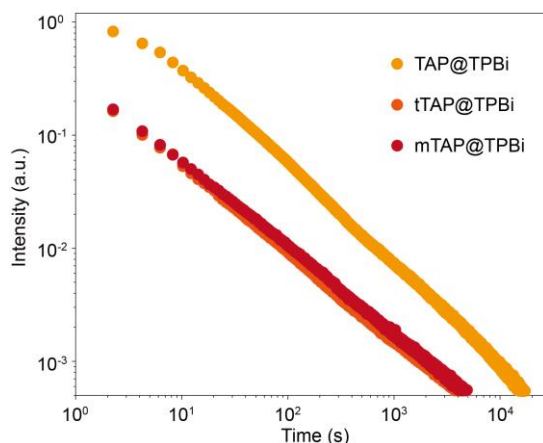
Figure S4.16 PersL decay curves of TAP@TPBi, tTAP@TPBi, and mTAP@TPBi. The decay curves as a function of time are displayed in a log-log coordinate. The excitation wavelength is 450 nm. The excitation time is 300 s. The PersL intensity after charging was monitored for 2 h at room temperature.
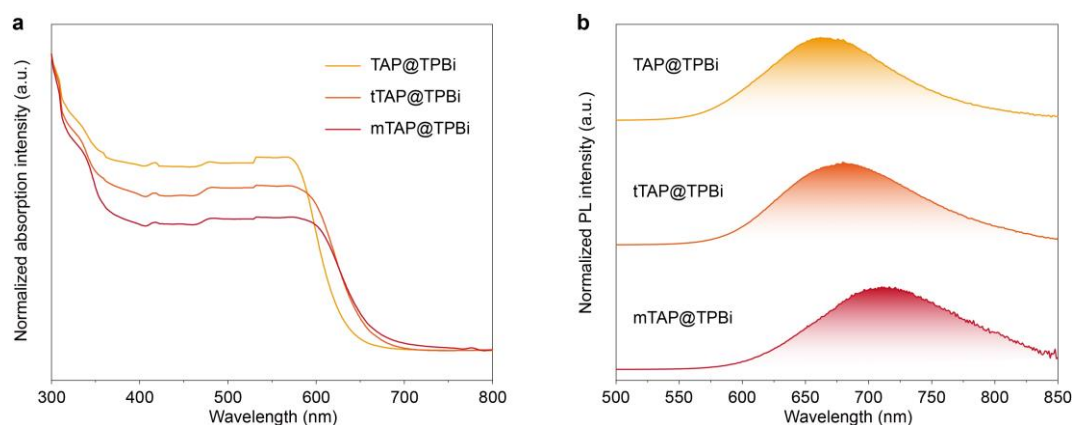
Figure S4.17 Photophysical properties of TAP@TPBi, tTAP@TPBi and mTAP@TPBi. **a,** Absorption spectra. **b**, PL spectra of the guest-host-systems under excitation at 450 nm.
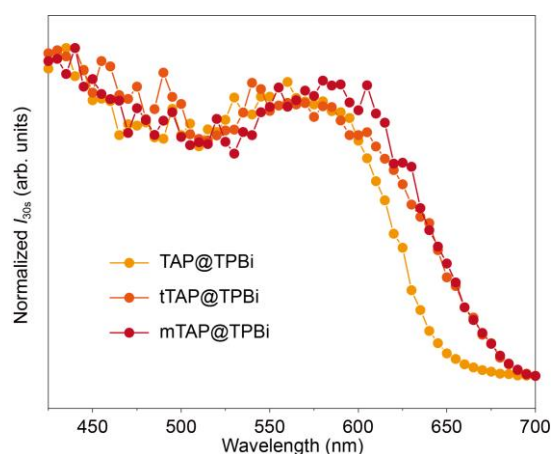
Figure S4.18 PersL excitation spectra of 1 wt% TAP, tTAP and mTAP@TPBi melt-casting film. For each wavelength, the film was charged by monochromatic light for 1 min (~37.5 mW/cm^2). The PersL intensity at 30 s after ceasing the excitation source (I_{30s}, λ_{mon} = 700±20 nm) was recorded.
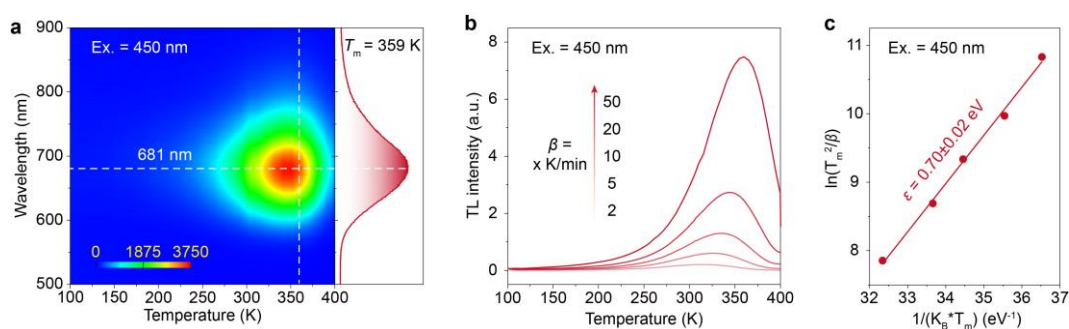
Figure S4.19 TL features of the 1 wt% TAP@TPBi film after blue light (450 nm) charging. a, Intensity-wavelength-temperature TL glow graph (3D-plot) with a heating rate of 50 K/min. PersL spectra (right part) are obtained from the 3D-plot. **b,** TL glow curves with different heating rates from 2, 5, 10, 20, to 50 K/min (excitation time 5 min, excitation temperature 100 K, scanning range 100 to 400 K). **c,** Estimation of the trap depth the Randall-Wilkins model.
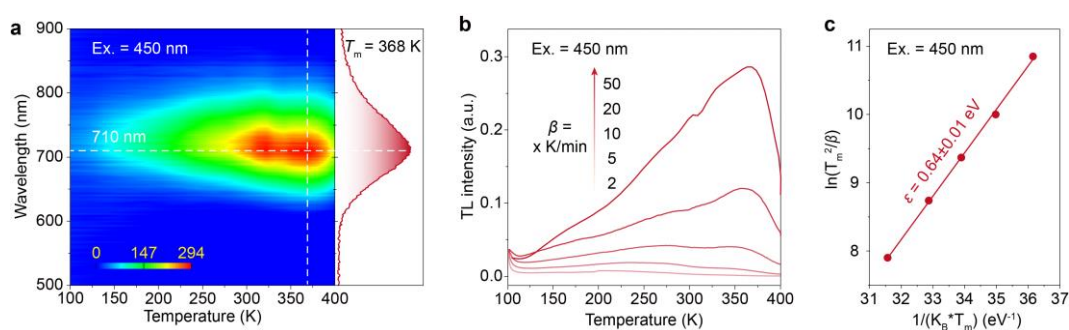
Figure S4.20 TL features of the 1 wt% tTAP@TPBi film after blue light (450 nm) charging. a, Intensity-wavelength-temperature TL glow graph (3D-plot) with a heating rate of 50 K/min. PersL spectra (right part) are obtained from the 3D-plot. **b,** TL glow curves with different heating rates from 2, 5, 10, 20, to 50 K/min (excitation time 5 min, excitation temperature 100 K, scanning range 100 to 400 K). **c,** Estimation of the trap depth the Randall-Wilkins model.
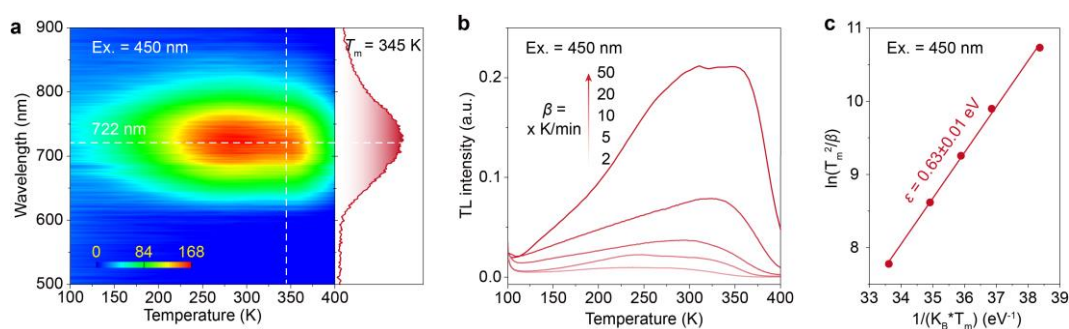
Figure S4.21 TL features of the 1 wt% mTAP@TPBi film after blue light (450 nm) charging. a, Intensity-wavelength-temperature TL glow graph (3D-plot) with a heating rate of 50 K/min. PersL spectra (right part) are obtained from the 3D-plot. **b**, TL glow curves with different heating rates from 2, 5, 10, 20, to 50 K/min (excitation time 5 min, excitation temperature 100 K, scanning range 100 to 400 K). **c**, Estimation of the trap depth the Randall-Wilkins model.

Table S4.1 Schematic diagrams showing the chemical structure and energy levels based on the TD-DFT calculations and main orbital configurations of TPBi, TAP, pTAP, tTAP, and mTAP.
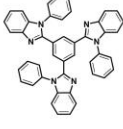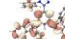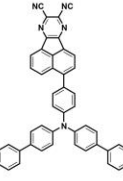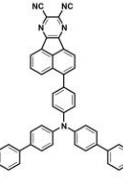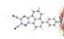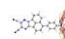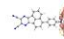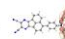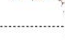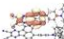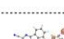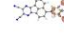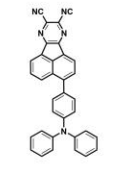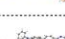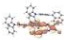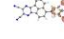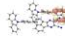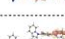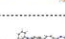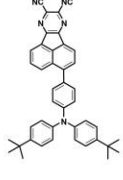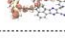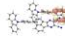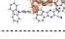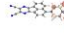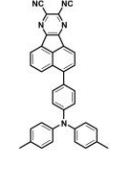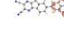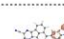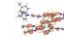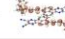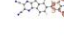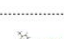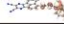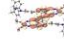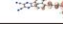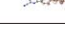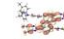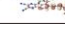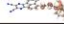
Name	Structure	Calculated LUMO and HOMO distribution (eV)				
		Molecule	Radical cation (α)	Radical cation (β)	Radical anion (α)	Radical anion (β)
TPBi		-1.59 / -5.99	-4.60 / -8.78	-8.04 / -8.49	1.18 / 0.49	1.27 / -2.91
pTAP	Monomer	-3.29 / -5.59	-5.30 / -8.78	-7.63 / -9.02	-0.08 / -0.87	-0.07 / -3.24
	Dimer	-3.40 / -5.34	-5.22 / -7.51	-6.79 / -7.02	-1.11 / -1.60	-0.73 / -3.44
TAP	Monomer	-3.29 / -5.70	-5.60 / -9.27	-8.04 / -9.34	0.59 / -0.81	0.41 / -3.17
	Dimer	-3.47 / -5.70	-5.53 / -8.40	-7.53 / -7.88	-0.90 / -1.44	-0.73 / -3.62
tTAP	Monomer	-3.25 / -5.53	-5.40 / -9.02	-7.73 / -9.17	0.63 / -0.78	0.45 / -3.13
	Dimer	-3.27 / -5.65	-5.21 / -8.30	-7.39 / -7.79	-0.64 / -1.19	-0.44 / -3.64
mTAP	Monomer	-3.24 / -5.55	-5.48 / -9.01	-7.82 / -9.24	0.62 / -0.78	0.45 / -3.10
	Dimer	-3.34 / -5.50	-5.36 / -8.03	-7.16 / -7.42	-0.93 / -1.46	-0.59 / -3.41

Table S4.2 Summaries of some key optical performances in various guest@TPBi systems.

Guest@TPBi	Ex. (nm)	PL (nm)[a]	PersL (nm)[b]	PersL duration (h)[c]
pTAP	365	683	695	-
	450	684	693	4.6
	520	683	696	1.2
	620	686	697	0.4
TAP	450	664	681	4.6
tTAP		680	710	1.2
mTAP		711	722	1.3

[a] Peak wavelength of the PL spectra at room temperature.

[b] Peak wavelength of the PersL spectra.

[c] Lasting duration of the PersL recorded by a PMT after ceasing the irradiation light.

Table S4.3 Summaries of trap depth in various guest@TPBi systems.

Guest@TPBi	Ex. (nm)	$\varepsilon_{cal.}$ (eV)[a]				$A\varepsilon_{cal.}$ (eV)[b]	ε_{MV} (eV)[c]	$\Delta\varepsilon$ (eV)[d]
		$\alpha_{TPBi} - \beta_G$	$\alpha_{TPBi} - \alpha_G$	$\beta_{TPBi} - \alpha_G$	$\beta_{TPBi} - \beta_G$			
pTAP	365						1.15 ± 0.01	0.15 ± 0.01
	450	1.25	1.26	1.35	1.34	1.30	1.17 ± 0.03	0.13 ± 0.03
	620						1.16 ± 0.01	0.14 ± 0.01
TAP	450	0.77	0.59	0.68	0.86	0.73	0.70 ± 0.02	0.03 ± 0.02

tTAP		0.73	0.55	0.64	0.82	0.69	0.64 ± 0.01	0.05 ± 0.01
mTAP		0.73	0.56	0.65	0.82	0.69	0.63 ± 0.01	0.06 ± 0.01

[a] Calculated trap depth from the D-value between the LUMO of TPBi radical anion and that of guest radical anion at the B3LYP/def2-SVP level of theory.

[b] Average calculated trap depth.

[c] Measured trap depth value from plotting $\ln(T_m^2/\beta_h)$ against $1/(k_B \cdot T_m)$ under TL measurement using the Randall-Wilkins model.

[d] Difference in of $\varepsilon_{cal.}$ and ε_{MV}.

Chapter 5

Trap-Induced Persistent Luminescence in Organic Light-Emitting Diodes

Note: This work resulted in a publication titled "Trap-Induced Persistent Luminescence in Organic Light-Emitting Diodes" in *InfoMat* and just been accepted, presented here.

5.1 Abstract

Luminescence in organics that lasts for seconds to a few hours after light excitation has been reported recently, showcasing significant application potentials in flexible electronics and bioimaging. In contrast, long-lasting luminescence that can be electrically excited, whether in organics or inorganics, is much rarer and often less efficient. In this study, we report persistent luminescence (PersL) in organic light-emitting diodes (OLEDs) that lasts over 100 s and an energy storage effect beyond 60 min after charging with a direct-current electric field. Thermoluminescence studies reveal that the PersL in OLEDs is induced by traps formed in a host-guest molecular system serving as an emission layer (EML) with a trap depth of approximately 0.24 eV, consistent with the results from the same EML materials under light irradiation. Integrating results from transient absorption spectra, electronic spin resonance, and density functional theory calculations, we propose a model delineating the charge carrier migration responsible for the trap-induced PersL in OLEDs. This study on trap-induced PersL in OLEDs may deepen our understanding of the luminescence mechanism in organic semiconductors and pave the way for expanding their applications in optoelectronics, energy storage and biological detection technologies.

5.2 Introduction

Luminescence in organics has garnered extensive interest over recent decades due to its inherent structural flexibility, high emission efficiency, controllable luminescence dynamics, and widely applicable semiconductor properties.[1,2] It has catalyzed the development of advanced displays, wearable devices, and flexible electronics technologies.[3-5] Historically, room temperature phosphorescence (RTP) and thermally activated delayed fluorescence (TADF), which involve spin-forbidden electronic transitions of triplet and singlet states, have been the primary strategies for achieving long-lasting luminescence in organic systems.[6] Through well-studied strategies such as enhancing the production of triplet excitons, stabilizing triplet excited states, or mitigating nonradiative pathways, the development and application of organic materials with RTP and TADF properties have seen remarkable success.[7-18] Only recently, a new form of long-lasting luminescence, known as persistent luminescence (PersL), with decay characteristics distinct from RTP and TADF, has been identified in organics.[19-26] While the exact PersL mechanism in organics requires further in-depth exploration, it is observed that the long-lasting decay characteristics, energy storage capacity, thermoluminescence (TL) effect, and the relevance to traps in certain PersL organic materials are consistent with those of typical inorganic PersL phosphors.[27] Consequently, a model describing charge carrier migration in host-guest luminescent molecular systems after turning off light excitation, including charge separation, trapping, detrapping and recombination, has been proposed (Figures 5.1a-5.1b). This model establishes a bridge between the widely accepted PersL mechanism in inorganic phosphors and organic materials with wide-bandgap semiconductor properties.[28-33]

Light irradiation, particularly at short wavelengths, is the primary energy source for producing long-lasting luminescence in both organic and inorganic materials.[34,35] On the other hand, electric power, which is the most commonly utilized excitation method for devices offering exceptional user-friendliness and controllability, is the energy source for the majority of artificial light, including various light-emitting diodes

(LEDs).[36-40] Despite this, progress in realizing electrically excitable long-lasting luminescence is slow, which is incongruous with the substantial application value of electrically driven light-emitting devices. Recently, several types of long-lasting luminescence have been reported in organic LEDs (OLEDs).[41-44] These OLEDs leverage the efficient charge carrier injection of organic semiconductors, and utilize organic luminescent materials, such as deuterated RTP emitters, TADF dimers, or PersL exciplex films as the emission layer (EML) materials to achieve long-lasting luminescent OLEDs that last for seconds or minutes after the electric power supply is turned off. The long-lasting luminescence in OLEDs opens a new avenue for organic luminescent materials to attain novel optoelectronic properties and applications. However, achieving electrically excited PersL with ultralong lifetimes remains a significant challenge, which inevitably impedes the development of effective material design methodologies and high-performance optoelectronic devices.

In this study, we developed electrically chargeable long-lasting luminescent OLEDs by combining the inherent charge carrier injection structure of OLEDs with the charge carrier trapping capacity of EML materials, and investigated the intermediate products during long-lasting luminescence to unravel the underlying mechanism (Figure 5.1c). TL measurements on the OLEDs after electric charging were conducted to assess the generated traps and trap depths, which were compared with those of the same EML materials after light irradiation, yielding similar results. In addition, transient absorption (TA), electronic spin resonance (ESR), and density functional theory (DFT) calculations were employed to further confirm the existence of traps as intermediate products after charging. The findings clearly indicate that the long-lasting luminescence in the OLEDs should be primarily attributed to the trapping-detrapping effect of traps, with the charge carrier migration in the OLEDs after electric charging similar to the trap-induced PersL model in organics after light irradiation (Figure 5.1d). The fabricated OLEDs exhibit long-lasting PersL over 100 s, temperature-dependent decay characteristics, and energy storage effects within the EML, thus enabling them to find

new applications, such as time-temperature indicators (TTIs).[45]
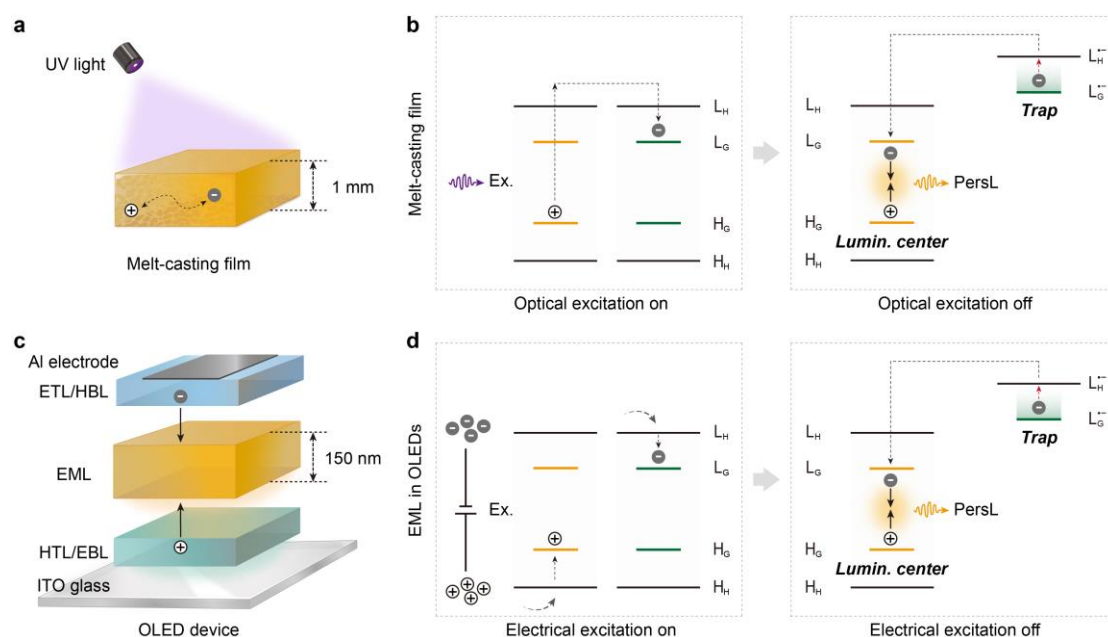
Figure 5.1 Trap-induced PersL charged by light irradiation or an electric field. **a**, Schematic diagram of the host-guest EML materials under UV light irradiation. **b**, Mechanism of the trap-induced PersL in organics charged by light irradiation. During light excitation, some electrons are moved from the guest molecules (luminescent centers), captured by other neighboring guest molecules *via* the host, and form traps in a radical anion state (trap centers). The captured electrons can be released from the traps under thermal stimulation and subsequently recombine with the luminescent centers to give PersL. **c**, Device configuration of typical OLEDs. **d**, Proposed mechanism of the trap-induced PersL in OLEDs charged with an electric field. Under an electric field, charge carriers are injected into the EML from two sides. In addition to direct recombination to generate electroluminescence (EL), some electrons can be temporally captured by traps, similar to the case of light irradiation. The captured electrons are released from traps under thermal stimulation and finally recombine with the holes to give PersL. Abbreviations and labels: electrons (gray balls), holes (white balls), luminescent centers (Lumi. center), electron transporting layer (ETL), hole blocking

layer (HBL), emission layer (EML), hole transporting layer (HTL), electron blocking layer (EBL), indium tin oxide (ITO), lowest unoccupied molecular orbital (LUMO), highest occupied molecular orbital (HOMO), frontier orbitals of luminescence centers (orange bars), and frontier orbitals of traps (green bars).

5.3 Experimental Procedure

5.3.1 Materials and Characterizations

All reagents and chemicals were of reagent grade, commercially available and used without further purification. Materials for OLEDs fabrication, including 1,4,5,8,9,11-hexaazatriphenylene hexacarbonitrile (HAT-CN), N,N'-bis(1-naphthalenyl)-N,N'-bis-phenyl-(1,1'-biphenyl)-4,4'-diamine (NPB), 1,3-bis(N-c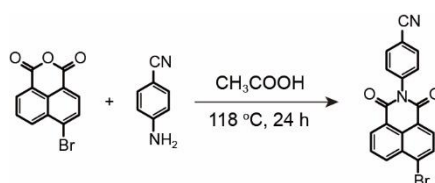arbazolyl)benzene (mCP), and 1,3,5-tris(1-phenyl-1H-benzimidazol-2-yl)benzene (TPBi), were sourced from Luminescence Technology Corp. and Xi'an Polymer Light Technology Corp. without additional purification.

Synthesis of NABN

Scheme 5.1 Synthetic route of 4-(6-bromo-1,3-dioxo-1*H*-benzo[*de*]isoquinolin-2(3*H*)-yl)benzonitrile (**NABN**) molecules.

Synthesis of NABN. To a 250 mL round-bottom flask containing (2.89 g, 10 mmol) of 4-bromo-1,8-naphthalic anhydride (96%) in 100 mL of glacial acetic acid, (6.03 g, 50 mmol) of 4-aminobenzonitrile (98%) was added. The mixture was refluxed for around 24 h until precipitation occurred in the solution. After the reaction was finished, the mixture was poured into ice water. The resulting precipitates were filtered and purified by recrystallization from acetone. Gray powders were obtained, and the yield was 37.0%. ^{1}H NMR (500 MHz, CDCl$_3$) δ 8.67 (dd, J = 14.3, 7.9 Hz, 2H), 8.44 (d, J = 7.9 Hz, 1H), 8.09 (d, J = 7.9 Hz, 1H), 7.89 (dd, J = 8.5, 7.4 Hz, 1H), 7.83 (d, J = 8.5 Hz, 2H), 7.45 (d, J = 8.5 Hz, 2H). ^{13}C NMR (126 MHz, CDCl$_3$) δ 163.47, 163.43, 139.44, 134.30, 133.27, 132.84, 131.95, 131.49, 131.44, 131.03, 130.17, 129.46, 128.45, 122.85, 121.94, 118.29, 112.93. ESI: calcd for C$_{19}$H$_9$BrN$_2$O$_2$ [M+Na]$^+$:

400.1862, found: 400.9720. Elemental analysis calcd for $C_{19}H_9BrN_2O_2$: C, 60.50; H, 2.41; N, 7.43, found: C, 60.53; H, 2.24; N, 7.39.

Synthesis of CPN
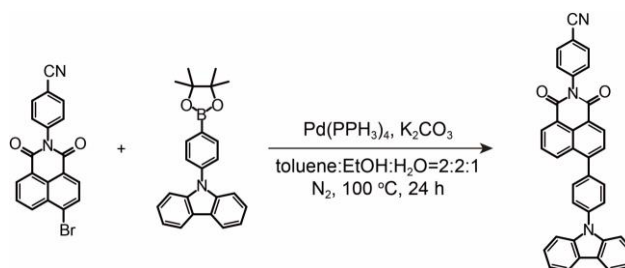
Scheme 5.2 Synthetic route of 4-(6-(4-(9*H*-carbazol-9-yl)phenyl)-1,3-dioxo-1*H*-benzo[*de*]isoquinolin-2(3*H*)-yl)benzonitrile (**CPN**).

NABN (377.20 mg, 1 mmol), 9-(4-(4,4,5,5-tetramethyl-1,3,2-dioxaborolan-2-yl)phenyl)-9*H*-carbazole (443.12 mg, 1.2 mmol), potassium carbonate (414.6 mg, 3 mmol), toluene, anhydrous ethanol and distilled water (25 mL, 2:2:1, v/v/v) were added and stirred for 1 h under a nitrogen atmosphere. After that, tetrakis(triphenylphosphine)palladium(0) (231.11 mg, 0.2 mmol) was quickly added, and the mixture was heated to 100°C under a nitrogen atmosphere for 24 h. After cooling to room temperature, the mixture was extracted with CH_2Cl_2, and the organic layer was washed with sodium chloride water and then dried over anhydrous $MgSO_4$ and concentrated. The crude product was purified by column chromatography on silica gel (petroleum ether/dichloromethane = 1:1-1:5, v/v) to give TN as an orange solid (yield = 89%). This compound was further purified by temperature gradient sublimation under vacuum. ^1H NMR (500 MHz, $CDCl_3$) δ 8.73 (dd, *J* = 11.7, 6.9 Hz, 2H), 8.50 (d, *J* = 7.6 Hz, 1H), 8.18 (d, *J* = 7.7 Hz, 2H), 7.88 (d, *J* = 7.4 Hz, 2H), 7.86-7.82 (m, 2H), 7.80 (d, *J* = 8.5 Hz, 2H), 7.77 (d, *J* = 8.5 Hz, 2H), 7.56 (d, *J* = 8.2 Hz, 2H), 7.50 (d, *J* = 8.5 Hz, 2H), 7.46 (t, *J* = 7.1 Hz, 2H), 7.33 (t, *J* = 7.4 Hz, 2H). ^{13}C NMR (126 MHz, $CDCl_3$) δ 164.29, 164.08, 147.09, 140.91, 139.87, 138.71, 137.70, 133.60, 133.50, 132.35, 131.85, 131.70, 130.57, 130.40, 129.49, 128.52, 127.62, 127.49, 126.43, 123.97, 122.97, 121.97, 120.80, 120.68, 118.55, 113.11, 110.00. ESI: calcd for

$C_{37}H_{21}N_3O_2$ [M+Na]$^+$: 562.5832, found: 562.1523. Elemental analysis calcd for $C_{37}H_{21}N_3O_2$: C, 82.36; H, 3.92; N, 7.79, found: C, 81.93; H, 4.09; N, 7.64.

5.3.2 Synthesis of CPN@TPBi Melt-Casting Films

A mixture of CPN and TPBi (~1 mmol in total) was heated to 350°C on a quartz substrate in a glovebox. Upon melting, the mixture was stirred homogeneously and rapidly cooled to room temperature. The sample was encapsulated in glass cases (~20 × 20 × 1 mm^3) by using UV-light-cured epoxy resin as an encapsulant.

5.3.3 Fabrication of OLEDs

The OLEDs were fabricated via thermal evaporation onto ITO-coated glass substrates (Suzhou Fangsheng Optoelectronics) in a high vacuum environment (*ca.* 5.0 × 10^{-5} Pa). The substrates were carefully cleaned with detergent, distilled water, acetone, and isopropanol, dried in a drying oven at 80°C, and then treated with a plasma cleaner (Diener Femto) for 30 min before vacuum deposition. When the vacuum degree of the evaporating cave reached 5×10^{-5} Pa, the organic materials were evaporated at a rate of 1-1.5 Å/s, the LiF was evaporated at a rate of 0.1 Å/s, and the aluminum was evaporated at 5 Å/s. All the OLEDs were encapsulated and measured in a standard dry nitrogen glovebox. The voltage, current, luminance, and radiant flux characteristics were measured using a source meter (2400, Keithley) and an absolute EQE measurement system (C9920-12, Hamamatsu).

5.3.4 Photophysical Characterization

Emission spectra and luminescence decay curves were collected with a fluorescence spectrometer (FLS980, Edinburgh). ESR spectra were obtained using an X-band EPR spectrometer (EMXplus-9.5/12, Bruker). Photographs and videos of the samples were taken with a digital camera (EOS 5D Mark II, Canon and *α*7SIII, Sony). The PersL decay curves and TL glow curves were recorded using a homemade measurement system. Briefly, the samples were placed on a cooling-heating stage (THMS600E, Linkam) with a controllable temperature range of 100 to 800 K. The sample chamber

was filled with dry nitrogen gas, and quartz glass was installed at the top of the chamber. The samples were excited by electric power (for the OLEDs, different voltages) or ultraviolet light (for the CPN@TPBi films, excitation power density ~5 mW/cm^2) for 5 minutes. The intensity of the PersL or TL after ceasing the excitation sources was monitored with a filter-attached photomultiplier tube (R928P, Hamamatsu). The spectra of PersL or TL were recorded simultaneously using a multichannel spectrometer (QE-Pro, Ocean Optics). In a typical TL measurement, the OLEDs or samples were cooled to 150 K and charged with the excitation sources for 5 minutes. After a preset waiting time of 20 s, the OLEDs or samples were heated to 350 K at a certain heating rate (100, 75, 50, 35, or 20 K/min), and the emission intensity was recorded by photodetectors. The above measurement system was driven by a computer program based on the LabVIEW system.

5.3.5 Cyclic Voltammetry Tests

The energies of the HOMO and LUMO levels were also measured via cyclic voltammetry with a PalmSens 4 electrochemical workstation using Pt as the working electrode, platinum wire as the auxiliary electrode, and Ag wire as the reference electrode standardized against ferrocene/ferrocenium. The solutions were prepared inside a glovebox to ensure an oxygen-free atmosphere, and the reduction and oxidation potentials were measured in anhydrous CH_2Cl_2 solutions containing 0.1 M tetrabutylammonium hexafluorophosphate (n-Bu$_4$NPF$_6$) as the supporting electrolyte at a scan rate of 0.1 V s^{-1}.

5.3.6 Energy Level Calculations

The time-dependent density functional theory (TD-DFT) method was used to evaluate the excitation energy and oscillator strength (f) of the excited states (S$_1$ and T$_1$) based on the equilibrium configuration of the ground state (S$_0$) at the B3LYP/def2-SVP level. We calculated the HOMO and LUMO levels using the Gaussian 16 package. All neutral molecules were optimized at the B3LYP/def2-SVP level for stable equilibrium

geometries in the ground state (S_0) using the Gaussian 16 program. The geometries of the anions and cations were obtained on the basis of the neutral S_0 structures. All the molecular orbitals were depicted for the closed-shell and open-shell systems.

5.4 Results and Discussion

To validate the proposed scheme, we adopted the typical device configuration of OLEDs and selected a host-guest molecule system as the EML material (see Figure 5.1c). As a representative example, 1,3,5-tris(1-phenyl-1*H*-benzimidazol-2-yl)benzene (TPBi) was used as the host molecule due to its fast electron mobility, and 4-(6-(4-(9*H*-carbazol-9-yl)phenyl)-1,3-dioxo-1*H*-benzo[*de*]isoquinolin-2(3*H*)-yl)benzonitrile (CPN) was chosen as the guest molecule due to its nearly 100% exciton harvesting capability as a potential TADF emitter (Figure 5.2a).[46] CPN was synthesized in two steps including dehydration reaction and palladium catalyzed Buchwald-Hartwig cross-coupling reaction, followed by comprehensive characterization via ^{1}H/^{13}C nuclear magnetic resonance (NMR) spectroscopy, liquid chromatography-mass spectrometry (LC-MS), and elemental analysis (Figures S5.1-S5.2). The synthesized CPN shows excellent thermal stability with an elevated decomposition temperature (T_d, corresponding to a 5% weight loss) at 419°C and a high glass transition temperature (T_g) at 331°C (Figure S5.3). The doping ratio of CPN with respect to the TPBi host varied from 1 to 100 wt%. According to the photoluminescence quantum yield (Φ_{PL}) measurements, the optimal doping ratio of CPN was 10 wt%, and the maximum Φ_{PL} reached 96.4% (Figure S5.4).

The multilayered configuration and energy levels of the fabricated OLEDs are depicted in Figure 5.2b. The OLEDs consist of ITO/1,4,5,8,9,11-hexaazatriphenylene hexacarbonitrile (HAT-CN, 10 nm, hole injecting layer)/N,N'-bis(1-naphthalenyl)-N,N'-bis-phenyl-(1,1'-biphenyl)-4,4'-diamine (NPB, 40 nm, hole transporting layer)/1,3-bis(N-carbazolyl)benzene (mCP, 10 nm, EBL)/10 wt% CPN@TPBi (30 or 150 nm , EML)/TPBi (60 nm, ETL)/LiF (1 nm, electron injecting layer)/Al (120 nm). The EL characteristics of the OLEDs with 10 wt% CPN doping ratios and different EML thickness (30 or 150 nm) are illustrated in Figures 5.2c-5.2e and Table 1. The OLEDs with 30 and 150 nm EML thickness both showed sky-blue emission with emission peaks at 478 nm (Figure 5.2c). OLEDs with a 30 nm emissive layer (EML)

exhibited a lower turn-on voltage of approximately 3.5 V at an EL brightness of 1 cd m^{-2}, whereas the device with a 150 nm EML displayed a relatively higher turn-on voltage of 6.6 V (Figure 5.2d). Both OLEDs exhibit high luminescence output of 9764.4-9905.5 cd m^{-2} (Figure 5.2d). As shown in Figure 2E, the OLEDs with 30 nm EML thickness show a maximum current efficiency (CE) of 6.02 cd A^{-1}, a maximum power efficiency (PE) of 1.08 lm W^{-1}, and a maximum external quantum efficiency (EQE) of 2.59%. In contrast, the LEDs with 30 nm EML exhibit higher maximum efficiencies of 13.81 cd A^{-1} (CE), 11.05 lm W^{-1} (PE), and 12.69% (EQE). Notably, the maximum EQE of device with 30 nm EML surpasses the theoretical limit of 5% for fluorescent-type OLEDs, which verifies the efficient exciton recombination probability of the host-guest molecule system used.[47] Additionally, compared to the OLEDs with 1 or 5 wt% CPN doping ratios, the devices with 10 wt% CPN@TPBi as EML exhibits the highest EQE$_{max}$ (Figure 5.2e, Figure S5.5 and Table S5.1). Although the PersL intensity decreased with increasing guest concentration (Figure S5.6), a doping ratio of 10 wt% CPN was selected for subsequent experiments to optimize device performance.
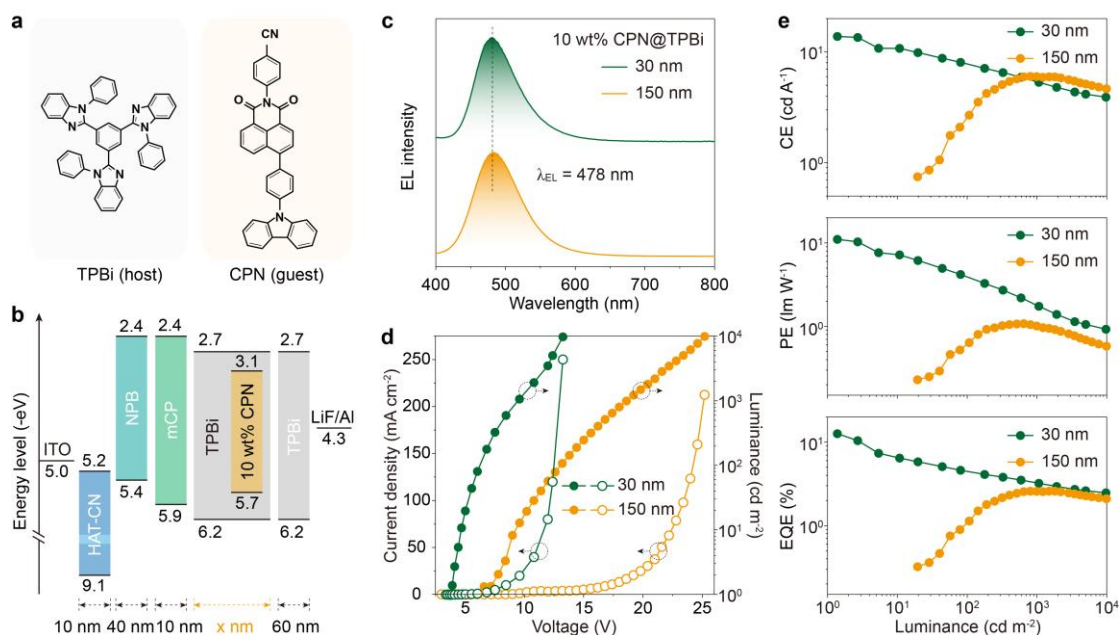

Figure 5.2 EL performance of the OLEDs using CPN@TPBi as the EML material.

a, Chemical structures of TPBi (host molecule) and CPN (guest molecule). **b**, Energy level diagram and multilayered configuration of the fabricated OLEDs. **c**, EL spectra of OLEDs using 10 wt% CPN@TPBi with different EML thickness (30 and 150 nm). **d**, Luminance and current density of the OLEDs working at different voltages. **e**, Current efficiency (CE), power efficiency (PE), and external quantum efficiency (EQE) as a function of luminance.

Table 1 | EL performance of the OLEDs fabricated using 10wt% CPN@TPBi with different 30 nm and 150 nm EML thickness.

EML thickness [nm]	V_{on}[a) [V]	L_{max}[b) [cd m^{-2}]	CE_{max}[c) [cd A^{-1}]	PE_{max}[d) [lm W^{-1}]	EQE_{max}[e) [%]	λ_{EL}[f) [nm]
30	3.8	9764.4	13.81	11.05	12.64	478
150	6.6	9905.5	6.02	1.08	2.59	478

[a] Voltage at 1 cd m^{-2}.

[b] The maximum luminance.

[c] The maximum current efficiency.

[d] The maximum power efficiency.

[e] The maximum external quantum efficiency.

[f] Measured at the maximum luminance.

Subsequently, the PersL behavior of the OLEDs after turning off the driving electric field was studied. Four OLEDs with different thicknesses of the EML materials (10 wt% CPN@TPBi) were fabricated. As depicted in Figure 5.3a, all the OLEDs show PersL lasting for more than 10 s after ceasing the electric power. Notably, all the recorded PersL decay curves deviate significantly from the single-exponential decay functions

(Figure S5.7), and they approximate straight lines in log-log coordinates (Figure 5.3a). This indicates that the PersL of the OLEDs after electric charging is clearly different from the typical RTP process. In addition, when we fix the EL intensity of the OLEDs at 11,300 mcd m^{-2} (under electric charging), the PersL intensity increases with increasing EML thickness. The variation in the PersL-to-EL intensity ratio suggests that the PersL and EL might be attributed to two different charge carrier migration processes (*i.e.*, direct recombination to give EL and transport via traps to give PersL), and increasing the EML thickness (*i.e.*, longer transport distances) is conducive to improving the probability of PersL. Impressively, the PersL decay time (defined as the time when the PersL intensity decays to the noise ratio of the photodetector) of the OLEDs recorded at RT exceeds 60 s when the EML thickness is greater than 150 nm. Considering that an excessively thick EML (*e.g.*, 250 nm) significantly increases the turn-on voltage and reduces the EL efficiency of the OLEDs (Figure S5.8 and Table S5.2), we used 150 nm as the EML thickness in the following studies.

The PersL performance of the OLEDs after charging at different voltages was investigated. The PersL intensity is improved with increasing driving voltage, and it becomes saturated above 12.5 V (Figure 5.3b). In fact, the OLEDs show different PersL decay curves at various working temperatures. The initial PersL intensity (1 s after ceasing the electric field) increases as the working temperature decreases from 350 to 100 K, and the longest decay time (> 100 s) is found at 150 K (Figure 5.3c). This indicates that the PersL of the OLEDs is a temperature-dependent process and again it is different from the previously reported afterglow phenomenon.[41,43,44] After the PersL intensity decays to a low value, the intensity could be recovered to the initial value by electric recharging (Figure 5.3d). From this point of view, one can consider that electric charging and PersL decay are two reversible processes. Finally, we recorded the PersL decay curves as the temperature increased by half. After the OLEDs were charged at 150 K for 1 min, they were kept power-off at 150 K for 30 s and subsequently heated to a higher temperature of 250, 300, or 350 K at a heating rate of 150 K/min.

Interestingly, the PersL intensity increases during heating, while the intensity decays even faster after reaching the target temperature (Figure 5.3e). To summarize the above results, the PersL of OLEDs after electric charging is an energy storage and thermally activated process, which is the same as that of trap-induced PersL in organics caused by light irradiation.[27] Therefore, the minute-level PersL of the electrically charged OLEDs should be attributed to the traps.
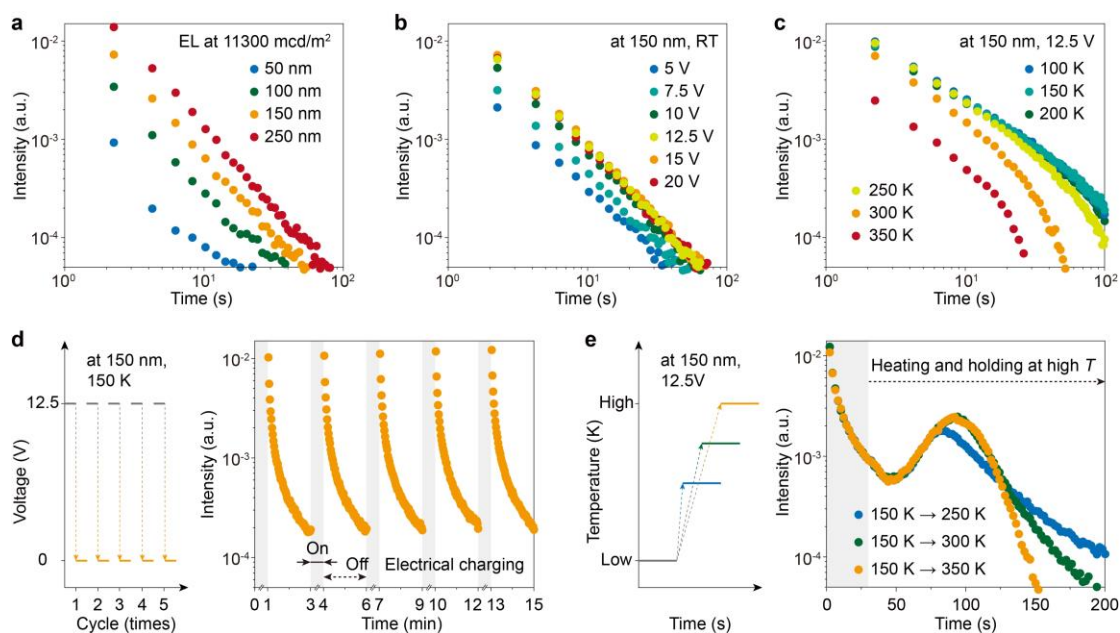

Figure 5.3 PersL properties of the OLEDs after charging with an electric field. **a**, PersL decay curves of the OLEDs with different EML thicknesses of CPN@TPBi from 50 to 250 nm after turning off the electric power. The doping ratio of CPN was 10 wt%. The EL intensity under the electric field was set at 11300 mcd/m^2 by controlling the driving voltage in the ranges of 10 to 15 V. The measurements were performed at RT. **b**, PersL decay curves after turning off the electric field at voltages varying from 5 to 20 V. The EML thickness was 150 nm. The measurements were performed at RT. **c**, PersL decay curves recorded at different temperatures. The EML thickness was 150 nm, and the driving voltage was 12.5 V. **d**, PersL decay curves of the OLEDs under intermittent electric charging (right) and the applied voltage profile (left). EML

thickness, 150 nm; driving voltage, 12.5 V; temperature, 150 K; electric charging time, 1 min; recording time, 2 min in 1 cycle. **e**, PersL decay curves of the OLEDs using a temperature course changed at halfway (right) and the applied temperature profile (left). EML thickness, 150 nm; driving voltage, 12.5 V; start temperature, 150 K; target temperature, 250, 300, or 350 K; heating rate, 150 K/min.

The frontier molecular orbitals (FMOs) and electronic states of CPN were obtained by density functional theory (DFT) calculations based on the optimized ground-state geometries. As shown in Figure 5.4a, the HOMO and LUMO are predominantly localized on the 9-phenyl-9*H*-carbazole segment and 4-(1,3-dioxo-1*H*-benzo[*de*]isoquinolin-2(3*H*)-yl)benzonitrile (NABN) cores, respectively. The calculated energy levels of the HOMO and LUMO are approximately -5.86 and -2.94 eV, respectively. These values are in agreement with the HOMO and LUMO levels (-5.68 and -3.05 eV) obtained from cyclic voltammetry (CV) measurements (Figure S5.9). The energy difference between the lowest triplet and singlet states of CPN (ΔE_{ST}) was calculated to be 0.20 eV. The small value of ΔE_{ST} is attributed to the significant separation of the HOMO and LUMO.

The fluorescence spectra of the pure CPN film at 77 K exhibit a broad band centered at 545 nm, and the delayed fluorescence spectra (delay time, 20 ms) show two bands at 545 and 610 nm (top panel of Figure 5.4b). The energy levels of S_1 and T_1 are 2.28 and 2.03 eV, respectively, with respect to the S_0 level, and the ΔE_{ST} is 0.25 eV. Moreover, the intensity of the delayed fluorescence is enhanced as the temperature increased from 77 to 300 K, which also verifies the TADF feature of CPN (Figure S5.10). The steady-state fluorescence spectra and delayed fluorescence spectra of the CPN@TPBi film (middle and bottom panels of Figure 5.4b) are similar to those of pure CPN molecule in neat film and CPN in toluene (top panel of Figure 5.4b and Figure S5.11), suggesting that CPN is the luminescent center in the CPN@TPBi guest-host system. Notably, both the steady-state fluorescence and delayed fluorescence in CPN@TPBi show a slight

blueshift in emission. This could be ascribed to the effects of CPN molecule aggregation and TPBi polarization. Nevertheless, the ΔE_{ST} value is almost unchanged for pure CPN (0.25 eV) and CPN@TPBi (0.26 eV). Due to the small value of ΔE_{ST}, the probability of reverse intersystem crossing (RISC) is high at RT.[38] It is thus understandable that the delayed fluorescence spectra of the CPN@TPBi film (delay time of 20 ms, bottom of Figure 5.4b) and the PersL spectra at RT (1 min or 2 h after ceasing the light excitation, Figure S5.12) are dominated by the S_1-S_0 emission band at 510 nm.

To explore the origin of the PersL, thermoluminescence (TL) glow curves of the OLEDs after electric charging and those of the CPN@TPBi melt-casting film after UV light irradiation were measured (Figure 5.4c). We record similar TL glow curves in the two measurements, which show peaks in the temperature range of 220~250 K, and the peak temperature turns higher with a larger heating rate. The trap depths (ε) in the two measurements were estimated using the Randall-Wilkins model:[48]

$$\frac{\beta \varepsilon}{k_B \cdot T_m^2} = s \cdot \exp\left(\frac{-\varepsilon}{k_B \cdot T_m}\right) \quad \text{(Equation 5.1)}$$

where k_B is the Boltzmann constant, T_m (K) is the peak temperature obtained from the TL glow curves, and s (s^{-1}) is the frequency factor. The results show that the estimated trap depths are close, with 0.24 ± 0.01 and 0.28 ± 0.01 eV for the electrically charged OLEDs and light-charged CPB@TPBi film, respectively (Figure 5.4d). The temperature-wavelength-intensity mapping (3D-plot) of TL in CPB@TPBi further indicates that the TL in the whole range of 100 to 400 K is primarily attributed to the S_1-S_0 transition of CPN (Figure 5.4e). It is reasonable to believe that in both cases of electric charging or light irradiation, a part of the input energy is stored by traps in CPN@TPBi, and the trapped charge carriers could be thermally released to give TL (PersL) at the luminescence centers of CPN.

Furthermore, ESR spectra of the CPN@TPBi melt-casting film were recorded (Figure 5.4f). After UV excitation, ESR signals with a g-factor of ~2.0241 are obtained. These ESR signals correspond to the formation of radical species with unpaired

electrons.[49] The ESR intensity is lowered as the excitation temperature increases from 100 to 300 K, indicating that more radical species return to neutral states at higher temperatures. The decrease in the ESR intensity is consistent with the decrease in the PersL intensity with increasing temperature, as shown in Figure 5.3c.

Moreover, the femtosecond transient absorption (fs-TA) spectroscopy was used to investigate the dynamics of the charge carrier transition. Using a fs-laser at 365 nm as the pumping source, we first detect positive TA signals at 505 nm (lifetime ~2.10 ns) and 635 nm (lifetime ~0.93 ns) in the pure TPBi film (Figure S5.13). These TA signals are attributed to the excited-state absorption (ESA) of the TPBi radical species. In the pure CPN film, as shown in Figure S5.14, TA signals due to the ESA of CPN radical species are found at 525 nm (lifetime ~0.03 ns). As for the CPN@TPBi sample, we detect similar TA signals at 525 and 635 nm with a much higher intensity (Figure 5.4g). Importantly, the lifetimes of these TA signals are ~0.62 ns at 525 nm, which are markedly longer than those of the pure CPN film (Figure S5.15). The TA spectra suggest that the formation of metastable radical species is significantly promoted in the host-guest system. Finally, the FMOs of both closed-shell (TPBi and CPN) and open-shell ($TPBi^{•+}$, $TPBi^{•-}$, $CPN^{•+}$, and $CPN^{•-}$) species were analyzed via DFT calculations at the B3LYP/def2-SVP level of theory (Figure 5.4h, Figure S5.16 and Table S5.3). Considering two different electron spin densities in an open-shell system (spin α and spin β), the energy gaps between the LUMO levels of $TPBi^{•-}$ and $CPN^{•-}$ were calculated to be 0.08, 0.21, 0.29, and 0.42 eV, respectively (Figure 5.4h). The average energy gap (~0.25 eV) closely aligns with the experimental trap depth (0.24-0.28 eV), indicating that the traps in CPN@TPBi are probably due to the energy difference between the LUMO levels of $CPN^{•-}$ and $TPBi^{•-}$.
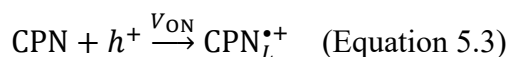
Based on the above results, a possible model for the PersL mechanism in the CPN@TPBi OLEDs is proposed (see Figure 5.1d). Under electric charging, electrons and holes are injected into the EML from two sides, and they may combine with the CPN guest molecules to form radical species of $CPN_T^{•-*}$ and $CPN_L^{•+}$ (steps i and ii).

The radical species are metastable, the electrons may escape from the guest to host molecules, and they require activation energy to cross the barrier between the energy levels of $CPN_T^{\bullet-*}$ and $TPBi^{\bullet-*}$ (*i.e.,* trap depth). Consequently, the trapped electrons could be released under thermal stimulation (step iii) and then recombine with the luminescent centers to give PersL (step iv). The four steps are briefly described as follows:
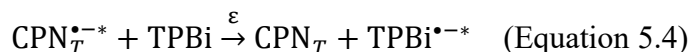
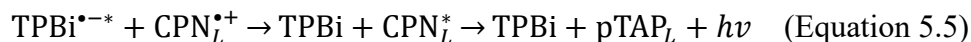[i] Electron injection and radical anion formation:

$$CPN + e^- \xrightarrow{V_{ON}} CPN_T^{\bullet-*} \quad \text{(Equation 5.2)}$$
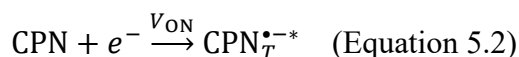
[ii] Hole injection and radical cation formation:

$$CPN + h^+ \xrightarrow{V_{ON}} CPN_L^{\bullet+} \quad \text{(Equation 5.3)}$$

[iii] Detrapping:

$$CPN_T^{\bullet-*} + TPBi \xrightarrow{\varepsilon} CPN_T + TPBi^{\bullet-*} \quad \text{(Equation 5.4)}$$

[iv] Charge recombination and photon emission:

$$TPBi^{\bullet-*} + CPN_L^{\bullet+} \rightarrow TPBi + CPN_L^* \rightarrow TPBi + pTAP_L + h\nu \quad \text{(Equation 5.5)}$$

where the asterisk denotes that the active site contains an electron in the LUMO levels, and the subscripts L and T denote that the CPN molecules work as luminescent centers and trap centers, respectively. The above PersL mechanism is similar to that of trap-induced PersL in organics after light irradiation. The proposed mechanism reveals that, in addition to light irradiation, an electricity supply is available for energy storage and long-lasting emission in organics, which may provide new possibilities for the application of organic luminescent materials.
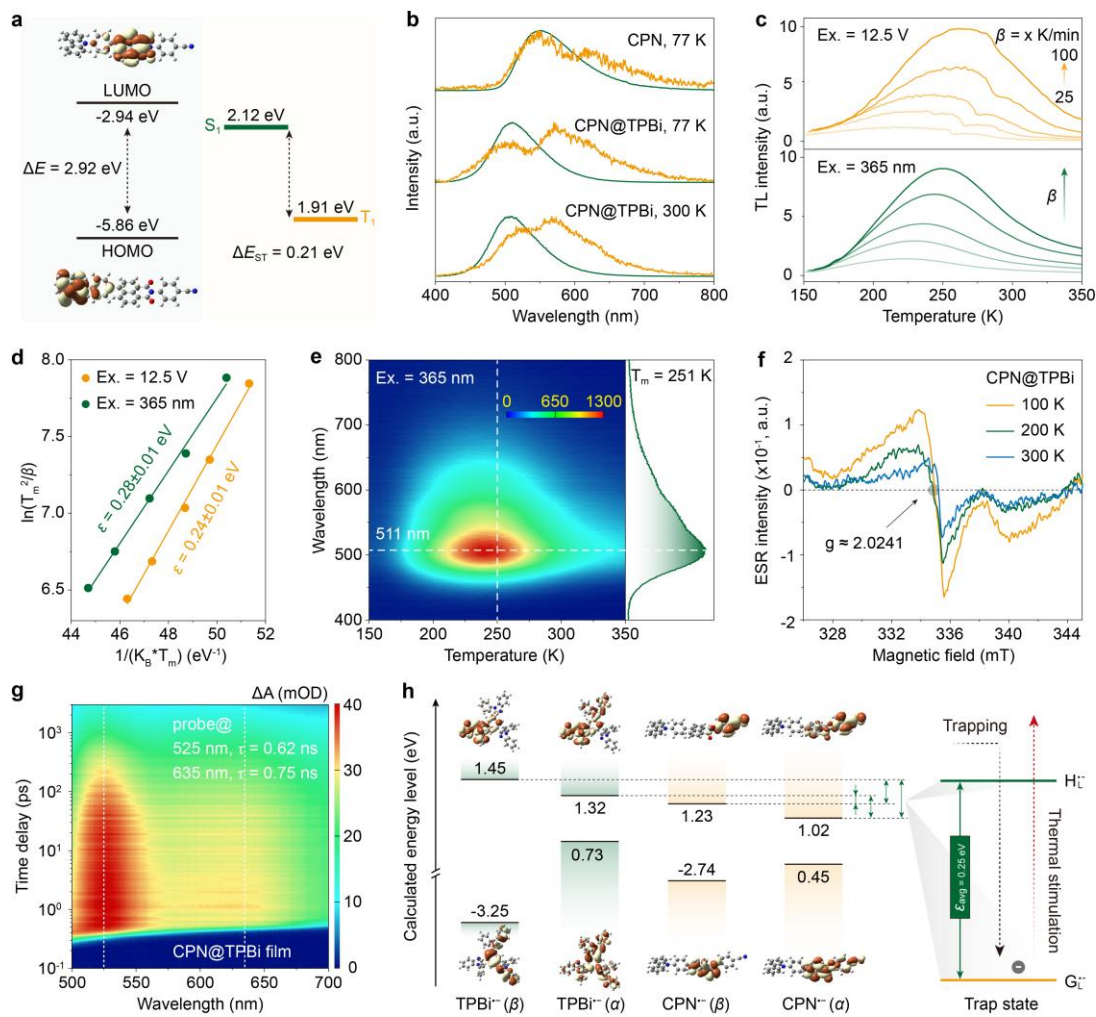
Figure 5.4 Luminescent centers and traps in the CPN@TPBi host-guest system. **a**, Electron density distribution and energy levels of the HOMO and LUMO in CPN according to DFT calculations. The right part shows the energy levels of S_1 and T_1 determined by time-dependent density functional theory (TD-DFT). **b**, Steady-state fluorescence (green curves) and delayed fluorescence spectra (delay time 20 ms, orange). The top, middle, and bottom panels are the results for the pure CPN film at 77 K and the 1 wt% CPN@TPBi melt-casting film at 77 and 300 K, respectively. **c**, TL glow curves of the electrically charged OLEDs and light-charged CPN@TPBi melt-casing film. The charging voltage for the OLEDs was 12.5 V; the excitation wavelength for the CPN@TPBi film was 365 nm; the charging time was 5 min; the charging temperature was 150 K; and the heating rates were 20, 35, 50, 75, and 100 K/min. **d**, Estimation of trap depths by using the Randall-Wilkins model. **e**, Temperature-

wavelength-intensity mapping (3D-plot) of TL in CPB@TPBi. The excitation wavelength was 365 nm, and the heating rate was 50 K/min. **f**, ESR spectra of the CPN@TPBi film recorded after UV light irradiation at 100 (orange), 200 (green), and 300 K (blue). **g**, Pseudocolor TA plots of CPN@TPBi using a fs-laser at 365 nm as the pumping source. The positive signals of ΔA (absorption difference) at 525 and 635 nm indicated the ESA of radical species. **h**, Schematic diagrams of the primary orbital configurations of TPBi$^{\bullet-}$ and CPN$^{\bullet-}$. The depth distributions of the traps formed by the LUMOs of TPBi$^{\bullet-}$ and CPN$^{\bullet-}$ are depicted on the right.

Finally, we demonstrated the potential applications of the electrically chargeable PersL in the field of time-temperature indicators (TTIs).[50,51] In general, TTIs can transform the time-temperature history into accessible information for users, which facilitates the monitoring of perishable foods, pharmaceuticals, or specialty chemicals throughout the entire transport-storage process. Since the liberation of charge carriers from traps is a kinetic process dependent on thermal activation, which is similar to the temperature-time-related loss rate of active ingredients in perishable products, the trap-induced PersL has been considered a valuable principle for the development of novel TTI technologies.[45] As schematically shown in Figures 5.5a-5.5b, charge carriers can be stored in the OLEDs by prior electric charging, and more carriers will be released in photon emission as the working temperature increases or the time is extended. Based on this principle, the time-temperature history of the OLEDs after charging can be reflected through the number of residual charge carriers in the OLEDs.

By utilizing the energy storage ability and time-temperature-related charge carrier release of the OLEDs, a new TTI method to monitor the quality of products for cold-chain transport is proposed, as shown in Figure 5.5c. In brief, charge carriers are prestored into OLEDs (TTIs) at 150 K under electric charging. The TTIs are subsequently kept at a certain temperature and transported along with the monitored products. Finally, the residual charge carriers in the TTIs are read out in the form of

optical information (by means of TL spectra) and compared with the standard curves to determine the time-temperature history experienced by the products. Based on the proposed scheme, we charged the OLEDs at 12.5 V at 150 K for 5 min. We set the standard storage temperature at 150 K and recorded the integral TL intensity of the OLEDs after different storage times (Figures 5.5d-5.5e). The integral TL intensity enables us to establish the standard curve of the TTIs working at 150 K. In the cases when the storage temperature is unexpectedly higher or lower than the standard temperature or in the cases when the storage time is longer or shorter than the preset time, the recorded TL intensity will be lower or higher than the values in the standard curves, respectively. The results will fall into the unsafe and safe regions determined by the standard curves, thus achieving the TTI function (Figure 5.5f). It should be noted that here, we simply demonstrate the conceptual applications of new TTIs based on the principle of the trap-induced PersL, which shows interesting electricity chargeability and reusability. However, more efforts, including increasing the trap density, enhancing the emission efficiency, and extending the storage time, should be made before these new-concept TTIs can be further considered for practical applications.
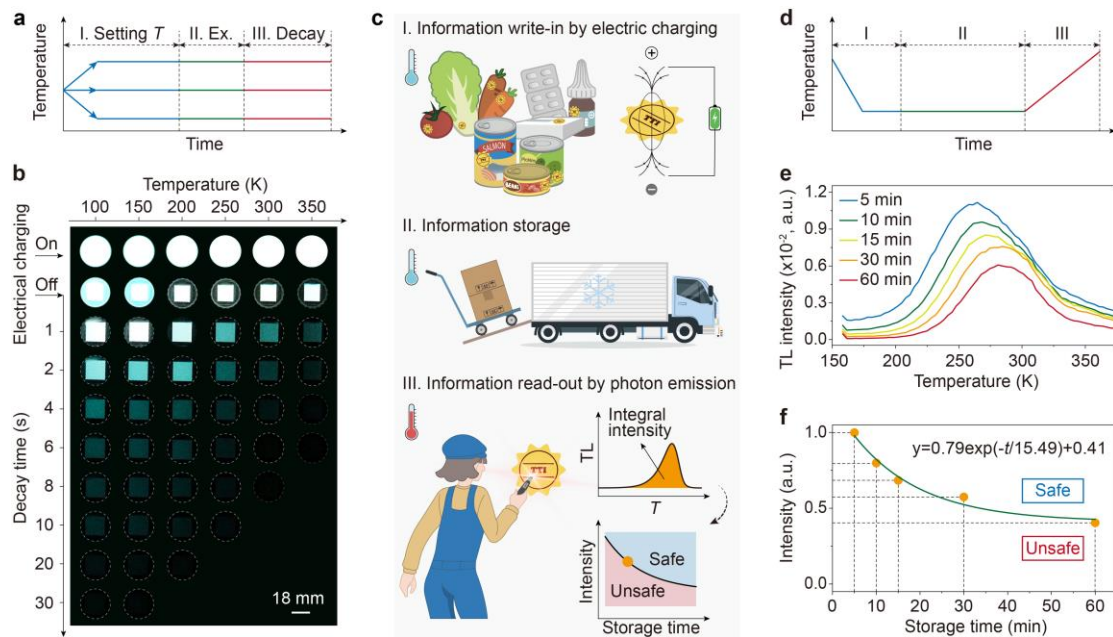
Figure 5.5 Demonstration of TTI application based on the principle of trap-induced PersL in OLEDs. **a**, Schematic temperature profile for the measurements of the energy storage ability of OLEDs. **b**, Optical photographs of the OLEDs (10 wt% CPN@TPBi) at different working temperatures and with different storage times after charging at 12.5 V. **c**, Schematic of the TTI application based on the principle of trap-induced PersL in OLEDs. It includes the steps of information write-in (I), information storage (II), and information read-out (III). **d**, Schematic temperature profile for the TTI application. **e**, TL glow curves after being kept at 150 K for different storage times (5, 10, 15, 30, and 60 min). **f**, Integral TL intensity as a function of storage time. The obtained results were used to fit the standard curve (green), which divided the chart into safe and unsafe regions. During the write-in and read-out cycles, the OLEDs were charged at 12.5 V for 5 min (write-in, I) and heated (read-out, III) to 350 K at a heating rate of 100 K/min.

5.5 Conclusion

In this work, we fabricated OLEDs with host-guest CPN@TPBi molecules as EML materials, which show over 100 s PersL intensity and beyond 1 h energy storage ability after ceasing electric charging. We revealed that the electrically chargeale PersL was attributed to trapping-detrapping processes of charge carriers. The trap depth of the trap-induced PersL in the fabricated OLEDs after electric charging was estimated to be 0.28 ± 0.01 eV, which is consistent with the results of the CPN@TPBi film after light irradiation. The traps in the studied host-guest system were assigned to the energy difference between the LUMO levels of $CPN^{\bullet-}$ and $TPBi^{\bullet-}$ in radical anions, which was supported by DFT calculations, ESR measurements, and TA spectra. Finally, due to the energy storage ability and time-temperature-related charge carrier release of the fabricated OLEDs, a new TTI method based on the principle of trap-induced PersL possible for cold-chain transport applications was proposed. We believe that this work may deepen the understanding of PersL in organics chargeable with different excitation sources and extend the applications of organic semiconductors in multifunctional photoelectric devices.

5.6 Reference

[1] B. Zhou, D. Yan, *Adv. Funct. Mater.* **2023**, 33, 2300735.

[2] Q. Li, Y. Tang, W. Hu, Z. Li, *Small.* **2018**, 14, 1801560.

[3] Y. Huang, E.-L. Hsiang, M.-Y. Deng, S.-T. Wu, *Light Sci. Appl.* **2020**, 9, 105.

[4] P. C. Chow, T. Someya, *Adv. Mater.* **2020**, 32, 1902045.

[5] H. Ling, S. Liu, Z. Zheng, F. Yan, *Small Methods* **2018**, 2, 1800070.

[6] W. Zhao, Z. He, B. Z. Tang, *Nat. Rev. Mater.* **2020**, 5, 869-885.

[7] W. Ye, H. Ma, H. Shi, H. Wang, A. Lv, L. Bian, M. Zhang, C. Ma, K. Ling, M. Gu, Y. Mao, X. Yao, C. Gao, K. Shen, W. Jia, J. Zhi, S. Cai, Z. Song, J. Li, Y. Zhang, S. Lu, K. Liu, C. Dong, Q. Wang, Y. Zhou, W. Yao, Y. Zhang, H. Zhang, Z. Zhang, X. Hang, Z. An, X. Liu, W. Huang, *Nat. Mater.* **2021**, 20, 1539-1544.

[8] N. Zhang, L. Qu, S. Dai, G. Xie, C. Han, J. Zhang, R. Huo, H. Hu, Q. Chen, W. Huang, H. Xu, *Nat. Commun.* **2023**, 14, 2901.

[9] Z. An, C. Zheng, Y. Tao, R. Chen, H. Shi, T. Chen, Z. Wang, H. Li, R. Deng, X. Liu, W. Huang, *Nat. Mater.* **2015**, 14, 685-690.

[10] Y. Liang, P. Hu, H. Zhang, Q. Yang, H. Wei, R. Chen, J. Yu, C. Liu, Y. Wang, S. Luo, G. Shi, Z. Chi, B. Xu, *Angew. Chem. Int. Ed.* **2024**, e202318516.

[11] B. Zhou, D. Yan, *Angew. Chem. Int. Ed.* **2019**, 131, 15272-15279.

[12] Y. Xie, Y. Ge, Q. Peng, C. Li, Q. Li, Z. Li, *Adv. Mater.* **2017**, 29, 1606829.

[13] Chen C, Chi Z, Chong K C, et al. *Nat. Mater.* 2021;20(2):175-180.

[14] C. W. Ju, X. C. Wang, B. Li, Q. Ma, Y. Shi, J. Zhang, Y. Xu, Q. Peng, D. Zhao, *Proc. Natl. Acad. Sci.* **2023**, 120, e2310883120.

[15] Y. Miao, F. Lin, D. Guo, J. Chen, K. Zhang, T. Wu, H. Huang, Z. Chi, Z. Yang, *Sci.*

Adv. **2024**, 10, eadk3354.

[16] W. Xie, W. Huang, J. Li, Z. He, G. Huang, B. S. Li, B. Z. Tang, *Nat. Commun.* **2023**, 14, 8098.

[17] L. Zhou, J. Song, Z. He, Y. Liu, P. Jiang, T. Li, X. Ma, *Angew. Chem. Int. Ed.* **2024**, e202403773.

[18] J. Yu, Z. Sun, H. Ma, C. Wang, W. Huang, Z. He, W. Wu, H. Hu, W. Zhao, W. H. Zhu, *Angew. Chem. Int. Ed.* **2023**, 135, e202316647.

[19] R. Kabe, C. Adachi, *Nature.* **2017**, 550, 384-387.

[20] K. Jinnai, R. Kabe, Z. Lin, C. Adachi, *Nat. Mater.* **2022**, 21, 338-344.

[21] W. Li, Z. Li, C. Si, M. Y. Wong, K. Jinnai, A. K. Gupta, R. Kabe, C. Adachi, W. Huang, E. Zysman-Colman, I. D. W. Samuel, *Adv. Mater.* **2020**, 32, 2003911.

[22] P. Alam, N. L. C. Leung, J. Liu, T. S. Cheung, X. Zhang, Z. He, R. T. K. Kwok, J. W. Y. Lam, H. H. Y. Sung, I. D. Williams, C. C. S. Chan, K. S. Wong, Q. Peng, B. Z. Tang, *Adv. Mater.* **2020**, 32, 2001026.

[23] X. Liang, Y. X. Zheng, J. L. Zuo, *Angew. Chem. Int. Ed.* **2021**, 60, 16984-16988.

[24] P. Alam, T. S. Cheung, N. L. C. Leung, J. Zhang, J. Guo, L. Du, R. T. K. Kwok, J. W. Y. Lam, Z. Zeng, D. L. Phillips, H. H. Y. Sung, I. D. Williams, B. Z. Tang, *J. Am. Chem. Soc.* **2022**, 144, 3050-3062.

[25] K. Jiang, Y. Wang, C. Lin, L. Zheng, J. Du, Y. Zhuang, R.-J. Xie, Z. Li, H. Lin, *Light Sci. Appl.* **2022**, 11, 80.

[26] Y. Zhou, P. Zhang, Z. Liu, W. Yan, H. Gao, G. Liang, W. Qin, *Adv. Mater.* **2024**, 2312439.

[27] C. Lin, Z. Wu, H. Ma, J. Liu, S. You, A. Lv, W. Ye, J. Xu, H. Shi, B. Zha, W. Huang, Z. An, Y. Zhuang, R.-J. Xie, *Nat. Photonics.* **2024**, 18, 350-356.

[28] L. Liang, J. Chen, K. Shao, X. Qin, Z. Pan, X. Liu, *Nat. Mater.* **2023**, 22, 289-304.

[29] X. Ou, X. Qin, B. Huang, J. Zan, Q. Wu, Z. Hong, L. Xie, H. Bian, Z. Yi, X. Chen, Y. Wu, X. Song, J. Li, Q. Chen, H. Yang, X. Liu, *Nature* **2021**, 590, 410-415.

[30] Z. Pan, Y.-Y. Lu, F. Liu, *Nat. Mater.* **2012**, 11, 58-63.

[31] Y. Li, M. Gecevicius, J. Qiu, *Chem. Soc. Rev.* **2016**, 45, 2090-2136.

[32] Y. Wei, C. Gong, M. Zhao, L. Zhang, S. Yang, P. Li, Z. Ding, Q. Yuan, Y. Yang, *J. Rare Earths* **2022**, 40, 1333-1342.

[33] J. Ueda, *Bull. Chem. Soc. Jpn.* **2021**, 94, 2807-2821.

[34] J. Xu, S. Tanabe, *J. Lumin.* **2019**, 205, 581-620.

[35] B. Walfort, N. Gartmann, J. Afshani, A. Rosspeintner, H. Hagemann, *J. Rare Earths*. **2022**, 40, 1022-1028.

[36] C. W. Tang, S. A. VanSlyke, *Appl. Phys. Lett*. **1987**, 51, 913-915.

[37] M. A. Baldo, D. F. O'Brien, Y. You, A. Shoustikov, S. Sibley, M. E. Thompson, S. R. Forrest, *Nature* **1998**, 395, 151-154.

[38] H. Uoyama, K. Goushi, K. Shizu, H. Nomura, C. Adachi, *Nature* **2012**, 492, 234-238.

[39] L. Wang, L. Xiao, H. Gu, H. Sun, *Adv. Opt. Mater.* **2019**, 7, 1801154.

[40] H. Lv, H. Tang, Y. Cai, T. Wu, D. Peng, Y. Yao, X. Xu, *Angew. Chem. Int. Ed.* **2022**, 134, e202204209.

[41] R. Kabe, N. Notsuka, K. Yoshida, C. Adachi, *Adv. Mater.* **2015**, 28, 655-660.

[42] H.-T. Feng, J. Zeng, P.-A. Yin, X.-D. Wang, Q. Peng, Z. Zhao, J. W. Y. Lam, B. Z. Tang, *Nat. Commun.* **2020**, 11, 2617.

[43] S. Tan, K. Jinnai, R. Kabe, C. Adachi, *Adv. Mater.* **2021**, 33, 2008844.

[44] W. Qiu, D. Liu, Z. Chen, Y. Gan, S. Xiao, X. Peng, D. Zhang, X. Cai, M. Li, W. Xie, G. Sun, Y. Jiao, Q. Gu, D. Ma, S.-J. Su, *Matter*. **2023**, 6, 1231-1248.

[45] Y. Song, J. Du, R. Yang, C. Lin, W. Chen, Z. Wu, H. Lin, X. Chen, Y. Zhuang, R.-J. Xie, *Adv. Opt. Mater.* **2023**, 11, 2202654.

[46] Y. Im, M. Kim, Y. J. Cho, J.- A. Seo, K. S. Yook, J. Y. Lee, *Chem. Mater.* **2017**, 29, 1946-1963.

[47] W. Liu, C. Zhang, R. Alessandri, B. T. Diroll, Y. Li, H. Liang, X. Fan, K. Wang, H. Cho, Y. Liu, Y. Dai, Q. Su, N. Li, S. Li, S. Wai, Q. Li, S. Shao, L. Wang, J. Xu, X. Zhang, D. V. Talapin, J. J. de Pablo, S. Wang, *Nat. Mater.* **2023**, 22, 737-745.

[48] A. J. Bos, *Materials* **2017**, 10, 1357.

[49] J. Xue, J. Xu, Q. Liang, Y. Dai, R. Wang, Y. Yi, J. Qiao, *Adv. Funct. Mater.* **2023**, 33, 2301312.

[50] W. McMinn, T. Magee, *Food Bioprod. Process.* **1997**, 75, 223-231.

[51] R. Singh, D. Lund, F. Buelow, *J. Food Sci*. **1983**, 48, 939-944.

5.7 Supporting Information
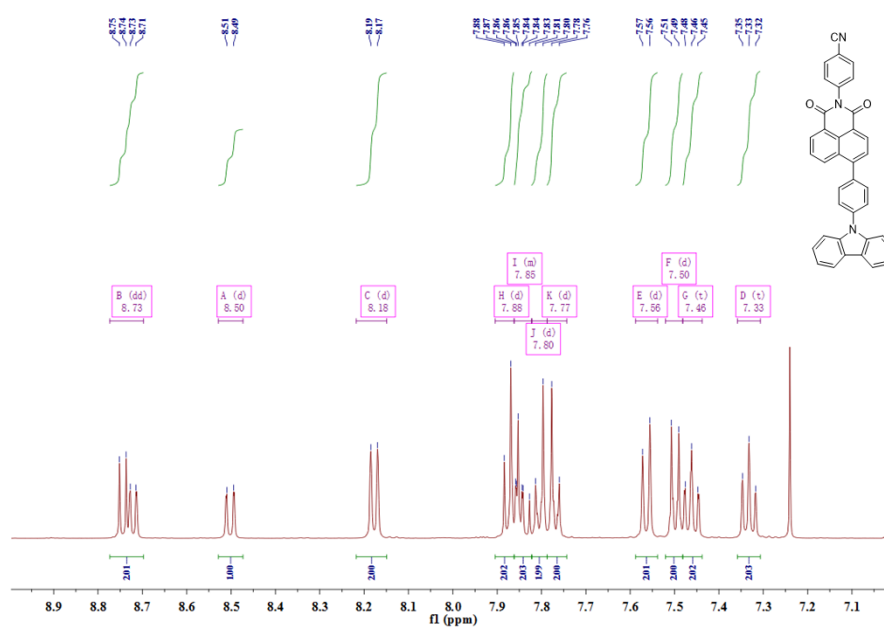
Figure S5.1 ^{1}H-NMR spectra of CPN.
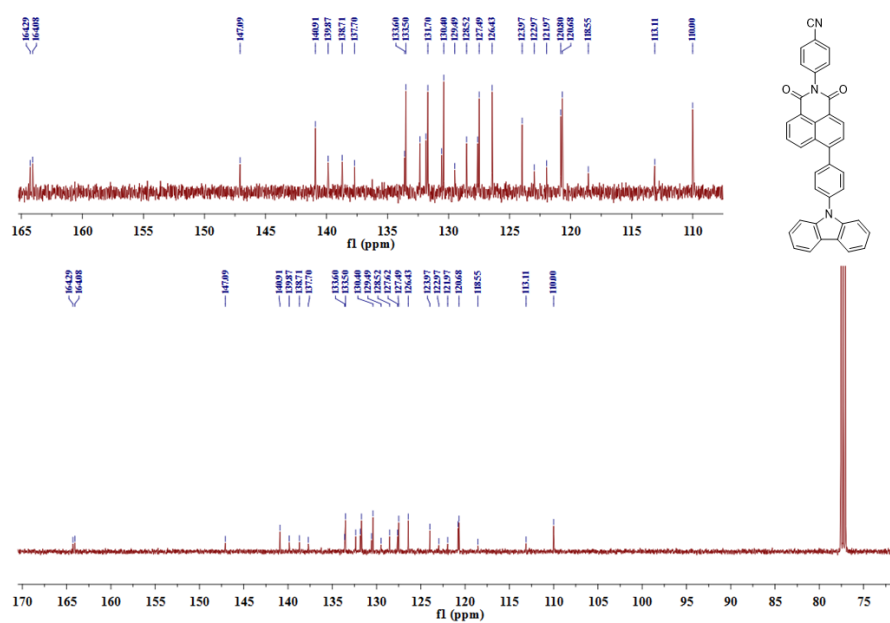
Figure S5.2 ^{13}C-NMR spectra of CPN.
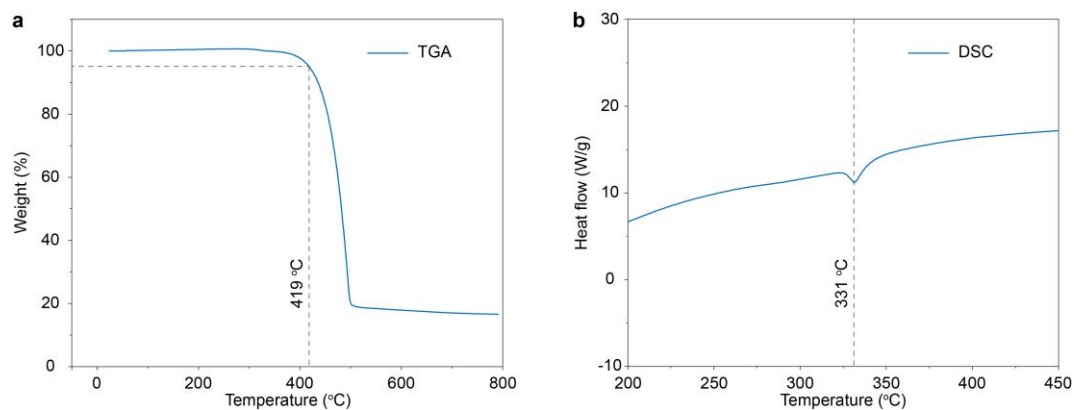
Figure S5.3 Thermal stability analysis of CPN. **a**, Thermogravimetric analysis (TGA). **b**, Differential scanning calorimetry (DSC) curve.
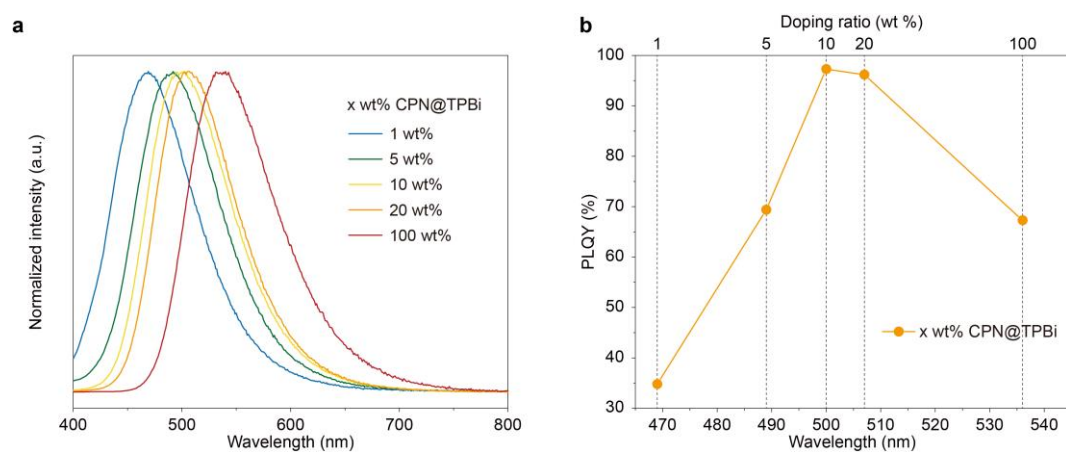
Figure S5.4 Photoluminescence (PL) spectra and PL quantum yield (PLQY, ΦPL) of CPN in TPBi vacuum-deposited films at various doping concentrations. **a**, PL spectra. **b**, ΦPL and emission peak wavelengths.
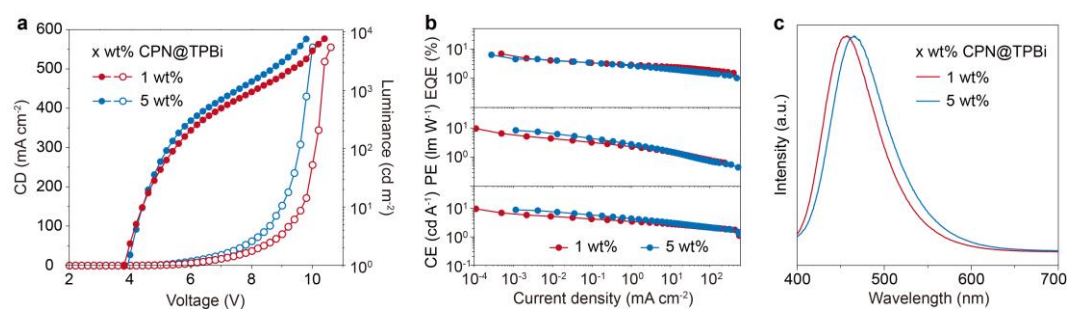
Figure S5.5 Device performances of the 1 and 5 wt% CPN@TPBi OLEDs with 30 nm EML thickness. a, Luminance-voltage-current density characteristics. **b**, External quantum efficiency, power efficiency, and current efficiency as a function of luminance. **c**, EL spectra.
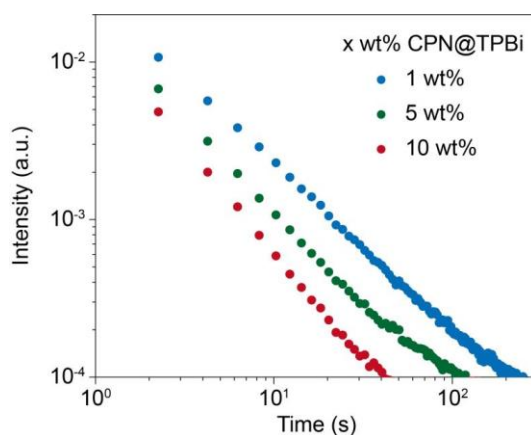

Figure S5.6 PersL decay curve of CPN@TPBi-based OLED with different guest doping concentrations after electrical excitation. The thickness of the CPN@TPBi EML was 150 nm.
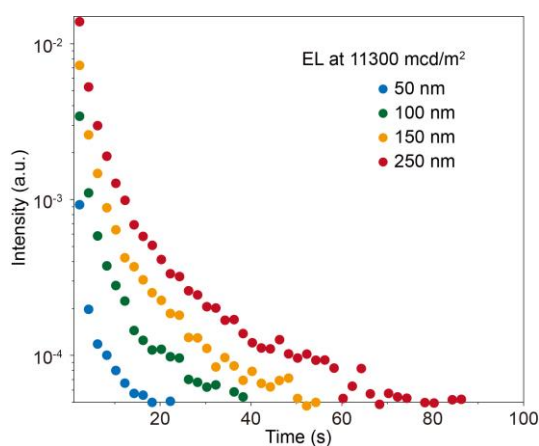
Figure S5.7 PersL decay curves after turning off the electric field in four OLEDs. The OLEDs were fabricated with different thicknesses of the EML material CPN@TPBi ranging from 50 to 250 nm. The curves are plotted in log-linear

coordinates. The doping ratio of CPN was 10 wt%. The EL intensity under an electric field was set at 11300 mcd/m^2 by controlling the driving voltage. The measurements were conducted at room temperature (RT).
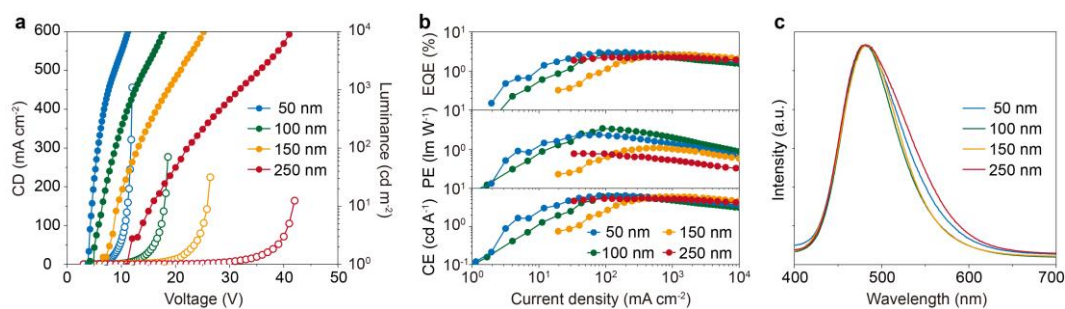
Figure S5.8 Device performances of the 10 wt% CPN@TPBi OLEDs with different EML thicknesses (50, 100, and 200 nm). **a**, Luminance-voltage-current density characteristics. **b**, External quantum efficiency, power efficiency, and current efficiency as a function of luminance. **c**, EL spectra.
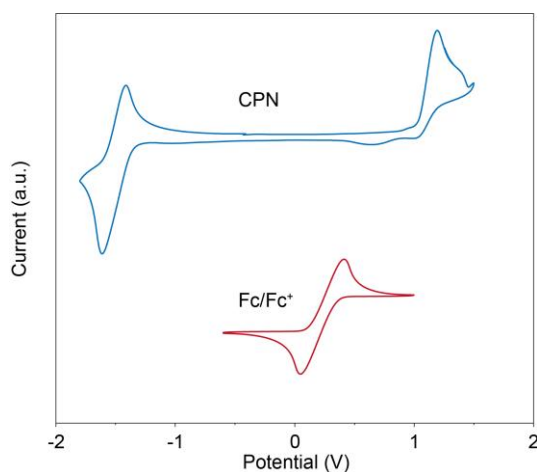
Figure S5.9 Cyclic voltammograms of CPN recorded versus Fc/Fc$^+$ at 298 K under N$_2$ atmosphere.
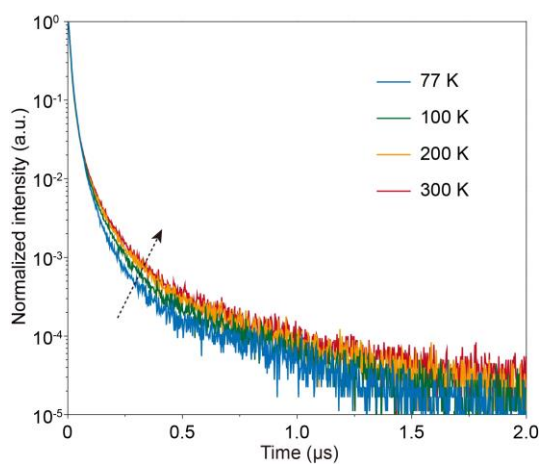
Figure S5.10 Phosphorescence decay curves of the 10 wt% CPN melt-casting film recorded at different temperatures. The intensity was normalized to 1 at the peak values.
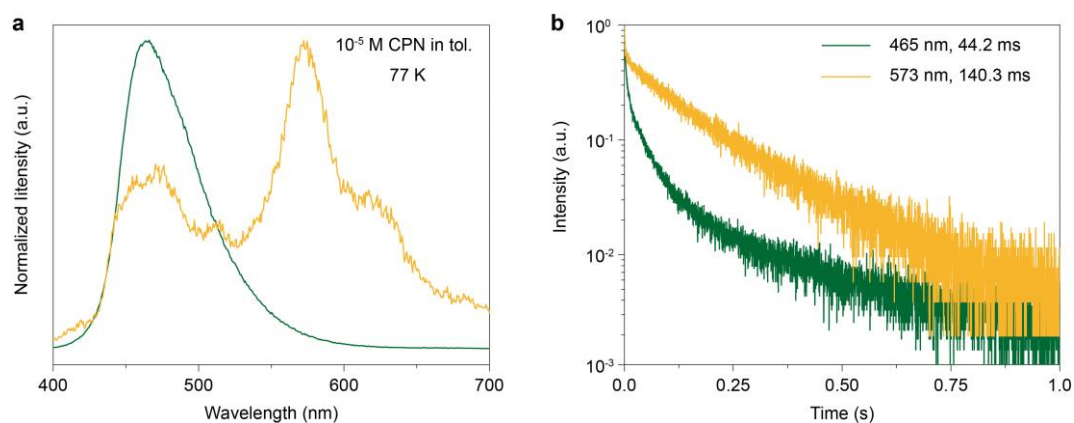
Figure S5.11 a, Steady-state spectra (green line) and delayed spectra (delayed time 1 ms) of 10^{-5} M CPN in toluene at 77K. **b**, Transient decay curves of 10^{-5} M CPN in toluene at 77K.
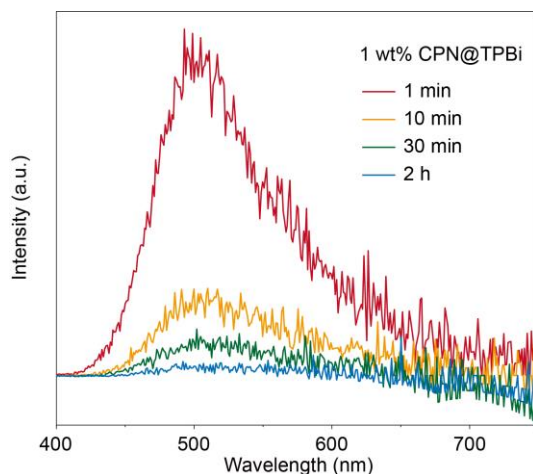
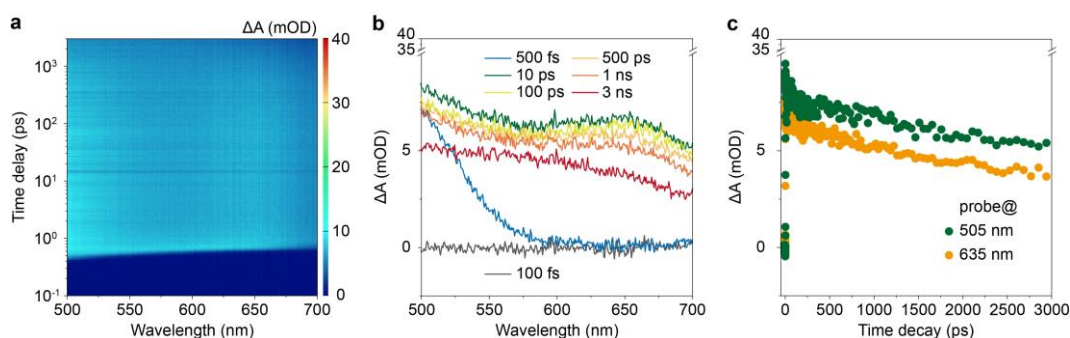**Figure S5.12** PersL spectra of 1 wt% CPN@TPBi recorded at 1 min, 10 min, 30 min, and 2 h after ceasing the 365 nm excitation light.

Figure S5.13 Transient absorption (TA) spectra of the TPBi melt-casting film. **a**, Pseudocolor TA plot. **b**, TA spectra at specified delay times from 100 fs to 3 ns. **c**, Decay dynamics of excited-state absorption probed at 505 and 635 nm.
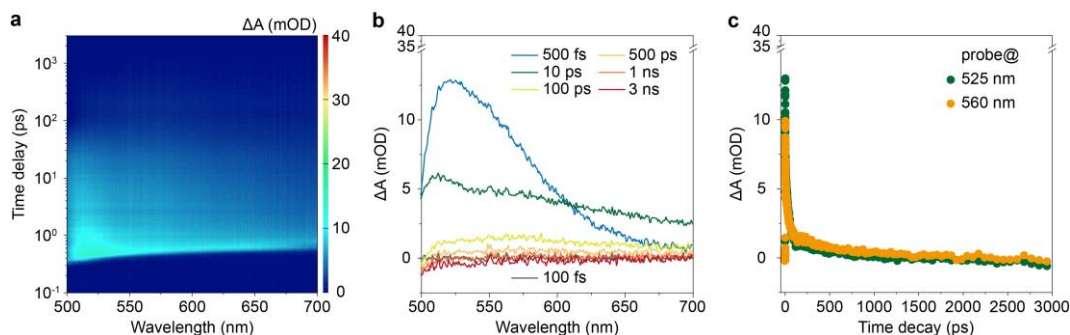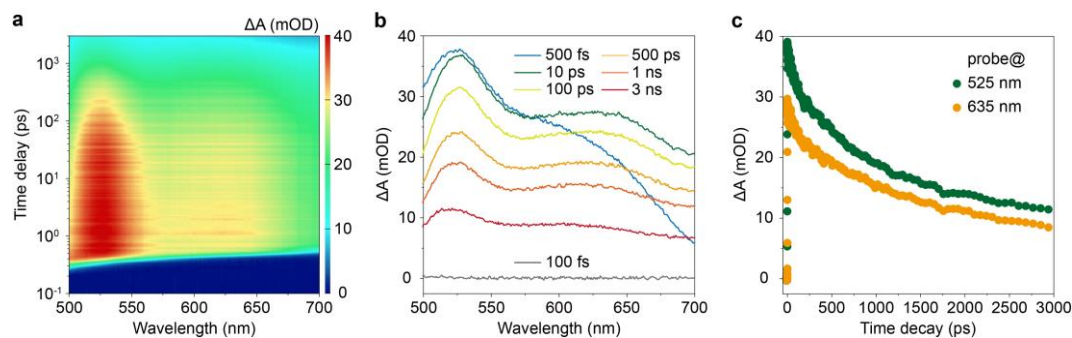

Figure S5.14 TA spectra of the CPN melt-casting film. **a**, Pseudocolor TA plot. **b**, TA

spectra at specified delay times from 100 fs to 3 ns. **c**, Decay dynamics of excited-state absorption probed at 525 and 560 nm.

Figure S5.15 TA spectra of the CPN@TPBi melt-casting film. **a**, Pseudocolor TA plot. **b**, TA spectra at specified delay times from 100 fs to 3 ns. **c**, Decay dynamics of excited-state absorption probed at 525 and 635 nm.
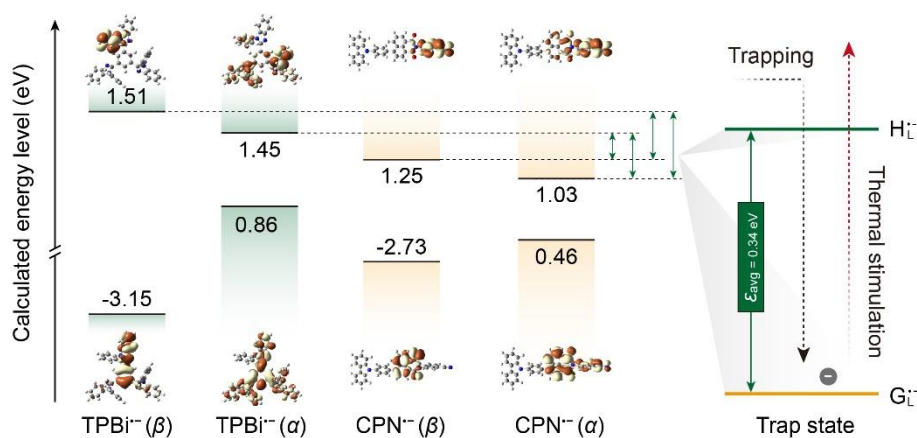
Figure S5.16 Schematic diagrams of the primary orbital configurations of TPBi- and CPN$^{\bullet-}$. The depth distributions of the traps formed by the LUMOs of TPBi$^{\bullet-}$ and CPN$^{\bullet-}$ are depicted on the right. The structural optimization for the excited-state geometries of CPN and TPBi anions were performed at the B3LYP/def2-SVP level using time-dependent density functional theory (TDDFT) method implemented in the Gaussian 16 program.

Table S5.1 Summary of the EL performances of devices based on 30 nm CPN@TPBi EML with different doping ratio.

Doping ratio [wt%]	V_{on}[a) [V]	L_{max}[b) [cd m^{-2}]	CE_{max}[c) [cd A^{-1}]	PE_{max}[d) [lm W^{-1}]	EQE_{max}[e) [%]	λ_{EL}[f) [nm]
1	4.0	7606.8	9.66	9.48	6.89	456
5	3.9	7684.1	8.92	8.24	6.34	465
10	3.8	9764.4	13.81	11.05	12.64	478

[a] Voltage at 1 cd m^{-2}.

[b] Maximum luminance.

[c] Maximum current efficiency.

[d] Maximum power efficiency.

[e] Maximum external quantum efficiency.

[f] Measured at maximum luminance.

Table S5.2 Summary of the EL performances of devices based on 10 wt% CPN@TPBi with different EML thicknesses.

Thickness [nm]	V_{on}[a) [V]	L_{max}[b) [cd m^{-2}]	CE_{max}[c) [cd A^{-1}]	PE_{max}[d) [lm W^{-1}]	EQE_{max}[e) [%]	λ_{EL}[f) [nm]	τ_{Persl}[g) [s]
50	4.0	9952.7	6.08	3.40	2.71	478	18
100	5.0	10041.3	6.46	2.35	3.01	478	29
150	6.6	9905.5	6.02	1.08	2.58	478	40
250	12	8954.9	5.44	0.78	2.31	478	76

[a] Voltage at 1 cd m^{-2}.
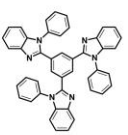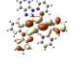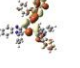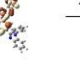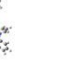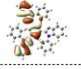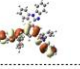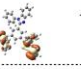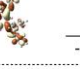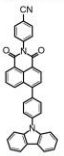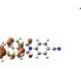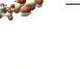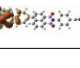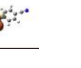
^b Maximum luminance.

^c Maximum current efficiency.

^d Maximum power efficiency.

^e Maximum external quantum efficiency.

^f Measured at maximum luminance.

^g Measured when the decay intensity decreased to 5.0×10^{-4}.

Table S5.3 Schematic diagrams showing the chemical structure and TD-DFT-calculated energy levels and main orbital configurations of TPBi and CPN.

Name	Structure	Calculated LUMO and HOMO distribution (eV)				
		Molecule	Radical cation (α)	Radical cation (β)	Radical anion (α)	Radical anion (β)
TPBi		-1.89 / -6.02	-4.00 / -8.86	-8.10 / -8.42	1.32 / 0.73	1.45 / -3.25
CPN		-2.94 / -5.86	-5.30 / -8.72	-8.38 / -8.69	1.02 / 0.45	1.23 / -2.74

Chapter 6

Electrically Chargeable Inorganic Persistent Luminescence in an Alternating Current Driven Electroluminescent Device

Note: This work resulted in a manuscript titled " Electrically Chargeable Inorganic Persistent Luminescence in an Alternating Current Driven Electroluminescent Device" in *Communications Materials* and still under revision, presented here.

6.1 Abstract

Persistent luminescence (PersL) in inorganic materials, lasting from seconds to even days, has attracted considerable attention and has been expanded to optoelectronic device applications. Despite the promise of electric power-driven PersL for lighting and display device applications due to its convenience and manageability, studies on electrically driven inorganic PersL are lacking. Here, we report an unprecedented inorganic PersL in electroluminescent devices (ELDs), which shows an energy storage effect that persists beyond 24 hours after charging with an alternating current (AC) electric field at 250 K. The spin-coating method-prepared emission layer (EML) composites consist of a small bandgap copper-doped zinc sulfide core, a high dielectric constant alumina shell and a chemically passivated dielectric polydimethylsiloxane medium ($ZnS:Cu@AlO_x@PDMS$), and these composites exhibit well-distributed electric fields and excellent operational stability. Thermoluminescence characterization reveal that PersL with an ~0.3 eV trap depth in ELDs mainly arises from the charge separation via hot-electron impact excitation and charge trapping within trap states in the EML; this result is consistent with those from identical EML materials under light irradiation. This study on electrically chargeable PersL in AC-driven ELDs can enhance

our understanding of luminescence mechanisms in inorganic semiconductors and facilitate broader applications in information storage and medical detection technologies.

6.2 Introduction

Persistent luminescence (PersL) materials are capable of storing photon energy in trap states and delaying light emission for several seconds to hours after excitation and have motivated ongoing explorations of their better performance in many advanced applications, such as information storage, alternating-current driven light-emitting diodes (AC-LEDs), bioimaging and sensing.[1-6] Through the continuous effort of researchers, a variety of PersL materials with appealing properties have been successfully created in both inorganic and organic systems.[7-10] Generally, PersL can be described as an electron trapping-detrapping process, as shown in Figures 6.1a-6.1b.[11] This process begins with band-to-band excitation, where electrons are directly excited from the valence band (VB) to the conduction band (CB) of host materials and then partially captured by traps. After ceasing excitation, the trapped charge carriers can escape from the traps under external stimuli such as thermal activation or near-infrared stimulation and return to CB; finally, these charge carriers recombine with holes in the luminescence centers to produce PersL. However, most reported afterglow materials, especially inorganic phosphors with superior PersL properties, can only be subjected to photoexcitation. Therefore, their application is limited in lighting and display devices, and this deficiency motivated our research for the attainment electro-excited PersL.[12,13] For instance, electrically excitable PersL not only addresses flicker problems but also facilitates device miniaturization and integration by eliminating the need for an additional inorganic phosphor layer in AC-LEDs.[14,15] In this context, developing PersL materials that can be electrically excited is highly important for extending their applications in optoelectronic devices.

This motivation has resulted in great efforts in exploring novel electrically excitable PersL materials, and significant advances have been achieved in organic PersL compounds. For example, a series of organic light-emitting diodes (OLEDs) have been successfully assembled by incorporating organic room-temperature phosphorescence (RTP) emitters, thermally activated delayed fluorescence (TADF) dimmers, or long-

persistence luminescence (LPL) compounds as electroluminescent layers to achieve intriguing electro-excited afterglow performance.[16-19] Despite these impressive breakthroughs, the practical applications of these organic materials are still significantly limited by their relatively short afterglow lifetime (*i.e.*, several seconds) and their sensitivity to environmental moisture and oxygen.[20,21] In addition, these OLEDs are driven by direct current (DC), which causes serious charge accumulation problems as well as significant energy loss when connected to generally available AC power sources (*i.e.*, 110/220 V, 50/60 Hz).[22] Compared with their organic counterparts, inorganic PersL phosphors usually have a longer afterglow duration and superior environmental stability; thus, they are highly promising candidates for electroluminescent devices (ELDs) to attain outstanding PersL. However, to the best of our knowledge, no studies have been reported on electrically driven afterglow emission in inorganic phosphors. Therefore, attaining an electrically excitable PersL in inorganic phosphors and understanding its corresponding underlying electron behaviors are crucial for their future application in optoelectronic devices.

Herein, for the first time, we report the fabrication of an electro-excited PersL in an inorganic zinc sulfide (ZnS) phosphor within an AC-driven ELD structure (Figure 6.1c). AC-driven ELDs, with frequent reversal of the electric field, effectively prevent charge accumulation and improve power efficiency. A metal-doped ZnS PersL phosphor (ZnS:Cu) with a small bandgap was coated with high dielectric constant aluminum oxide (AlO_x), increasing the probability of hot-electron impact band-to-band excitation, thereby promoting efficient carrier separation and trap electron capture (Figure 6.1d).[23,24] The phosphor@polydimethylsiloxane (PDMS) ultrathin dielectric layer (~100 μm), fabricated through a spin coating method, enables precise electric field distribution around particles and effectively inhibits direct current injection and electrochemical reactions. The thermoluminescence (TL) measurements were conducted on $ZnS@AlO_x@PDMS$-based ELDs after electrical charging to assess the generated traps and trap depth, which were found to be comparable to those of the same

EML materials after light irradiation. The fabricated ELDs exhibit minute-level PersL, temperature-dependent decay characteristics, and hour-level energy storage effects within the EML, thus facilitating novel applications such as medical identification labels.
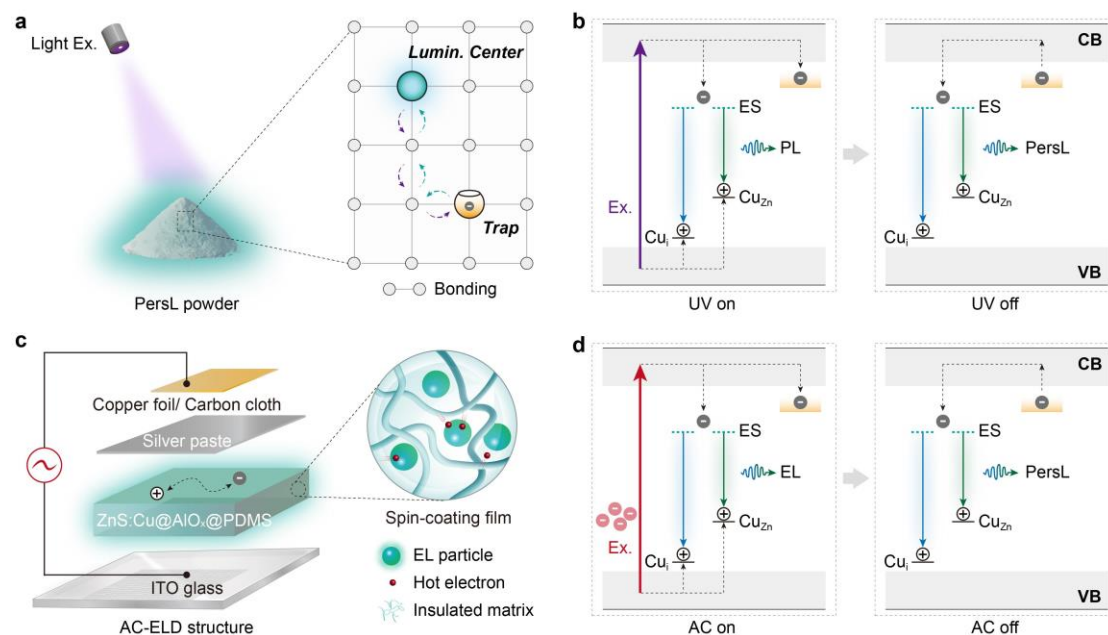

Figure 6.1 Schematic diagram of the PersL under light irradiation and AC charging. **a**, Diagram of PersL powder under optical excitation. **b**, PersL mechanism with light excitation on and off. Under optical excitation, the radiative transition of electrons results in PL. Partial holes and electrons are captured by the luminescent center and trap, respectively. The trapped charge carriers escape and subsequently recombine at the luminescent center to obtain the PersL. **c**, Structure of AC-ELD. **d**, Proposed PersL mechanism with electrical charging on and off. Under AC excitation, the electrons in the VB are excited by the AC-generated hot electrons, resulting in EL. Similar to optically excited PersL, some carriers are separated and trapped in the trap state. PersL appears after the combination of holes and electrons in the luminescent center. Abbreviations and labels: light excitation (purple line), hot electron and related excitation (red balls and line), luminescent centers: interstitial Cu_i (blue-Cu) and

substitutional Cu_{Zn} (green-Cu), excited state (ES, cyan dotted line), trap state (orange line), electron (gray ball), and hole (white ball).

6.3 Experimental Procedure

6.3.1 Chemicals and Materials

All reagents and chemicals utilized were of reagent grade and commercially available and were used without additional purification. ZnS:Cu (GBF-2F) phosphor was procured from Japan Nemoto & Co., Ltd. ZnS:Cu@AlOx (D502CT), ZnS:Cu,Al (D417S), and ZnS:Mn (D611S) phosphors were sourced from Shanghai Keyan Phosphor Technology Co.,Ltd. Polydimethylsiloxane (PDMS, Dowsil 184) was obtained from Dow Corning. ZnS (99.99%) and NaCl (99%) were purchased from Shanghai aladdin Biochemical Technology Co., Ltd and $CuCl_2 \cdot 2H_2O$ (AR) was sourced from Xilong Scientific Co., Ltd.

6.3.2 Preparation of ZnS:Cu Phosphors

The ZnS and $CuCl_2 \cdot 2H_2O$ were mixed in a molar ratio of 99.99% to 0.01% and placed into a mortar, followed by the addition of anhydrous ethanol for grinding for 45 minutes. Subsequently, the mixed powder was transferred to an alumina crucible, and a mass of NaCl equal to 1.5 times the mass of the mixed powder was added. The crucible was then placed in a muffle furnace and sintered at 900°C (cubic phase)/1050°C (hexagonal phase) for 3 hours. After cooling, the samples were washed and dried to obtain the pure ZnS:Cu powder.

6.3.3 Preparation of ELD

The PersL phosphors were blended with PDMS to form the emission layer of the ELD. The weight ratios of the PersL phosphors to the PDMS precursors (including curing agents) were maintained at 1:1. The ratios of the precursors to the corresponding curing agents for PDMS were 10:1 by weight. After vigorous stirring, the mixtures were vacuumed in an oven for 10 minutes to eliminate air bubbles. Subsequently, the bubble-free mixture was coated into a thin film using the spin coating method (with speeds ranging from 500 to 6000 rpm). The spin-coated film was then dried at 80°C for 2 hours.

Following this, a conductive silver paste was applied onto the emission layer using a scraping method and dried at 80°C for 30 minutes. To facilitate testing, copper foil or carbon cloth was attached to the upper layer of the silver electrode.

6.3.4 Characterizations of Photophysical Properties

The XRD patterns of the phosphors were captured utilizing a Bruker D8 Advance X-ray diffractometer, employing Cu Kα radiation ($\lambda = 0.15406$ nm) at 40 kV and 40 mA. Surface morphology and elemental mapping were conducted using a field emission scanning electron microscopy (SU70, Hitachi) instrument, which was equipped with EDX spectroscopy. VUV spectroscopy in $ZnS:Cu@AlO_x$ at 10 K was conducted using the beamline BL3B at the UVSOR facility (Institute for Molecular Science, Okazaki, 24IMS6020). Transient decay curve was collected in a fluorescence spectrometer (Acton SP 2300i, Princeton Instruments). Temperature-dependent PL spectra were obtained using customized measurement equipment. The sample was excited with a 254 nm optical parametric oscillator laser (NT342B-20-SH/SF, Ekspla) and initially cooled to 100 K before being heated to 450 K at a predefined rate of 2 K/min, with the emission intensity recorded in real-time a CCD detector (Roper Scientific, LN/CCD-100EB-GI). Photographs and videos of the samples were taken with a digital camera (α7SIII, SONY).

6.3.5 Characterizations of PersL and TL

The PersL decay curve and TL glow curve spectra were recorded using a custom-built measurement system. Initially, samples were positioned on a cooling-heating stage (THMS600E, Linkam Scientific Instruments) capable of maintaining temperatures from 100 to 600 K. The sample chamber was purged with dry nitrogen gas, and a quartz glass cover was fitted on top. For excitation, samples were either subjected to a specific voltage (for ELDs) using waveform generators (DG821, RIGOL) and high voltage amplifier (HA-820, PINTECH) or exposed to ultraviolet light through the quartz glass (for films) at an excitation power density of approximately 5 mW/cm² for 1 minute.

Monitoring of PersL intensity (or PersL decay profiles and TL emission) after excitation cessation was accomplished using a filter-attached photomultiplier tube (PMT, R928P, Hamamatsu photonics), a multimeter (2400, KEITHLEY), and a high-voltage power supply (HVC1800, ZOLIX). Simultaneously, PersL spectra were captured using a multichannel spectrometer (QE-Pro, Ocean Photonics) during TL measurements. In a typical TL measurement, the sample was initially cooled to 100 K and stimulated by the excitation sources for 1 minute. After a 20-second delay following excitation cessation, the sample was heated to 450 K at a predefined heating rate (5, 10, 20, 30, or 50 K/min), and emission intensity was recorded in real-time. The entire measurement system was controlled by LabVIEW-based computer programs. And a TL glow curve starting from 10 K was measured using a custom-built setup, which included a cryostat (VPF-800, Janis), an excitation source consisting of a Xe lamp with a cold mirror (LAX-101, Asahi spectra), and a detector composed of a PMT covered by a longpass filter (FELH0450, Thorlabs).

6.4 Results and Discussion

To validate our hypothesis, we selected the $ZnS:Cu@AlO_x$ PersL complex as a typical example, among which $ZnS:Cu$ and AlO_x served as a PersL core and a high dielectric constant shell, respectively.[25] The X-ray diffraction (XRD) patterns show that the $ZnS:Cu$ powders contain both cubic and hexagonal phases, and the substitution of Cu^+ and coating with AlO_x have no impact on the phase purity (Figure 6.2a). Energy dispersive X-ray (EDX) spectroscopy mappings reveal a uniform distribution of Al and O on the particles (Figure 6.2b). The average particle size is determined to be approximately 22.5 μm by randomly collecting 161 particles (Figure 6.2c). The smaller particle size facilitated the formation of a dense and smooth doped thin $ZnS:Cu@AlO_x@PDMS$ film (Figure 6.2d-i). The thin film thickness is influenced by the spin coating rate, demonstrating a thinning trend at higher rotational speeds (Figure S6.1). Nevertheless, doping more semiconductor powders in the thinnest possible layer was advantageous for enhancing the EL and PersL brightness of the device. An optimized speed of 500 rpm was used to achieve a film thickness of approximately 124.2 μm according to the alternating current (AC) charging PersL decay duration (Figure 6.2d-ii and Figure S6.2).

To evaluate the optical properties of the complex in AC electroluminescent devices (ELDs), we subsequently conducted high-resolution vacuum ultraviolet (VUV) spectroscopy (150-400 nm) on the $ZnS:Cu@AlO_x$ phosphor (Figure 6.2e). The host excitation energy at 10 K was estimated to be 3.82 eV (at ~325 nm); this was further adjusted by multiplying it by 1.08 to incorporate the electron-hole binding energy, and a final value of 4.12 eV was obtained (Figure 6.2e-ii).[26] AC charging readily generates hot electrons with energy equal to or exceeding the ZnS band gap.[23] Numerous studies have reported blue and green emissions from copper-activated ZnS phosphors, yet the nature of the key emission process is debatable.[27-32] We ascribe the luminescent centers of the two typical photoluminescence (PL) peaks at approximately 450 and 515 nm to interstitial Cu_i and substitutional Cu_{Zn}, respectively (Figure 6.2e-iii).[33,34] The

associated excited state scenario is highly complex, involving factors such as CB, sulfide vacancy (V_s), and substitutional Al_{Zn}; therefore, we refrain from providing clear deductions here. Compared to blue light, green light exhibits a longer lifetime of 0.56 ms at 0.17 ms under UV excitation (Figure 6.2f).
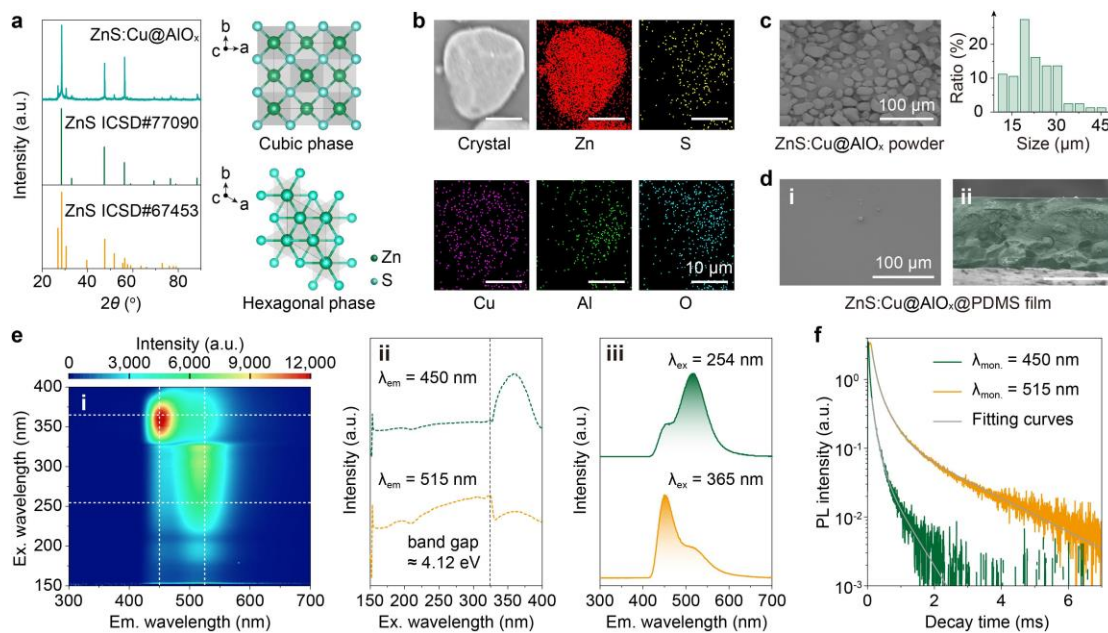

Figure 6.2 Photophysical properties of the ZnS:Cu@AlOx phosphor. **a**, XRD pattern and crystal structure of ZnS:Cu@AlO$_x$ powder (cubic phase: ICSD#77090 and hexagonal phase: ICSD#67453). **b**, Elemental distribution mapping of ZnS:Cu@AlO$_x$ powder. **c**, SEM image and particle size distribution of ZnS:Cu@AlO$_x$ powder. **d**, Vertical view (i) and front view (ii) of the SEM images of the ZnS:Cu@AlO$_x$@PDMS film (spin-coating speed = 500 rpm). **e**, Excitation-emission wavelength 2D contour plot of the PL intensity of ZnS:Cu@AlO$_x$ powder at 10 K and 10^{-7} Pa (i) and corresponding excitation spectra (ii, λ_{em} = 450 and 515 nm) and emission spectra (iii, λ_{ex} = 254 and 365 nm). **f**, PL decay curves of the ZnS:Cu@AlO$_x$ powder (λ_{ex} = 300 nm, λ_{em} = 450 nm, and λ_{em} = 515 nm).

Subsequently, we determined the PersL duration of ELDs under various electrical field excitation conditions. First, varying stimulation times did not result in significant differences; here, we selected a stimulation period of 1 to 3 minutes (Figure S6.3). As illustrated in Figure 6.3a, the attenuation duration significantly increased as the atmospheric temperature decreased, likely due to the greater retention of the shallow trap electrons at lower temperatures than at higher temperatures. Remarkably, the ELD decay time exceeded 600 s at temperatures below 300 K. In consideration of practical applications in low-temperature storage, we employed a storage temperature of 250 K for subsequent characterization of the targeted ELDs. Moreover, the performance of the PersL duration improved with increasing driving AC voltage and tended to saturate at 400 V (Figure 6.3b). Notably, while PDMS facilitates powder dispersion and prevents short-circuiting, its effective insulating properties contribute to a PersL turn-on voltage exceeding 100 V. In parallel, elevated frequencies produce a surplus of hot electrons, amplifying the accumulation of electrons within trap states and thereby enhancing the PersL intensity. Nevertheless, the finite nature of the trap density needs to be highlighted since charging saturation was achieved at frequencies greater than 1 kHz (Figure 6.3c). Simultaneously, elevated voltage and frequency potentially induce an increase in device temperature, accelerating the release of the charge carriers from traps and consequently minimizing the duration. Hence, the AC voltage and frequency were set to 400 V and 1 kHz, respectively, in subsequent experiments. As depicted in Figure 6.3d, the PersL can be reliably reproduced under the recommended conditions (voltage = 400 V, frequency = 1 kHz, temperature = 250 K) even after undergoing multiple cycles of electrical charging. After charging at 250 K for 300 s, certain charge carriers persisted within the emission layer. Notably, they could be released at a heating rate of 150 K/min when the temperature is elevated (Figure 6.3e). These distinct TL signals provided supplementary evidence for the existence of traps with continuous depth distributions. The properties of electrical energy storage and photon release at 250 K are shown in Figure 6.3f.
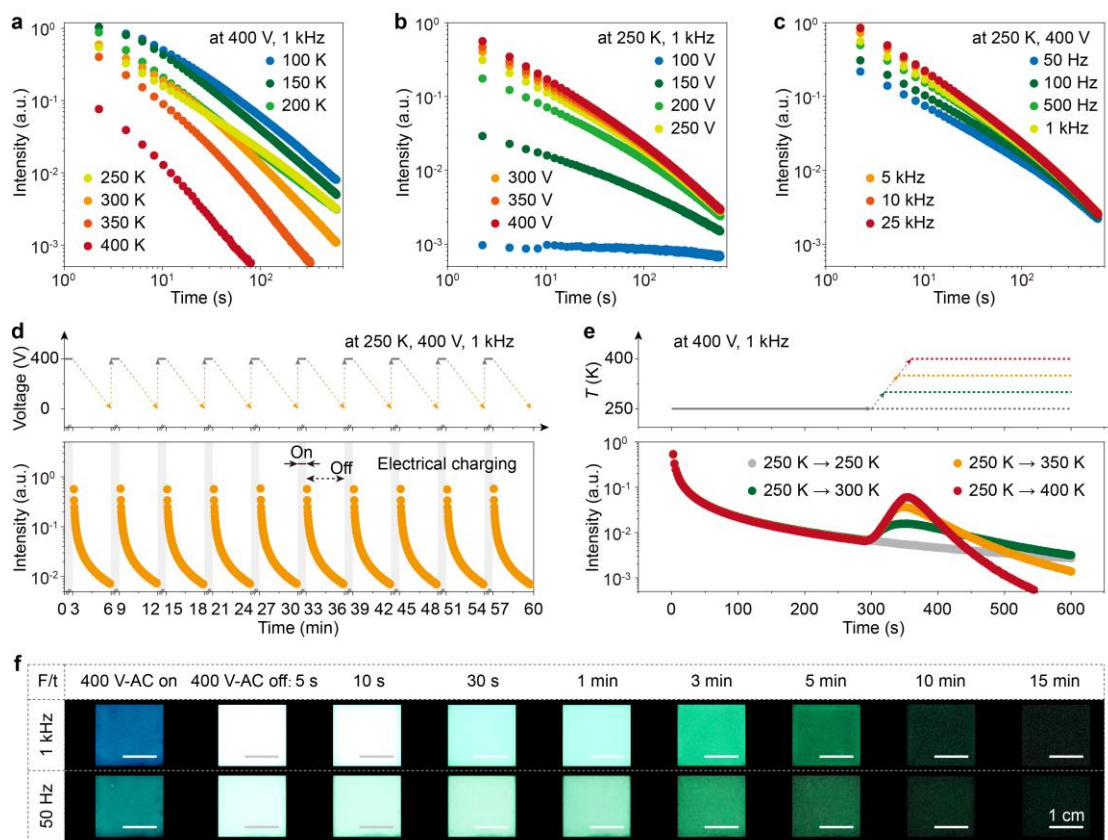
Figure 6.3 Electrically driven PersL properties of the ZnS:Cu@AlOx@PDMS-based ELD. **a**, Temperature-dependent PersL decay curves (setting V = 400 V and F = 1 kHz). **b**, Voltage-dependent PersL decay curves (setting T = 250 K and F = 1 kHz). **c**, Frequency-dependent PersL decay curves (setting T = 250 K and V = 400 V). **d**, Actual voltage profile (top) and 10 repeated PersL decay curves of the ELD after electrical charging (bottom, T = 250 K, V = 400 V, F = 1 kHz, t_{ex} = 3 min, and $t_{mon.}$ = 3 min). **e**, Actual temperature profile (top) and PersL decay curve of the ELD (bottom, V = 400 V, F = 1 kHz, t_{ex} = 3 min, and $t_{mon.}$ = 5 min) at 250 K and then heated to 250, 300, 350, and 400 K (heating rate = 150 K/min and $t_{mon.}$ = 5 min). **f**, Photographs of the ELD under AC charging (T = 250 K, V = 400 V, F = 1 kHz and 50 Hz, and t_{ex} = 3 min) and after ceasing electrical charging.

To gain deeper insights into the luminescent center characteristics, we initially conducted EL spectroscopy at different voltage excitations (Figure S6.4). The EL intensity was obtained when the voltage exceeded 100 V, with the emission spectrum remaining consistent in the ELD (Figure 6.3b and Figure S6.4). Interestingly, varying frequencies solely impacted the color of EL light without exerting any impact on the color of PersL after the AC excitation was ceased (Figure 6.3f and Figure 6.4a). As documented in numerous studies, the color variation of EL is contingent upon thelifetime of the radiative transitions within the ZnS:Cu phosphor. At elevated frequencies, the EL predominantly consisted of short-lived blue light, whereas at lower frequencies, it primarily comprised long-lived green light (Figure 6.2f).[35] The consistent emission of the AC-charging PersL can be attributed to electrons returning from the trap to the luminescent center, resulting in simultaneous dual emissions from the interstitial Cu_i and substitutional Cu_{Zn}, wherein the dominant emission is green light emitted by the latter. We further discovered a temperature-dependent PL spectrum excited at 254 nm that resembled the PersL spectrum following electrical excitation; this featured bimodal emission with predominantly green light peaking at 515 nm (Figure 6.4b). This could be attributed to the emission processes originating from the CB or adjacent excited states to the ground state of the luminescent center. Furthermore, TL glow contour mapping at a heating rate of 50 K/min was obtained after AC charging (Figure 6.4c). As the temperature increased from 100 to 450 K, the TL spectra gradually exhibited bimodal emission, characterized by fluctuating intensity while maintaining nearly unshifted peak positions. This pattern also mirrored that of the PL excited by 254 nm UV light, indicating efficient band-to-band separation by hot excitons and charge recombination under thermal stimulation. The short-lived blue light was prone to nonradiative transitions at elevated temperatures, consequently resulting in the material primarily emitting green light at high temperatures.

In a subsequent series of experiments, the TL glow curves were collected at various heating rates (β_h) to compare the trap state characteristics of different kinds of samples

under different charging methods. We estimated the trap depth by utilizing the heating rate plot derived from the Randall-Wilkins model,[36]

$$\frac{\beta\varepsilon}{k_B \cdot T_m^2} = s \cdot \exp\left(\frac{-\varepsilon}{k_B \cdot T_m}\right) \quad \text{(Equation 6.1)}$$

where k_B is the Boltzmann constant, T_m (K) is the peak temperature obtained from the TL glow curves, and s (s^{-1}) is the frequency factor. Under 254 nm excitation, the estimated deepest trap depths (ε) decreased with increasing temperature from 285 to 335 K, reaching 0.46±0.01 eV for the ZnS:Cu phosphor, 0.35±0.01 eV for the ZnS:Cu@AlO$_x$ phosphor, and 0.31±0.01 eV for the ZnS:Cu@AlO$_x$@PDMS ELD (Figures 6.4d-6.4e and Figures. S6.5-S6.7). The shallower trap depths likely resulted from the passivation of surface defects, which was particularly evident after coating with the AlO$_x$ shell. A significant shift (> 50 K decrease in T_m) was also observed for the TL peaks at lower temperatures when the TL performance was compared between the pure ZnS:Cu and ZnS:Cu@AlO$_x$ powders under UV excitation (Figures S6.5 and S6.6). Additionally, further validation confirmed that the traps induced by the PDMS coating became shallower (~10 K) in both the cubic phase and hexagonal phase of the ZnS:Cu powders, as well as in the related phosphor doped into the PDMS films (Figure S6.8). However, AlO$_x$ and PDMS coatings are essential for enhancing the performance of AC charging PersL and preventing short circuits in devices, respectively. Importantly, depths of approximately 0.32±0.01 eV were consistently obtained for the ELDs under UV excitation and AC (Figures 6.4d-iii and 6.4d-iv, Figure S6.7, and Figure S6.9). These results indicated that electrical excitation could serve as an effective means of charging trap states. Notably, the initial attenuation observed in the TL curve during temperature elevation (100-150 K) was not attributed to the phosphorescence of the PDMS binder (Figure S6.10). Rather, this could be ascribed to the coverage of intrinsic defects in the powder, further shifting the main peak temperature of the TL glow curves toward unobservable lower temperatures (Figure S6.11). Building upon the above results, we propose a mechanism for the electrically driven PersL in ELDs. In the proposed mechanism, during AC charging, electrons in the VB are excited by hot

electrons, and the separated charge carriers are subsequently captured by the trap state. The trapped electron will be released with external stimulation and then combine with the luminescent center, resulting in PersL emission with distinct thermal activation characteristics.

Furthermore, to assess the universality of the proposed approach for AC charging of PersL in inorganic materials, the ZnS:Cu,Al and ZnS:Mn phosphors coated with AlO_x, with particle sizes of approximately 3.7 μm and 6.0 μm, respectively, were selected (Figures S6.12a-S6.12b and Figures S6.13a-6.13b). Compared to ZnS:Mn@AlO_x phosphors, ZnS:Cu@AlO_x- and ZnS:Cu,Al@AlO_x-based ELDs demonstrate a deeper trap depth (T_m > 300 K with a heating rate of 50 K/min) after electrical excitation, leading to a longer decay duration and high TL intensity (Figures S6.12c and S6.13c). Notably, the luminescence of this system can be easily regulated by doping different luminescent centers. As depicted in Figures S6.12d and S6.13d, the colors of the AC-charging PersL were controllably extended to cyan and orange, with peak wavelengths at 515 nm and 450 nm for ZnS:Cu, Al@AlO_x, and 585 nm for ZnS:Mn@AlO_x, respectively.
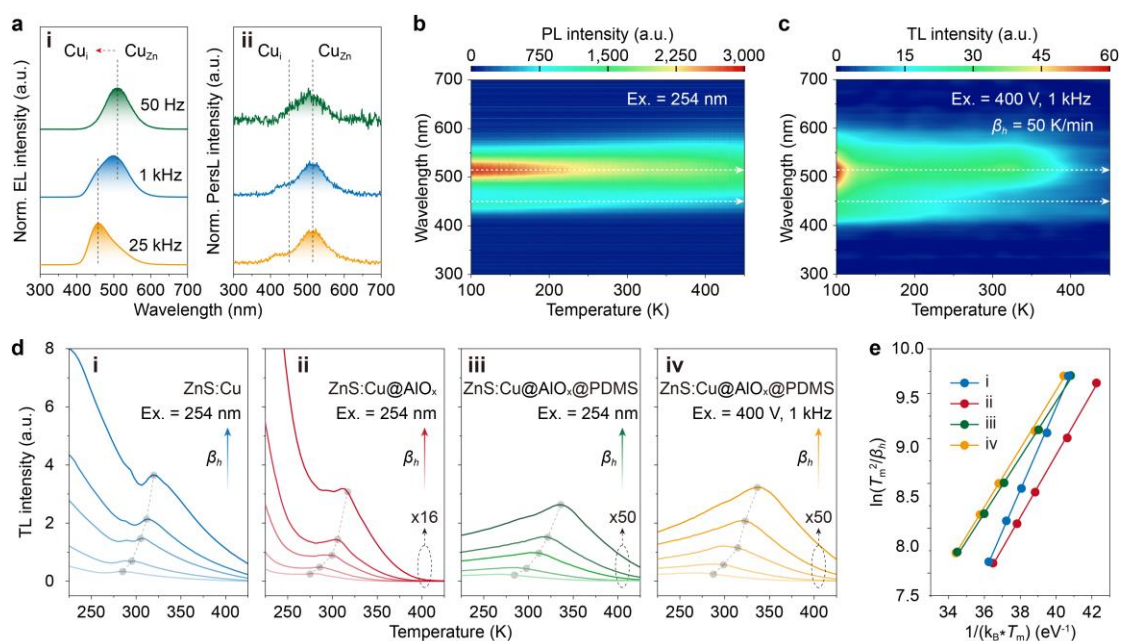
Figure 6.4   Luminescent center and trap profiles of the ZnS:Cu@AlOx@PDMS-based systems. **a**, Normalized EL and PersL of the ZnS:Cu@AlO$_x$@PDMS-based ELD under and after AC charging at various frequencies of 50 Hz, 1 kHz, and 25 kHz (V = 400 V and T = 100 K). **b**, PL emission wavelength−temperature contour plots of the ZnS:Cu@AlO$_x$@PDMS film excited with 254 nm UV light. **c**, TL glow contour map of the ZnS:Cu@AlO$_x$@PDMS-based ELD with a heating rate of 50 K/min after AC charging (V = 400 V, F = 1 kHz, T = 100 K, and t$_{ex}$ = 1 min). **d**, TL glow curves of the ZnS:Cu phosphor (i), ZnS:Cu@PDMS film (ii), and ZnS:Cu@PDMS-based ELD under 254 nm excitation (iii, T = 100 K, and t$_{ex}$ = 1 min) and the ZnS:Cu@PDMS-based ELD under AC charging (iv, V = 400 V, F = 1 kHz, T = 100 K, and t$_{ex}$ = 1 min) with different heating rates (5, 10, 20, 30, and 50 K/min). **e**, Estimation of the trap depths of the ZnS:Cu phosphor (i), ZnS:Cu@PDMS film (ii), and ZnS:Cu@PDMS-based ELD under 254 nm excitation (iii) and ZnS:Cu@PDMS-based ELD under AC charging (iv, V = 400 V, F = 1 kHz, T = 100 K, and t$_{ex}$ = 1 min) by using the Randall-Wilkins model.

The time-temperature indicator (TTI) can transform the time-temperature history into easily accessible information, facilitating the monitoring of perishable foods, pharmaceuticals, or specialty chemicals throughout the entire transport-storage process.[37] The liberation of trapped carriers in PersL systems is a kinetic process dependent on thermal activation, and this process exhibits a temperature-time relationship similar to the loss of active ingredients in transporting objects. We developed PersL-type TTI technologies for both inorganic and organic systems using UV light excitation; however, serious concerns remain regarding their photobiological toxicity, photothermal effect, and operational convenience.[9,38] Herein, we first achieved AC charging of PersL TTIs in inorganic systems (Figure 6.5a). As shown in Figures 6.5b-6.5d, after lowering the atmospheric temperature to 100 K, the film underwent a 3 min AC charging process. Subsequently, the temperature was increased to specific values, and the film was maintained for 3 minutes to replicate the indicator

conditions. Finally, the stored electrical energy was released through TL measurements. Notably, the stored energy in the label rapidly dissipates when exposed to temperatures exceeding 300 K ($I_{>300K} < 50\% I_{100K}$). As shown in Figure 6.5e, to generate the simulated standard curve for the label maintained at 250 K over various storage times, we initially lowered the atmospheric temperature to 250 K and charged the label at 400 V and 1 kHz for 3 min. Subsequently, the label was maintained at 250 K for durations of 1, 3, 6, 12, and 24 h. The stored electrical energy was quantified via the TL measurements, and the standard curve was established by exponentially fitting the integral intensity of the TL spectra. This curve was used to assess the duration and safety of transporting medical items. (Figures 6.5f-6.5g).
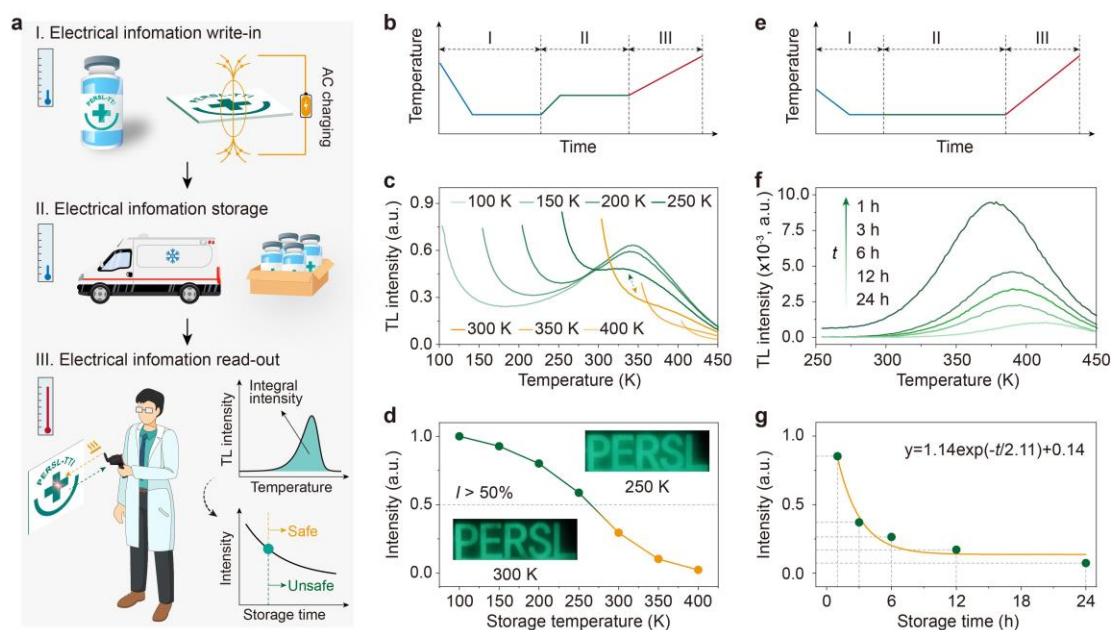
Figure 6.5 Demonstration of a ZnS:Cu@AlOx@PDMS ELD with electrical energy storage properties for TTI applications. **a**, Schematic of PersL TTIs used for electrical information write-in (I), storage (II), and read-out (III) processes. The electrical energy could be stored in the indicator at 250 K after the AC charging is ceased. Then, the medical chemicals are transported to the hospital at a certain time. The energy stored in the label (the integral intensity of the TL spectra) is monitored by

heating the label and is then compared to a standard curve to determine whether the medical chemicals have been mutated. **b**, Actual temperature profile for different storage temperatures. **c**, TL glow curves after being stored at different temperatures (100, 150, 200, 250, 300, 350, and 400 K) for 5 min. **d**, Normalized integral intensity of the TL spectrum for each storage temperature. Insert: Photographs of labels charged at 250 and 300 K for 60 s. **e**, Actual temperature profile for different storage times. **f**, TL glow curves after being maintained at 250 K for different storage times (1, 3, 6, 12, and 24 h). **g**, Normalized optical signal intensity as a function of delay time. In the write-in and read-out cycles, the label was irradiated (write-in, I) by AC for 5 min and heated (read-out, III) to 450 K at a heating rate of 50 K/min.

6.5 Conclusion

In conclusion, we propose a versatile methodology to achieve electrically chargeable inorganic PersL with tunable emission wavelengths and trap depths, leveraging conventional AC-driven device architectures. Coating inorganic PersL phosphors with AlO_x and embedding them in PDMS leads to shallower trap depths, while the high dielectric constant of AlO_x and the ultrathin thickness of the EML ensure a uniform electric field distribution during electrical excitation; this facilitates the efficient charge separation at the luminescent center and electron capture at the trap. The trap depths remain consistent at approximately 0.32±0.01 eV after AC charging and light irradiation is ceased; this result indicates that the electric field can function as an alternative excitation source. This work has potential to advance the understanding of inorganic PersL charged with different excitation sources and can extend the applications of inorganic semiconductors in multifunctional photoelectric devices.

6.6 Reference

[1] H. Yamamoto, T. Matsuzawa, *J. Lumines.* **1997**, 72-74, 287-289.

[2] Y. Li, M. Gecevicius, J. Qiu, *Chem. Soc. Rev.* **2016**, 45, 2090-2136.

[3] X. Ou, X. Qin, B. Huang, J. Zan, Q. Wu, Z. Hong, L. Xie, H. Bian, Z. Yi, X. Chen, Y. Wu, X. Song, J. Li, Q. Chen, H. Yang, X. Liu, *Nature* **2021**, 590, 410-415.

[4] T. Maldiney, A. Bessiere, J. Seguin, E. Teston, S. K. Sharma, B. Viana, A. J. Bos, P. Dorenbos, M. Bessodes, D. Gourier, D. Scherman, C. Richard, *Nat. Mater.* **2014**, 13, 418-426.

[5] Q. Miao, C. Xie, X. Zhen, Y. Lyu, H. Duan, X. Liu, J. V. Jokerst, K. Pu, *Nat. Biotechnol.* **2017**, 35, 1102-1110.

[6] F. Chun, B. Zhang, Y. Gao, X. Wei, Q. Zhang, W. Zheng, J. Zhou, Y. Guo, X. Zhang, Z. Xing, X. Yu, F. Wang, *Nat. Photon.* **2024**, 18, 856-863.

[7] J. Xu, S. Tanabe, *J. Lumines.* **2019**, 205, 581-620.

[8] R. Kobe, C. Adachi, *Nature* **2017**, 550, 384-387.

[9] C. Lin, Z. Wu, H. Ma, J. Liu, S. You, A. Lv, W. Ye, J. Xu, H. Shi, B. Zha, W. Huang, Z. An, Y. Zhuang, R.-J. Xie, *Nat. Photon.* **2024**, 18, 350-356.

[10] C. Lin, Z. Wu, J. Ueda, R. Yang, S. You, A. Lv, W. Deng, Q. Du, R. Li, Z. An, J. Xue, Y. Zhuang, R.-J. Xie, *Adv. Mater.* **2024**, e2401000.

[11] J. Ueda, S. Miyano, S. Tanabe, *ACS Appl. Mater. Interfaces* **2018**, 10, 20652-20660.

[12] L. Liang, J. Chen, K. Shao, X. Qin, Z. Pan, X. Liu, *Nat. Mater.* **2023**, 22, 289-304.

[13] W. Zhao, Z. He, B. Z. Tang, *Nat. Rev. Mater.* **2020**, 5, 869-885.

[14] H. Lin, J. Xu, Q. Huang, B. Wang, H. Chen, Z. Lin, Y. Wang, *ACS Appl. Mater. Interfaces* **2015**, 7, 39, 21835-21843.

[15] H. Lv, H. Tang, Y. Cai, T. Wu, D. Peng, Y. Yao, X. Xu, *Angew. Chem. Int. Ed.* **2022**, 61, e202204209.

[16] R. Kabe, N. Notsuka, K. Yoshida, C. Adachi, *Adv. Mater.* **2016**, 28, 655-660.

[17] S. Tan, K. Jinnai, R. Kabe, C. Adachi, *Adv. Mater.* **2021**, 33, 2008844.

[18] W. Qiu, D. Liu, Z. Chen, Y. Gan, S. Xiao, X. Peng, D. Zhang, X. Cai, M. Li, W. Xie, G. Sun, Y. Jiao, Q. Gu, D. Ma, S.-J. Su, *Matter* **2023**, 6, 1231-1248.

[19] H.-T. Feng, J. Zeng, P.-A. Yin, X.-D. Wang, Q. Peng, Z. Zhao, J. W. Y. Lam, B. Z. Tang, *Nat. Commun.* **2020**, 11, 2617.

[20] Y. Yu, Q. Ma, H. Ling, W. Li, R. Ju, L. Bian, N. Shi, Y. Qian, M. Yi, L. Xie, W. Huang, *Adv. Funct. Mater.* **2019**, 29, 1904602.

[21] J. Peng, S. Sokolov, D. Hernangomez-Perez, F. Evers, L. Gross, J. M. Lupton, J. Repp, *Science* **2021**, 373, 452-456.

[22] L. Wang, L. Xiao, H. Gu, H. Sun, *Adv. Optical Mater.* **2019**, 7, 1801154.

[23] A. A. Douglas, J. F. Wager, D. C. Morton, J. B. Koh, C. P. Hogh, *Appl. Phys. Lett.* **1993**, 63, 231-233.

[24] Y. Zhuang, X. Li, F. Lin, C. Chen, Z. Wu, H. Luo, L. Jin, R.-J. Xie, *Adv. Mater.* **2022**, 34, 2202864.

[25] G. Lee, S. Song, W. H. Jeong, C. Lee, J. S. Kim, J. H. Lee, J. Choi, H. Choi, Y. Kim, S. J. Lim, S. M. Jeong, *Small*, **2024**, e2307089.

[26] P. Dorenbos, *Phys. Rev. B* **2013**, 87, 035118.

[27] H. Arbell, A. Halperin, *Phys. Rev.* **1960**, 117, 45-52.

[28] Q. Peng, G. W. Cong, S. C. Qu, Z. G. Wang, *Optical Mater.* **2006**, 29, 313-317.

[29] S. Kawashima, *Jpn. J. Appl. Phys.* **1996**, 5, 1161.

[30] F. Clabau, X. Rocquefelte, T. Le Mercier, P. Deniard, S. Jobic, M. H. Whangbo,

Chem. Mater. **2006**, 18, 3212-3220.

[31] K. B. Lin, Y. H. Su, *Appl. Phys. B* **2013**, 113, 351-359.

[32] S. W. Shin, J. P. Oh, C. W. Hong, E. M. Kim, J. J. Woo, G. S. Heo, J. H. Kim, *ACS Appl. Mater. Interfaces* **2016**, 8, 1098-1103.

[33] K. Urabe, S. Shionoya, A. Suzuki, *J. Phys. Soc. Jpn.* **1968**, 25, 1611-1617.

[34] Y.-T. Nien, I.-G. Chen, *Appl. Phys. Lett.* **2006**, 89, 261906.

[35] S. M. Jeong, S. Song, H. Kim, *Nano Energy* **2016**, 21, 154-161.

[36] A. J. J. Bos, *Materials* **2017**, 10, 1357.

[37] W. A. M. McMinn, T. R. A. Magee, *Food Bioprod. Process.* **1997**, 75, 223-231.

[38] Y. Song, J. Du, R. Yang, C. Lin, W. Chen, Z. Wu, H. Lin, X. Chen, Y. Zhuang, R.-J. Xie, *Adv. Optical Mater.* **2023**, 11, 2202654.

6.7 Supporting Information
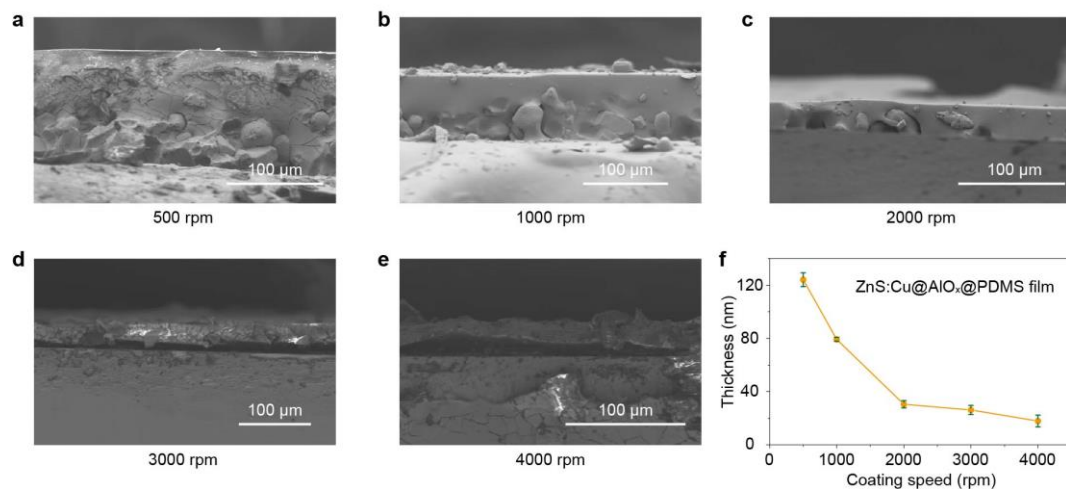
Figure S6.1 SEM images of the ZnS:Cu@AlOx@PDMS film manufactured at various spin-coating speeds: (**a**) 500 rpm, (**b**) 1000 rpm, (**c**) 2000 rpm, (**d**) 3000 rpm, and (**e**) 4000 rpm. **f**, Thickness distribution of ZnS:Cu@AlOx@PDMS film at various spin-coating speeds. The films prepared at spin-coating speeds of 500 rpm and 1000 rpm adhere to the tape, whereas those prepared at speeds exceeding 2000 rpm are too thin to be peeled off and were tested after breaking the glass.
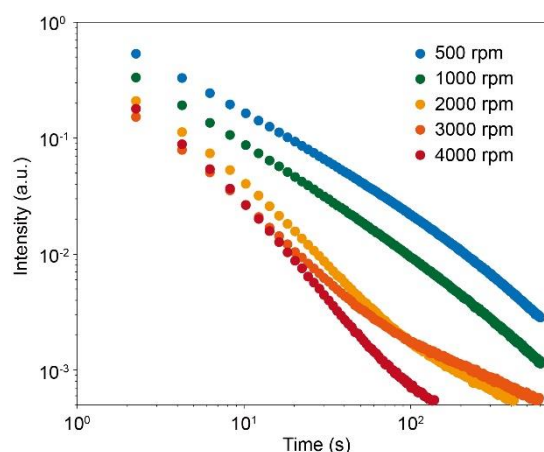
Figure S6.2 Spin-coating speed dependent PersL decay curves (Setting excitation time = 1 min, temperature = 250 K, voltage = 400 V and frequency = 1 kHz).
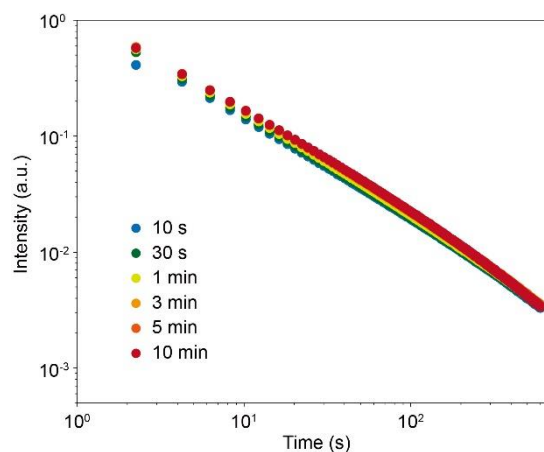
Figure S6.3 Time dependent PersL decay curves (Setting temperature = 250 K, voltage = 400 V and frequency = 1 kHz).
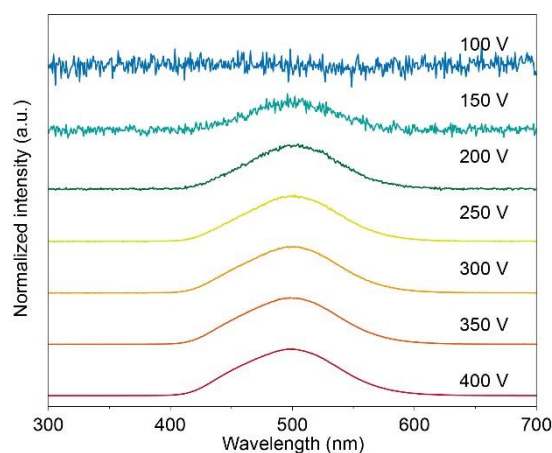
Figure S6.4 Normalized EL spectra of ZnS:Cu@AlO$_x$@PDMS-based ELD under AC charging (frequency = 1 kHz) at voltage range from 100 V to 400 V.
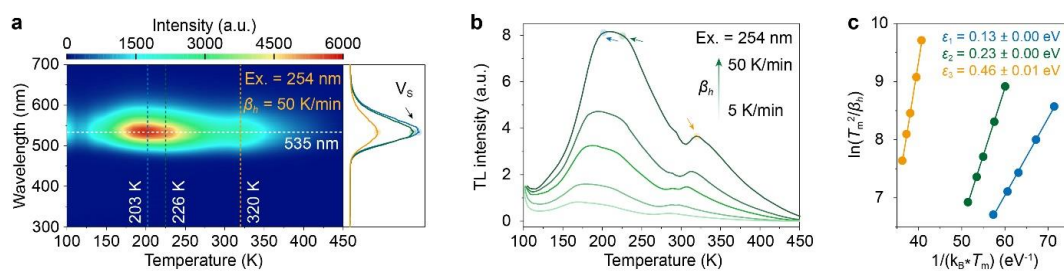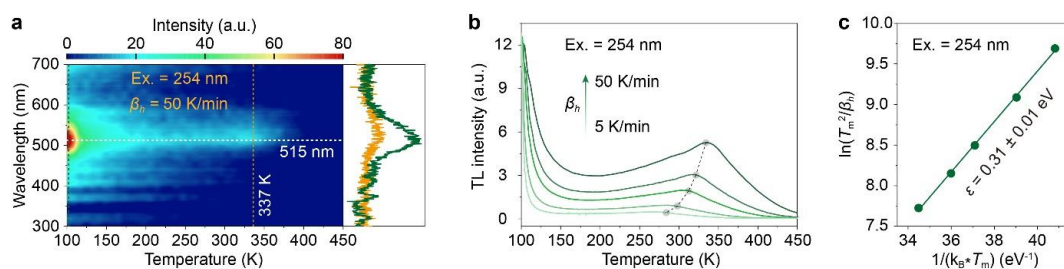

Figure S6.5 TL feature of the ZnS:Cu phosphor after 254 nm UV light charging.

a, Intensity-wavelength-temperature TL glow graph (3D-plot) with a heating rate of 50 K/min. PersL spectra (right part) are obtained from the 3D-plot. **b**, TL glow curves with different heating rates from 5, 10, 20, 30 to 50 K/min (t_{ex} = 1 min, T = 100 K). **c**, Estimation of the trap depth by using the Randall-Wilkins model.
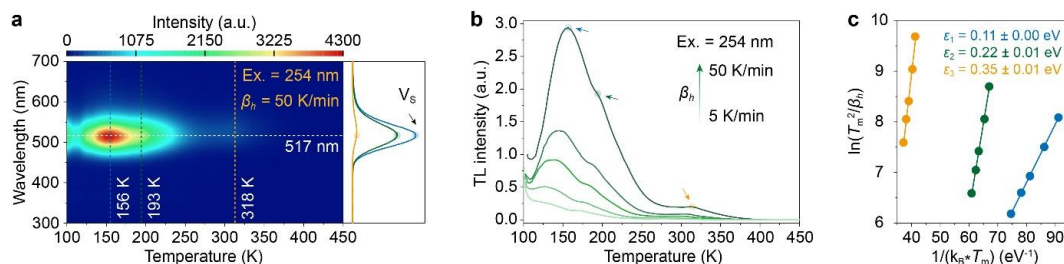
Figure S6.6 TL feature of the ZnS:Cu@AlO$_x$ phosphor after 254 nm UV light charging. **a**, Intensity-wavelength-temperature TL glow graph (3D-plot) with a heating rate of 50 K/min. PersL spectra (right part) are obtained from the 3D-plot. **b**, TL glow curves with different heating rates from 5, 10, 20, 30 to 50 K/min (t_{ex} = 1 min, T = 100 K). **c**, Estimation of the trap depth by using the Randall-Wilkins model.

Figure S6.7 TL feature of the ZnS:Cu@AlO$_x$@PDMS film after 254 nm UV light charging. **a**, Intensity-wavelength-temperature TL glow graph (3D-plot) with a heating rate of 50 K/min. PersL spectra (right part) are obtained from the 3D-plot. **b**, TL glow curves with different heating rates from 5, 10, 20, 30 to 50 K/min (t_{ex} = 1 min, T = 100 K). **c**, Estimation of the trap depth by using the Randall-Wilkins model.
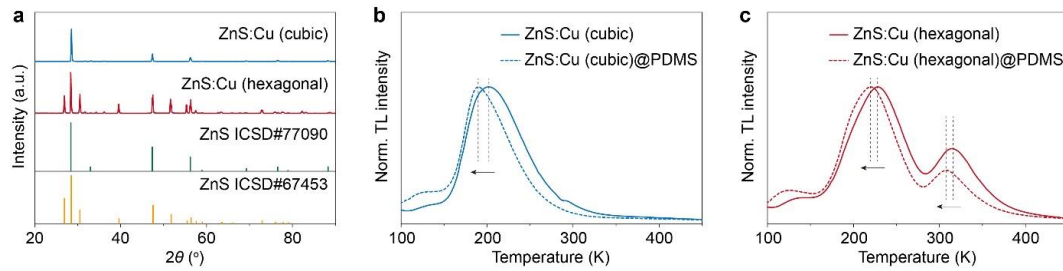
Figure S6.8 TL feature of the ZnS:Cu phosphor and ZnS:Cu@PDMS film after 254 nm UV light charging. **a**, XRD patterns of pure cubic and hexagonal phases of ZnS:Cu powders. **b**, TL glow curves at a heating rate of 50 K/min for cubic phase ZnS:Cu phosphor and its PDMS-coated film. **c**, TL glow curves at a heating rate of 50 K/min for hexagonal phase ZnS:Cu phosphor and its PDMS-coated film.
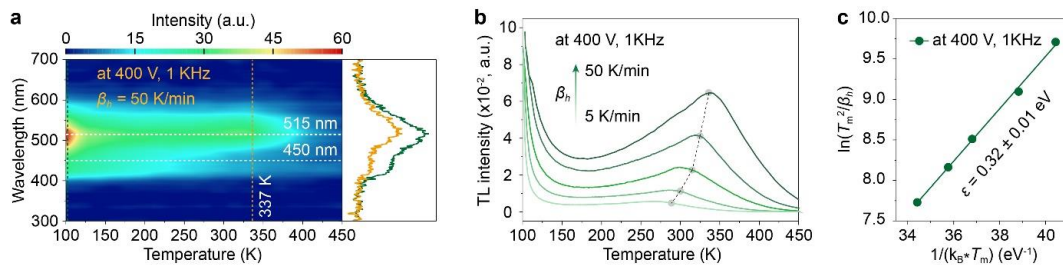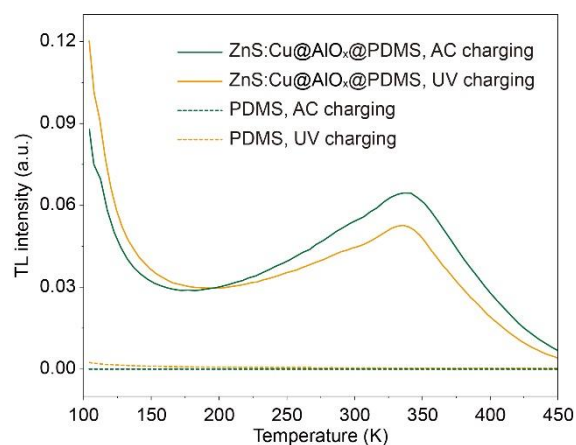

Figure S6.9 TL feature of the ZnS:Cu@AlOₓ@PDMS film after AC charging. **a**, Intensity-wavelength-temperature TL glow graph (3D-plot) with a heating rate of 50 K/min. PersL spectra (right part) are obtained from the 3D-plot. **b**, TL glow curves with different heating rates from 5, 10, 20, 30 to 50 K/min (V = 400 V, F = 1 kHz, t_{ex} = 1 min, T = 100 K). **c**, Estimation of the trap depth by using the Randall-Wilkins model.

Figure S6.10 TL feature of pure PDMS film. TL glow curves at a heating rate of 50 K/min for PDMS film and ZnS:Cu@AlOx@PDMS film based ELD after 254 nm UV light (t_{ex} = 1 min, T = 100 K) and AC (V = 400 V, F = 1 kHz, t_{ex} = 1 min, T = 100 K) charging.
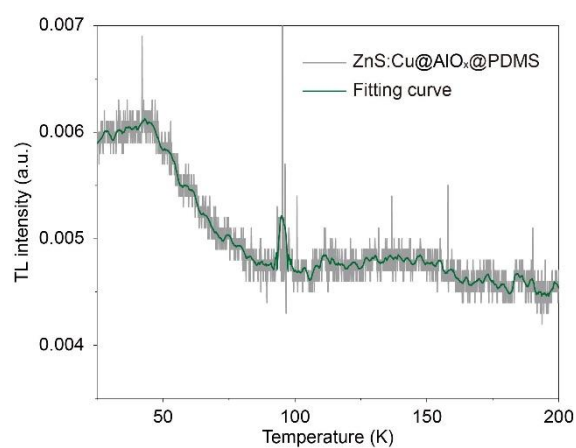
Figure S6.11 TL glow curves of the ZnS:Cu@AlO$_x$@PDMS film from 25 K to 200 K (t_{ex} = 1 min, Ex. = 300 nm, T = 10 K, heating rate = 5 K/min).
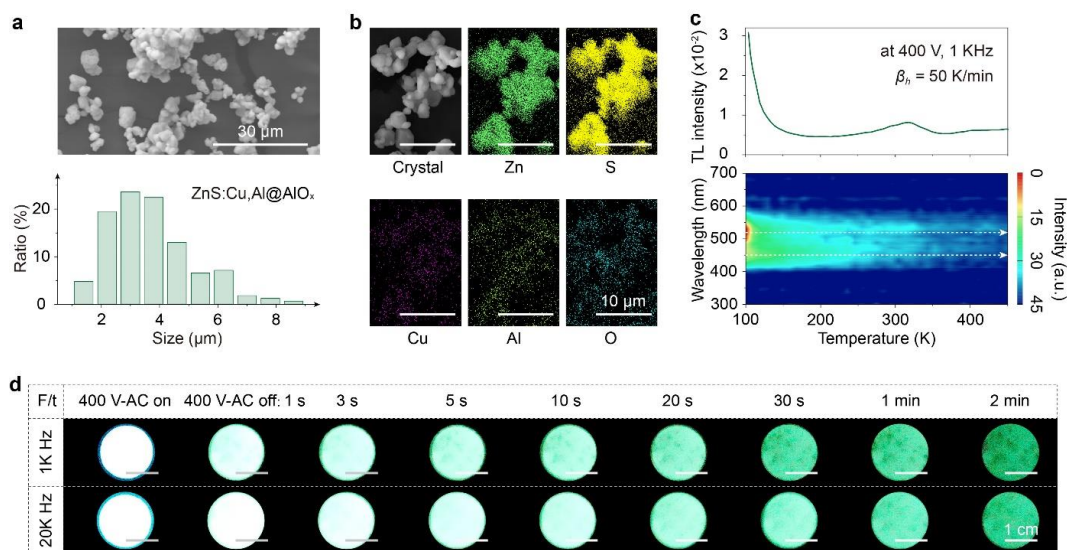
Figure S6.12 Photophysical properties of ZnS:Cu,Al@AlOₓ phosphor and its ELD. **a**, SEM image and particle size distribution of ZnS:Cu,Al@AlOₓ powder. **b**, Elemental distribution mapping of ZnS:Cu,Al@AlOₓ powder. **c**, TL glow curve (top) and TL glow contour mapping (bottom) with different heating rates at 50 K/min of ZnS:Cu,Al@AlOₓ@PDMS-based ELD under AC charging (V = 400 V, F = 1 kHz, T = 100 K, and t_{ex} = 1 min). **d**, Photographs of ELD under AC charging (T = 200 K, V = 400 V, F = 1 kHz and 20 kHz, and t_{ex} = 3 min) and after ceasing the AC charging.
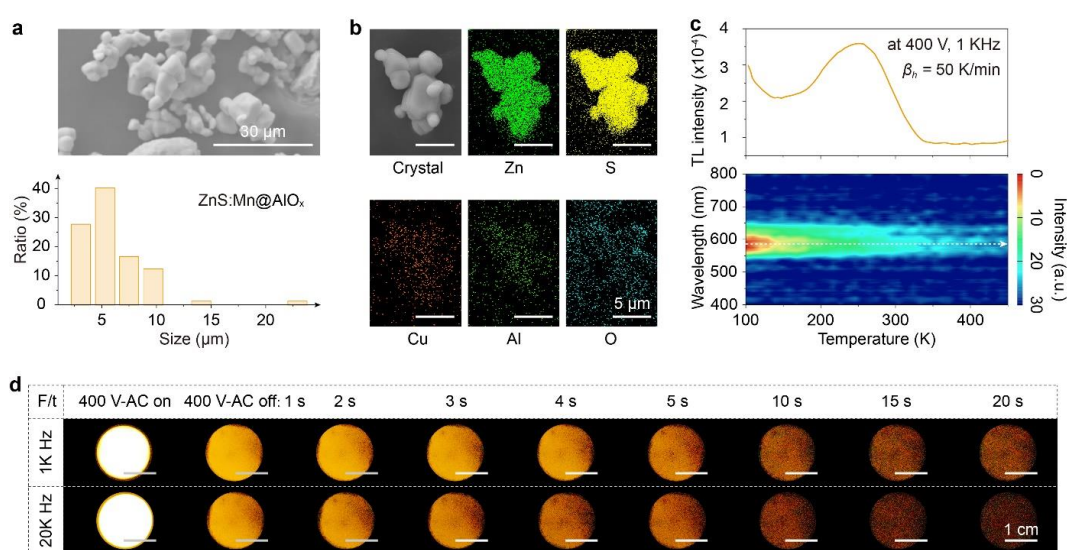
Figure S6.13 Photophysical properties of ZnS:Mn@AlOₓ phosphor and its ELD.

a, SEM image and particle size distribution of ZnS:Mn@AlO$_x$ powder. **b**, Elemental distribution mapping of ZnS:Mn @AlO$_x$ powder. **c**, TL glow curve (top) and TL glow contour mapping (bottom) with different heating rates at 50 K/min of ZnS:Mn@AlO$_x$@PDMS-based ELD under AC charging (V = 400 V, F = 1 kHz, T = 100 K, and t_{ex} = 1 min). **d**, Photographs of ELD under AC charging (T = 200 K, V = 400 V, F = 1 kHz and 20 kHz, and t_{ex} = 3 min) and after ceasing the AC charging.

List of Publications

[1] **<u>Cunjian Lin</u>**, Rujun Yang, Yang Li, Chenhan Zhan, Yajing Wang, Zixuan Zhang, Zishuang Wu, Da Xiong, Wenting Deng, Shihai You, Ying Lv, Yixi Zhuang, Rong-Jun Xie, Jumpei Ueda*, Deep trap management in organic persistent luminescence for multi-mode optical information storage, *Advanced Optical Materials*, **2024**, under revision. (Q1, IF: 8.0, **Chapter 3**)

[2] **<u>Cunjian Lin</u>**, Zishuang Wu, Jumpei Ueda, Rujun Yang, Shihai You, Anqi Lv, Wenting Deng, Qiping Du, Renfu Li, Zhongfu An, Jie Xue,* Yixi Zhuang,* and Rong-Jun Xie*, Enabling visible-light-charged near-infrared persistent luminescence in organics by intermolecular charge transfer, *Advanced Materials*, **2024**, 2401000. (Q1, IF: 29.4, **Chapter 4**)

[3] Zishuang Wu,[#] **<u>Cunjian Lin</u>**,[#] Rujun Yang, Chenhan Zhan, Yajing Wang, Kai-Ning Tong, Shihai You, Ying Lv, Guodan Wei, Jumpei Ueda,* Yixi Zhuang,* Rong-Jun Xie*, Trap-induced persistent luminescence in organic light-emitting diodes, *InfoMat*, **2024**, accepted. (Q1, IF: 22.7, **Chapter 5**)

[4] **<u>Cunjian Lin</u>**,[#] Rujun Yang,[#] Zishuang Wu, Yajing Wang, Chenhan Zhan, Hirohisa Miyata, Xiankan Zeng, Yuantian Zheng, Shihai You,* Ying Lv,* Yixi Zhuang, Rong-Jun Xie, Jumpei Ueda*, Electrically chargeable inorganic persistent luminescence in an alternating current driven electroluminescent device, *Commun. Mater.* **2024**, under revision. (**Chapter 6**)

Presentations in Conferences

[1] **<u>Cunjian Lin</u>**, Yixi Zhuang, Rong-Jun Xie, and Jumpei Ueda, Full-color ultralong afterglow in nitrogen-doped carbon dots (*Poster presentation*), The Ceramic Society of Japan, 2023.10, Hokuriku, Japan.

[2] **<u>Cunjian Lin</u>**, Jie Xue, Yixi Zhuang, Rong-Jun Xie, and Jumpei Ueda, Enabling visible-light-charged near-infrared persistent luminescence in organics by intermolecular charge transfer (*Poster presentation*), JAIST International Symposium on Nano-Materials for Novel Devices, 2024.01, Kanazawa, Japan.

[3] **<u>Cunjian Lin</u>**, Shihai You, Ying Lv, and Jumpei Ueda, Electrically driven inorganic persistent luminescence (*Oral presentation*), The Ceramic Society of Japan Annual Meeting, 2024.03, Kumamoto, Japan.

[4] **<u>Cunjian Lin</u>** and Jumpei Ueda, Deep trap management in organic persistent luminescence for multi-mode optical information storage (*Poster presentation*), The 16th workshop of the JSAP Frontier Research Group of Extreme Excitation and Quantum Energy Conversion and the 32nd Workshop on Next-generation Front-edge Optical Science Research, 2024.07, Fukui, Japan.

[5] **<u>Cunjian Lin</u>**, Jie Xue, Yixi Zhuang, Rong-Jun Xie, and Jumpei Ueda, Enabling visible-light-charged near-infrared persistent luminescence in organics (*Oral presentation*), Phosphor Safari 2024 and the 13th International Symposium on Luminescent Materials, 2024.08, Taipei, Taiwan. **Best Award Oral Presentation**.

Acknowledgements

Cunjian Lin

2024.11.18